A Study of Whistlers and Related VLF Phenomena

by

Brett Delport

Submitted in fulfillment of the requirements for the degree of Doctor of Philosophy in the School of Chemistry and Physics, University of KwaZulu-Natal.

As the candidate's Supervisor I have/have not approved this thesis for submission

Signed: ..... Name: ..... Date: .....

Durban, December 2012.

Abstract

Whistlers are naturally occurring Very Low Frequency (VLF) phenomena which are the result of lightning-radiated electromagnetic waves propagating in Earth's plasma environment. Major research into whistlers and their generation began in 1951 and since then much has been discovered about them. This has allowed whistlers to be used as magnetospheric probes. Many issues concerning whistlers are still disputed, however, such as the relationship between the lightning location and the conjugate point of the receiver. A correlation between whistlers detected by the DEMETER satellite above South Africa and lightning located by WWLLN was used to determine the source region for these whistlers. The whistlers were found to originate from lightning strokes as far away as $10000\ \mathrm{km}$. This result is statistically significant.

During the course of this research an interesting observation of chorus was made on Marion Island. Since this was the first observation of chorus made on the sub-antarctic Marion Island, conditions surrounding the event were studied in great detail. This led to several interesting observations about the nature of this observation. In particular, during the evolution of the emission, it transformed to hiss, which makes this observation relevant to recent results suggesting that hiss is generated by chorus. It was also found that Marion Island was close to the plasmapause during the observation, which has further implications related to the chorus-hiss relationship.

A study of the occurrence of twin whistlers received at Rothera and SANAE IV was conducted. These were whistlers which had propagated from a single ionospheric exit point to both receivers. Rothera and SANAE IV share the same whistler source region, yet the average number of whistlers received at Rothera is an order of magnitude greater than that received at SANAE IV. The twin whistler analysis showed that the most probable reason for this disparity is that whistlers from the source region enter the waveguide preferentially closer to Rothera, making it more likely for them to be received at Rothera than SANAE IV. These results have implications on the nature of sub-ionospheric propagation of whistlers, which is not the same as that of spherics.

Finally, a method for tracking tropical cyclones using lightning locations from WWLLN was developed. During the course of this thesis, tropical cyclone Irena was the result of damage on the east coast of South Africa. This presented an opportunity to investigate the ability of WWLLN data to describe the passage of these destructive phenomena near South Africa. The details of this new method are discussed. While the algorithm developed has room for improvement, its performance was tested on the recent tropical cyclone Irina which occurred during 2012.

PREFACE

The experimental work presented in this dissertation was carried out in the School of Chemistry and Physics, University of KwaZulu-Natal, Westville Campus from February 2010 to December 2012, under the supervision of Dr. Andrew B. Collier.

These studies represent original work by the author and have not otherwise been submitted in any form for any degree or diploma to any tertiary institution. Where use has been made of the work of others it is duly acknowledged in the text.

DECLARATION 1 - PLAGIARISM

I, ..., declare that

1. The research reported in this thesis, except where otherwise indicated, is my original research.
2. This thesis has not been submitted for any degree or examination at any other university.
3. This thesis does not contain other persons' data, pictures, graphs or other information, unless specifically acknowledged as being sourced from other persons.
4. This thesis does not contain other persons' writing, unless specifically acknowledged as being sourced from other researchers. Where other written sources have been quoted, then:
   (a) Their words have been re-written but the general information attributed to them has been referenced
   (b) Where their exact words have been used, then their writing has been placed in italics and inside quotation marks, and referenced.
5. This thesis does not contain text, graphics or tables copied and pasted from the Internet, unless specifically acknowledged, and the source being detailed in the thesis and in the References sections.

Signed: .....

DECLARATION 2 - PUBLICATIONS

DETAILS OF CONTRIBUTION TO PUBLICATIONS that form part and/or include research presented in this thesis (include publications in preparation, submitted, in press and published and give details of the contributions of each author to the experimental work and writing of each publication)

- B. Delport, A. B. Collier, J. Lichtenburger, C. J. Rodger, M. Parrot, M. A. Clilverd, and R. H. W. Friedel. Simultaneous observation of chorus and hiss near the plasmapause. *Journal of Geophysical Research*, (in press).
- B. Delport and A. B. Collier, J. Lichtenberger, P. Steinbach, and M. Parrot. Correlating fractional hop whistlers detected on DEMETER with WWLLN lightning. *Proceedings of the SAIP Annual Conference, Pretoria, South Africa* (2012).
- B. Delport and A. B. Collier, J. Lichtenberger, P. Steinbach, and M. Parrot. Correlating fractional hop whistlers detected on DEMETER with WWLLN lightning. *In preparation*.
- B. Delport and A. B. Collier. Lightning through VLF-coloured spectacles. *Proceedings of the South African Society for Atmospheric Sciences conference, Cape Town, South Africa* (2012).

Signed: .....

Acknowledgements

I would like to thank SANSA Space Science, for funding me throughout the course of this degree. The research leading to these results has received funding from the European Community's Seventh Framework Programme (FP7/2007-2013) under grant agreement 263218. I would like to thank J. J. Berthelier, the PI of the DEMETER electric field experiment for the use of their data. Also a thanks to our friends and collaborators from Hungary, Dr János Lichtenberger and Dr Péter Steinbach, for the access to whistler data from various receivers, and help with the use of their code, and for treating me so well during my trips to their homeland. I would like to acknowledge the South African Weather Service who provided me with data from the South African Lightning Detection Network. Dr. Reiner H. W. Friedel has my thanks for the LANL satellite data used, and Dr. Mark A. Clilverd for the access to data from Halley Bay. A big thank you to Dr. Jyrki Manninen and Tero Raita and the SGO who were such gracious hosts during the month I spent in Finland. I also wish to thank the World Wide Lightning Location Network (http://wwlln.net), a collaboration among over 50 universities and institutions, for providing the global lightning location data used in this thesis.

Of course, a big thank you to my supervisor, Dr. Andrew Collier, for the guidance provided, the friendship offered, and of course for those bunnies at lunch. Hopefully all the long days (and nights no doubt) of reading drafts and suggesting corrections have bared the fruit you hoped for. I would also like to thank my peers, Etienne Koen, Farran Henning and Sherry Bremner, as well as Fred Fourie, who each took some time to proof-read my thesis. You all helped get it to where it is now. Next are my parents, who brought me up, provided my education, and gave me the chance to study at a university in the first place. Without the foundations you provided, I would not be where I am today. To my Monique, a huge thank you for all the support and encouragement, and for putting up with me being away all those times. This marks the end of a chapter for us too, and the beginning of a new one. Finally, I am in awe of God, who provided us with this unusual universe, which us curious human beings cannot but be surprised by. Without His grace and love, this would all be for naught.

Contents

List of Figures

List of Symbols

A	-	Anisotropy
AE	-	Auroral electrojet index
$\mathbf{B}$	-	Magnetic Field
B_{eq}	-	Equatorial magnetic field strength
c	-	Speed of light in a vacuum
Dst	-	Disturbance storm time index
$\mathbf{E}$	-	Electric Field
$\mathrm{K_p}$	-	Planetary K index
$\mathbf{k}$	-	Wave vector
L	-	McIlwain's Parameter
L_{pp}	-	L-value of the plasmapause
m	-	Mass
N	-	Particle Density
n_T	-	Total plasma mass density
n_{eq}	-	Equatorial electron density
n	-	Refractive index
q	-	Charge
r_L	-	Larmor radius
$T_\parallel$	-	Parallel particle temperature
$T_\perp$	-	Perpendicular particle temperature
$\mathbf{v}$	-	Velocity
$v_\parallel$	-	Velocity parallel to $\mathbf{B}$
$v_\perp$	-	Velocity perpendicular to $\mathbf{B}$
v_g	-	Group velocity

$W_{\parallel}$	-	Parallel energy
$W_{\perp}$	-	Perpendicular energy
α	-	Pitch angle
ϵ_0	-	Permativity of free space
λ	-	Geomagnetic latitude
λ_D	-	Debye Length
μ_0	-	Permeability of free space
μ_M	-	Magnetic moment
μ	-	Arithmetic mean
Ω	-	Gyrofrequency
Ω_e	-	Electron Gyrofrequency
ω	-	Wave frequency
ω_{LH}	-	Lower hybrid resonance frequency
σ	-	Standard deviation

Chapter 1

Introduction

1.1 VLF Emissions

Electromagnetic waves in the Very Low Frequency (VLF) range are actively studied phenomena which have numerous applications in Space Physics. These waves, which have both natural and man made sources on Earth, can be detected at virtually any location within Earth's atmosphere. They are also readily observed in space, and propagate within a magnetised plasma (such as that found within our magnetosphere) as a circularly polarised wave [Tsurutani and Lakhina, 1997]. The VLF band technically covers frequencies from 3 to 30 kHz, but more practically in space physics the range of frequencies considered is between 300 Hz and 50 kHz.

VLF waves have a large skin depth in water, meaning that VLF communication with submarines is possible while they are still submerged. Various navies have taken advantage of this fact by setting up VLF transmitters around the globe. These transmitters are large, and consume an incredible amount of energy to radiate VLF signals with powers as high as ~ 1 MW. These signals are readily observed by VLF antennas on the ground and can also be seen in space. They have been found to contribute to radiation belt losses [Sauvaud *et al.*, 2008]. These signals provide a free source for scientific applications, with many uses appearing in the literature, from the detection of solar flares [Thomson *et al.*, 2005] and energetic particle precipitation [Kulkarni *et al.*, 2008], to the more controversial prediction of seismic activity [Molchanov and Hayakawa, 1998].

Terrestrial lightning is the most obvious natural source of VLF waves. Lightning strokes are so frequent, and radiate with so much power, that the signals produced by lightning dominate most of the VLF band. These signals, called spherics (from the word atmospherics), are able to propagate a significant distance in the cavity between the conducting ionosphere and Earth's surface. This cavity is called the Earth Ionosphere WaveGuide (EIWG). VLF waves propagate within the EIWG with low attenuation rates compared to higher frequencies such as High Frequency (HF).

Other forms of VLF waves are frequently observed in recorded data as bursts of increased amplitude at specific frequencies. These bursts are frequently not random, but take on definite structure. These structured VLF phenomena are called VLF emissions, and they have many forms and generation mechanisms. These include commonly observed phenomena, like whistlers, chorus, and hiss, and other less commonly observed phenomena such as fallers (emissions whose frequency decrease with time), risers (emissions whose frequency increase with time) and hooks (emissions with a sharp "corner" in their structure). Sometimes, noise bursts occur with a fixed or nearly fixed period. These are referred to as periodic or quasiperiodic emissions. A detailed description of these and other emissions is presented in Helliwell [1965, Chapter 7.1].

The VLF frequency range largely overlaps with the human audio range, meaning that these signals can be heard if they are played through a speaker system. For instance, spherics manifest themselves aurally as short clicks, while a whistler has the sound of a decreasing whistling tone

lasting one or two seconds. The sound of chorus resembles the chirping of a flock of birds.

The history of VLF observations was discussed by Helliwell [1965, Chapter 2]. The first observations were on long range communication systems in the late 19^{th} and early 20^{th} centuries. Since the VLF wavelength is long, $\sim 10 - 100$ km, telephone and other communication cables act as antennas for receiving these signals. Operators listening on these communication devices often heard whistling tones or chirps (or clicks, but these were already known to be produced by lightning). These were the first VLF listening devices used for scientific study, and from these the frequency range of whistlers was found to be from 300 to 1000 Hz.

In later research distinctions were made between 2 types of whistlers, long and short, referring to their duration. In long whistlers, the change in frequency was slower than in short whistlers. It was also noted that sometimes, whistlers were preceded by a spheric. Finally, their occurrence was linked to magnetic indices, such that more whistlers were observed during periods of higher geomagnetic activity [Helliwell, 1965, Chapter 2].

From these early beginnings, the field of VLF research has evolved to where it is now. For the purposes of this thesis, two particular VLF emissions will be introduced: whistlers and chorus.

1.1.1 Whistlers

The basic idea of whistler generation has been around since it was initially introduced by Storey [1953]. While this mechanism is rather complicated, with several steps, it can be simplified into a few independent processes.

When lightning strikes it radiates an intense, impulsive burst of electromagnetic radiation called a spheric. The VLF portion of this signal propagates in the EIWG with little attenuation, until it reaches a point at which it penetrates through the ionosphere into the magnetosphere. This signal is then guided by Earth's magnetic field lines to the conjugate hemisphere, where some portion of the energy enters back into the EIWG. During its passage through the magnetosphere the signal is dispersed by the magnetospheric plasma, transforming the initial impulse into a complex tone. The energy which enters into the EIWG travels virtually unhindered, experiencing only minimal dispersion and low attenuation rates, to the point at which it is detected by the receiver. The nose frequency arrives first, followed by frequencies above and below the nose frequency. For low- and mid-latitude whistlers the nose frequency is typically not visible in the spectra, resulting in a strictly descending tone structure. At high latitudes the nose frequency is visible. Above the nose frequency, the frequency increases with time.

Since the degree of dispersion is a function of the plasma density and magnetic field strength along the path traveled through the magnetosphere, as well as the path length, a number of useful parameters can be extracted from the study of the shape of a whistler trace. One can determine the integrated plasma density along the guiding field line, the latitude of the field line, and the magnetic field strength along the field line [Carpenter and Anderson, 1992].

Whistlers are frequently observed at South African VLF receivers at SANAE IV, Antarctica, and Marion Island. Sample spectrograms are displayed in Figure 1.1. A spectrogram shows the frequency evolution of a VLF emission, with frequency on the y-axis, and time on the x-axis. Amplitude is shown by the colour scale with black signifying high power, and white little power. Figure 1.1(a) shows a set of 3 fairly isolated whistlers recorded at SANAE IV. Figure 1.1(b), a detailed spectrogram of one of these whistlers, shows the complicated internal structure. One whistler is in fact made up of several whistler traces, each with a slightly different propagation path through the magnetosphere, resulting in slightly different dispersions. One can also see several traces which have the nose frequency visible around 37 s. Figure 1.1(c) shows a remarkable period of whistler observations made on Marion Island. There are many different and overlapping whistler traces, some of which are echoes of preceding ones. This shows the extent to which whistler activity levels can vary, with only a few whistlers observed at some times, and nearly

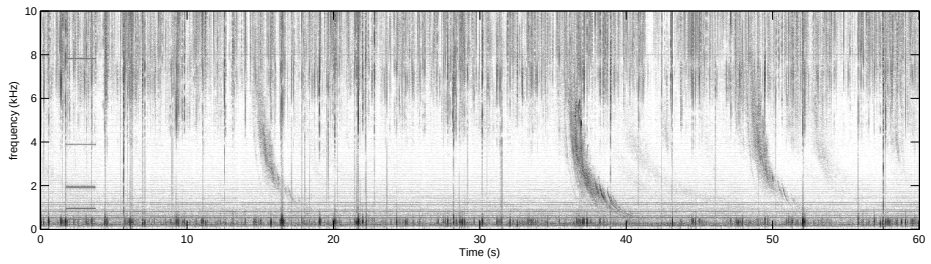

(a) Typical Whistlers

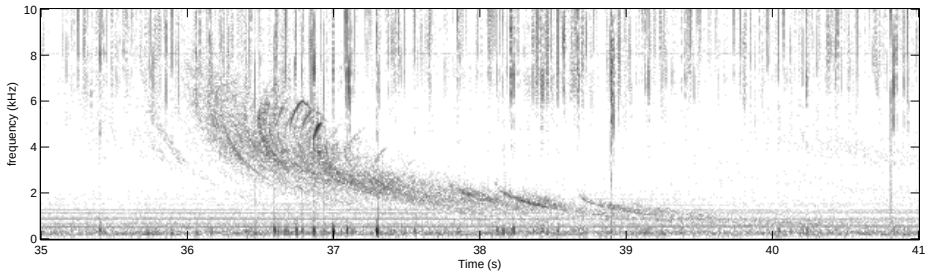

(b) Expanded Whistler

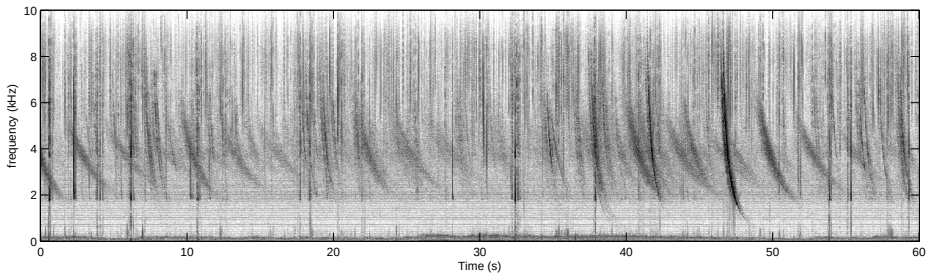

(c) Many Whistlers

Figure 1.1: Various whistler spectrograms. The top panel (a) shows whistlers recorded at SANAE IV. The middle panel (b) shows an expanded spectrogram of one of the whistlers above. The final panel (c) shows a period of high whistler activity at Marion Island. A number of whistler echoes are also evident in this spectrogram.

continuous whistlers observed at others. In all these spectrograms, spherics are visible as vertical lines. These have been generated by lightning in the same hemisphere as the receiver

1.1.2 Chorus

Chorus is described as a "*sequence of closely spaced, discrete events, often overlapping in time*" [Helliwell, 1965, Page 207]. They are usually rising tones, with each element lasting a very short time, on the order of a second. The emission sounds like the chirping of birds, and was thus named for its unique audio signature.

The current theory of chorus generation suggests that it is the result of Doppler Shifted Cyclotron Resonance. This is described by [Tsurutani and Smith, 1974], and references therein. Counter streaming electrons and VLF whistler mode waves in the magnetosphere resonate, causing energy exchange between the electrons and the waves, leading to an enhancement of the amplitude of the VLF waves at the resonance frequency. This in turn causes the electrons to be scattered and ultimately precipitated through collisions in the neutral atmosphere. The chorus waves then

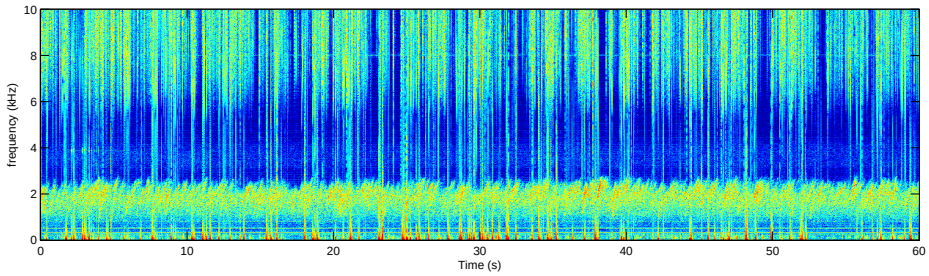

(a) Chorus at SANAE IV

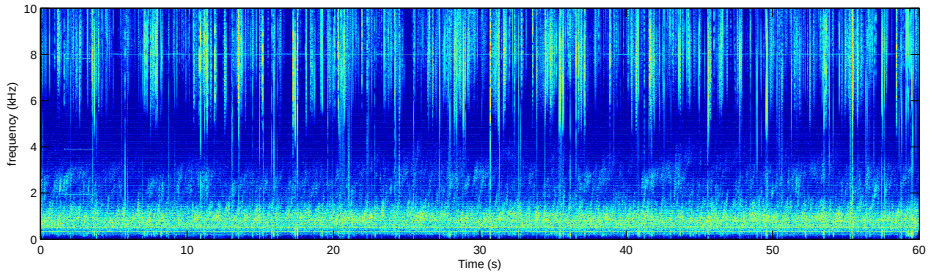

(b) Chorus at Marion Island

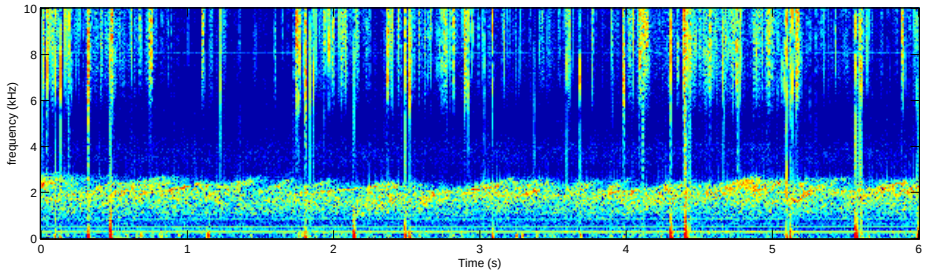

(c) Expanded Chorus

Figure 1.2: Various chorus spectrograms. (a) shows typical chorus at SANAE IV, with the chorus band found below 2 kHz while (b) shows chorus recorded at Marion Island, where the chorus band is at a higher frequency. (c) shows the finer structure of the chorus shown in (a), and the individual chorus elements can be discerned.

penetrate into the EIWG where they can be detected by VLF receivers. Due to the manner in which these emissions are generated, observations of chorus are often accompanied by particle precipitation.

Chorus emissions can be used as magnetospheric probes, as they can yield information about the particles which were in resonance with the waves. This makes their study as well as the development of the theory of chorus generation very important.

In Figure 1.2 three samples of chorus are plotted. These spectrograms use a different colour scale, with red indicating high power, and blue less power. These show fairly typical examples of chorus which can be observed at either Marion Island or SANAE IV, although the difference between the SANAE IV and Marion Island chorus is visible. This is to be expected, as the two receivers sample a significantly different part of the magnetosphere. This will be elaborated on later.

1.2 The Near-Earth Space Environment

The lower layer of the Earth's neutral atmosphere provides a relatively sheltered environment for biological life to sustain itself. This layer is called the troposphere and extends to a maximum altitude of $17\ \mathrm{km}$. Above this is the stratosphere, where particle densities are orders of magnitude lower than in the troposphere, and the ambient temperatures are well below $0^{\circ}{}^{\circ}\mathrm{C}$. In this region the Ozone layer is found, which protects the atmosphere below it from harmful UV radiation from the Sun. The stratosphere extends to an altitude $\sim 50\ \mathrm{km}$. Still higher is the mesosphere which extends to $90\ \mathrm{km}$, and finally the thermosphere which extends to $\sim 600\ \mathrm{km}$ altitude[Hargreaves, 1992, Page 98]. Beyond this layer is space, and while it is obvious that space is big, of particular interest here is the tiny bubble of space which surrounds the Earth, called the magnetosphere.

1.2.1 Ionosphere

Within the thermosphere the concentration of charged particles begins to increase, although the ratio of charged particles to neutrals remains small. This marks the layer of the atmosphere called the ionosphere. It extends from $\sim 100\ \mathrm{km}$ to $\sim\ 1000\mathrm{km}$. Within the ionosphere, several layers are defined based on their peak electron density. The lowest permanent layer of the ionosphere is called the E-region. Here typical densities of ionised particles are $2000\ \mathrm{cm}^{-3}$, although during the night the absence of the ionising action of the Sun results in densities lower by an order of magnitude. Next is the F-region (which is further divided into the F1- and F2-regions). Since this layer receives much more direct radiation from the Sun, it has much higher charged particle densities, with as much as $20 \times 10^5\ \mathrm{cm}^{-3}$ during the day, and as few as $2 \times 10^5\ \mathrm{cm}^{-3}$ at night. During the day, the ionising action of the Sun creates the D-region, which extends from around $60\ \mathrm{km}$ to just below the E-region. Densities here during the day are $\sim 1000\ \mathrm{cm}^{-3}$. Due to its low altitude, there is a much higher proportion of neutral atoms here than in the other ionospheric layers. At night, the charged particles in the D-region quickly recombine to form neutral atoms once again, and the layer virtually disappears [Ratcliffe, 1972, Page 37].

Since the ionosphere contains charged particles, it represents a conducting surface which reflects electromagnetic waves. The layer which a particular wave frequency reflects is determined by the density of charged particles, with higher frequencies requiring higher densities to effect this reflection. An ionosonde is a sounder, which measures the time it takes for particular frequencies to be reflected back to the ionosonde. They use the relationship between the reflection frequency and charged particle density to determine the density profile of the ionosphere. The peak density in the ionosphere occurs in the F2-region. The ionosphere is transparent to waves of higher frequencies. This maximum reflected frequency is labeled f_0F2. For this reason, terrestrial ionosondes can only measure the profile up to this height, and top side sounders are required to produce the profile above this height.

A useful model for the ionospheric profile, called the International Reference Ionosphere (IRI), can be used to determine a representative ionospheric profile at a particular location and time of day. Although there can be large discrepancies in the model results, they do provide a useful starting point for studying ionospheric densities. Profiles produced by the IRI are shown in Figure 1.3. Panel (a) shows day and night ionospheric profiles for Summer above South Africa and panel (b) shows similar profiles for Winter. These show that the densities at all heights are higher at both day and night during the Summer as compared to Winter. Also, the large differences in densities between day and night ionospheres are evident. In Winter the difference between day and night ionospheres is also greater than it is during Summer. The importance of these profiles for the propagation of (HF) waves is in the value of the peak density. At night, the ionosphere is transparent to a wider range of frequencies than during the day. For reasons which will become apparent later, propagation of VLF waves below the ionosphere is favoured during the night.

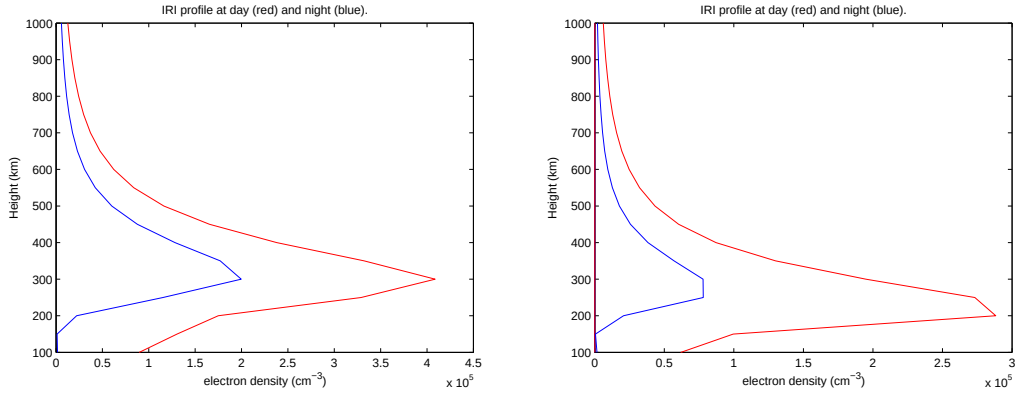

(a) Summer (b) Winter

Figure 1.3: Day (red) and night (blue) ionospheric profiles above South Africa during Summer (a) and Winter (b).

1.2.2 Magnetosphere

Beyond the ionosphere is the magnetosphere, where the physics is largely governed by the Earth's magnetic field. The magnetosphere extends out to the interface between the Earth's magnetic field and the solar wind, called the magnetosheath. Here, the solar wind which consists of energetic charged particles, is largely denied access into the magnetosphere by the Earth's magnetic field. Inside the magnetosphere, matter exists in the plasma state, which is defined as "*a quasi-neutral gas, which displays collective behavior*" [Chen, 1984]. Typical plasma (proton and electron) number densities in the magnetosphere outside of the plasmasphere are $\sim 10\ \mathrm{cm}^{-3}$.

Basic Plasma Physics

A plasma consists of atoms and molecules which have been fully iononised, and some neutral particles. As viewed from a sufficiently large distance (given by the Debye length, λ_D), the plasma is a neutral body. This defines quasi-neutrality. Within λ_D, however, the net charges of each of the ionised particles act on all the other ionised particles, which means that the plasma has a collective behavior. The motion of the plasma within the magnetosphere is governed by the Earth's magnetic field, via the Lorentz force, which is given by

$$\mathbf{F} = q(\mathbf{E} + \mathbf{v} \times \mathbf{B}), \tag{1.1}$$

which is the force $\mathbf{F}$ experienced by a particle with charge q, traveling with velocity $\mathbf{v}$, through electric and magnetic fields $\mathbf{E}$ and $\mathbf{B}$ respectively. This force results in several characteristic motions of the particles. The simplest of these motions to describe is the gyration of particles about magnetic field lines. Particles will gyrate about a magnetic field line with a frequency given by

$$\Omega = \frac{1}{2\pi}\frac{qB}{m}\mathrm{Hz}, \tag{1.2}$$

which is called the gyro-frequency, where m is the mass of the particle. Obviously, electrons have a much larger gyrofrequency than protons. Another characteristic frequency is the electron plasma frequency, given by

$$\Pi = \frac{1}{2\pi}\sqrt{\frac{Nq^2}{\epsilon_0 m}}\mathrm{Hz}, \tag{1.3}$$

where N is the electron number density. This frequency arises as electrons oscillate about a static background of ions.

It is convenient to define particle motions with respect to the magnetic field, since these motions are so strongly governed by it. Velocities are conveniently broken up into parallel ($v_\parallel$) and perpendicular ($v_\perp$) components. $v_\perp$ determines the gyration (Larmor) radius of the particle, which is given by

$$r_L = \frac{v_\perp}{\Omega}. \tag{1.4}$$

If the particle has a non-zero $v_\parallel$, then it will move along the magnetic field line about which it is gyrating. A useful invariant which exists in the magnetosphere is the magnetic moment

$$\mu_M = \frac{W_\perp}{B} = \frac{m v_\perp^2}{2B}, \tag{1.5}$$

where $W_\perp$ is the perpendicular energy of the particle. μ_M is conserved during the motion of the particle if the magnetic field is roughly constant during the period of a single gyration. As a particle moves towards one of the magnetic poles, the magnetic field experienced by the particle increases. In order to conserve μ_M, $W_\perp$ must also increase, thereby decreasing $W_\parallel$ ($= \frac{1}{2} m v_\parallel^2$) and consequently $v_\parallel$. At some point $v_\parallel$ reaches zero, at which point the particle changes direction, and moves in the opposite direction along the field line. This process is called magnetic mirroring magnetic mirroring.

The pitch angle α is defined by

$$\alpha = \arctan\left(\frac{v_\perp}{v_\parallel}\right). \tag{1.6}$$

In order for a particle to reflect because of magnetic mirroring, it must do so before it encounters Earth's atmosphere, or it will be lost by collisions in the atmosphere. This will occur if the pitch angle is less than a critical value given by

$$\alpha_{lc} = \arcsin\left(\frac{B_{eq}}{B_{h=100}}\right)^{\frac{1}{2}}, \tag{1.7}$$

where B_{eq} and $B_{h=100}$ are the equatorial and $100\ \mathrm{km}$ altitude values of the magnetic field. If the particle has not mirrored by the time it reaches $100\ \mathrm{km}$ altitude, then it will be lost to collisions with neutrals. α_{lc} defines what is called a loss cone. Particles with equatorial pitch angles within this cone will not be mirrored at their respective mirror points, but rather lost in the atmosphere.

Plasmasphere

The plasmasphere is the high density region which is immediately above the ionosphere and consists mostly of cold (ie: low energy) plasma. Number densities within the plasmasphere are $\sim 100 - 1000\ \mathrm{cm}^{-3}$, which are much higher than in the rest of the magnetosphere. The plasmasphere is a field aligned bubble which is held together by the magnetic field of Earth, and extends to about 5 Earth radii in the equatorial plane (the extent of the plasmasphere is better defined in terms of McIlwain's Parameter, which is described later). As will be explained later, the high densities within the plasmasphere favour the generation of certain VLF emissions, while the generation of others are favoured outside of it. The outer edge of the plasmasphere is the plasmapause, where the plasma density rapidly drops off from the high plasmaspheric levels, within about half an Earth radius. This is of significance for the generation of VLF waves as will become clear later.

Van Allen Radiation Belts

The Van Allen radiation belts overlap partially with the plasmasphere. These belts are divided into an inner and outer belt, which are divided by a slot region at around 2.5 Earth radii above the surface of the Earth. This slot region is mostly devoid of hot plasma, while on either side of the slot are the high energy belts. The high levels of energetic radiation within the belts make it a dangerous environment for astronauts and man-made satellites. The existence of the slot is thus fortunate, since it provides a space in which the density of harmful electrons is lower than in the actual belts.

1.2.3 Dipole Field

The intrinsic magnetic field of the Earth is thought to be produced by the flow of molten iron within the core of the Earth. This field is well approximated by a dipole magnetic field which is tilted and shifted with respect to the rotation axis of Earth. The actual configuration of the Earth's magnetic field, except in close proximity to Earth, is very different from a simple dipole. The solar wind which impinges on the Earth's magnetic field compresses it on the day-side, and stretches it out on the night-side, resulting in a complex magnetic field structure. This complex structure means that geomagnetic and geographic coordinate systems are significantly different from each other, and the extent of these deviations change with time. The magnetic field is more accurately described by the International Geomagnetic Reference Field (IGRF). The IGRF is updated every few years to incorporate the changes to the magnetic field which take place over time.

Schematics of the plasmasphere, Van Allen belts, and the dipole structure of the magnetic field can be found in most space physics text books, such as Kivelson and Russel [1995, Page].

McIlwain's Parameter

A useful parameter used to identify field lines in the magnetosphere is McIlwain's parameter, L. The L-value of a particular field line is defined by the distance from the Earth, in Earth radii, at which that field line crosses the equatorial plane. The L-value tags an entire field line, all the way to the surface of the Earth, so that a particular location on the Earth has an L-value, determined by its geomagnetic latitude. Assuming a dipole field, the L-value is calculated using

$$L = \left(\frac{1}{\cos^2 \lambda} \right), \tag{1.8}$$

where λ is the geomagnetic latitude. Since most activity in the magnetosphere is confined to magnetic field lines, the L-value of a location on Earth tells one what portion of the magnetosphere is linked to that location. An L-shell is mapped into the magnetosphere by a given geomagnetic line of latitude. With the use of the L-value, the extent of the plasmasphere is better defined. The plasmapause, which is the field aligned outer boundary of the plasmasphere, is found at $L = 5$ during quiescent periods.

1.2.4 Content of the Thesis

This thesis presents research relating to various aspects of VLF waves. First, the question of the source region of whistlers is addressed. Recent results using correlation analyses have been able to identify the source region for whistlers received at terrestrial receivers at three different locations. Others have used satellite data to determine the maximum range from which an initiating stroke can launch a whistler into the magnetosphere. DEMETER data from above South Africa are used to address this question.

During the course of this research, chorus was observed on Marion Island. This was the first time which chorus was observed on Marion Island, and so this event was studied in detail. The analysis of the event showed that both chorus and hiss were observed during the evolution of the event. It was also found that Marion Island was near to the plasmapause during the event. This alluded to the possibility that the chorus generated the hiss which was observed. This has particular relevance in view from recent results showing that chorus was responsible for the generation of hiss.

Concurrent whistler data from two nearby sites during a period of three months. These presented a unique opportunity to investigate the differences in whistler reception at two locations. Correlation analyses have shown that the source region for whistlers at these two locations are quite similar, and yet the number of whistlers received at each location was different by an order of magnitude on average. The research here shows some reasons for this stark difference.

During 2012 a tropical cyclone made landfall in South Africa. This presented an opportunity to use the lightning data used extensively in other avenues of VLF research to track this tropical cyclone. The work presented here provides some groundwork for such an automatic tracking algorithm which could be developed.

Chapter 2

Background

The above introduction provides a brief overview of some important space physics concepts. These are of interest in any aspect of space physics research. In this Chapter, a more detailed description of the behavior of VLF waves within the atmosphere and the magnetosphere is provided. These should provide adequate background for the understanding of the research results which are presented in the remainder of the thesis.

2.1 VLF Propagation

2.1.1 Propagation in the Earth Ionosphere WaveGuide

The surface of the Earth and the base of the ionosphere are two conducting boundaries, separated by approximately $100\ \mathrm{km}$. VLF waves propagate between these two layers, reflecting off each boundary during the propagation. This ray description provides a very accurate approximation when dealing with wavelengths shorter than those of VLF waves. However, VLF wavelengths extend from $10\ \mathrm{km}$ to $100\ \mathrm{km}$, which means that the waves will propagate within this cavity in a waveguide mode. ELF and VLF waves propagate within the waveguide with a much lower attenuation than High Frequency (HF) and higher frequency waves. For a complete understanding of the propagation of VLF waves within the EIWG, one needs to think in terms of waveguide mode propagation, which is described in detail in the literature [Wait, 1965; Bernstein *et al.*, 1974]. For this study, however, one can generally ignore the waveguide theory, and use the ray ideas which are technically only correct when dealing with distances $\leq 1000\ \mathrm{km}$ [Barr *et al.*, 2000].

A ray treatment of the propagation of whistler mode waves within the EIWG is detailed in Helliwell [1965, Section 3.10]. Consider a source and a receiver. The waves will travel along the direct ray, and over several paths which require successively more and more bounces between the surface of the Earth and the ionosphere. At each reflection the wave must satisfy the boundary conditions. These boundary conditions which serve to eliminate many possible propagation paths, and thus the propagated signal is the sum of a finite number of waves. Due to the curvature of the Earth, at sufficiently large distances the direct ray path is no longer possible. As the distance increases still further, paths with single bounces, and then two bounces, and so on, are no longer possible. Thus a particular source and receiver pair will have a finite number of ray paths along which the wave will propagate. The wave at the receiver will then be a superposition of the signal propagation along all these paths.

At each reflection along the propagation path, the wave is attenuated. Attenuation at the Earth's surface occurs since the Earth is not a perfect conductor. When waves are reflected at the ionosphere, the ionised particles are excited by the waves which then proceed to re-radiate. During this period of excitation, if energy is lost to collisions with neutrals, then the power radiated at the

ionosphere will be less than the incident power. The wave is thus attenuated at this reflection. The existence of the D-region during the day results in VLF waves experiencing much higher attenuation than at night times. This occurs because the waves reflect at a lower altitude during the day, and at this altitude the higher number of neutrals result in more energy being lost to collisions with neutrals. At night, lack of ionising radiation from the Sun results in the D-region disappearing, making the E-region the lowest level of the ionosphere. The E-region has a much lower concentration of neutral atoms, and so VLF attenuation is less severe under the night time ionosphere. This results in VLF waves propagating significantly further at night than during the day.

Typical attenuation rates of VLF waves in the waveguide are discussed by Barr *et al.* [2000]. This summary of other results showed that the attenuation of VLF waves at night is $\sim 10\,\mathrm{dB/Mm}$. While this value is typical for night time propagation, during the day it is twice as much [Bernstein *et al.*, 1974]. Work by Crary and Crombie [1972] and Westerlund and Reder [1973] showed that VLF attenuation was higher over propagation paths which contained ice, due to the lower conductivity of ice. These studies showed that the attenuation rates over ice were at least $17\,\mathrm{dB/Mm}$ higher than those over sea water.

2.1.2 Propagation in the Magnetosphere

The Whistler Mode

The whistler mode is described in detail by Helliwell [1965, Chapter 3]. The whistler mode is a right hand circularly polarised wave. When VLF waves propagate within a magnetised plasma, they do so in this mode. The dispersion relation of whistler mode waves in the magnetosphere is approximated by

$$n^2 = \frac{\Pi^2}{\omega(\Omega\cos\theta - \omega)} \tag{2.1}$$

where ω is the wave frequency. Typically, a further approximation can be made, in which the wave is assumed to travel nearly parallel to the magnetic field direction, and so $\theta \approx 0$, which results in

$$n^2 \approx \frac{\Pi^2}{\omega(\Omega - \omega)}. \tag{2.2}$$

The dispersion relation allows one to identify when there will be a resonance or cutoff during the propagation. A resonance occurs where the refractive index tends to infinity, and a cut off occurs when the refractive index is zero. In the whistler mode, there is a resonance when $\omega = \Omega$ which will be discussed later.

The group velocity v_g for the whistler mode is given by

$$v_g = \frac{2c\sqrt{\omega}(\Omega\cos\theta - \omega)^{3/2}}{\Pi\Omega\cos\theta} \tag{2.3}$$

where the same quasi-longitudinal approximation can be made as before. An additional approximation is to assume that $\omega \ll \Omega$. Application of these two approximations yield

$$v_g = \frac{2c\sqrt{\omega\Omega}}{\Pi}, \tag{2.4}$$

and is called the Eckersley-Storey approximation. (2.4) shows that higher frequencies travel faster through the magnetosphere. During the formation of a whistler, this results in higher frequencies arriving in the conjugate hemisphere first, and subsequently lower frequencies arrive later. This results in the characteristic decreasing frequency structure of whistlers. This approximation however does not explain the existence of the nose frequency.

Ducting

While magnetic field lines in the presence of a background of charged particles do provide some guidance for whistler mode waves, the guiding is not sufficient to ensure transmission through the ionosphere into the EIWG. The probability that a whistler will pass through the ionosphere is significantly greater if the waves propagate nearly parallel to the magnetic field line, and have their $\mathbf{k}$ perpendicular to the gradient of charge density. This near parallel propagation can be achieved by a process known as ducting.

Within the magnetosphere, the Lorentz force acts against other forces to bind plasma to magnetic field lines. This means that plasma can clump around field lines, creating tubes of enhanced plasma density along the field line. These tubes are called ducts. Since plasma is being clumped along some field lines, there are others which have less plasma around them. These too are named ducts. A duct is defined as a tube of enhanced or diminished plasma density centered along a magnetic field line. The ducts of density enhancement are called crests, while those that have a density depletion are called troughs. These ducts act to guide whistler mode waves, in much the same way that fiber optic guides photons.

Crests are able to trap waves with wave frequency much lower than Ω, while as the wave frequency approaches Ω, only troughs are able to trap them. Since the majority of VLF emissions occur with $\omega \ll \Omega$, the ducting discussion will focus on crests.

Consider a simple crest, with a magnetic field line of constant strength at its center, and the plasma density varying only as a function of radial distance from the field line. Ducting is described using this simple picture. A wave is propagating within the duct, with a direction at some angle to the magnetic field. As this wave propagates further along the field line, it moves into a region of lower plasma density, and consequently a lower refractive index. Application of Snell's law here means that the wave is refracted towards the magnetic field line, reducing the angle between it's propagation direction and the magnetic field line. This will continue until the wave reaches the outer layer of the duct, or is turned around. If the wave has not undergone total internal reflection by the time it exits the duct, then the wave is not trapped. A maximum angle θ_c for which trapping can occur is defined as the initial angle within the duct which will propagate parallel to the magnetic field at the edge of the duct. Waves which enter the duct with initial directions outside of this angle will not be ducted. Detailed figures depicting this process are shown in Helliwell [1965, Pages 44 and 47].

With the use of man made VLF transmitters, Clilverd *et al.* [2008] demonstrated that below $L = 1.5$ there was very little evidence of ducted waves. This was attributed to the orientation of magnetic field lines relative to the ionosphere at low L being unfavorable for the trapping of waves. However, at $L > 1.5$, where the magnetic field line configuration was more favorable, the presence of ducts allowed the vast majority of the wave power to be ducted.

LHR reflection of whistler mode waves

Whistler mode waves propagating in the magnetosphere (such as plasmaspheric hiss and whistlers) can reach a layer within the ionosphere where their frequency is equal to or below the local Lower Hybrid Resonance (LHR) frequency. At this layer there is a cut-off, and so the waves are reflected thus denying access to the EIWG of waves with a frequency lower than the LHR frequency of the highest density layer within the ionosphere. Waves which are parallel propagating are able to bypass this cutoff [Kimura, 1985; Jiříček *et al.*, 2001]. The LHR is given by

$$\frac{1}{\omega_{LH}} = \frac{1}{\Omega_i \Omega_e} + \frac{1}{\Pi_i} \tag{2.5}$$

where Ω_i and Pi_i are the ion cyclotron and plasma frequency respectively.

2.1.3 Ducting action of the plasmapause

Inan and Bell [1977] discussed the ability of the plasmapause to guide whistler mode waves. This effect is rather similar to the guiding effect offered by ducts. Within the plasmapause exist steep density gradients. These serve to guide the waves through gradient trapping of VLF energy. This guiding is possible at both the inner (higher plasma density) and outer (lower density) edges of the plasmasphere, and is more effective with stronger density gradients. This guiding can allow waves to propagate all the way to the ground in spite of LHR reflection which might occur, just as waves propagating within a duct, which makes the plasmapause an important feature when determining the access of waves into the EIWG. The plasmapause might be considered more important than ducts here, since the location of the plasmapause can be estimated using simple models [Carpenter, 1967; Carpenter and Park, 1973], whereas the location of ducts can only be inferred from experimental data.

This guiding effect was first proposed after the Imp 6 satellite discovered whistler echo trains guided parallel to the Earth's magnetic field lines by cold plasma density gradients found along the plasmapause [Inan *et al.*, 1977a,b]. The authors employed ray tracing models, using various plasmapause configurations to show that the plasmapause acts as a one sided duct which confined waves to travel very nearly parallel to the magnetic field direction for an extended period of time. In certain cases, the guiding was so strong that the waves were confined to 6° to 7° latitude range during the propagation from one hemisphere to the other. The mechanism for gradient trapping is described as follows:

- The large density gradients encountered at the plasmapause refract the ray inwards (towards lower L).
- As the ray moves towards lower gradients, the guiding effect of the curved magnetic field dominate, refracting the ray outwards (towards higher L).
- The outward propagating ray is now moving towards higher gradients, and so the refraction is again towards lower L.
- The ray is guided as long as the above steps are maintained.

It was found that waves starting with small wave normal angles (The angle between $mathbfk$ and $mathbfB$), just inside the plasmapause, eventually converge to the plasmapause. Once they reach the latitude at which they were generated, they are refracted inwards once again towards lower L. The outer edge of the plasmapause was also able to guide the waves, although the guiding effect was not as strong in this case. The region to which the waves were confined was much lower than for the case of inner edge trapping. More detailed analysis of the inner edge guiding showed that there was a range of initial magnetic latitude $51^\circ - 58^\circ$ for which the guiding was most effective [Inan and Bell, 1977].

2.1.4 WWLLN

Reliable lightning locating systems are of both scientific and commercial interest. The commercial benefits extend to aviation, forestry, electric supply and insurance, all of which are heavily influenced by occurrence of lightning. The scientific applications include climatology, since lightning occurrence is a proxy to climate change, and several lightning generated phenomena such as Transient Luminous Events (TLEs) and Terrestrial Gamma-ray Flashes (TGFs), and most importantly for this work, whistler studies. This makes an automated lightning location system a very important tool in studies related to these fields. This section will describe the operation of the

WWLLN network. Data from WWLLN will be used extensively in the whistler analysis presented in Chapter 3.

There are two traditional ways of detecting lightning, each with their own drawbacks:

- Using a satellite based lightning locater: A sensitive imager records when and where lightning occurs. Using this technique provides a very accurate and highly efficient lightning detector within the field of view of the satellite. However, as with any satellite based measurement, one is dealing with a detector which moves through space very quickly. One can thus only make continuous measurements at one point of the Earth's surface for a very short period of time. One could use geo-stationary satellites, but it would require many of these in order to cover the entire globe completely. Nevertheless, they do provide a useful measure of average lightning activity on the globe. This type of lightning detection was employed by Christian *et al.* [2003] to produce an annualised lightning distribution map. This required the use of many years of data from the Lightning Imaging Sensor (LIS) and Optical Transient Detector (OTD).

- Many countries/ use HF receivers to triangulate the time and locations of lightning strokes. These systems typically offer very high efficiency ($\sim 95\%$) once the required density of receiving stations (nodes) is achieved. This allows one to continuously receive lightning locations from anywhere within the network. HF networks, however, require a relatively high node density (due to the high attenuation at HF), and thus creating a global network is virtually impossible. The detection efficiency drops off rapidly as one leaves the area enclosed by the network. Examples of this network include the NLDN in the USA, EUCLID in Europe, and South African Lightning Detection Network (SALDN) which is operated by the South African Weather Service (SAWS). For instance, the NLDN requires a node density of 1 per Mm to effectively cover the continental United States.

The limitations discussed above mean that neither of the two methods are suitable for producing continuous measurements over the entire globe. This is where the World Wide Lightning Location Network (WWLLN) comes into its own. WWLLN consists of a network of VLF receivers distributed around the globe. Each sends the Time Of Group Arrival (TOGA) of each detected spheric back to a central processing site. A triangulation technique is then employed on these TOGAs, so that the location and time of the initiating spheric is determined. A more detailed description of the TOGA method is provided in Dowden *et al.* [2002]. Due to the low attenuation of VLF in the EIWG, the density of receivers required for efficient operation of the network is much lower than that of HF networks. This means that one could detect lightning strokes anywhere on the Earth with relatively few stations.

An initial case study on the performance of WWLLN was performed by Rodger *et al.* [2006a]. In April 2006, the network consisted of 25 nodes. A global distribution of strokes detected during 2004 revealed detection peaks over the 3 equatorial land regions in Africa, Central America and the Maritime Continent (which are commonly referred to as the chimney regions). There were also many detections in tropical regions such as over the Amazon and South Africa, where a great deal of lightning occurs over the highveld. Additionally, the system sees much lightning over warm ocean currents such as off the east coasts of the USA, South Africa and Australia. As previously mentioned, these ocean regions would be nearly impossible to monitor using a HF network. A rough comparison to the results of Christian *et al.* [2003] show that WWLLN is seeing lightning in most of the expected places. There are, however, some major differences between the two distributions. Firstly, the absolute value of stroke densities differ substantially, with WWLLN reporting significantly less lightning. The WWLLN network has a much lower Detection Efficiency (DE) which accounts for these reduced values. This lower DE is, however,

not the same everywhere on the globe. As of 2006, the Maritime Continent had a much larger DE than equatorial Africa and America. This results in the WWLLN data indicating that the largest lightning contributor is the Maritime Continent, which in actuality is the smallest of the chimney regions. Christian *et al.* [2003] revealed that the largest chimney region exists over Africa, and the second largest over the Americas. There are other relative efficiency differences in the WWLLN network. These DE asymmetries all stem from the way the stations are spread out over the globe. There are many receivers concentrated around the Maritime Continent and Europe, and a good few spread over the Americas. There was only one station in Africa (in Durban) at that time which is the reason for Africa having the lowest DE.

A comparison between WWLLN and the New Zealand Lightning Detection Network (NZLDN) was carried out by Rodger *et al.* [2006a]. A number of features of the lightning strokes which WWLLN detects were determined from this analysis. During the period of this study (1 October 2003 to 31 December 2004) $\sim 3\%$ of NZLDN detected events were also detected by WWLLN. It was found that the mean timing offset of WWLLN from NZLDN was between $[-0.2, 0.2]$ ms. The distribution of NZLDN peak currents for strokes detected by both systems were plotted. The shape of this plot resembled a bath tub (or valley), with low number of detected strokes for low values of absolute peak current, and an increasing number of events at greater absolute peak currents. This was attributed to the fact that the signals from stronger strokes propagate further within the EIWG, and are therefore easier for WWLLN to detect. WWLLN detected $\sim 10\%$ of strokes with absolute value of peak current > 50 kA, which again points to WWLLN being more effective for strokes with higher peak currents. WWLLN also exhibits a higher DE at night, since VLF waves propagate further under a night time ionosphere.

The distances between strokes and the receiver of the spheric for which a TOGA could be determined were investigated, and revealed some interesting features. During the day, the majority of spherics from < 8000 km away could have their TOGAs found. This upper limit is imposed by the VLF attenuation in the EIWG. At night this range was extended due to the reduced attenuation. The number of events detected by a station decreases at a distance < 500 km and this reduction is greater during the night than the day. This might seem counter intuitive, but the reason for this effect is that nearby signals saturate the receiver, and the reduced attenuation at night means that this saturation is more probable at night.

Since the commissioning of the system, the DE as a whole has improved significantly. The status of the system, and the improvements made since 2003, were discussed by Rodger *et al.* [2009]. The number of receivers grew from 11 in 2003 to 30 in 2007. The increase in receiver density had an immediate effect on the DE, raising the number of strokes detected annualy from $\sim 10^7$ in 2003 to $\sim 3 \times 10^7$ in 2007. Despite this dramatic increase, more than half of all spherics detected by each station could not have a lightning location assigned to them due to the inability of the algorithm to process them in the required amount of time. An improved algorithm is discussed in Rodger *et al.* [2009], the implementation of which led to an additional increase in detected strokes of 63% for all stroke peak currents, which equates to a total global DE of 3%. This increase is as much as 300% for strokes with larger peak currents.

Rodger *et al.* [2009] also presented a plot showing the location accuracy of WWLLN as a function of position on the globe. This showed that for the vast majority of the globe, that locations were accurate to within 20 km although some well covered areas have location accuracies below 10 km. There are some regions which are outliers where the location accuracy is only within 40 km. Since 2009 the number of receivers (and consequently the DE) have grown significantly, to roughly 50 receivers at the time of writing this thesis.

In Figure 2.1, global stroke rate density maps for years 2007, 2009 and 2011 are shown. These annualised maps show the development of the WWLLN network from year to year. Assuming that lightning activity is constant from year to year, these plots show the consequent increase in

WWLLN's DE with time. These increases are due only to an increase in the number of receivers in the network, since the historical data has been reprocessed by the newer algorithm discussed above. One can see that there was a large increase in the number of detections from 2007 to 2009, especially over the Americas and Africa where many new stations were installed. From 2009 to 2011 the performance increased more or less uniformly across the globe, although Africa is still severely misrepresented. Figure 2.2 shows the difference between the annualised WWLLN stroke rate densities from 2007 to 2011. It is clear that the DE is on an upward trend.

Despite the various drawbacks of the WWLLN system, it remains an important tool for research, and the other domains where its data is of importance. Access to continuous, global lightning coverage allows for many interesting applications.

2.2 Whistlers

Since the discovery of whistlers, there have been many studies about their generation and occurrence patterns. The works important to this study are summarised below.

The currently accepted theory for the generation of whistlers was first proposed by Storey [1953]. Whistlers were described as belonging to two types, either long or short. The long type were found to always follow a spheric with a short delay ($\sim 1\mathrm{s}$). In these cases, the initiating spheric was found to come from not further than $2000\mathrm{km}$ away, and that the greater this distance, the lower the resulting whistler's amplitude. The dispersion of a whistler is the measure of how slowly the frequency varies with time. The long whistlers have greater dispersion than the short whistlers (See Figure 1.1(c) for examples of both long and short whistlers). The idea of echo trains was also introduced by Storey [1953], a regular repetition of whistler occurrence, each one with a greater dispersion than the last one. The occurrence statistics of whistlers were also discussed. It was found that whistler occurrence rates were greater at night. The long whistlers occurred more frequently in summer, while the short whistlers were preferentially observed in winter. It was also found that whistler occurrence had a small positive correlation with magnetic disturbance.

Based on these observations, the following mechanism was proposed by Storey [1953]. The radiation produced by a lightning stroke penetrates through the ionosphere into the magnetosphere, where it is guided by a magnetic field line to the magnetic conjugate point. The waves are only weakly guided by the magnetic field lines, but additional guiding is sometimes provided by ducts. The plasma encountered along this path disperses the whistler into its characteristic descending tone structure. This exact process is suggested to produce short whistlers. Since the initiating spheric occurs in the opposite hemisphere, the attenuation in the EIWG means that the initiating spheric is not able to propagate to the receiver, and thus short whistlers are generally not preceded by spherics. Long whistlers on the other hand are suggested to result from the same process, up to the point where the whistler arrives at the conjugate hemisphere. Here, instead of propagating into the EIWG in the opposite hemisphere, they are reflected back to the hemisphere from which they originated. They are then detected by the VLF receiver in this hemisphere. Since they are detected in the same hemisphere in which their initiating spheric occurs, the spheric is detected shortly before the whistler on the same receiver. Also, since they have traveled essentially twice as far through the dispersive medium, they are dispersed twice as much, and hence are a longer emission than the short whistlers. Multiple reflections are responsible for the observation of whistler trains, which exhibit successively more and more dispersion.

This ground breaking work was published even before the presence of the Van Allen radiation belts was confirmed in 1958, and is well ahead of its time, especially considering that it is still accepted as the whistler generation mechanism. Many of the ideas put forward in this paper have been expanded upon.

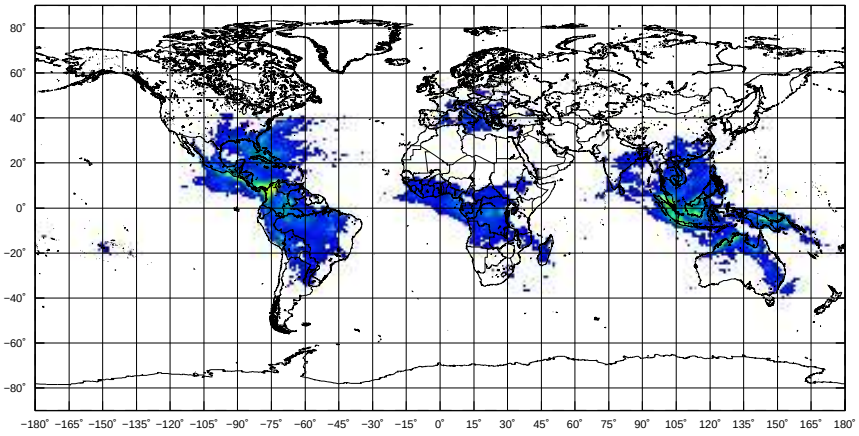

(a) 2007

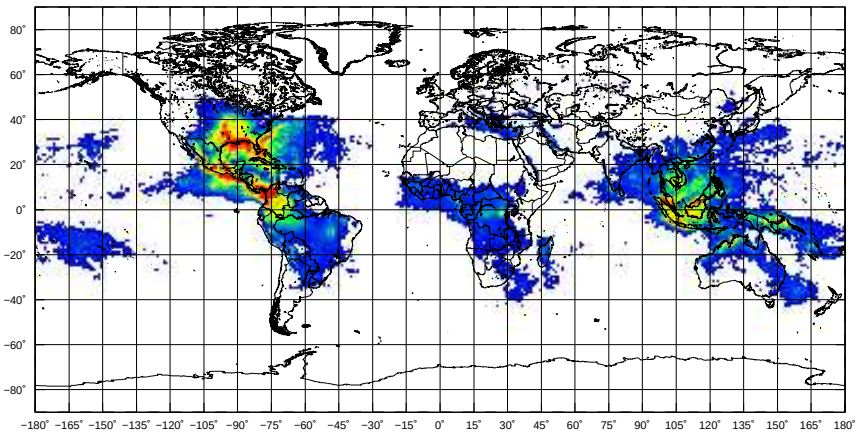

(b) 2009

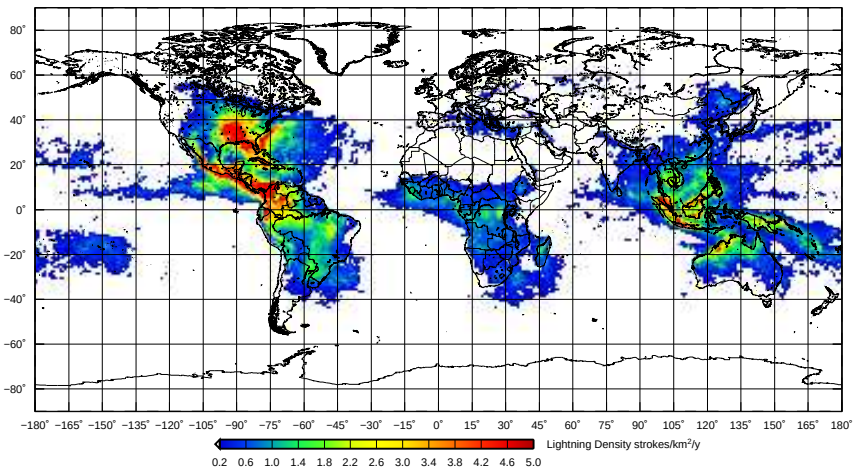

(c) 2011

Figure 2.1: Anualised WWLLN stroke rate densities for 2007 (a), 2009 (b), and 2011 (c). The colour scale is chosen to be consistent from year to year. A marked increase in detection efficiency is visible from 2007 to 2011.

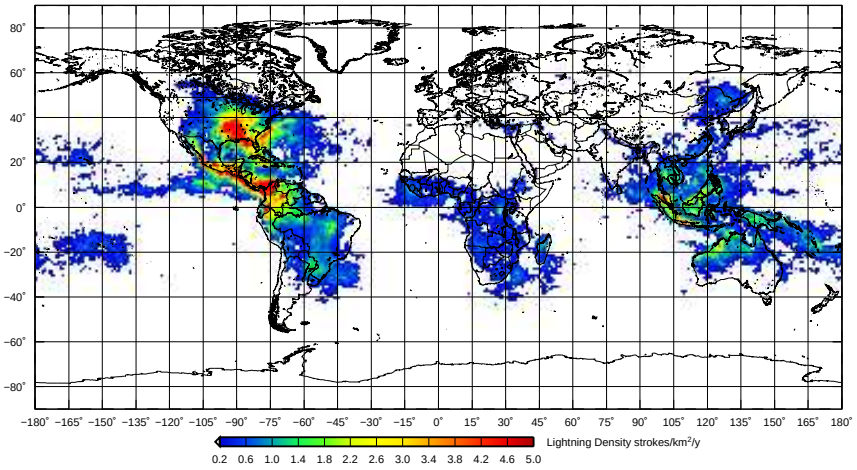

Figure 2.2: The difference between 2011 and 2007 annualised WWLLN stroke rate densities. This shows that larger gains in DE were made in the Americas and Maritime Continent than in Africa. Nevertheless, the performance of the system improved significantly over the entire globe over the five years.

2.2.1 The Automatic Whistler Detector and Analyser

The mechanism proposed by Storey [1953] for the generation of whistlers showed that the amount of dispersion experienced by a particular whistler trace on its journey through the magnetosphere was proportional to the length of the field line, as well as the magnetic field strength and plasma density along the propagation path. This dependence makes it possible to determine these parameters by measuring the dispersion of a set of whistler traces. This method was employed successfully by Carpenter [1967] to empirically determine a model for the location of the plasmapause for a given level of geomagnetic activity. In fact, the discovery of the plasmapause by Carpenter [1963] was made possible by this relationship. This relationship then provides a simple method for determining plasma densities in the magnetosphere. The steps to determine the plasma density from broadband VLF data source are:

1. Locate whistlers in the data.

2. Obtain frequency-time pairs of the whistler traces in the spectrogram (this is called scaling). This is done by marking points along each whistler trace on the spectrogram.

3. Apply a model using the scaled frequency-time pairs to determine the L-value of the duct through which the whistler traveled, the equatorial electron number density n_{eq}, and the integrated plasma density of the duct n_T [Bernard, 1973].

Since whistlers occur naturally, and the equipment required to record a whistler and show its $f - t$ profile is relatively cheap, this method for determining magnetospheric plasma densities is a rather attractive one. However, the problem is not as simple as one might imagine for two reasons:

1. It is a rather laborious, time intensive task to wade through numerous spectrograms looking for suitable whistlers, and

2. although it takes a single person a few minutes to determine the plasma density from a single whistler trace, it is another matter altogether to perform this task for the thousands of whistlers which may be recorded at a particular station, on a given day.

The Automatic Whistler Detector and Analyser (AWDA) system is described by Lichtenberger *et al.* [2008], and Lichtenberger *et al.* [2010]. The AWDA system was designed with exactly this notion in mind. The FP7 funded PLASMON project aims to set up a global AWDA network, to provide real time, global magnetospheric densities to researchers. The first step in determining plasmaspheric densities from VLF data is performed by the Automatic Whistler Detector (AWD), while the second two are performed by the Automatic Whistler Analyser (AWA). The AWD [Lichtenberger *et al.*, 2008] has been implemented since 2002 in Tihany, Hungary. The AWD network has several AWDs set up around the world, but initially the data were only analysed by a single AWA in Hungary, since this is a far more computationally intensive process, and it was not yet feasible to install the computer systems required to perform the task at each AWD site. Within the PLASMON project, a new method for analysing whistlers has been developed, using off the shelf GPU processors. This has allowed for full AWDA systems to be installed on location with VLF receivers. The SPRI's involvement in the PLASMON project has led to two AWDA installations, one on Marion Island and another at SANAE IV. A third is planned for installation in the KZN midlands, in South Africa, in 2013.

Automatic Whistler Detector

The details of the AWD are described by Lichtenberger *et al.* [2008]. The AWD can currently run on an off-the-shelf desktop computer. It logs the times of whistler detection and stores a high resolution broadband VLF data snippet of the whistler for later processing by the AWA.

The AWD requires the signal to be free of man-made noises such as power line harmonics and VLF transmitter signals, as well as naturally occurring noises, the major one being spherics. The presence of noise can often lead to false positives manifesting in the data. The AWD removes the power line harmonics and transmitter signals by using a subset of the available $20\ \mathrm{kHz}$ which usually does not contain these signals, $4.5 - 11.5\ \mathrm{kHz}$. The spherics are, however, harder to eliminate, since they occur in the same frequency band as whistlers. The spherics are removed by setting the data which contains spherics to zero, thereby removing a vertical slice in the spectrogram. While this removes 100% of the spherics, it also removes the information of any whistlers contained in that slice. Thus, a whistler which has too many spherics overlapping it, will have enough of the whistler information removed for the AWD to miss that particular whistler. This is called a missed detection, and its occurrence is preferred to false detections.

The whistler detection algorithm employs a 2-D moving image correlation. A reference whistler image is generated, where every pixel belonging to the whistler is assigned a value of one, and all other pixels are zero. The shape of this whistler is based on the expected shape of whistlers received at the given station using the Bernard [1973] approximation. This image is then correlated with the VLF spectra and the image is "moved across", and the correlation repeated. A dynamically determined detection threshold is also computed. This detection threshold is proportional to the total averaged signal strength of the VLF recording. If the value of the 2-D correlation exceeds the detection threshold, then the system records a whistler at that time.

It is of course important to know the efficiency of the system. To this end, two different types of efficiency are introduced. First is the efficiency related to false detection, ie: detection of whistlers which do not actually exist in the data. This equals one minus the false detection rate, which means that a high false detection efficiency implies fewer false detections. Second is the missed detection efficiency, which is related to whistlers which are in the data, but are missed by the detector. This equals one minus the missed detection rate, which means that a high missed detection efficiency implies a low number of missed detections. The missed detection efficiency can be improved by lowering the detection threshold, but this will in turn reduce the false detection efficiency. This presents a balancing act, where the two efficiencies need to be optimised. At the time Lichtenberger *et al.* [2008] went to print, the misdetection efficiency for countable whistlers

(whistlers which are detected, but are not necessarily possible to scale) was ~$80-85\%$, while for false detection it was ~$50-80\%$.

During the 6 years between 27 February 2002 and 26 February 2008, 911328 whistlers were detected at Tihany, Hungary. Statistics of these whistlers are discussed by Lichtenberger *et al.* [2008]. The annual and diurnal variations of whistler activity recorded at Tihany are shown in Figure 2.3.

These two plots are in basic agreement with the ideas which Storey put forward, namely that whistlers are more common at night (Local Time at Tihany is UT+2), and when there is significant conjugate lightning, ie: during the Austral summer (there will be further discussion pertaining to these data in Chapter 4). 94 325 of these automatically detected whistlers were automatically scaled, and from this the L-value at which they traveled through the magnetosphere was determined. It was found that calculated L-values were somewhat higher than that of Tihany, which means the whistlers would have to propagate a significant distance ($\sim 1000\mathrm{km}$) in the EIWG before arriving at Tihany.

Lichtenberger *et al.* [2008] showed that large statistical whistler data sets can be gathered by the AWD, and are useful for whistler studies. The AWD at Tihany was only the first, and to date many more have been set up and operated nearly continuously.

Automatic Whistler Analyser

The Automatic Whistler Analyser (AWA) described by Lichtenberger *et al.* [2010] outlines the automated procedure of determining plasmaspheric electron densities and magnetic field strengths from whistler dispersions. Measuring these parameters from whistler dispersions led to the discovery of the plasmapause [Carpenter, 1963], and could be a useful remote sensing tool. However, the analysis required to extract these parameters from a whistler trace (even when the whistler is automatically detected in broadband data using the AWD) is an extremely time consuming task. The AWA automates this process moving the burden from humans to machine. The algorithm assumes a simple plasmapause independent model for the equatorial electron density, n_{eq}, given by [Lichtenberger *et al.*, 2010]

$$\log_{10} n_{eq} = A + BL, \tag{2.6}$$

where $1.4 < L < 8$. The L-value is determined from the whistler's dispersion. The parameters A and B are then recursively varied, giving many possible values for n_{eq}. For each set of A and B obtained, a reverse dispersion proportional to the resulting n_{eq} value is applied on the original spectrogram. This transforms the whistlers into more vertical structures. When the correct combination of A and B are selected, the whistlers are transformed into perfectly vertical lines (resembling spherics), and the spherics transform into mirror images of the original whistlers. This process is called Vertical Trace Transform (VTT). At this point one can calculate n_{eq} from (2.6). This system is implemented in parallel, so that it can be run alongside the pre-existing AWD systems.

The combination of these two systems forms the AWDA system. The implementation of this system forms one component of the PLASMON project, which aims to create a data assimilative model of the plasmaspheric plasma densities, across all L-values and Magnetic Local Times (MLTs). The density values are obtained from a network of AWDA stations (AWDAnet) and are fed into a data assimilative model, along with mass densities obtained from Field Line Resonance (FLR) measurements (see Menk [1999, 2004] for a description of this method), to produce the plasmaspheric model.

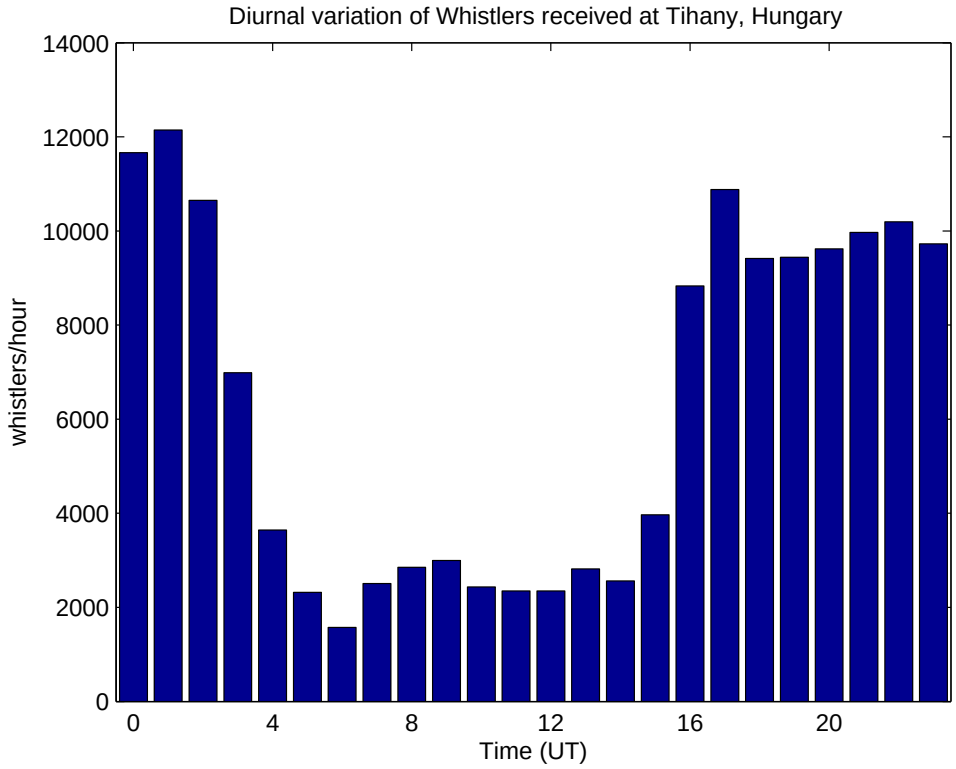

(a) Diurnal Distribution

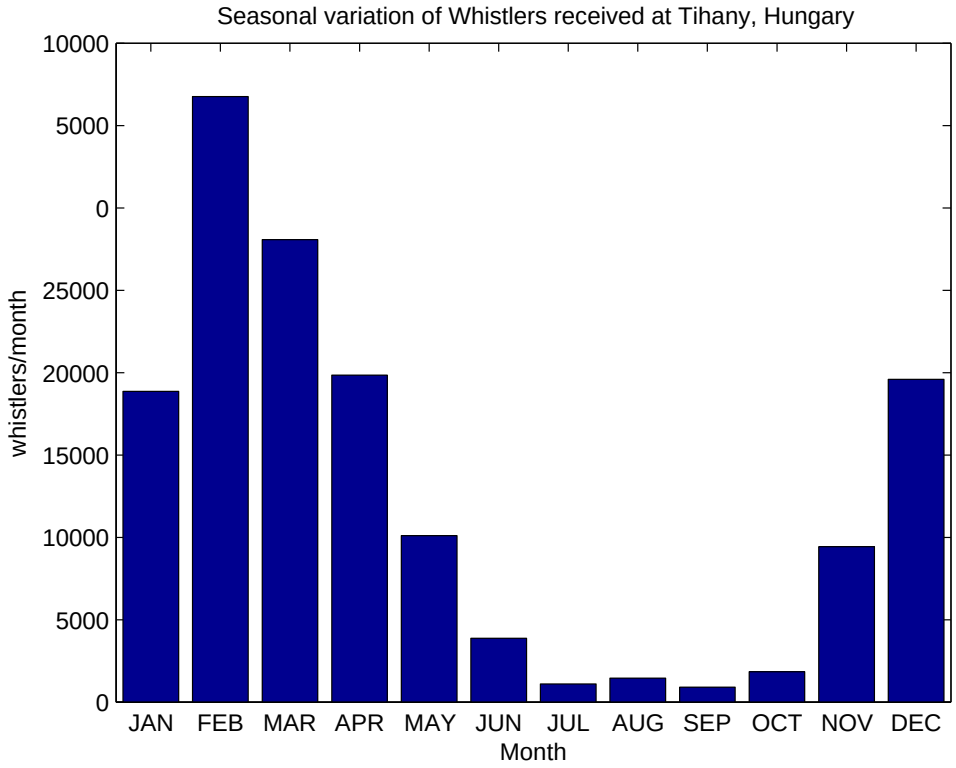

(b) Annual Distribution

Figure 2.3: Diurnal and annual variation of whistlers received at Tihany from 2002 to 2008 after Lichtenberger *et al.* [2008].

2.2.2 Correlation Studies

The mechanism proposed by Storey [1953] predicts that a whistler detected on the ground should have its initiating lightning stroke somewhere near the geomagnetic conjugate point. There is of course room for some deviation from this prediction. Due to the low attenuation of VLF in the EIWG the spheric can travel a significant distance in the waveguide before passing through the ionosphere. The whistler which re-enters the EIWG in the conjugate hemisphere can also travel some distance before being detected by a VLF receiver. For this reason, the source region for whistlers received at a particular location has been a hotly debated issue for some time now. Some recent whistler-lightning correlation studies which attempt to settle this dispute are presented on the following pages.

Tihany

Collier *et al.* [2009] performed a correlation between global lightning and whistlers received at Tihany, Hungary. This revealed that the highest concentration of initiating strokes occurred within $1000\ \mathrm{km}$ of Tihany's conjugate point, which is off the south eastern coast of South Africa. This region, which is over a warm ocean current, exhibits moderate levels of lightning activity all year round. The overland region of South Africa, which is still in close proximity to the conjugate point, experiences its peak lightning activity during the Austral summer, and a minimum during the winter [Christian *et al.*, 2003; Collier and Hughes, 2011]. The net effect of these two lightning sources is a moderate level of lightning during the Austral winter, and higher levels during the summer. The peak in conjugate lightning activity corresponds rather well to the peak in whistler reception at Tihany, which is during the Boreal winter. In addition to this the majority of whistlers are received during the local night hours at Tihany, which corresponds to the time of peak lightning activity of the over-sea region near the conjugate point. Even though the daytime Austral summer lightning activity is far higher than the night time values, the peak in whistler activity at Tihany is during the night. This is most likely due to increased trans-ionospheric attenuation on both sides of the field line when the ionosphere is illuminated. This is compelling evidence that Tihany's conjugate point is one of the main sources of whistler producing lightning strokes. In addition to the conjugate point, however, the authors found secondary regions of positive correlation in central Africa, South America and the Maritime Continent. These last two regions are $\sim 10000\ \mathrm{km}$ away from Tihany's conjugate point. This suggests that the signals are able to travel these great distances within the EIWG, and still excite ducts to propagate to the conjugate hemisphere.

Dunedin

In a similar study, Collier *et al.* [2010] performed a correlation analysis between global lightning and whistlers received at Dunedin, New Zealand ($L = 2.75$). The conjugate point of Dunedin, which is over the Aleutian Island Chain, (west of Alaska) does not experience much lightning. This presents a stark contrast to the conjugate point of Tihany, which experiences significant lightning activity. Another anomaly of Dunedin whistlers is that the majority of whistlers received at Dunedin occur during the daylight hours, in spite of increased trans-ionospheric attenuation. As expected, since there is no lightning there, the conjugate point is not found to be a source region for whistlers at Dunedin. The primary source of whistlers was found to be over the western coast of Central America. There were other regions of positive correlation smeared out over the northern Pacific Ocean. This indicates that spherics are able to travel a significant distance within the EIWG before exciting ducts.

Rothera

A third and final correlation analysis was conducted by Collier *et al.* [2011]. In this work, the source region for whistlers occurring at Rothera, Antarctica ($L = 2.71$) was investigated. The conjugate point of Rothera is on the east coast of the USA near Boston, Massachusetts. Rothera experiences an extremely high whistler occurrence rate, in contrast to Tihany and Dunedin. Rothera experiences a daily average of 18309 whistlers, while Tihany and Dunedin experience average daily rates of 575 and 504 respectively. The average daily whistler rate at Rothera may be skewed due to the presence of a few days which produced enormous quantities of whistlers. The day of highest whistler occurrence followed a few days after a moderate geomagnetic storm on 22 July 2009 (The mechanism for a relation between whistler occurrence and geomagnetic activity is not yet understood). However, even if these days of extreme whistler activity are excluded from the average calculation, the average rate is only reduced to 15372, which is still ~ 30 times greater than the other two stations.

The seasonal and diurnal variations of whistlers observed at Rothera are discussed by Collier *et al.* [2011]. The majority of whistlers are observed during July and August, which is during the peak of the Boreal summer, when lightning is more prevalent in the northern hemisphere. This period corresponds to the Austral winter, and during this time, the base of the ionosphere (~ 100 km altitude) at Rothera is illuminated by the Sun for only a few hours per day. During the Austral winter, the peaks in the diurnal distribution occur when both ends of the field line are illuminated. One expects that this would hamper trans-ionospheric propagation of whistlers into the EIWG in the southern hemisphere. However, given the whistler reception rates, this does not seem to be a major factor. The peak extends until after the Sun has set, so that it appears that illumination of the base of the ionosphere above Rothera does little to lessen the detection of whistlers there. This seems contradictory to the generally accepted occurrence of whistler observation.

Lightning rates are considerable near Rothera's conjugate point, but in addition to this, there is a region of intense lightning activity not far from the conjugate point, over the Gulf Stream. The annual variation of lightning over the conjugate point follows the same pattern as the annual variation of whistlers at Rothera. A correlation analysis similar to the ones performed at Tihany and Dunedin was conducted for Rothera. The correlation showed a region of moderate positive correlation centered on the conjugate point, and a higher correlation extending over the Gulf Stream. Unlike the correlation analysis for Tihany, the chimney regions which are active lightning producing regions actually show a negative correlation. There is also a region of positive correlation over the Far East.

A negative correlation was found for a grid cell when there was consistent periods of whistlers at Tihany and no lightning in the cell, or consistent periods of lightning when no whistlers were detected at Tihany. A negative correlation is thus expected in locations whose peak lightning season is different from the peak in whistler reception at Tihany (the Austral summer), or Rothera (the Boreal summer).

In addition to the correlation analysis used in the two other studies, a more direct technique was employed. Only lightning strokes which occurred between 1.3 s and 0.2 s before a whistler were considered. This yielded a very interesting result, that there were only 2 regions of significance. The first is the same region which displayed positive correlation from using the first method. The second is a narrow band off the west coast of Mexico. As in the case of Dunedin, this source which is distant from the conjugate implies that there is significant EIWG propagation before ducts are excited.

Both of the correlation techniques indicate that there are higher correlations between Rothera whistlers and the oceanic lightning near the conjugate point, despite the nearby continental region which exhibits a high level of lightning activity. This provides the interesting possibility that

lightning which occurs over oceans is favoured for producing whistlers at Rothera when compared to lighting over land. It has been determined that oceanic lightning is on average brighter than terrestrial lightning, which might be attributed to higher stroke energies [Boccippio *et al.*, 2000; Lyons *et al.*, 1998]. Higher stroke energies would certainly account for the bias towards oceanic lightning found in the correlation analyses.

These correlation analyses indicate that when a conjugate point is a lightning producing region, then this will be a significant source region for whistlers, but when there is not much lightning around the conjugate point, then the source region is more dispersed. Additionally, lightning from a significant distance away from the conjugate point can result in whistlers.

2.2.3 Other Observational Studies

Satellite Observations

In another attempt to determine the source region for whistlers, Chum *et al.* [2006] used a novel method to link lightning strokes, on a one-to-one basis, to whistlers detected on the DEMETER satellite. They used lightning data from a European lightning detection network, EUCLID, and broadband VLF data from DEMETER. An automatic detection algorithm similar to the one employed by the AWD was used to automatically detect the times of whistler occurrence. With a whistler and lightning time series they then use an empirical method to determine the delay between the initiating stroke and the whistler detected on DEMETER. This method is as follows:

- For each whistler time (t_{wi}), the delay between it and every lightning stroke time (t_{lj}) is computed, and using all whistlers in this way, an array t_{ij} is constructed.
- A histogram of these t_{ij} is plotted, with $25\ \mathrm{ms}$ resolution.
- the peak of this histogram is then the delay between the lightning strokes and whistlers.

During the construction of t_{ij}, any unreasonably large delays (those which are obviously not of a lightning-whistler linked pair) are discarded. The above assumes that sub-ionospheric propagation time is negligible, which is the case for close lightning strokes as used in this study. This delay is attributed to ionospheric propagation delay, and timing offsets between DEMETER and EUCLID (which is GPS-time synced). The ionospheric delay is a function of ionospheric density, which changes with time of day and day of year. It can be assumed to be constant for the period of a DEMETER half orbit. An analogous method was used for the MAGION-5 satellite. It was found that energy from lightning up to $1500\ \mathrm{km}$ away could penetrate through the ionosphere to be detected by satellites. It was also found that the number of these events which were able to launch energy through the ionosphere was inversely proportional to distance from the footpoint of the satellite, ie: the further the energy propagated through the EIWG, the less likely it was to penetrate through the ionosphere.

In a follow up study, Fiser *et al.* [2010] correlated whistlers on DEMETER to lightning detected by EUCLID, for periods when DEMETER was above active thunderstorms. They found that the highest number of detected whistlers were from lightning strokes directly below the satellite, and that this number fell off at points further from the satellite. It was also found that the amplitude of the detected whistlers was inversely proportional to the distance between the satellite and the lightning stroke location. They also found that the number of whistlers launched through the ionosphere was greater (at all distances) for strokes with higher peak currents. Finally, it was found that whistlers detected at night had higher amplitudes than those detected during the day (for whistlers from strokes of comparable peak current and distance away from the satellite footpoint).

The above mentioned satellite studies used regional lightning data, and thus the maximum range from an initiating stroke which whistlers could be detected from is limited by the extent

of the regional network. Another such comparison between fractional hop whistlers and global WWLLN lightning comparison was made by Jacobson *et al.* [2011]. They matched WWLLN lightning strokes to whistlers received by the C/NOFS satellite. The number of initiating strokes versus the distance of those strokes from the footpoint of the satellite was computed. This showed that as the distance increased from $0 - 4000\,\mathrm{km}$, the number of detected whistlers increased, and that this number decreased again as distance increased up to $10000\,\mathrm{km}$. These results suggest that the majority of fractional hop whistlers are not initiated by strokes directly below the satellite, but by those which are significantly far away. This differs significantly from those results presented here. One reason for this apparent difference may be that the locations of the C/NOFS satellite were not subset to a particular area of the globe, which is not the case for those studies mentioned above, and so the distance to matched strokes would vary greatly as the satellite moved over regions of typically high or low lightning activity.

Another fractional hop whistler and lightning comparison was made by Jacobson *et al.* [2011]. Here, WWLLN data was used, so that initiating stroke locations were not artificially limited to a geographical location by the data used. They matched WWLLN lightning strokes to whistlers received by the C/NOFS satellite. The number of initiating strokes versus the distance of those strokes from the footpoint of the satellite was computed. This showed that as the distance increased from $0 - 4000\,\mathrm{km}$, the number of detected whistlers increased, and that this number decreased again as distance increased up to $10000\,\mathrm{km}$. These results suggest that the majority of fractional hop whistlers are not initiated by strokes directly below the satellite, but by those which are significantly far away. It should be noted however, that the orbits of C/NOFS were not subset in any way.

Whistlers, Trimpis and Triggered Lightning

Trimpis (also referred to as lightning-induced electron precipitation or LEP) are the modification of a VLF transmitter's amplitude or phase resulting from changes in the ionisation of the ionosphere, which modifies the propagation conditions in the EIWG. These ionisation changes result from particle precipitation caused by wave-particle interactions between whistlers and electrons [Helliwell *et al.*, 1973].

A study of Trimpis received on Marion Island was conducted by Rice and Hughes [1998]. These were detected through recording of the naval transmitter signal originating from the North West Cape of Australia (aptly named NWC). The initiating spheric, resulting whistler and the Trimpi event were all detected by VLF recording instruments on Marion Island. The mechanism for this set of circumstances is as follows:

- A lightning stroke occurs in the northern hemisphere, and the spheric from this propagates on to Marion Island.
- This spheric also launches a whistler into a magnetospheric duct in the northern hemisphere, propagating towards the south.
- The whistler interacts with northward traveling electrons via the Doppler Shifted Cyclotron Resonance interaction, reducing their pitch angle, before entering the EIWG in the southern hemisphere.
- The particles mirror in the northern hemisphere and precipitate in the southern hemisphere, resulting in the Trimpi observed there.

A total of 11 such Trimpi-whistler pairs were found on the Marion-NWC transmitter path. Signals from transmitters in France (HWU) and Great Britain (GQD) also showed a good signal

to noise ratio, although no Trimpis were evident in these data. These transmitter paths originate from the north, and run through the northern hemisphere, and so this may indicate that particle precipitation was only experienced in the southern hemisphere. During the period of Trimpi observations, whistlers were recorded at a rate of 10 per minute, however, those whistlers which were associated with Trimpis exhibited a significantly higher amplitude than the others. This may indicate that the whistlers which produced Trimpis were amplified via wave-particle interactions.

The particles have their pitch angles changed while traveling northward, but are reflected in the northern hemisphere, and precipitated in the southern hemisphere. This can only occur if there is a sufficient asymmetry in magnetic field strength between the two hemispheres at the longitude of Marion Island. This is the case, due to the South Atlantic (Magnetic) Anomaly (SAA). Another interesting observation made by the broadband receiver was that each of the 11 whistlers which were received was followed by a second weaker whistler, which were called ghost whistlers. These ghost whistlers were different from echoes, where each subsequent whistler group exhibits greater dispersion than the previous one in the train. The ghost whistler group exhibited dispersions nearly identical to the leading whistler group, which means they had likely traveled along the same duct, but were initiated by an independent spheric. Furthermore, the delays between each ghost and its preceding whistler were the same (within a $10\ \mathrm{ms}$ window). This suggests that there was a common delay between the initiating spheric of the first whistler group, and that of the ghost whistler group. It was postulated that particle precipitation from the first whistler group triggered the initiating stroke of the ghost whistler group. Armstrong [1987] suggested that particle precipitation could cause lightning discharges to occur.

2.3 Chorus

Chorus is a naturally VLF emission which can be recorded with the same VLF instruments which record whistlers. During the course of this Thesis, receivers on Marion Island recorded chorus for the first time. this prompted an in-depth study of the chorus. Relevant literature on the subject is abundant, and so the most important and relevant aspects of chorus are described below.

2.3.1 Characteristics

A review of Chorus Emissions

Sahzhin and Hayakawa [1992] reviewed the literature of chorus emissions. Chorus was defined as a VLF phenomena which had a spectrum of close or overlapping small bandwidth emissions. The frequency range in which the chorus band can typically be observed extends from a few hundred hertz up to $5\mathrm{kHz}$. The individual elements can be risers, falling tones, hooks (falling tone joined to a rising tone), inverted hooks, or have some more complicated structure. Chorus has been observed in the magnetospheres of other planets, such as Jupiter [Inan *et al.*, 1983]. The term chorus comes from the aural sound of the emission, which resembles the chirping of birds. Initial results concluded that chorus activity was highest at 06:00 LT, but more detailed analysis by the same authors revealed that, while this was true of mid-latitude stations, the peak shifted towards 12:00 LT at higher latitudes. Later, others investigated the occurrence of auroral chorus, and found that the peak in activity was in the post midnight hours [Hayashi and Kokubun, 1971]. Another type of chorus was observed in the auroral zone spanning the frequency range from $6 - 9\mathrm{kHz}$ [Francis *et al.*, 1983]. Observations of chorus are divided into ground based and satellite observations.

Ground based observations

Mid-latitude chorus is observed on the ground in the sub-auroral zone, although it can be observed outside of this zone, at L-values as high as 5. It is mainly observed in the frequency band $2-4\,\mathrm{kHz}$, but sometimes this range is extended to $1.5 - 5\ \mathrm{kHz}$ [Kokubun *et al.*, 1981]. These frequency ranges tended to decrease from dawn to noon, and increase from noon to dusk, and be lower during summer, and higher during the equinoxes [Pope, 1963]. The first evidence of the electron precipitation caused by chorus emissions was the simultaneous observation of X-ray bursts by balloons, and simultaneous observation of chorus [Rosenberg *et al.*, 1971]. A further link between chorus and particle precipitation was attributed to a correlation between chorus and pulsating aurora. The frequency-time steepness of individual chorus elements was found to increase with $\Sigma \mathrm{K_p}$ (the sum of $\mathrm{K_p}$ values for a given day) [Allcock and Mountjoy, 1970]. Chorus is often observed with associated hiss [Helliwell, 1969].

Polar chorus is most commonly observed in the noon sector, with $\mathrm{K_p} \sim 2 - 3$, during periods of increased solar wind speed and pressure. Polar chorus, like mid-latitude chorus, is closely connected to hiss, and often appears at the highest frequency of the hiss. Polar chorus occurs at lower frequencies than mid-latitude chorus, namely $400 - 1500$ Hz, with a bandwidth up to 500 Hz [Egeland *et al.*, 1965]. The top edge of the frequency envelope of individual chorus elements increases from noon to dusk, and also as $\mathrm{K_p}$ increases. Compression of the magnetosphere (shown by an increased Dst index) during a Storm Sudden Commencement (SSC), often triggers, or intensifies existing chorus, while a decrease in Dst during the main phase of the storm decreases the intensity, or completely ends the chorus emission. Polar chorus is usually observed simultaneously at conjugate stations. Direction finding showed that in the morning sector, chorus originated from the west and east with equal probability, while in the noon sector the emissions came almost exclusively from the west. The chorus generation region was to the north in the morning, shifting to the south, while shifting back to the north in the afternoon [Sahzhin and Hayakawa, 1992].

Auroral chorus is considered different from polar chorus, mainly because it is observed predominantly during the midnight hours. The typical frequency range of auroral chorus is $0.5 - 2$ kHz. It is observed much less frequently than the other two types, mainly because it has a relatively low power flux [Sato and Kokubun, 1981].

$6 - 9$ kHz chorus is observed at $L \sim 4$. These high frequency chorus elements occur in two frequency bands, $6.0 - 7.7$ kHz and $7.8 - 9.4$ kHz, with a clear 500 Hz gap separating the two. Chorus was observed in both bands simultaneously [Sahzhin and Hayakawa, 1992].

Satellite Observations

Chorus observations by satellites provide unique insight into generation and propagation mechanisms, which greatly augment ground based observations. The chorus observed on board satellites is not subjected to ionospheric losses, but time evolutions in a single location are practically impossible to record.

In space chorus often occurs in two frequency bands, split at $0.5\Omega_e$ (where Ω_e is the equatorial electron gyrofrequency). Only lower band chorus is observed on the ground [Sahzhin and Hayakawa, 1992]. The extent of the magnetosphere in which chorus exists during solar minimum was investigated by Bunch *et al.* [2011] using data from the Polar satellite, who showed that the chorus was generally confined outside $L = 4$, with small excursions to lower L in the equatorial plane. They also showed that chorus is found at all MLTs, but is most prominent in the noon and midnight-dawn sector (albeit over a smaller latitude range), and that apart from in the dusk sector, chorus activity was found to increase with increasing geomagnetic activity.

Observations in the topside ionosphere up to $0.5R_E$ were made by several satellites [Bullough *et al.*, 1969; Hayakawa *et al.*, 1977]. A good correlation between chorus and increased 40 keV

electron flux was observed [Oliven and Gurnett, 1968]. It was observed that peaks in chorus intensity do not coincide with electron flux peaks, which can be attributed to the asymmetry required for wave growth. Put simply, wave growth is favoured when the electron $T_\perp > T_\parallel$, which results in lower electron fluxes [Kennel and Petschek, 1966]. Both the lower and upper boundary of the frequency envelope of dayside chorus were found to decrease with L, and are almost always below $0.5\Omega_e$. This trend was not evident for dawn, evening or midnight chorus occurrences [Ondoh *et al.*, 1982]. It was also found that the frequency band was higher outside the plasmapause than inside it, and that a gap existed between these two frequency regimes. The intensity of the emissions was many times greater on satellite than on the ground.

Observations by the OGO-5 satellite in the magnetosphere equatorial plane revealed that post-midnight chorus was generated within 2° of the magnetic equator, while for dayside chorus the generation region was as far as 25° from the magnetic equator [Tsurutani and Smith, 1977]. Chorus emissions were found to be accompanied by high energy electrons (at least $\sim 10\ \mathrm{keV}$) [Anderson and Maeda, 1977]. The GEOS-1 satellite was the first to simultaneously observe chorus and hiss emissions [Cornilleau-Wehrlin *et al.*, 1978]. OGO-3 data showed that chorus frequency was approximately proportional to L^{-3}. The occurrence of the upper band chorus was more common in the vicinity of the equatorial plane. The frequency gap was always at a lower frequency than the local $0.5\Omega_e$, which implies that the chorus originates from an area of lower magnetic field strength such as in the equatorial plane. Chorus emissions were often accompanied by bursts of electrostatic waves at frequencies below the electron plasma frequency. These were thought to be generated by the electrostatic two stream instability. Risers were the most commonly observed chorus elements (77%), followed by falling tones (16%) [Burtis and Helliwell, 1969].

These early observations of chorus have all added to the understanding of chorus emissions, and have led to chorus being a well understood VLF emission. Despite all these observations however, there are a few aspects of the emission which are not properly understood.

Ground Based VLF Observations near $L = 2.5$ During the Halloween Storm in 2003

A very unusual observation of chorus was made at Palmer Station, Antarctica, after the the dramatic reconfiguration of the outer radiation belts caused by the Halloween Storm in 2003 [Baker *et al.*, 2004]. SAMPEX data showed that for $3 \leq L \leq 4$ there was considerable depletion in the Earth's radiation belts. Using the knowledge that the frequency range of chorus typically lies between $0.1\Omega_e$ and $0.45\Omega_e$, an estimate was made of the source region of the chorus.

The evolution of the chorus event was described in detail by Spasojevic and Inan [2005]. Some important aspects of its evolution are detailed here for later reference. It was found that on 29 October 2003 the chorus which spanned $\sim 7 - 11\ \mathrm{kHz}$ originated from the range between $L = 2.25 - 3.25$. Chorus was observed from 03:00 to 07:00 LT, after which it changed to hiss.

On the 30 October 2003, while Dst was in the recovery phase, the calculated range of generation was between $L = 3 - 4$ for lower band chorus. The chorus activity peaked at $\sim$ 00:00 LT, and by 01:00 LT, it had converted to hiss. The hiss then expanded to higher frequencies, while the chorus remained at a low frequency. The hiss had faded out by 02:35 LT, and the chorus by 08:05 LT.

On the 31 October, after the Dst index reached a second minimum, the plasmasphere was highly eroded, with the plasmapause moving inwards to $L = 1.5$. VLF observations showed minimal activity on this day. Activity increased again on 1 November, seeming to originate from between 02:20 - 04:20 LT. However, at this time there was an increase in wave activity received at Halley Bay, Antarctica ($L = 4.3$), for which the calculated generation region is between $L = 2.75 - 4.0$. IMAGE EUV data showed that the plasmapause was at $\sim L = 2.75$. After this, no further chorus was observed at Palmer over the next few days.

The depletion of the Van Allen radiation belts which occurred as a result of the Halloween Storms was investigated by Baker *et al.* [2004]. The Halloween Storms were the result of a series of Coronal Mass Ejection (CME) impacts on the Earth's magnetosphere. At its peak, the storm pushed the outer radiation belts, which are usually found at $20000\ \mathrm{km}$ altitude, to within $10000\ \mathrm{km}$ of Earth's surface. Satellite data showed that the peak of electron fluxes, which are found near $L = 4$ during quiescent conditions, had moved to $L = 2.5$. They remained at this level for a period of 2 weeks before moving back to their regular location. Following this return to their normal configuration, particle flux enhancements appeared below $L = 2$, and endured for months. This redistribution of plasma density made the unusual observation of chorus at Palmer possible.

Statistics From 10 Years of Automatic Chorus and Hiss Detection

Golden *et al.* [2011] employed an automatic detection algorithm using a neural network to identify chorus and hiss in terrestrial broadband data received at Palmer Station, Antarctica ($L = 2.5$) over the ten years from May 2000 to May 2010.

The diurnal and seasonal variation of chorus and hiss at Palmer Station are studied using the automatically detected events from the ten years of data. The diurnal variation of chorus shows that it occurs only in the morning, between $3 - 9$ MLT. The typical frequency range of this chorus is between $1 - 4\ \mathrm{kHz}$, with some chorus extending up to $5\ \mathrm{kHz}$. The diurnal variation shows that hiss occurs throughout the day, but with peaks near dawn and dusk. In addition to this, the peak in activity around dusk extends to a higher frequency range ($3\ \mathrm{kHz}$) than the dawn occurrences ($1\ \mathrm{kHz}$).

The variation of chorus and hiss occurrence per month showed that there is more chorus and hiss detected when levels of geomagnetic disturbance (as measured by $\mathrm{K_p}$ and AE indices) increase. Chorus occurrence seems more sensitive to the changes in these indices. Finally, the seasonal variation of chorus and hiss showed that even though there was not a strong seasonal variation in geomagnetic activity, there was a strong seasonal effect visible in both the chorus and hiss variations. The hiss showed only a slight seasonal variation (50% change over the year), while chorus showed quite a drastic change (400% change over the year). Both of these changes are attributed to the extent of the day night terminator during the various seasons. The general trend was that when there were more hours of darkness (towards winter) more emissions were observed. This is consistent with the fact that trans-ionospheric and EIWG attenuation are greater when the ionosphere is illuminated. This is further reinforced by plots showing monthly averaged spectrograms. There are virtually no chorus observations at Palmer after sunrise. The automated identification method employed by Golden *et al.* [2011] may easily be modified to work at a different site, or even to detect the presence of whistlers, although no mention is made of what these modifications might be for the latter case.

The Latitudinal Extent of Chorus Observed in Space

Chorus observations were made by the Sweep Frequency Receiver (SFR) of the Plasma Wave Instrument (PWI) on board the Polar spacecraft [Bunch *et al.*, 2011]. Their results built on previous work by Dunckel and Helliwell [1969], Russel *et al.* [1969] and Moiser *et al.* [1973], among others.

The SFR observes chorus outside the plasmasphere in the off-equatorial region. The chorus is confined between $0.05\Omega_e$ and $0.65\Omega_e$. Between 25 March 1996 and 16 September 1997 chorus was observed on 459 of 1388 half orbits. Plots are made in the meridional plane, of the mean chorus power spectral density received as a function of magnetic latitude and radial distance. Due to the nature of the orbit, a range of L-values are only sampled in the northern hemisphere, but

one can safely assume that chorus observed in the northern hemisphere will travel to the conjugate regions.

The region in which chorus is observed is smallest in the midnight sector, and largest is the morning to noon sector (03-15 MLT), and somewhere between in the dusk sector. The chorus is mainly observed at $L \geq 4$, with small excursions beneath this value in the equatorial plane. The variation of chorus activity with geomagnetic activity is also discussed, with 3 regimes used: $AE < 100$ nT, 100 nT $< AE < 300$ nT and $AE > 300$ nT. There is an increase in chorus activity as AE increases, except for the dusk case, where the activity decreases as AE increases. In addition to a comparison with AE, the level of chorus activity is compared between cases where solar wind speed (V_{SW}) is either above or below 450 km/s. The data showed that there was slightly less chorus activity with $V_{SW} > 450$ km/s for midnight and dawn, and a marginal increase for dusk, with a substantial increase for noon, when compared to the $V_{SW} < 450$ km/s case.

Meredith *et al.* [2003] presented results of an analysis looking for favourable regions of the magnetosphere for chorus enhancement, and comparing these to actual chorus observations by CRRES at different geomagnetic activity levels. This revealed that at moderate levels of geomagnetic activity, the dayside region of chorus generation was limited in L and MLT. Additionally, the latitudinal extent of this region extended to latitudes of $\sim 30^{\circ}$ north and south on the dayside. A pronounced symmetry between the northern and southern hemisphere chorus generation regions in the equatorial plane was also evident.

2.3.2 Generation of Chorus

Particle Injections

Particles can be transferred from the solar wind into the magnetosphere by a number of processes. Interactions between the solar wind and the magnetosphere are described by Schindler [2007, Chapter 13]. Two of these injection events which are often associated with chorus are geomagnetic storms and substorms. A geomagnetic storm has three phases: the Storm Sudden Commencement (SSC), main and recovery phase. A geomagnetic storm occurs after a sudden enhancement in solar wind dynamic pressure (such as from a coronal mass ejection). This increase of pressure compresses the magnetic field on the dayside, briefly increasing the equatorial magnetic field strength. This also injects electrons and protons into the radiation belts, increasing the ring current density. The ring current flows westward around the Earth in the equatorial plane. This current generates a magnetic field which opposes the Earth's intrinsic magnetic field, which results in a decrease in magnetic field strength at the surface of the Earth [Ebihara *et al.*, 2008]. The ring current subsides to normal levels during the following days, and the magnetic field strength returns to normal levels. This is called the recovery phase.

The second injection mechanism is a substorm. At times the Interplanetary Magnetic Field (IMF) is directed southward. This opposes the direction of the Earth's magnetic field, which is always northward pointing. This allows for field lines in the IMF and the Earth's dipole field to merge, creating an open field line configuration. This creates a hole into which solar wind plasma can flow. The flow of the solar wind drags field lines from the dayside to the nightside, into the magnetotail. Once on the nightside, the field lines originating on Earth reconnect, trapping the excess plasma on the Earth side of the reconnection. This plasma is then injected into the magnetosphere at midnight, at the onset of the substorm. This model was proposed by Dungey [1961].

These particle injections supply a source of free energy for the amplification of chorus (and other) waves.

Doppler Shifted Cyclotron Resonance

Chorus and other VLF emissions are generated in the magnetosphere by Doppler Shifted Cyclotron Resonance [Brice, 1964; Tsurutani and Lakhina, 1997]. The whistler mode is a right hand circularly polarised wave, and electrons gyrating about a magnetic field line do so in a right handed sense. This means that electrons traveling along a magnetic field have the possibility of being in resonance with whistler mode waves traveling along the same field line, in the opposite direction. In Figure 2.4, a schematic showing a whistler mode wave and counter streaming electron is plotted. The resonance will occur if there is a constant phase relationship between the waves and particles. However, since whistler mode waves can only propagate with ω less than Ω, the waves must be Doppler shifted up to the electron gyrofrequency.

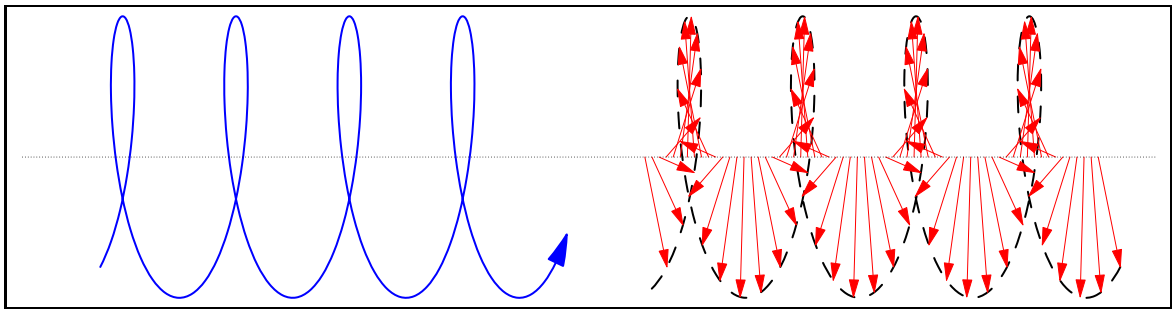

Figure 2.4: Schematic showing whistler mode waves (red) counter streaming electrons (blue).

Since the waves and particles are traveling towards each other, the required Doppler shift can occur if the electron parallel velocity is large enough. The condition for Doppler Shifted Cyclotron Resonance is,

$$n\Omega = \omega - \mathbf{k}\cdot\mathbf{v}, \tag{2.7}$$

where $\mathbf{k}$ is the wave vector, and n the order of the resonance. One can consider only parallel components, and thus calculate the amount of parallel electron velocity required for first order ($n = 1$) resonance with waves of a particular frequency. This is given by

$$v_{\parallel} = \frac{\Omega - \omega}{k_{\parallel}}, \tag{2.8}$$

and shows that the larger the gap between Ω and ω, the greater the parallel velocity that is required to fulfill the condition. Furthermore, the closer the waves are to parallel propagating, the lower the electron parallel velocity required for resonance. Thus, at a given L-value (fixing the value of Ω), higher parallel velocities are required to resonate with lower frequency waves. The above equation assumes non-relativistic velocities, and waves which are propagating nearly parallel to the magnetic field lines. Using (2.8), one can calculate the parallel energy required for resonance with waves of a particular frequency,

$$W_{\parallel} = \frac{1}{2}\frac{B^2\Omega}{\mu_0 N\omega}\left(1 - \frac{\omega}{\Omega}\right)^3, \tag{2.9}$$

where here N is the electron number density. From (2.9), one can see that along a particular magnetic field line, the energy requirements are minimised in the equatorial plane where B obtains its minimum value. This is the reason why Doppler Shifted Cyclotron Resonance interactions are thought to take place in the equatorial plane. As the generation region moves to higher L, the ambient equatorial magnetic field and consequently Ω decrease, resulting in a decrease in energy required for resonance. This change in the resonant energy required for resonance in the

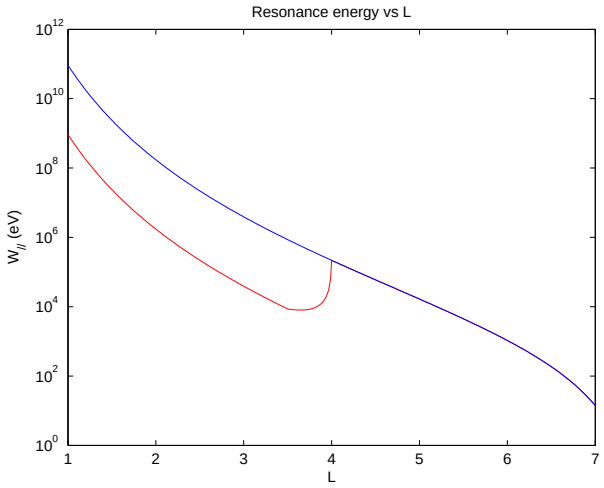

Figure 2.5: The variation of resonance energy with L-value, calculated in the equatorial plane, for a wave with $\omega = 2$ kHz. The blue curve represents a magnetosphere with no plasmapause, and the red curve includes a plasmapause at $L = 3.75$.

equatorial plane is plotted in Figure 2.5. Here, the blue curve represents a magnetosphere with no plasmapause (ie: density values vary smooth with L). Energy changes are due only to the change in L, and decrease monotonically. The inclusion of the plasmasphere is shown by the red curve, which merges with the blue curve outside the plasmasphere. This curve includes a plasmasphere where the density is two orders of magnitude higher than those outside the plasmasphere. The plasmapause is located at $L = 3.75$, with a width of $0.5L$ (a typical value as shown by Carpenter and Park [1973]). A simple linear relationship between N and L is assumed.

This figure shows the effect which the rapid density variation within the plasmapause has on the resonance energy. As already mentioned, the resonance energy decreases as wave frequency increases. This variation is shown in Figure 2.6. This figure is plotted for $L = 2.60$, and shows the decrease of resonance energy as ω increases. The effect of the plasmasphere is shown as two curves are plotted, where the blue curve represents resonance without a plasmasphere, and the red curve resonance with a plasmasphere included.

Particle Anisotropy

Kennel and Petschek [1966] showed how the direction of net energy flow between waves and particles is affected by the anisotropy, defined as

$$A = \frac{T_\perp}{T_\parallel} - 1. \tag{2.10}$$

The parallel temperature ($T_\parallel$) of a distribution of particles is proportional to the average $v_\parallel^2$ of the particles. Perpendicular temperature, ($T_\perp$), is similarly defined using $v_\perp^2$.

The direction of net energy flow is determined using A. $A > 0$ results in energy being transferred from the particles to the waves, resulting in wave growth, while $A < 0$ results in energy flowing from the waves to the particles, damping the waves. These energy exchanges always serve to homogenise the particle distribution, moving A towards zero. These various energy distributions are depicted graphically in Figure 2.7.

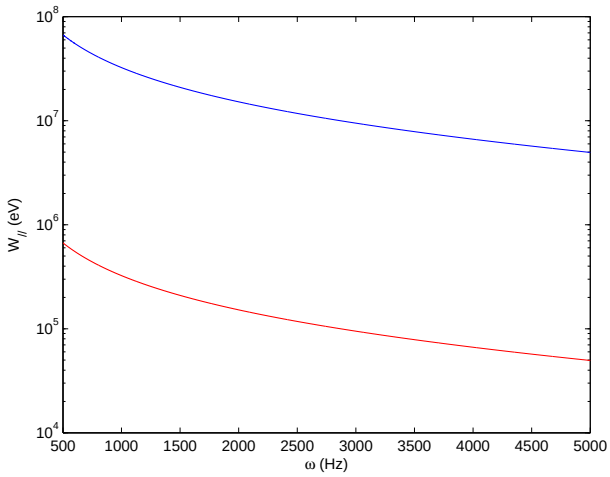

Figure 2.6: The variation of resonance energy with wave frequency. The blue curve represents resonance outside the plasmasphere, and the red curve resonance inside it. These plots are made using $L = 2.60$.

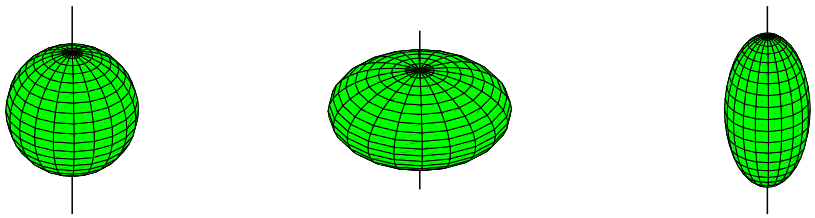

Figure 2.7: Graphical representations of particle distributions with (from left to right) $A = 0$, $A > 0$ and $A < 0$. These distributions are commonly referred to as isotropic, pancake and cigar distributions.

Summers *et al.* [1998] showed that significant energy exchange can occur between electrons and waves, resulting in a reduction of the parallel to perpendicular velocity ratio. This energy exchange is favoured in regions with low electron densities. This increase in Doppler Shifted Cyclotron Resonance efficiency in lower densities explains why chorus is generated outside the plasmasphere.

Chorus Generation

Prior to the observation of chorus, energetic particles are injected into the magnetosphere. These particles provide a source of free energy for the amplification of chorus waves. A background continuum of whistler mode waves exists. Those waves which satisfy the condition (2.7) are then involved in the energy exchange. If the particles have positive anisotropy, then energy will be given to the waves, causing amplification of those frequencies which satisfy (2.7).

This patch of resonant particles makes up the chorus generation region. These particles will be affected by gradient and curvature drifts, and so the generation region is expected to move. Once the wave enhancement has occurred, the waves must be guided to the ground for them to be observed by a terrestrial receiver. Since chorus waves propagate in the whistler mode, they are weakly guided by magnetic field lines from their generation region towards the ionosphere. Chorus would be subject to LHR reflection as discussed above, but it can penetrate through to the ground if appropriate guiding is achieved, either by the plasmapause or ducts.

The energy range of the particles and the L-value of the field line determine the frequency band of the chorus. The expected frequency of the chorus can be calculated using (2.9). This relationship means that chorus can be used as a magnetospheric probe, by inverting the calculation. The frequency of the chorus, and the L-value of the receiver can be used to estimate the energy of the particles in the generation region. Particle energies are usually assumed to obey a normal (or similar) distribution. This is seen in chorus spectra, as chorus typically spans a frequency band. The minimum frequency of the chorus corresponds to the highest energy particles.

Doppler Shifted Cyclotron Resonance interactions with whistler mode waves can scatter electrons into the bounce or drift loss cones [Koons *et al.*, 1981]. When the waves and particles are in resonance, energy is transferred either from the waves to the particles, or vice versa. The direction of net energy flow is determined by A of the electrons. Early observations associated chorus observations with particle precipitation [Rosenberg *et al.*, 1971; Foster and Rosenberg, 1976; Rosenberg *et al.*, 1981]. Parallel propagation is most readily realised with ducted waves [Tsurutani and Lakhina, 1997]. Some observations of high amplitude (with amplitudes an order of magnitude greater than the mean amplitudes) whistler mode waves were made by Culley *et al.* [2008]. These large amplitude waves can rapidly thrust particles into the loss cone [Kersten *et al.*, 2011].

Oblique propagation of whistler mode waves in the chorus source region

Observations of chorus near the equatorial plane at $L \sim 4.25$ by CLUSTER satellites were presented by Santolík *et al.* [2009]. These observations showed a case where chorus waves were not parallel propagating, as is assumed by most wave propagation and interaction models. It was noted that oblique propagation was not always the case, and that parallel propagation was still more commonly observed. Furthermore, it was found that hiss was also recorded on CLUSTER, a few minutes after the cessation of chorus observations. This indicated that both chorus and hiss could be generated in the chorus source region, or result from other sources.

Role of the Plasmapause in Dictating the Ground Accessibility of ELF/VLF chorus

Golden *et al.* [2010] studied the relationship between the occurrence of chorus at Palmer Station ($L = 2.4$) and the L value of the plasmapause (L_{pp}). Ground based observations are limited to those VLF signals which are able to penetrate through the ionosphere. These are either waves which have propagated naturally and have their wave normals inside the transmission cone, ducted waves whose wave normals are tightly bound to field lines, or waves that are scattered off irregularities into the transmission cone. The transmission cone is defined by the largest wave normal angle which will pass through the ionosphere. One might expect that since chorus is generated outside of the plasmasphere, that it should not be regularly observed within it. Recent results showed that chorus was routinely observed at Palmer Station, even during geomagnetically quiet periods when the plasmapause was far beyond Palmer [Golden *et al.*, 2011].

This study used 3 months of data in 2001, which was during solar maximum. The extent of the plasmapause was determined from IMAGE EUV data, and chorus data were obtained from the automated chorus detection system developed by Golden *et al.* [2011]. The AE activity index was used to determine the level of geomagnetic activity. Since the study was only concerned with Palmer Station, the location of the plasmapause was only determined at Palmer's MLT (MLT = UT - 4). After removing data gaps, approximately 230 hours of data were available.

Initial analysis of the data led immediately to the conclusion that chorus was most prevalent when AE was high, and L_{pp} low. A more in-depth analysis showed that for all frequencies the probability of receiving chorus was peaked when $L_{pp} \sim 2.6$. For lower frequencies the tail of the probability extended out to $L_{pp} \sim 5$, while for higher frequencies there was a narrow peak. Reverse ray tracing models were used to determine for which values of L_{pp} chorus can propagate to Palmer. These revealed that when $L_{pp} \geq 4.3$ no chorus was able to propagate from the source (outside L_{pp}) down to Palmer. The waves were either reflected off the plasmapause or heavily damped after crossing the plasmapause. For $L_{pp} = 2.9$ waves from as far as $L = 7$ were able to reach Palmer, although damping caused the peak chorus intensity to originate from $4.2 \leq L_{pp} \leq 4.6$. The maximum in total chorus waves was received when $L_{pp} = 2.9$. It was concluded that the instantaneous value of L_{pp} has a significant effect on the probability of chorus observation at Palmer.

Prevalence at Dawn

Chorus is most often observed in the dawn sector, although it can sometimes be observed in other MLT sectors [Sahzhin and Hayakawa, 1992]. Chorus typically occurs after a geomagnetic substorm, where particles are injected into the inner magnetosphere at around midnight. Gradient and curvature drifts cause the electrons to drift towards dawn. This accounts for the preferential observation at dawn. The drift itself is dispersive, meaning that higher energy electrons drift faster. These higher energy particles resonate with lower frequency waves. As successively lower energy particles arrive in the source region, higher wave frequencies satisfy the resonance condition, resulting in the often observed increase in maximum frequency [Smith *et al.*, 1996; Collier and Hughes, 2004].

2.3.3 Relationship to Hiss

Hiss is often observed simultaneously with chorus [Koons, 1981]. There is good reason that the two are so closely linked, namely that plasmaspheric hiss is believed to be generated by chorus waves which have refracted into the plasmasphere where they evolve into hiss [Bortnik *et al.*, 2008, 2009].

Hiss appears as a homogeneous band of waves in a VLF spectrogram. There are three varieties of hiss, each with its own spectral properties and occurrence pattern: auroral hiss [Sazhin *et al.*,

1993] observed in the auroral zone, mid-latitude hiss observed at mid-latitudes outside the plasmasphere, and plasmaspheric hiss observed inside the plasmasphere [Sahzhin and Hayakawa, 1992]. Plasmaspheric hiss is typically observed at lower frequencies, from several hundred to a few thousand hertz, while mid-latitude hiss extends up to more than $10\ \mathrm{kHz}$. Simultaneous observations of chorus and hiss in the same frequency range were first found in GEOS-1 data [Cornilleau-Wehrlin *et al.*, 1978]. Both chorus and hiss fell within the expected $0.05\Omega_e - 0.5\Omega_e$ frequency range of chorus.

The origin of plasmaspheric hiss has long been debated, but recently chorus has been identified as a likely candidate. Church [1983] first suggested that chorus may be the source of plasmaspheric hiss, and a satellite observation supporting this idea was discussed by Parrot *et al.* [2004]. These small case studies were followed later by theoretical analysis.

Bortnik *et al.* [2008] employed ray tracing models to investigate the propagation of chorus waves in the magnetosphere. Waves were launched with a range of wave normal angles from a point outside the plasmasphere. Only waves with a particular range of wave normal angles were able to penetrate through the plasmapause. The lower damping rates inside the plasmasphere extended the lifetime of these waves, which allowed them to magnetospherically reflect many times, filling the plasmasphere with their energy, generating a wave signature strongly resembling hiss. Using data from two THEMIS satellites, Bortnik *et al.* [2009] presented simultaneous observations of hiss inside the plasmasphere and chorus outside of it, concluding that chorus elements, after crossing the plasmapause and becoming dispersed, smear out to form hiss. These papers appear to provide a plausible explanation for the generation of plasmaspheric hiss.

2.4 Findings on the Nature of the Ionosphere and Plasmasphere

As is made clear by the above theory, the ionosphere and plasmasphere both play incredibly important roles in the generation and observation of VLF waves. Each of these topics warrant an in-depth study which is beyond the scope of this thesis. There are however a few aspects of these regions of space which should be discussed.

2.4.1 Ionosphere

Response of the D-region to the Total Solar Eclipse of 22 July 2009 in the Indian Sector

Singh *et al.* [2011] presented measurements of ionospheric reflection height and corresponding electron density at that height during the total solar eclipse of 22 July 2009. These values were obtained from tweek observations made during the solar eclipse, and compared to normal values obtained just before sunrise 30 minutes before the commencement of the eclipse. Observations were made at Allahabad (which experienced total solar eclipse), and Nainital, (which experienced 80% eclipse). The eclipse started at 00:00 UT (LT = UT + 5:30), peaked at 00:55 UT, and was over at 01:57 UT as viewed from Allahabad. The observation of ionospheric parameters during eclipse, just after sunrise has not been done before. These allow for the comparison of nighttime values with those achieved during eclipse. Typical values for the reflection height are $60 - 75\ \mathrm{km}$ during the day, and $75 - 95\ \mathrm{km}$ at night. During an eclipse, the blocking of radiation from the Sun by the Moon, in particular Lyman-α 1215 Å radiation, results in the ionosphere moving quickly towards night time levels.

Tweeks observed during the eclipse had a lower amplitude than their nighttime counterparts, and there was greater dispersion in the tweeks for the nighttime cases. The tweeks were observed between 00:30 – 01:30 UT, and higher order harmonics were visible for a 20 minute period centered on totality (only at Allahabad). The reflection height, and the electron density at that height was calculated from the tweeks recorded at Allahabad. These value were found to have stable

nighttime values until 23:00 UT, where the density began to increase, and the reflection height began to decrease. Leading up to totality this trend reversed, with reflection height increasing and density decreasing. These remained stable for 15 minutes either side of totality before moving sharply towards daytime values again between totality and the end of the eclipse. An interesting feature of these two periods is apparent, that the pre-totality increase of density (and corresponding decrease of reflection height) is significantly slower than the post totality decrease of density (and increase of reflection height). This indicates that recombination is a faster process than ionisation, at least during these periods of partial eclipse. At totality, the value of reflection height was $\sim 2-3$ km lower than normal nighttime conditions, and there was a ~ 5 km change in reflection height between totality and the beginning or end of the eclipse.

A study on the effect of the ionosphere near the conjugate location of an eclipse was performed by Le *et al.* [2009]. During a solar eclipse in the northern hemisphere they examined ionosonde and GPS Total Electron Content (TEC) data around the geomagnetic conjugate point of the solar eclipse. They found an increase in f_0F2, as well as an increase in TEC during this period. Simulations showed that this was attributed to a lowering of electron temperatures near the eclipse location.

Two important features of the ionosphere can be extracted from these studies:

- The change of the ionosphere from daytime to nighttime conditions occurs rapidly, so that the terminator forms a sharp boundary between nighttime and daytime ionospheres.
- When two ends of a field line are on different sides of the terminator, the day side exhibits higher levels of ionisation in its ionosphere. This is of particular importance near the geographic poles, where there is constant daylight in one hemisphere, and constant night in the other.

The above two facts may help explain the the ability of spherics to readily penetrate a daytime ionosphere in some exceptional cases.

2.4.2 Plasmapause Location

The most direct means of determining the location of the plasmapause is by *in situ* measurements. Satellites with means of detecting particle densities can determine the location of the plasmapause using these data. Other satellites, such as IMAGE, can view the plasmasphere from a position over the poles, by using imagers looking for extreme ultra-violet radiation emitted by plasmaspheric ions. While these observations are easy to use, satellites generally do not provide a continuous view of the plasmasphere. Since the plasmapause represents a boundary between two VLF wave generation regimes, its location is of great interest in VLF research.

Whistler Evidence of a Knee in the Magnetospheric Ionization Density Profile

The plasmasphere was discovered not by satellite, but by ground based measurements, namely the observation and inversion of whistlers. Carpenter [1963] presented his observation of knee whistlers. These whistlers are identified based on the distribution of whistler traces in a whistler group. A normal whistler group has traces whose nose frequencies decrease with successive traces, such that a smooth locus can be drawn through all the frequency-time pairs of nose frequencies. A knee whistler is different as there appear to be two superimposed whistler groups, such that the locus through nose frequencies is jagged. The knee whistlers were typically observed during geomagnetically disturbed condition ($\mathrm{K_p} \geq 5$). The mechanism proposed for the generation of knee whistlers, is that one group travels along a particular field line in a high density region of the magnetosphere, while the second along a nearby field line which has a significantly lower density.

Since the separation in L between the two groups is small, it can be concluded that knee whistlers occur when they propagate near a sudden decrease in plasma density. This sudden decrease in plasma density has since been identified as the plasmapause, and so analysis of knee whistlers allows one to ascertain L_{pp}.

2.4.3 Models of the Location of the Plasmapause

Various empirical models have been developed for determining the location of the plasmapause at any given time. Carpenter [1967] discussed the relationship between the dawn minimum location of the plasmapause, and geomagnetic activity via indices $\mathrm{K_p}$, Dst and local K. This showed that the plasmapause moved to lower L as the geomagnetic activity levels increased. A simple model using $\mathrm{K_p}$ was discussed by Carpenter and Park [1973].,

$$L_{pp} = 5.7 - 0.47\mathrm{K_{pmax}}, \tag{2.11}$$

where $K_{p\mathrm{max}}$ is the maximal $\mathrm{K_p}$ experienced during the preceding 24 hours. This model calculates L_{pp} for the dawn minimum position of the plasmapause, and uses that value as the representative value for the entire plasmapause.

This model was adjusted, and included an uncertainty measurement, by Moldwin *et al.* [2002],

$$L_{pp} = 5.39 \pm 0.072 - (0.382 \pm 0.019)\mathrm{K_{pmax}}. \tag{2.12}$$

A set of models derived from CRRES data, each based on different geomagnetic indices, were described by O'Brien and Moldwin [2003]. These models included a local time parameter, and were able to reproduce the bulge at dusk. The models based on AE, K_p and Dst respectively are given by

$$L_{pp} = -2.6(1 + (-0.30)\cos(\phi - 4.39))AE_{\mathrm{max}} + 11.6(1 + 0.20\cos(\phi - 1.046)), \tag{2.13}$$

$$L_{pp} = -0.39(1 + (-0.34)\cos(\phi - 4.34))\mathrm{K_{pmax}} + 5.6(1 + 0.12\cos(\phi - 0.7854)), \tag{2.14}$$

$$L_{pp} = -1.54(1 + (-0.04)\cos(\phi - 5.38))Dst_{\mathrm{max}} + 6.2(1 + 0.04\cos(\phi - 5.751)), \tag{2.15}$$

where ϕ is $2\pi(\mathrm{MLT}/24)$ and AE_{max}, $\mathrm{K_{pmax}}$ and Dst_{max} are the maximal value of each geomagnetic index obtained in the past 24, 36 and 36 hours respectively.

Finally, models of plasmaspheric equatorial density variation with L, from which the location of the plasmapause could be determined, were provided by Sheeley *et al.* [2001] and Carpenter and Anderson [1992]. The model described by Sheeley *et al.* [2001]is given by

$$n_{eq} = 1390(3/L)^{4.8} \pm 440(3/L)^{3.6}\mathrm{cm}^{-3}, \tag{2.16}$$

which is applicable for $3 < L < 7$. This model does not contain any geomagnetic activity or local time dependence.

Chapter 3

The Unresolved Issue of the Whistler Source Region

3.1 Introduction

Since the mechanism for whistler generation was first proposed by Storey [1953], research related to these VLF phenomena have uncovered much about their nature. Storey's initial theory came before man understood the near Earth space environment and before the discovery of the Van Allen radiation belts. The original theory put forward by Storey are now known to be an incomplete picture of whistler generation, but none the less his ideas were ground breaking, and the majority of his theory is still widely accepted as truth today. He put forward that whistlers are the result of lightning occurring at the geomagnetic conjugate point. The magnetic field of the Earth guides the waves to the magnetic conjugate point, although he also surmised that field aligned charged particle distributions are needed for this guiding to take place. Finally, he showed that the dispersion of a whistler is related to the density of charged particles in these field aligned structures. Storey proposed that these charged particles are from the ionosphere, which still has finite density at several Earth radii altitude.

Storey was also able to identify that two-hop whistlers were a result of the reflection of whistlers in the conjugate hemisphere. These are those whistlers that are received in the same location as the initiating spheric. The mechanism proposed for these whistlers was that upon reaching the conjugate hemisphere, whistlers undergo reflection off the ionosphere, and are then observed back at the spheric source location. These whistlers are always more dispersed that the single hop variety, and this fact means they have traveled further through the dispersive medium.

Storey originally stated that spherics from the exact geomagnetic conjugate point are most likely to produce a whistler. He went on to state that the source for whistlers at a particular location could possibly be a region with a radius of about $2000\ \mathrm{km}$ centered on the conjugate point. Studies by Fiser *et al.* [2010] showed that fractional hop (detected at LEO) whistlers were launched upwards from lightning strokes that occurred within a few degrees latitude and longitude of the satellite footpoint. There were far fewer whistlers which were found to originate from strokes as far as $2000\ \mathrm{km}$ away, but no further than this. This fits very well with Storey's theory. The data used by Fiser *et al.* [2010] was confined only to those which occurred above active thunderstorms.

Correlation analyses of the most probable source region for whistlers received at Tihany, Hungary; Dunedin, New Zealand; and Rothera, Antarctica, were performed by Collier *et al.* [2009], Collier *et al.* [2010] and Collier *et al.* [2011] respectively. The findings of these studies have been discussed already, but can be summarised as follows:

- If there was considerable lightning activity near the geomagnetic conjugate point, then this region was found to be the primary source of whistlers.
    - If there was considerable lightning activity near the geomagnetic conjugate point, and there were secondary sources of whistlers then the distance of these sources from the conjugate point ranged from $\sim 2000\ \mathrm{km}$ to $\sim 10000\ \mathrm{km}$.
- If there was very low lightning activity near the geomagnetic conjugate point, then the primary source of whistlers was found to be at another region of high lightning activity. The distance of this region was comparable to that of the secondary sources described above.
    - Even in this case, there were other secondary sources $\sim 2000\ \mathrm{km}$ to $10000\ \mathrm{km}$ away.

These findings agree with Storey's source region ideas to a point, in that the source location should be centered around the conjugate point. If there is no lightning near the conjugate point, then obviously Storey's mechanism cannot work. Also, these findings show that the location for whistler source lightning is much larger than previously believed. Now, one can break the whistler generation mechanism into two distinct parts.

1. A lightning stroke releases an intense pulse of radiation which propagates within the EIWG for thousands of kilometers. At some point, some of this energy penetrates through the ionosphere into the magnetosphere, is converted into the whistler mode, and is dispersed;
2. The whistler enters a duct, and propagates along the magnetic field line becoming more dispersed before arriving at the ionosphere in conjugate hemisphere. Here, since the propagation direction of waves is closely tied to the direction of the magnetic field line, the waves pass through the ionosphere into the EIWG. The waves propagate within the EIWG to the receiver.

The study in this chapter focuses on the first stage in this process, and asks: "from how far away can a lightning stroke launch whistlers into the magnetosphere above a certain location?". These fractional hop whistlers have only traveled a few hundred kilometers above the EIWG boundary. They are not necessarily ducted, and thus are not guaranteed to propagate along the magnetic field line to the conjugate hemisphere and re-enter the EIWG.

Previous study

The previous study by Collier *et al.* [2009] of the source region of whistlers received at Tihany showed that lightning over the conjugate point readily produced whistlers in Tihany. The main result from this paper is reproduced in Figure 3.1. The greatest source region is near the conjugate point, and a nearby region in Southern Africa. Other source regions, of lower significance, are located in South America and the Maritime Continent. These locations are $\sim 10000\ \mathrm{km}$ from the conjugate point of Tihany.

3.2 First Attempt at the Problem

3.2.1 Description of Data Sources and Method

In order to answer the question posed above, a method similar to that employed by Fiser *et al.* [2010] was employed. Whistlers were detected in broadband DEMETER data, and correlated with lightning strokes detected by WWLLN. In the case of Fiser *et al.* [2010], the lightning locations

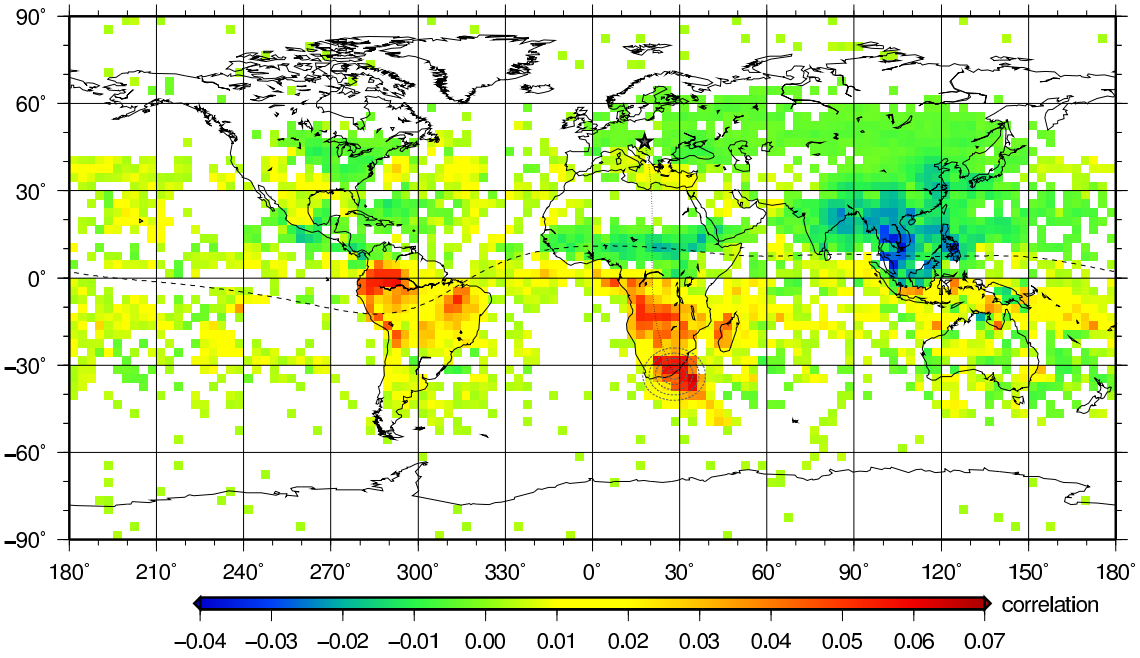

Figure 3.1: The main result from Collier *et al.* [2009] showing the source regions for whistler received at Tihany, Hungary (marked by the star). Distances from the conjugate point of Tihany in $200\ \mathrm{km}$ increments are marked with dashed circles. The major source regions are within $1000\ \mathrm{km}$ of the conjugate point. Secondary source regions are found in South America and the Maritime Continent.

were detected by the EUCLID network, a high efficiency network which operates across Europe. The drawback to using data from this network is that it only covers a relatively small region of the globe. Lightning events from outside of this region are not considered. In fact, since the spatial dimensions of Europe are $\sim 4000\ \mathrm{km}$, claims that the furthest a lightning stroke (detected by EUCLID) can launch a whistler into space is $2000\ \mathrm{km}$ are put into context. Results similar to those of Collier *et al.* [2009, 2010, 2011] cannot be achieved using such a data set due to its spatial limitations.

For this reason, the present study used WWLLN data. Detection efficiency is sacrificed for greater spacial coverage, spanning nearly the entire globe. For each individual whistler detected by DEMETER, the initiating stroke was found in WWLLN data, and the distribution of matched strokes was plotted.

DEMETER

DEMETER [Berthelier *et al.*, 2006] is a satellite in a $660\ \mathrm{km}$ altitude quasi sun-synchronous Low Earth Orbit (LEO). This means that at each location on Earth, the satellite passes overhead at roughly the same time (AM and PM) each day. There is one pass in the morning, and then a second pass ~ 12 hours later. The satellite has an orbital period of approximately 90 minutes, meaning that it crosses the same latitude twice every 90 minutes. The satellite nominally operates in a low resolution survey mode, where the data are averaged into several frequency bands. These data are not suitable for identifying whistlers. However, at certain predefined locations, the satellite switches into a high resolution burst mode, which allows for the detailed frequency structure of the data to be analysed. Only these burst mode data are suitable for the study conducted here. In Figure 3.2 a pair of maps showing the locations of the burst mode for 2005 and 2007, is displayed.

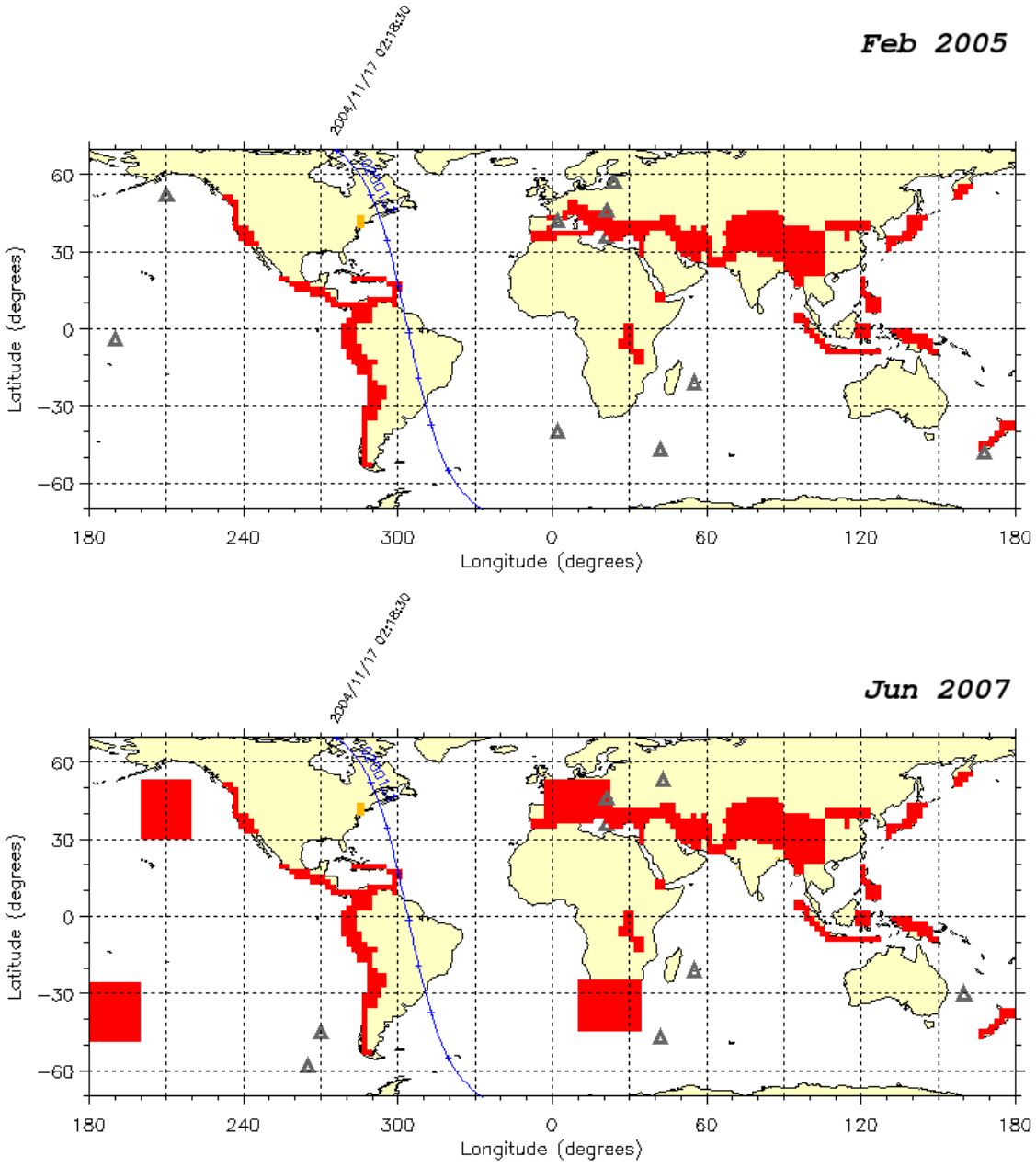

Figure 3.2: The regions, in red, above which the DEMETER satellite switched into high resolution burst mode for 2005 and 2007.

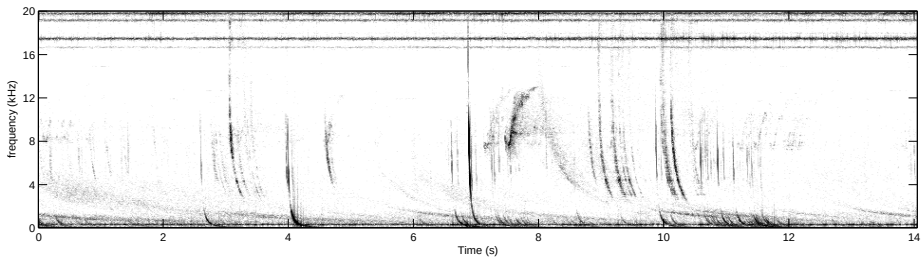

Figure 3.3: A snippet of burst mode DEMETER VLF data, recorded over the burst region, containing several whistler traces. The difference between up-going and down-going whistlers is apparent. Also notice that the signals from several VLF transmitters are visible in this spectrogram.

In the image for the 2005 data, the burst mode regions were typically confined to places known for seismic activity. This is because DEMETER was launched primarily to study electromagnetic signals associated with seismic activity. Between 2005 and 2007, however, the DEMETER team agreed to switch the satellite into burst mode over other regions. One of these regions is the rectangle over Southern Africa. This rectangle contains the conjugate point of Tihany, which is just off the south eastern coast of South Africa (the location of Tihany and its conjugate point are shown in Figure 3.1). One could thus use these measurements for a follow up analysis of Collier *et al.* [2009].

When in burst mode, DEMETER records VLF data sampled at 40 kHz, allowing for viewing of frequencies up to 20 kHz. The length of each data file is variable and depends on how long it takes the satellite to pass through the burst region. A sample of burst mode data containing several whistler traces is shown in Figure 3.3. In this sample one can see several independent whistler traces. One can also distinguish both up-going and down-going whistlers. Up-going whistlers have only traveled a few hundred kilometers, up to LEO, through the dispersive ionosphere, and so have very small dispersions. One such whistler is visible near 4 s in the spectrogram. Down-going whistlers have traveled virtually one full hop through the magnetosphere, and so have dispersions almost identical to those found on the ground at this L-value. A series of these whistlers is seen between 9 and 10 s. One whistler which has a much higher dispersion and considerably lower amplitude is seen at 8 s. This is either a whistler which has reflected several times, or propagated unducted from a different L-value.

In this analysis, only burst mode data from above the Southern Africa burst mode region, which contains the conjugate point of Tihany, were used. This region is from here on called the burst region. DEMETER passed through this region at roughly 08:00 and 20:00 UT each day (which corresponds to 10:00 and 22:00 LT). The data which were available within the burst region spanned three time periods, namely 2007/05/12 to 2007/11/24, 2008/10/29 to 2008/12/30 and 2009/01/01 to 2009/11/27, for a total of 590 days of observation. WWLLN data were available for all of these days.

Analysis Method

This study also used data from WWLLN. Here, the method used to match whistlers received on DEMETER with their initiating lightning stroke detected by WWLLN is discussed. Obviously one cannot get a one-to-one match in this case, since WWLLN does not find every lightning stroke which occurs on Earth, and therefore cannot match every whistler with its causative stroke.

Whistlers were located in the DEMETER data using a version of the code described by Licht-

enberger *et al.* [2008], modified to identify only upward going fractional hop whistlers. This is an important feature to note, since it means that the more dispersed down-going whistlers are not identified. If this distinction were not made, then this analysis would not only be looking at the source region for whistlers at Tihany, but also those received at Tihany's conjugate point, which are initiated by strokes in the northern hemisphere. With a list of whistler times at hand, matching with individual WWLLN events can proceed.

The matching occurs in a 2 stage process:

1. For each whistler, all possible initiating lightning strokes were identified by selecting those which occurred less than $67\ \mathrm{ms}$ before the whistler. This time corresponds to the time it takes light to travel half way around the globe.

2. For each of these candidate strokes, the delay between the whistler and stroke were compared to the time it takes light to travel between their locations. If these numbers matched, then the whistler was matched to that stroke. Here, due to timing or location inaccuracies, a $10\ \mathrm{ms}$ error window was allowed.

This matching process requires the use of the speed of light, since the VLF waves are an electromagnetic wave. Dowden *et al.* [2002] showed that a $12\mathrm{kHz}$ wave propagates through the waveguide at $0.9922c$. Propagation at c and $0.9922c$ respectively, over a distance of $40000\mathrm{km}$ (roughly the circumference of the Earth) results in a difference of $0.1\mathrm{ms}$, which is negligible in comparison to the timing accuracy of the AWD (and other errors which one should expect). The propagation velocity can thus be assumed to be c for studies of VLF wave propagation within the ionosphere.

The above two steps can be formalised as follows. All whistlers have an occurrence time, t_w, and each lightning stroke an occurrence time, t_l. Here, t_w is the whistler time returned from the AWD, which corresponds to the time of the whistler nose. Then those lightning strokes identified as possible initiating strokes (ie: step 1 above) for the whistler occurring at time t_w are those that satisfy

$$t_w - 0.067 \leq t_l \leq t_w. \tag{3.1}$$

Step 2 above can then be written as

$$|(t_w - t_l) - d/c| \leq 0.005 \tag{3.2}$$

where d is the distance between the location of the satellite footpoint and the lightning, and c is the speed of light in a vacuum. Since a $10\ \mathrm{ms}$ error window was used, there really is no need to be pedantic about the correct value of c to use within the EIWG. Due to the size of the error margin, it is possible that more than one stroke could be matched with a particular whistler. In these rare occurrences the stroke which minimises the value on the left hand side of (3.2) was used. A graphical representation of this matching is provided in Figure 3.4.

3.2.2 Result and Discussion

A total of 386159 whistlers were detected in the DEMETER data. Using the matching algorithm, 20169 matched lightning events were found. This means that matches could be found for approximately 5.2% of the whistlers, which is rather similar to the DE of WWLLN. The distribution of the number of matched strokes per $5^\circ \times 5^\circ$ grid cell is plotted in Figure 3.5, which shows that there are many matched lightning strokes over Central America and the Maritime Continent, a moderate number over Central Africa, and few in Europe, the Pacific Ocean and within the burst region.

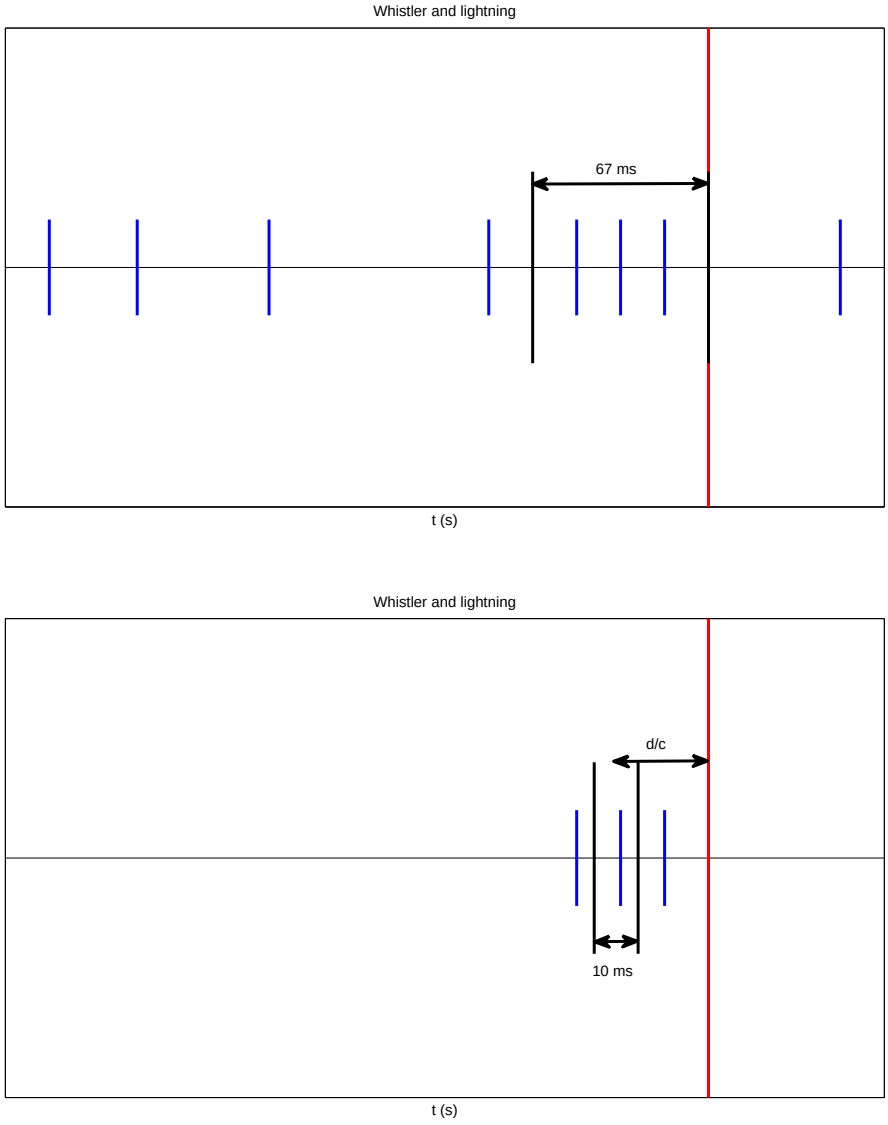

Figure 3.4: A graphical representation of the matching algorithm, where the whistler is marked by the red line, and lightning strokes by blue lines. Stage 1 is shown in the top panel, where all lightning strokes which occur less than $67\ \mathrm{ms}$ before the whistler are selected as candidate strokes, and move on to the second stage. In stage 2 (the lower panel), one stroke is matched if it falls within a $10\mathrm{ms}$ window, centered on a time d/c before the whistler.

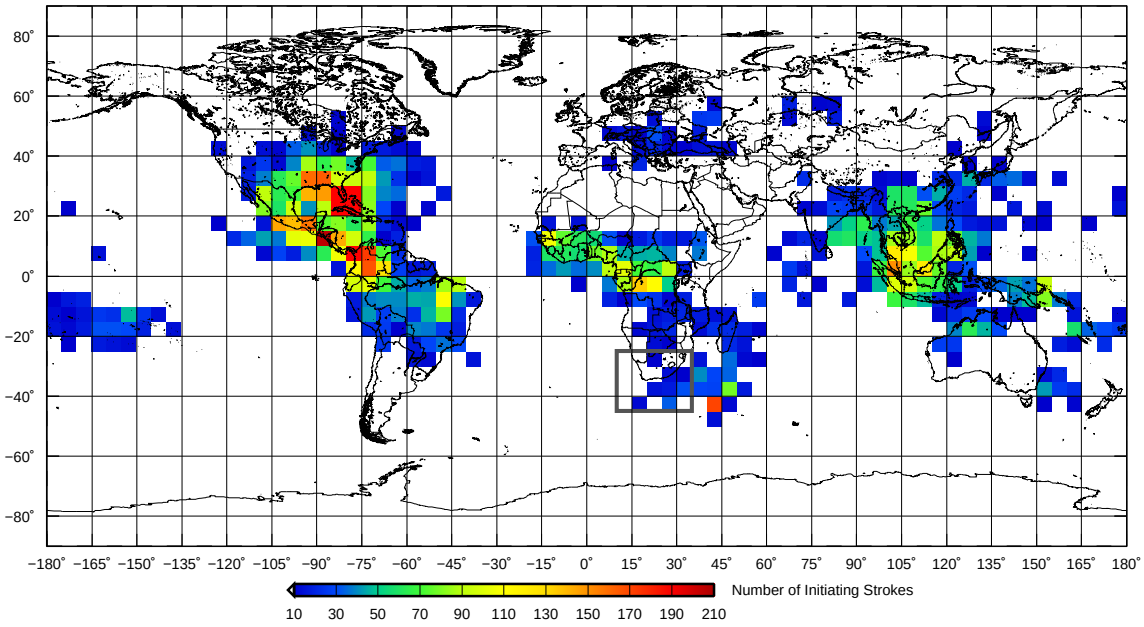

Figure 3.5: The distribution of lightning strokes matched to whistlers detected by DEMETER within the burst region, projected onto a $5^\circ \times 5^\circ$ grid. The colour scale ranges from blue for few events, to red for many. White on the map corresponds to fewer than 10 matched events, while the upper end of the scale represents 210 or more matched events. The burst region is enclosed by the grey box. There are peaks over Central America and the Maritime Continent, and a smaller peak over equatorial Africa.

These results are definitely surprising, especially when compared to those shown in Figure 3.1, which also shows high correlation near Central America and over the Maritime Continent. The new result, however, has a very low number of matched events within the burst region, and over nearby Central Africa. It is curious that these results should agree on some counts, but differ so substantially on the importance of the burst region as a source for whistlers. This would definitely be expected as a major source given the findings of Collier *et al.* [2009], and probably even more so, the mechanism proposed by Storey [1953]. One thing which was taken for granted was the timing accuracy of the DEMETER satellite. Chum *et al.* [2006] described how the timing offset between ground based GPS synchronised measurements from EUCLID and those on board DEMETER could be determined empirically. This delay is expected since it takes a finite amount of time for waves to propagate through the ionosphere, to the height of DEMETER. The speed of the waves through the ionosphere is significantly different from c, given the charged particle content of the ionosphere. Upon examining the technical documents of DEMETER, however, it was found that there was no mention of GPS time synchronisation on board the satellite. An email inquiry was sent to the operators of DEMETER, asking how the time on board was coordinated with time on the ground, and how often clock drift was corrected. The following was received as a personal communication from M. Parrot on 14 June 2011:

> `There is a clock onboard the satellite which give us UT time with an accuracy of 30-50 ms. The drift of the clock is regularly corrected by TC but I do not know how often.`

This essentially means that there is a random timing offset (either positive or negative) between the WWLLN data (which is GPS synchronised) and DEMETER data. This in turn means that

when the algorithm described searches for a causative stroke, it is not necessarily doing so in a way that one could expect would find the correct stroke. Essentially, a random stroke was being selected from the data, and not one which was causally related to the whistler. If one compares the result presented in Figure 3.5 to the WWLLN lightning distribution presented in Figure 2.1 (in particular (b) from 2009, which is representative of the majority of the WWLLN data used in the analysis), one notices a striking similarity. Ignoring the values of the colour scale, and instead just looking at the colours (so that the relative levels in each figure are compared), it is apparent that the peaks in either distribution are in the same place. Also, the relative value of each peak is roughly the same (ie: they are the same colour). This means that the result in Figure 3.5 is actually showing the underlying structure of the WWLLN data, and no preference is given to areas which are more likely to produce initiating strokes.

With the information about the timing offsets in DEMETER data, this is actually to be expected. If one were to select a random data point out of a particular distribution, then the probability of picking a point from a particular part of the distribution depends on the distribution itself. Thus, if one did this many times, and plotted the distribution of these random points, then it would surely be nearly identical to the original distribution (apart from the magnitude of peaks, and small statistical variances). Thus it is almost obvious that the result in Figure 3.5 would so closely resemble the underlying lightning data.

Also, the algorithm used in this study makes no correction for ionospheric delay. In order to account for these timing offsets, a method similar to that employed by Chum *et al.* [2006] is used below. This technique accounts for both the natural (although variable) delay attributed to propagation through the ionosphere, and the random delay caused by the drift of the clock on DEMETER. For this method, one requires a large amount of data from a lightning source within the burst region. Since this region is limited in extent, a local lightning network with high detection efficiency will suffice. The South African Weather Service (SAWS) operates such a lightning detection network within South Africa, the South African Lightning Detection Network (SALDN).

3.3 Using South African Lightning Detection Network

The SALDN is a commercial network similar to those used by other countries, such as NLDN in the United States, NZLDN in New Zealand or EUCLID in Europe. It provides very high detection efficiency within the network, by placing a high density of receivers distributed more or less uniformly over the land. The SALDN boasts a DE of $\sim 95\%$ over most of the country, except over the extreme south western corner, which is typically a very low lightning density zone, and consequently effective coverage was not needed there. This does not result in many missed detections however.

Before the problem of determining the timing offset for DEMETER is attempted, another interesting analysis can be conducted, namely a comparison between SALDN and WWLLN data. These sorts of analyses have been done on other local detection networks [Rodger *et al.*, 2006b]. Furthermore, they allow for a test of the SALDN data. Initially, access to only one month of data was allowed, namely July 2007. This month falls in the southern hemisphere winter, which is not during the peak South African lightning season. It does, however, mean that an initial test of the data's applicability to the intended problem can be performed.

3.3.1 Some Statistics of the SALDN Data

First the diurnal variation of the lightning activity is investigated. The diurnal variation of the lightning is plotted in Figure 3.6. One can see that there is a peak in lightning activity around mid-

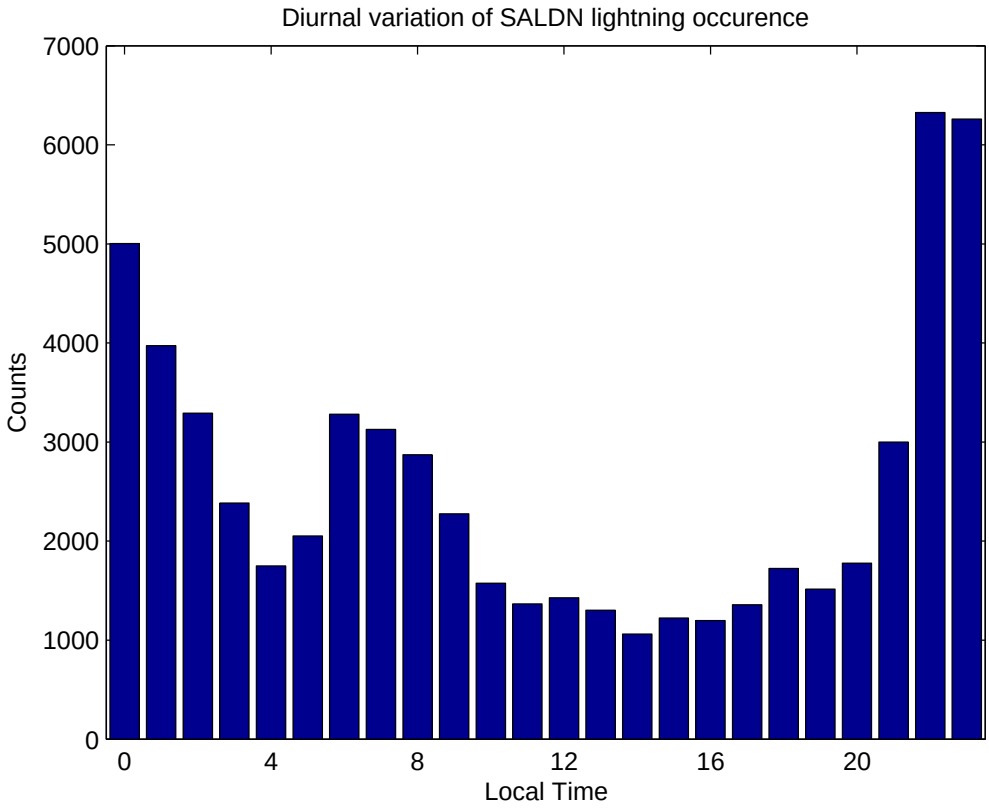

Figure 3.6: Diurnal variation of the SALDN data for July 2007. There is a peak in the night time hours, as well as the late morning. These are not typical of South African lightning, and are most probably only present during winter.

night, as well as at dawn. This is not what one would expect, since the majority of the lightning in South Africa occurs in the late afternoon, after intense heating causes uplift, resulting in the formation of cumulo-nimbus clouds, and consequent thunderstorms. This happens predominantly in summer though, and since the histogram in Figure 3.6 is for a single winter month, one cannot expect this behavior to be evident. During winter, thunderstorms usually occur when a cold front passes through, pushing the warmer moist air above the oceans upwards. Since there is no requirement for intense heating in this process, the time of day at which these storms occur is not related to the hottest part of the day [Collier *et al.*, 2011].

3.3.2 SALDN Data Validation

Since the SALDN data have not up to now been used extensively for VLF related research, one should first validate the timing accuracy, location accuracy and detection efficiency against a trusted data set such as the WWLLN data. The WWLLN data used in this comparison are confined to the geographic region between 22°– 35°S and 16°– 33° E.

Initially, one month of data was received from the SAWS, and only this data was used to determine whether the data would be suitable for the intended purpose. This month of data was thus thoroughly tested before more data was requested.

The first step in the data verification is to correct the timing offset between the data sets. The SALDN data times are in South African Standard Time (SAST) which is UT+2, while the WWLLN data is recorded at UT. The SALDN data was converted to UT. With this done, the data

could be compared directly. As a first check, the difference in lightning levels of both systems at the same time was investigated. The daily counts of lightning activity from the two networks for July 2007 are plotted in Figure 3.7 (a). One can see that the two time series have their peaks on the same days, although the SALDN data have much higher values. This is to be expected though, since the WWLLN network has a low average DE, which is even lower in Africa. WWLLN is known to have a much higher DE for strokes with high absolute values of peak current [Rodger *et al.*, 2006b]. The plot in Figure 3.7 (a) is thus repeated in Figure 3.7 (b), but only SALDN strokes which have a peak current greater than $60\ \mathrm{kA}$ are included. The values of the peaks in this second plot are now much more comparable, which shows how much the detection efficiency of WWLLN increases for strokes over $60\ \mathrm{kA}$.

There is an anomaly in Figure 3.7 (b) on the 7 July 2007, where it seems that the WWLLN network has detected more strokes than SALDN. This is not what one would expect, since the SALDN detection efficiency is vastly greater than that of WWLLN. A plot of the locations of the WWLLN events on this day shows that there are a significant number of events over the ocean, some distance from the land. Now, the SALDN network's efficiency drops off significantly outside the area of the receiving nodes, of which there are none on the ocean. WWLLN, however, would have a fairly uniform detection efficiency between the land and sea regions near South Africa. These strokes over the ocean are outside the coverage area of the SALDN network, but not that of WWLLN. This makes it possible for WWLLN to detect more strokes of higher power on a given day than SALDN, if there are sufficient strokes occurring over the ocean.

Figure 3.7 (b) shows that on the 27 July the number of high current lightning strokes detected by the two systems was nearly the same, and that this day showed amongst the highest levels of lightning activity for July. The locations of all SALDN and WWLLN strokes from this day are plotted in Figure 3.8. From this map one can see that there are definitely a number of strokes which have been detected by both systems, although some of them have slightly different locations. One expects that the SALDN HF network, which operates using shorter wavelengths than WWLLN, would have the higher location accuracy. In any event, there is a very high probability that those events detected by both networks within such close proximity are from the same strokes.

Both the WWLLN and SALDN networks sychronise their clocks with GPS satellite, and so one expects there to be no timing offset between the two data sets. One pair of events which appear to be from the same lightning stroke was selected. These events are clearly separated from any other events, which improves the probability that these detections did indeed arise from the same lightning stroke. This pair is indicated in Figure 3.8 by the large red circle. The distance between the locations of the detections by the two networks is $1.16\ \mathrm{km}$, and the difference in the recorded time between the events from each system was 2 hours (within a few milliseconds). This single event allowed us to identify that the SALDN data was recorded in UT +2 (which is South African Standard Time (SAST)). One can thus safely conclude that these two detections did originate from the same lightning event. All the SALDN data was converted to UT by subtracting 2 hours from the data.

Now it is possible to pair all strokes detected by both systems. This is done as follows:

- For each SALDN event, the distance and the absolute value of the delay between all WWLLN events were computed.
- If the delay between the SALDN event and a particular WWLLN event was less than $10\ \mathrm{ms}$, and the distance was less than $100\ \mathrm{km}$, then the WWLLN event was labeled as a possible match to the SALDN. $100\ \mathrm{km}$ is a very conservative (overestimated) value of the inaccuracy of WWLLN locations in South Africa. This large value is used since errors may arise from both WWLLN and SALDN detections.
- We refine the above selection, and select the pair for which the delay was minimised.

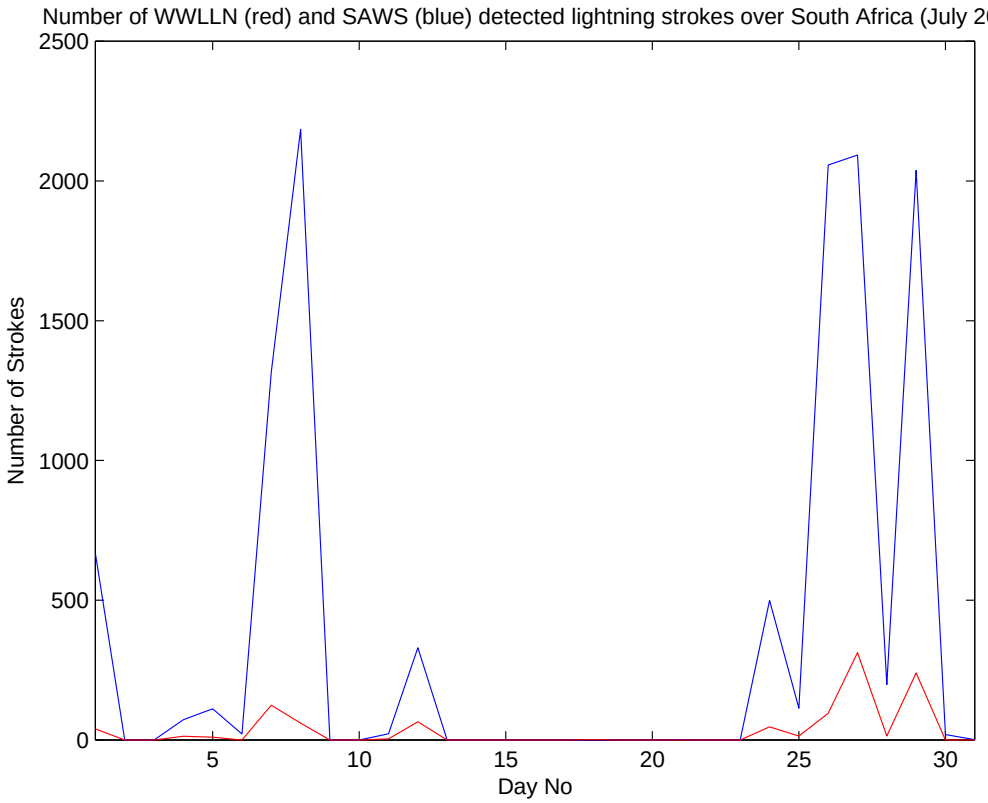

(a) All strokes

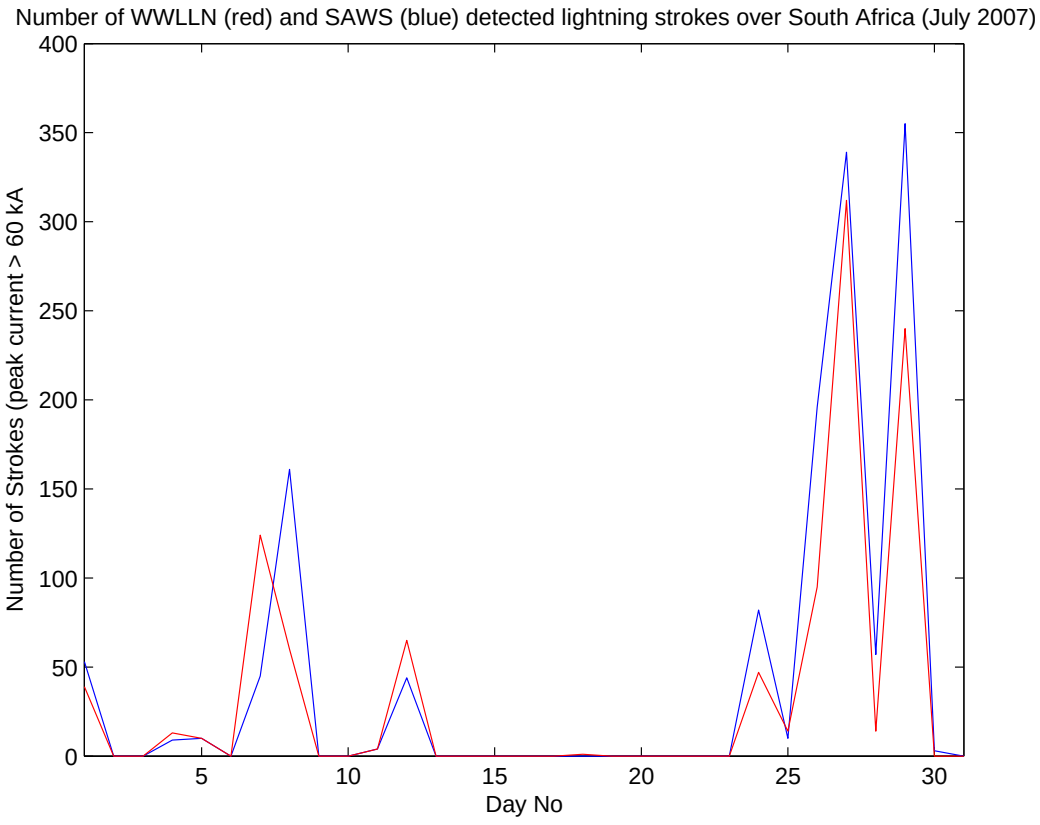

(b) All WWLLN strokes and SALDN strokes with peak current > 60 kA

Figure 3.7: Daily counts of lightning from WWLLN (red) and SALDN (blue) (a). A similar plot with SALDN strokes limited to those with peak current > 60 kA is also shown (b).

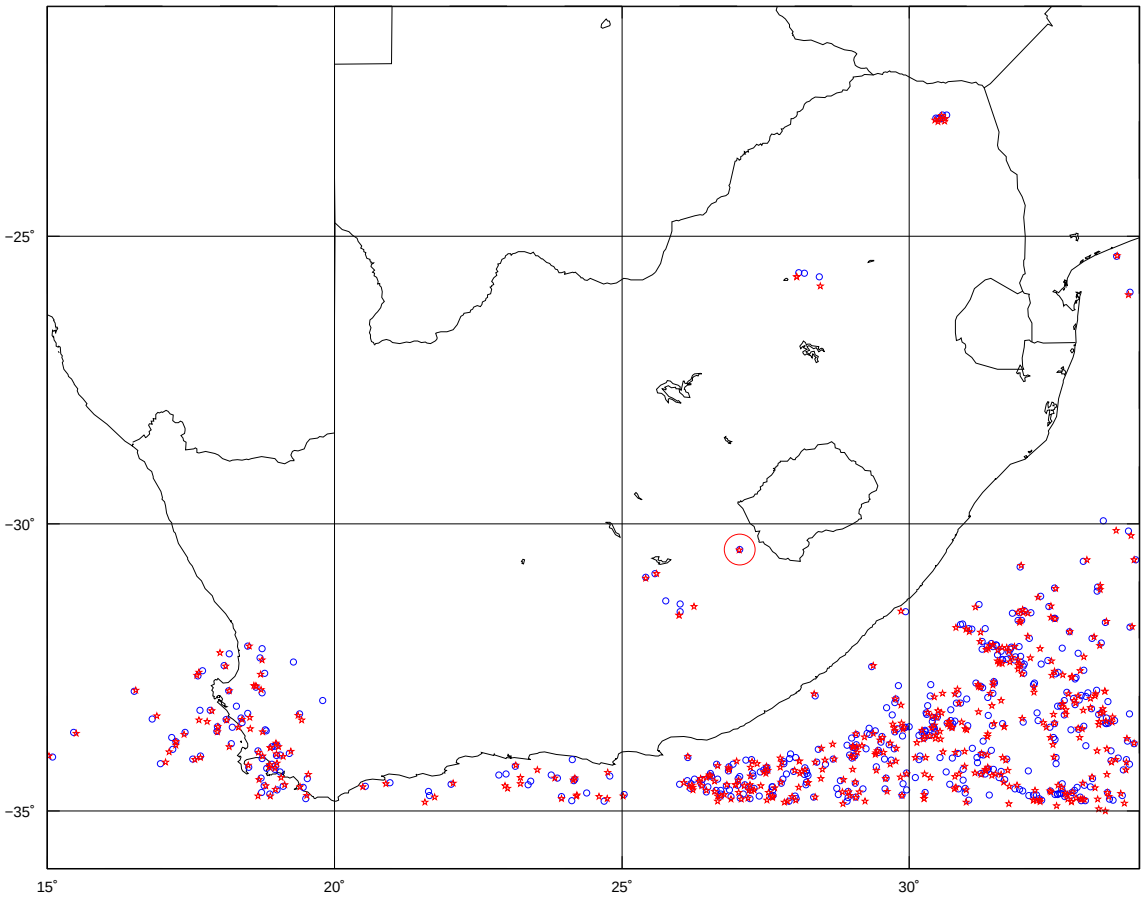

Figure 3.8: Locations of all SALDN (blue circles) and WWLLN (red stars) events on 27 July 2007. The events marked by the red circle are likely the same stroke detected by both networks.

Following the above algorithm, a single matching WWLLN event (if one exists) is obtained for each SALDN event. Doing this for July 2007, 479 matched events are found, out of a total of 11744 SALDN events for that month, which translates to a 4.01% detection efficiency. This value is comparable to the global average detection efficiency of WWLLN.

3.3.3 Statistics for 2007

Analysis of a single month of SALDN data show that the SALDN data could be of use for the analysis of DEMETER and WWLLN whistlers, further data were requested from SAWS. Data were obtained for the entire 2007, and from the 6 month period from 2008/11/01 to 2009/04/30. This allows for statistics of an entire year's data to be discussed. First, the diurnal and annual distribution of the data are plotted in Figure 3.9. This clearly shows that lightning activity is peaked during the months October to mid-April which is the Austral summer. The diurnal distribution shows a peak at approximately 16:00 LT, and it drops off gradually to a minimum at 09:00 LT on either side of the peak. This differs significantly from the plot shown in Figure 3.6 which was generated from a winter month's data.

Next, the distribution of lightning stroke peak current was investigated. In Figure 3.10, the distribution of the peak currents for 2007 is plotted. The overwhelming majority of strokes have negative polarity, and peak current magnitudes below $50\ \mathrm{kA}$. $\sim 0.3\%$ of strokes had magnitude of peak current larger than $90\ \mathrm{kA}$, while $\sim 1.5\%$ of strokes had magnitude of peak current larger than $50\ \mathrm{kA}$.

Matched Detections

In order to extract information about the performance of WWLLN in South Africa, various statistics for the strokes which were matched between the two systems (as described above) are discussed. Since results will be compared with those presented above, the matched statistics discussed here are from the 2007 data only. The first statistics presented are those which show how well the SALDN timing agrees with that of WWLLN. The distribution of timing differences between matched SALDN and WWLLN strokes is plotted in Figure 3.11. This shows that there is a clear peak at $0\ \mathrm{ms}$, which is 3 orders of magnitude higher than than the other peaks around it. There are very few strokes which have timing differences larger than $\pm 0.6\ \mathrm{ms}$. Remember that the matching algorithm required events where this timing difference was within $10\mathrm{ms}$. This figure also shows that in no cases were the magnitude of timing differences greater than $1\mathrm{ms}$. This confirms that there is no systematic timing difference between the two systems (other that the time zone difference which has already been corrected).

Next, the distribution of differences in position between matched events is plotted in Figure 3.12. This shows that the distances between the two matched events' positions were mostly below $10\ \mathrm{km}$, with some differences (with much reduced frequency) at greater ranges all the way to $100\ \mathrm{km}$. This is an indication of the typical location accuracy of WWLLN. Since the SALDN locations are accurate to within $500\ \mathrm{m}$, which is significantly lower than that of WWLLN, one can consider these locations correct. From this one can conclude that WWLLN faithfully finds the correct location within $10\ \mathrm{km}$ in over 80% of cases.

The distribution of peak currents for matched detections is shown in Figure 3.13. This shows that the majority of matched strokes have negative peak current values, as is the case for the raw SALDN data in Figure 3.10. These figures do differ from each other though. The matched events have a reduced proportion of negative peak current events. The proportion of events with magnitude of peak current above $90\ \mathrm{kA}$ is also substantially higher. This is due to WWLLN being biased towards strokes with greater peak currents, and the fact that positive strokes are typically more powerful.

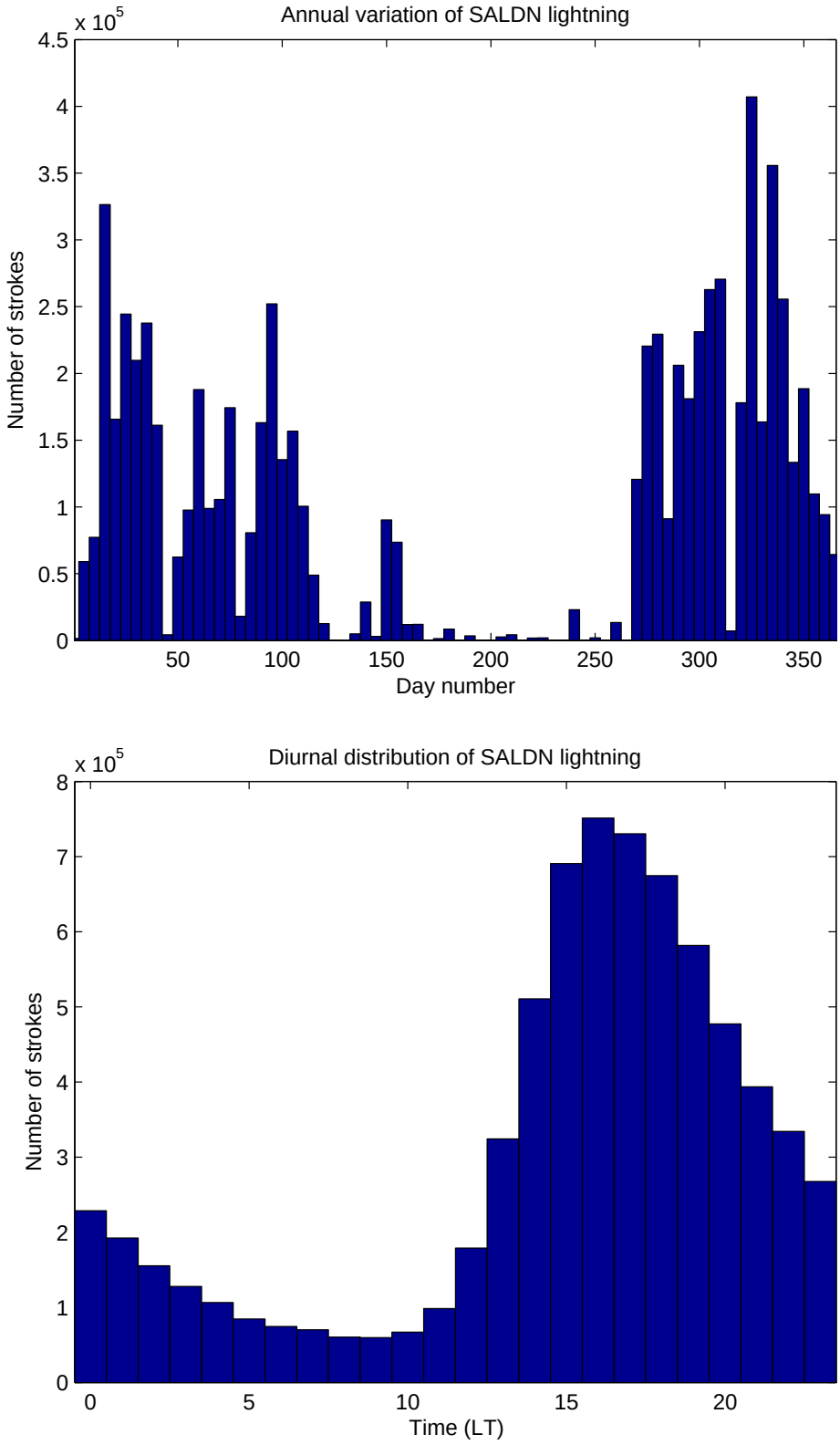

Figure 3.9: Annual (top) and diurnal (bottom) variation of the SALDN data for 2007. Lightning predominantly occurs in the Austral summer months, and lightning activity peaks in the late afternoon. Note the difference between this diurnal plot and that in Figure 3.6

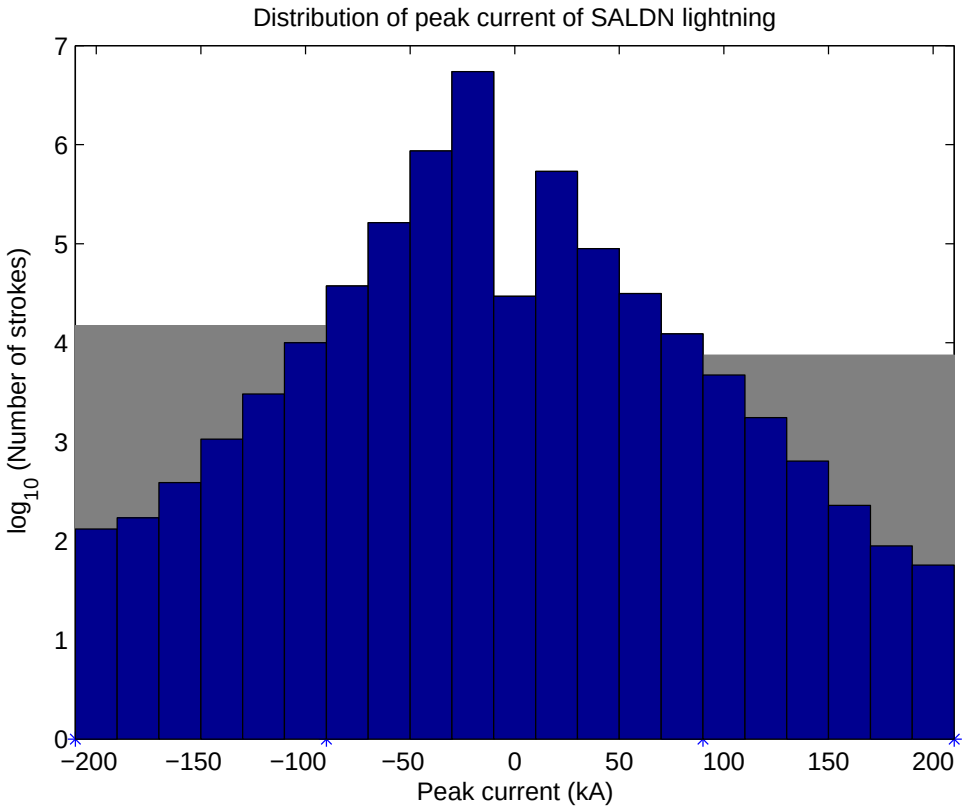

Figure 3.10: Peak current distribution of the SALDN data for 2007 shown by blue bars, each with a width of $20\ \mathrm{kA}$, shown on a log scale. The number of strokes with magnitude of current $> 90\ \mathrm{kA}$ are shown by the grey bars. The number of strokes which fall into this category is ~ 3 orders of magnitude lower than the peak.

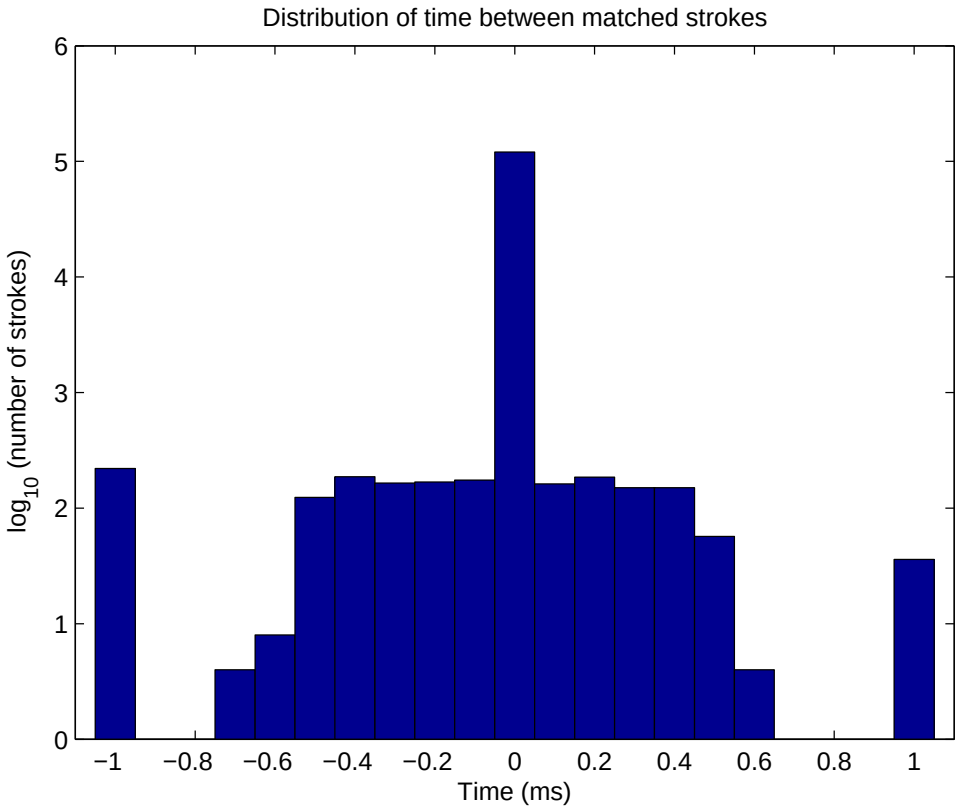

Figure 3.11: The distribution of delays between matched SALDN and WWLLN strokes, plotted with a logarithmic scale. The bins at ± 1 ms are the total delays outside of these limits. There is a clear peak at 0 ms.

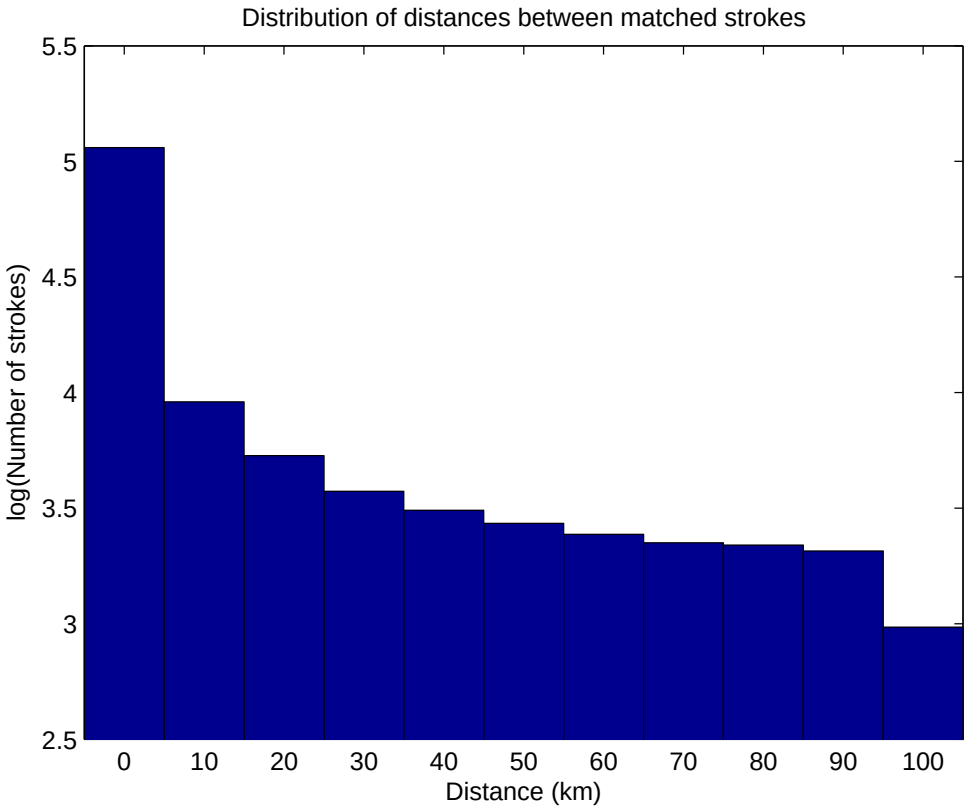

Figure 3.12: The distribution of distances between matched SALDN and WWLLN strokes plotted on a log scale. Most of the distance differences are $< 10\mathrm{km}$, and there is an order of magnitude less matches with distances $> 10\mathrm{km}$.

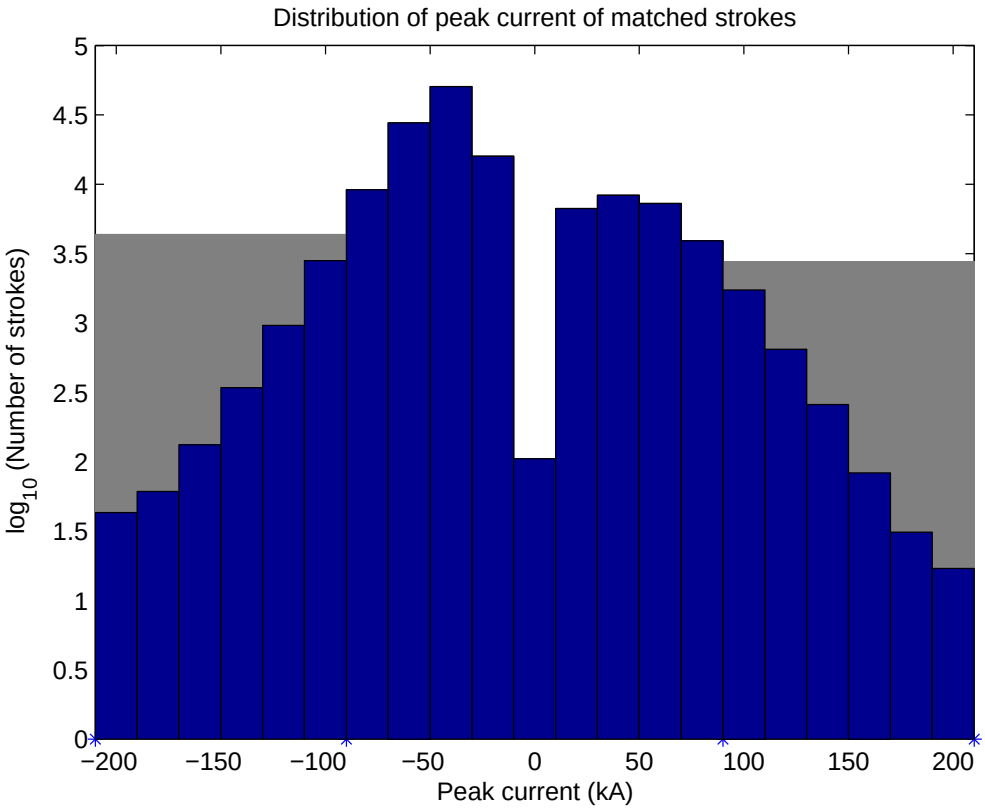

Figure 3.13: The peak current distribution of matched SALDN and WWLLN strokes, plotted with a log scale. There is significant bias towards negative peak currents evident, although not as extreme as in the SALDN data. A much greater proportion ($\sim 5.2\%$) of strokes have magnitude of peak currents > 90 kA than the SALDN current distribution.

Finally, the annual and diurnal distributions of matched events are plotted in Figure 3.14. The annual distribution plotted in the top panel has the same rough distribution as in Figure 3.9. This indicates that the DE of WWLLN in South Africa is not a function of season. Of course, this is to be expected at a low latitude location where the seasonal effect on day and night length is not as extreme as that at higher latitudes, where there would surely be a marked seasonal variation in WWLLN DE. The diurnal distribution does, however, differ significantly from that of the raw SALDN data shown in Figure 3.9 (lower panel). The peak in this case occurs at a much later LT, at $\sim$ 19:00. This is typically after sunset in South Africa in the summer months (when the majority of the lightning occurs). The reason for this is the increased DE of WWLLN after sunset, which has resulted in a much greater proportion of night time matched events.

Comparison of South African Lightning and Tihany Whistlers

At this point it becomes pertinent to discuss the Tihany whistler results presented in Figure 2.3, where the diurnal variation of whistlers received at Tihany is presented. Since the majority of whistlers received at Tihany should originate from lightning which occurs within South Africa, one would expect that the diurnal variations of these two data sets should look similar. To facilitate a comparison of the two figures (the diurnal variation of SALDN lightning is plotted in Figure 3.9, lower panel), they have been reproduced in Figure 3.15. Both data sets are plotted with UT time on the x-axis (which means the SALDN data here is shifted from that presented in Figure 3.9).

This figure shows that the majority of whistlers are received in Tihany during nighttime hours from 18:00 – 03:00 UT. This maximum is also rather flat, not varying substantially during the course of the night. This is due to the reduced attenuation experienced by whistler mode waves after the Sun has set, and the fact that whistler mode waves penetrate through the ionosphere into the EIWG more readily during night hours. The lightning data, however, shows a peak at 14:00 UT, tailing off sharply on either side of the peak, to a distinct minimum at 06:00 UT. From these two figures, one can conclude that ionospheric attenuation plays a much more significant role in the reception of whistlers at Tihany than the presence of conjugate lightning.

3.4 New Result

As described, the initial approach at correlating WWLLN lightning to DEMETER whistlers was incorrect, requiring the calibration of the DEMETER clock. With the SALDN data validated, it is used to correct for the systematic clock drift, and allowing for a new, correct result to be obtained.

3.4.1 Calibration of DEMETER from SALDN Data

With the SALDN data validated, it can now be used to determine the timing offset of DEMETER data. The details of this process are described by Chum *et al.* [2006], but for completeness, it will be described here. All lightning times from SALDN which occur during a particular DEMETER half orbit are stored in a vector $t_\ell = (t_{\ell 1}, t_{\ell 2}, t_{\ell 3}, \cdots, t_{\ell n})$. All of the whistler times reported from the AWD algorithm from that same half orbit are then stored in another column vector $t_\omega = (t_{\omega 1}, t_{\omega 2}, t_{\omega 3}, \cdots, t_{\omega m})$. Then, for each whistler time $t_{\omega i}$, the differences between it and each lightning time $t_{\ell j}$ is found, and these form the matrix t_{ij}, which would look like:

$$t_{ij} = \begin{pmatrix} t_{\omega 1} - t_{\ell 1} & t_{\omega 2} - t_{\ell 1} & \cdots & t_{\omega m} - t_{\ell 1} \\ t_{\omega 1} - t_{\ell 2} & t_{\omega 2} - t_{\ell 2} & \cdots & t_{\omega m} - t_{\ell 2} \\ \vdots & \vdots & \ddots & \vdots \\ t_{\omega 1} - t_{\ell n} & t_{\omega 2} - t_{\ell n} & \cdots & t_{\omega m} - t_{\ell n} \end{pmatrix}.$$

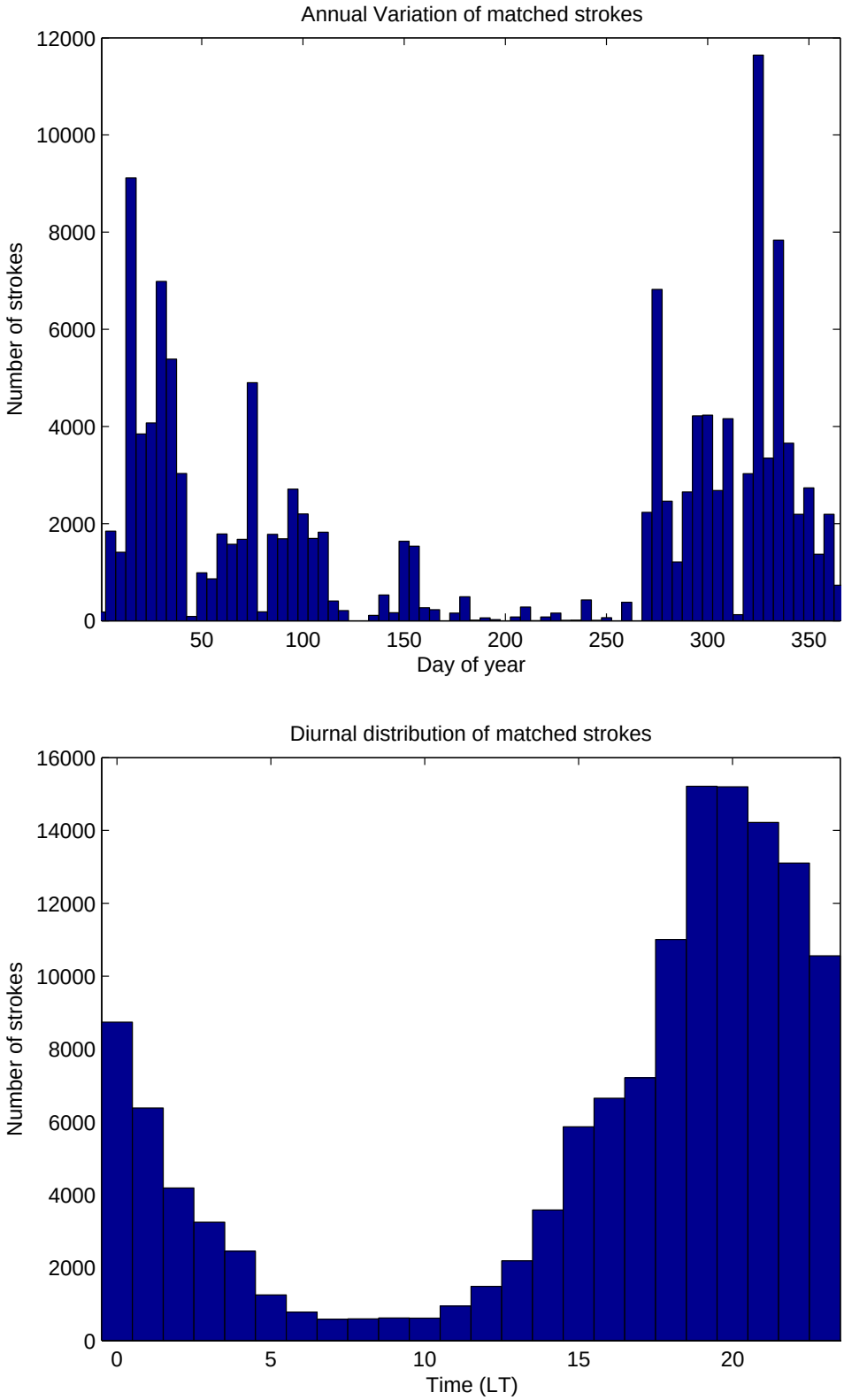

Figure 3.14: The annual (top) and diurnal (bottom) distribution of matched events. The annual trend follows that presented in Figure 3.9 (top panel), although with reduced values of the peaks, owing to the low DE of WWLLN. The peak of the diurnal distribution shown here is shifted towards night when compared to Figure 3.9 (bottom panel). This is due to the increased detection efficiency of WWLLN after sunset.

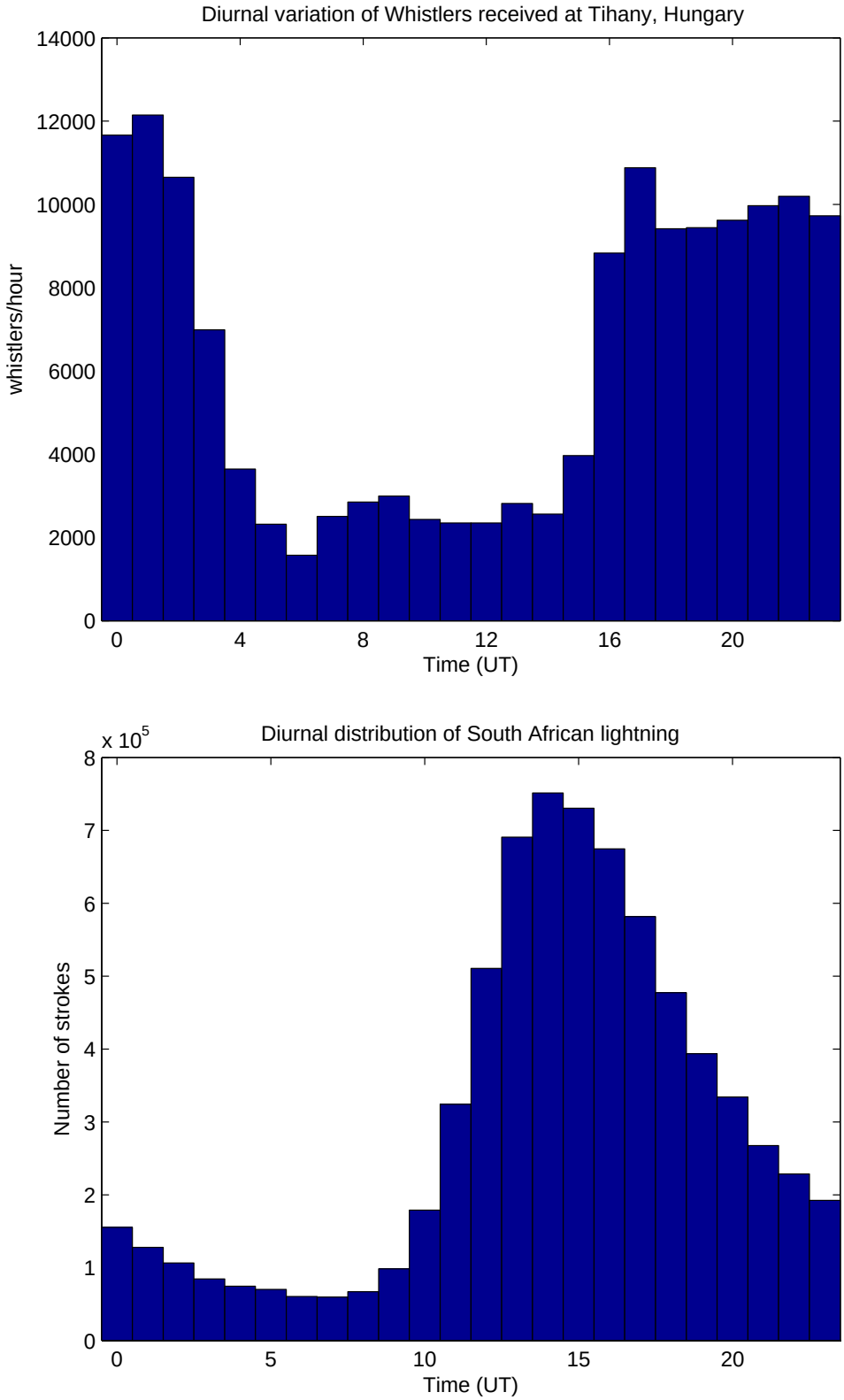

Figure 3.15: The diurnal variations of whistlers received at Tihany (top), and SALDN lightning (bottom). It is immediately obvious that the shapes of these distributions differ significantly. There is a sharp peak in lightning at 14:00 UT, and a definite minimum at 06:00 UT. The whistler distribution has a broad peak centered around 20:00 UT, and a broad minimum centered around 10:00 UT.

The values in t_{ij} are then used to generate a 1-d histogram, and the peak of this distribution will then be the calibration factor for that half orbit. Since a single DEMETER pass through the burst region only lasts $\sim$ 5 minutes, one can assume that the clock does not drift significantly during this time, and so the calibration factor is valid for a entire half orbit. Also, it is important to remember that this calibration factor takes into account not only the timing offset of DEMETER, but also any delay incurred in ionospheric transit.

The idea behind this method is simple. Lightning must surely launch whistlers into the magnetosphere directly above it. If DEMETER is nearby then it will record these whistlers. Since the lightning source is directly beneath the satellite, the only expected delay between the stroke and whistler reception is the vertical propagation time through the ionosphere. Additionally, an increase or decrease in this delay would come from the clock offset. The value of this calibration factor is always different, owing to different ionospheric profiles, and a different amount of clock drift. The random nature of the clock drift means that a value of t_c has no readily identified trend. Furthermore, this value is sometimes negative, which is only possible if the clock on DEMETER is slower than the GPS time of SALDN data. This is evidence of the clock drifting, since under no circumstance will ionospheric delay cause this.

One drawback of requiring such a calibration, is that the analysis can only proceed when there is enough SALDN data during the few minutes of a half orbit for a successful calibration. This implies that there is some lightning activity directly below the satellite during all half orbits for which the analysis can be done. This might skew the results in favour of the burst region, and one should bear this in mind when viewing the results.

3.4.2 New Result and Discussion

With the calibration values obtained, a new correlation can be performed using the same algorithm given by (3.1) and (3.2), with a slight modification for the second step. Here, the timing offset of DEMETER is taken into account. The $10\ \mathrm{ms}$ window for correlation is now shifted back in time by the calibration value, t_c. This can be expressed mathematically as

$$|(t_w - t_l) - d/c - t_c| \leq 0.005. \tag{3.3}$$

The above step can only be performed for half orbits where a value for t_c can be found, ie: when there is significant lightning in South Africa. Thus, due to the diurnal variation of lightning in South Africa, the 08:00 UT half orbit is rarely used in the final correlation. The lower panel of Figure 3.15 shows that lightning activity is near a minimum at 08:00 UT, and that there is vastly more lightning expected during the half orbits near 20:00 UT. As such, the majority of the whistler data used in the new correlation are measured at night. Fortunately, more whistlers are observed at night than during the day, and so this will have a less pronounced effect on the result of the correlation. Of the 590 half orbits used in the original study, calibration values could only be obtained for 204 half orbits. Of these, only 63 were daytime half orbits, meaning that 141 were night time half orbits.

The results of the correlation analysis are shown in Figure 3.16. This new result is clearly different from that shown in Figure 3.5. Firstly, the maximum number of initiating strokes on the colour bar is somewhat lower, but this is because of fewer half orbits being used in this calculation. Secondly, the distribution of initiating strokes is significantly different. There are now major peaks over the burst region and Central Africa. Furthermore, the peaks over the Americas and the Maritime Continent are much less significant. The peak over the Americas, which was largest over Central America in Figure 3.5, has now moved to Brazil. The peak over the Maritime Continent is very small, with only one cell having a value near the upper range of the colour bar. These regions of high correlation are in good agreement with the results of Collier *et al.* [2009].

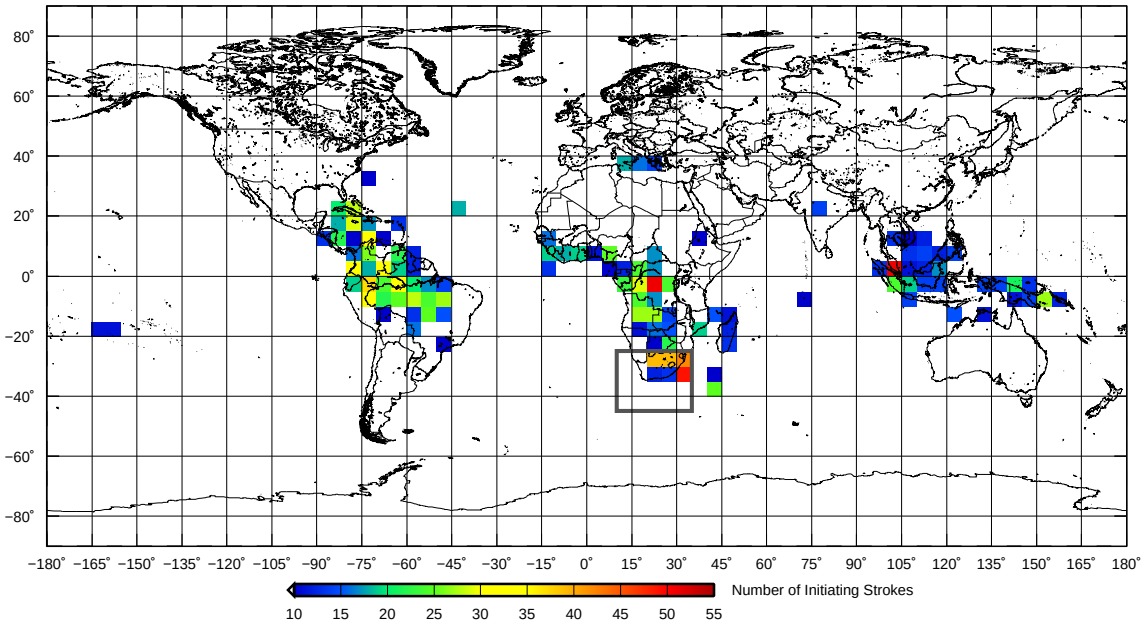

Figure 3.16: The distribution of lightning strokes matched to whistlers detected by DEMETER withing the burst region, using the DEMETER time correction algorithm. The resolution and colour scale is the same as that in Figure 3.5, except red here corresponds to 55 or more initiating strokes. There is a large peak over the burst region and Central Africa, and smaller peaks over Central America and the Maritime Continent.

There are also a few low value cells just to the north of the African Continent. These are not one hop whistlers which have propagated magnetospherically to the burst region, since the AWD excludes such whistlers from detection. Rather, they have propagated in the EIWG to the burst region before traveling up to the satellite. This might seem counter intuitive at first, but the distances involved are comparable to those between South America and the burst region.

3.4.3 Statistical Significance of Results

Producing a result that looks correct is one matter, but before it is given too much credence, the statistical significance of the results should be calculated. To do this a statistical approach was used. A p-value is the probability of achieving a result at least as extreme as any given result, given a completely random set of data. If the p-value is low, ie: there is low probability that a randomly generated set of readings can lead to the originally calculated result, then one can conclude that the original result was not a chance occurrence, but rather that there is an underlying physical reason for the result. Conversely, if a high p-value is found, then there is a high probability that random data could reproduce the result, ie: there is a good chance that the original result occurred due to chance.

But how does one apply this to the problem of lightning initiating a whistler? Intuitively, one might expect that in a high lightning density region, a chance occurrence of a link between a whistler and a lightning stroke is more likely. The converse would also seem plausible in a region of low lightning density. This idea will form the basis for the p-value calculation.

Determining p-values and refining the original result

Some terminology should be discussed here. Firstly, a mention of "the result" refers to the result obtained from the correlation of DEMETER whistlers and WWLLN data, which is shown in Figure 3.16. Data used in the determination of this result are called real data, while random or synthetic data are used to determine the p-value.

The definition of the p-value implies the use of random data. The analysis presented thus far has used 2 main data sources, lightning from WWLLN and whistler times from DEMETER. Since the whistler time series from DEMETER only has a temporal component, while the WWLLN data have a temporal and spatial component, it is easier to randomise the DEMETER data. Also, since the WWLLN data distribution varies with time of day, it is important that the times of the randomly generated whistlers are within a similar time window to those used in the determination of the result, otherwise a different random result will obviously be achieved. For this reason, the random whistler time series was confined to a few minutes on either side of 20:00 UT (08:00 was not used since the majority of half orbits used were around 20:00 UT). The length of time of each random whistler stream was chosen so that a similar length of random whistler data would be obtained from a year's worth of synthetic data as was from the real data measured from the 204 half orbits used.

A correlation between this random whistler series and the real WWLLN lightning data would then be expected to produce a distribution similar to that shown in Figure 3.16. If this distribution is sufficiently different from the result, then one can conclude that the result is statistically significant. The first step is to generate a random whistler series, and correlate it with the real lightning data. This process is represented graphically in Figure 3.17 (top panel). This time snippet contains a random whistler, represented by the red line, and actual lightning data, represented by the blue lines. In this situation, the whistler will likely be correlated with the lightning stroke which immediately precedes it in time. Extending this procedure over the entire random whistler stream, a distribution is obtained which is plotted in the lower panel of Figure 3.17. Since there is underlying structure in the WWLLN data, the peaks in this figure represent this structure, namely they occur where WWLLN sees most of its lightning.

In order to get good statistics, one should perform the above procedure many times, using the same lightning data, but a different random whistler stream each time. Performing the procedure again yields a new situation, which is represented graphically in the top panel of Figure 3.18. Here the random whistler will probably correlate with the lightning stroke directly before it, which is a different stroke than was selected in the previous run, and which may have occurred on the other side of the globe. Repeating the correlation with a different random stream of whistlers, one obtains the distribution which is plotted in the lower panel of Figure 3.18. This is very similar to that shown in the lower panel of Figure 3.17 since the same underlying lightning data were used for both of these. Close inspection, however, reveals that they are not identical.

This randomisation and correlation is repeated many times, each time producing a slightly different distribution. A collection of six more of these randomly created distributions is shown in Figure 3.19. Again, each of these resemble the others, but there are minor differences between them all. With many such sets of random whistler correlation distributions, a mean and standard deviation of the number of initiating strokes in each grid cell can be determined. Using these values allows for a normal distribution of the expected number of initiating strokes for each grid cell to be determined.

Each grid cell from the result is then tested using these normal distributions, and the number of initiating strokes determined for that grid cell of the result (ie: those values plotted in Figure 3.16). For each grid cell, the normal distribution determined for it from random data is integrated from the value which corresponds to the result, towards positive infinity. This integration comes directly from the definition of the p-value, namely, the probability of obtaining a result *at least as*

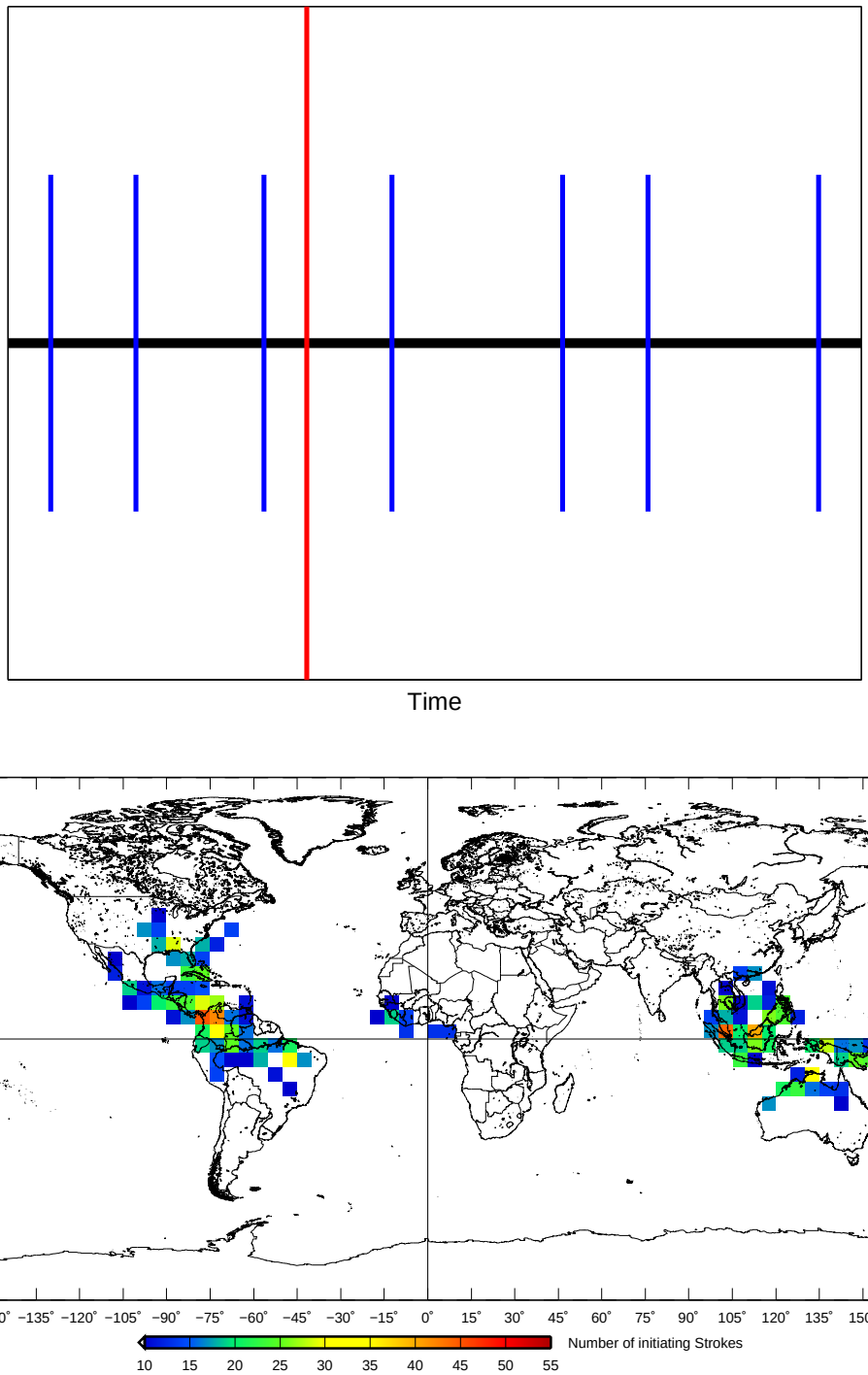

Figure 3.17: A graphical representation of the random whistler time and real lightning times, where the whistler is probably correlated to the lightning stroke immediately preceding it (top panel). The result of this correlation of random whistlers with real lightning is shown in the lower panel.

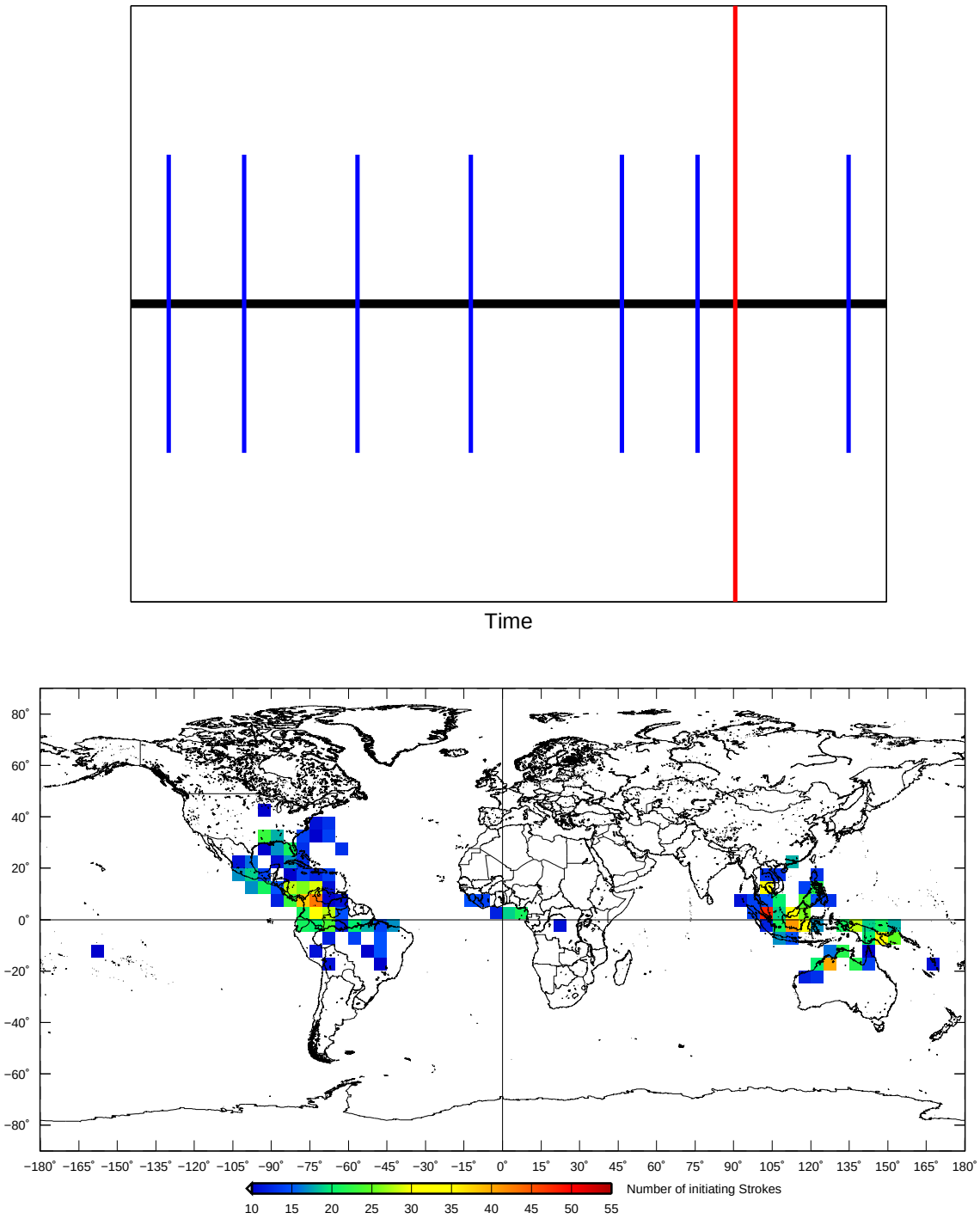

Figure 3.18: A different random whistler is correlated with the real lightning times, where the whistler is probably correlated to the lightning stroke immediately preceding it (top panel). The result of this correlation of random whistlers with real lightning is shown below it. This distribution is very similar to Figure 3.17, but close inspection shows small deviations.

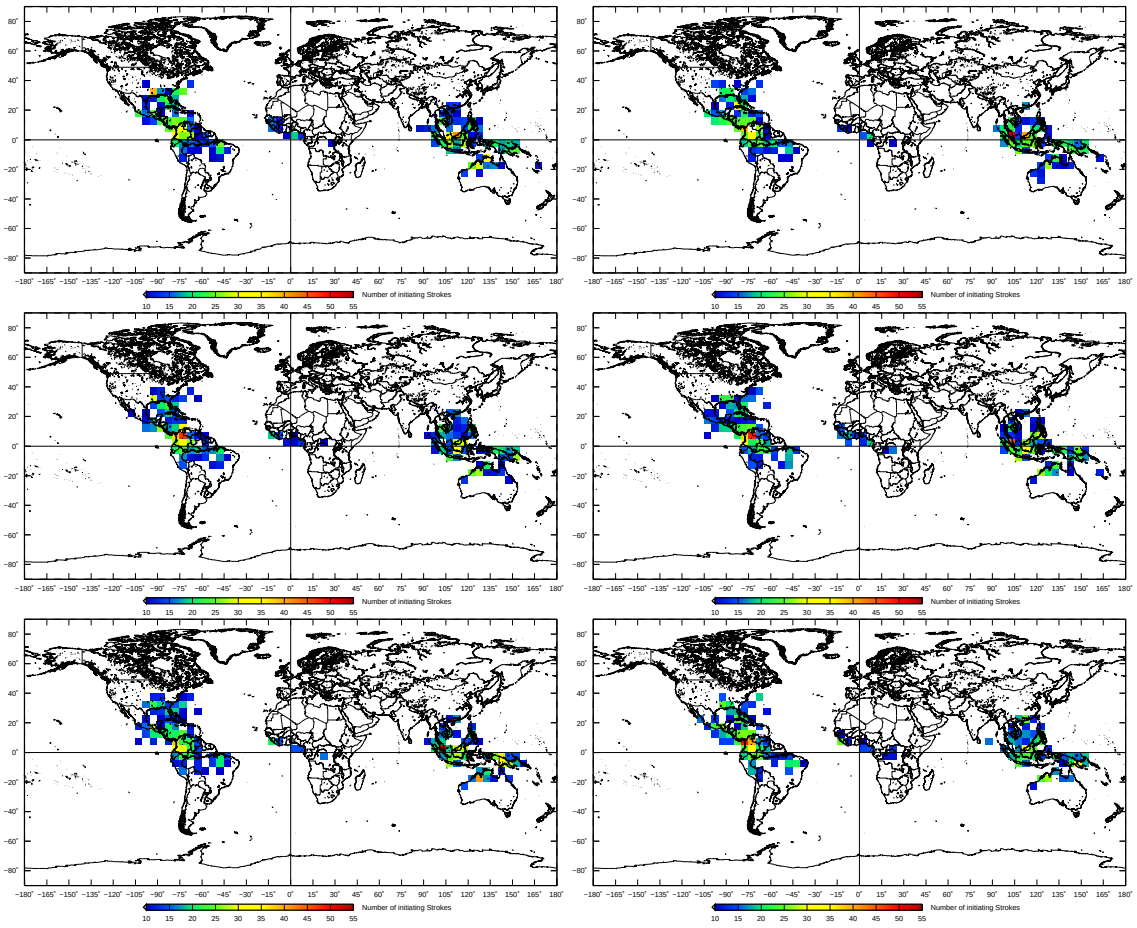

Figure 3.19: Six randomly generated whistler-WWLLN lightning distributions. All of these look similar, but there are small differences between each. These six are distinct from the ones shown in Figures 3.17 and 3.18.

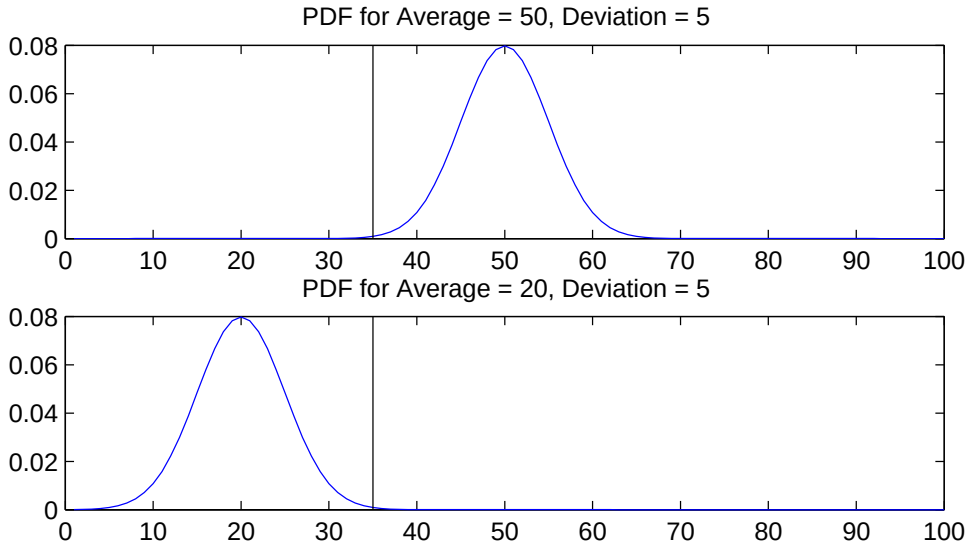

Figure 3.20: Two normal distributions of random results from a grid cell which has a true result of 35 initiating strokes, shown by the vertical line. To obtain the p-value, one must integrate the distribution from this line towards positive infinity. The top panel represents the case of a statistically insignificant result, while the result in the lower panel is of statistical significance.

extreme as the result, from random data. In Figure 3.20, two cases are shown, one where the value of the result is significantly lower than the mean of the normal distribution of random data (top panel), and another where the value of the result is significantly higher than this mean (bottom panel). In the first case, integrating through to positive infinity, one obtains a p-value close to 1, and therefore one can conclude that this result is not statistically significant. In the second case, integrating on to positive infinity, the p-value obtained is small, and so this result is deemed to be statistically significant.

A calculation similar to that outlined above is performed for each grid cell on the map, and thus a p-value is obtained for each such cell. A result is called statistically significant if it falls within the 5% confidence interval, or in other words, if it has $p \leq 0.05$. This means that there is at most a 5% chance of obtaining such a result in random data. A complimentary quantity, called statistical significance, can be calculated directly from the p-value. This is defined at $1 - p$, and so a statistically significant result has significance ≥ 0.95. In Figure 3.21, the statistical significance of each grid point is plotted. All statistically insignificant cells in this map are white.

There are two main regions of clustered significance evident on the map. First, the burst region and parts of Southern Africa outside of it, and a region in South America. As a final step in this test, the result from Figure 3.16 is filtered, so that only cells for which the result is of statistical significance are retained. The result is plotted in Figure 3.22, and a copy of the first result from Figure 3.16 is placed here for reference.

3.4.4 Discussion

The use of statistical significance has had three major impacts on the original result:

- The high correlation in the burst region and Southern Africa has remained.
- The correlation in South America has been somewhat reduced, but there are still significant levels of correlation there.

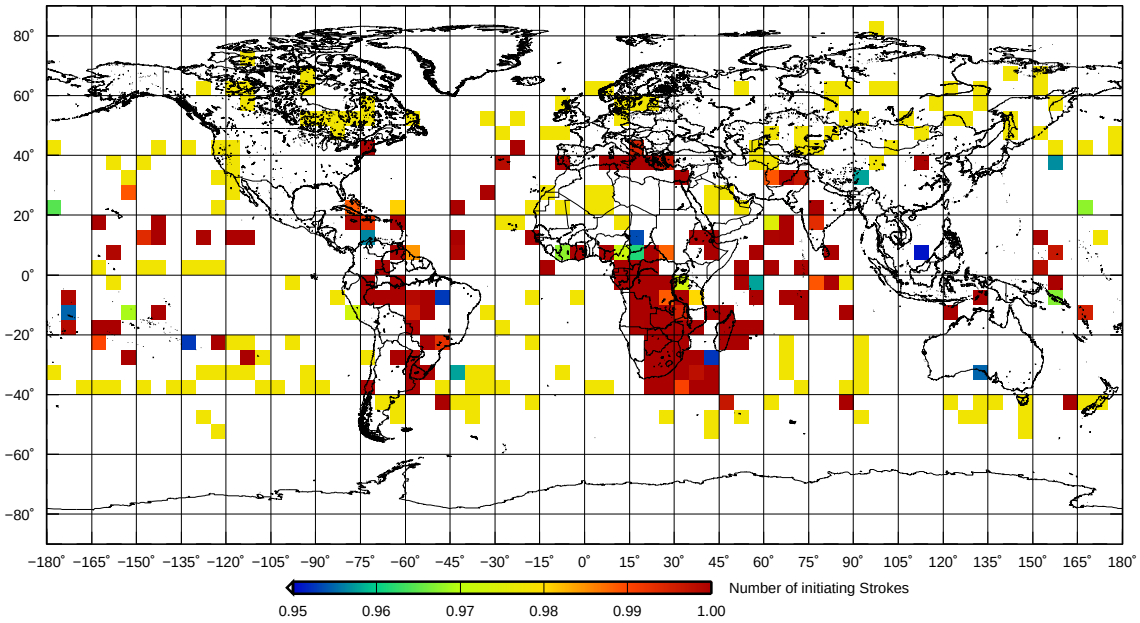

Figure 3.21: The statistical significance of each grid cell. Cells which have a significance ≤ 0.95 are displayed in white.

- The of correlation that was near the Maritime Continent has been removed.

The first two of these confirm the result of Collier *et al.* [2009], that the conjugate point, Central Africa and South America are all source regions for whistlers received in Tihany. There seems to be a disagreement, however, with the results presented here not indicating that the Maritime Continent is a source region. This can be explained, however, if one considers the times for which this analysis was conducted. The DEMETER satellite was only over the burst region at 08:00 and 20:00 UT, and many of the morning passes were precluded due to the unavailability of SALDN lightning. The terminator configuration on the Austral summer solstice at 20:00 UT is shown in Figure 3.23. The date corresponds roughly to the annual peak in South African lightning. This shows that the Maritime Continent is in darkness, just before dawn. This means that one would typically not expect much lightning here at this time, since the land is cool, and any convective activity from the previous day would have dissipated. For this reason, one does not expect much correlation from the Maritime Continent, given the period of data coverage. At the burst region on the other hand, it is late at night, a period where there is still appreciable lightning activity, while South America is experiencing late afternoon, when one expects a high level of lightning activity. Another possible cause for this difference is the asymmetry in the attenuation of eastward and westward propagating waves. These explain why these results agree with Collier *et al.* [2009] on 2 out of 3 of the source regions.

The results presented here should be compared with those of Jacobson *et al.* [2011]. As discussed, they showed that the maximum number of initiating strokes were $4000\ \mathrm{km}$ from the footpoint of the C/NOFS satellite. While this agrees with the findings presented here that whistlers can be initiated at LEO by strokes several thousand kilometers away, there is a disagreement about which strokes should be most likely to initiate these whistlers. On possible reason for this may be that the positions of the C/NOFS data used were not subset in any way. This means that the probability of having a whistler originate from beneath the satellite varies as the satellite moves over regions of typically high or low lightning activity. This is quite a big difference to the whistlers which were used in this Chapter, which were confined to the burst region.

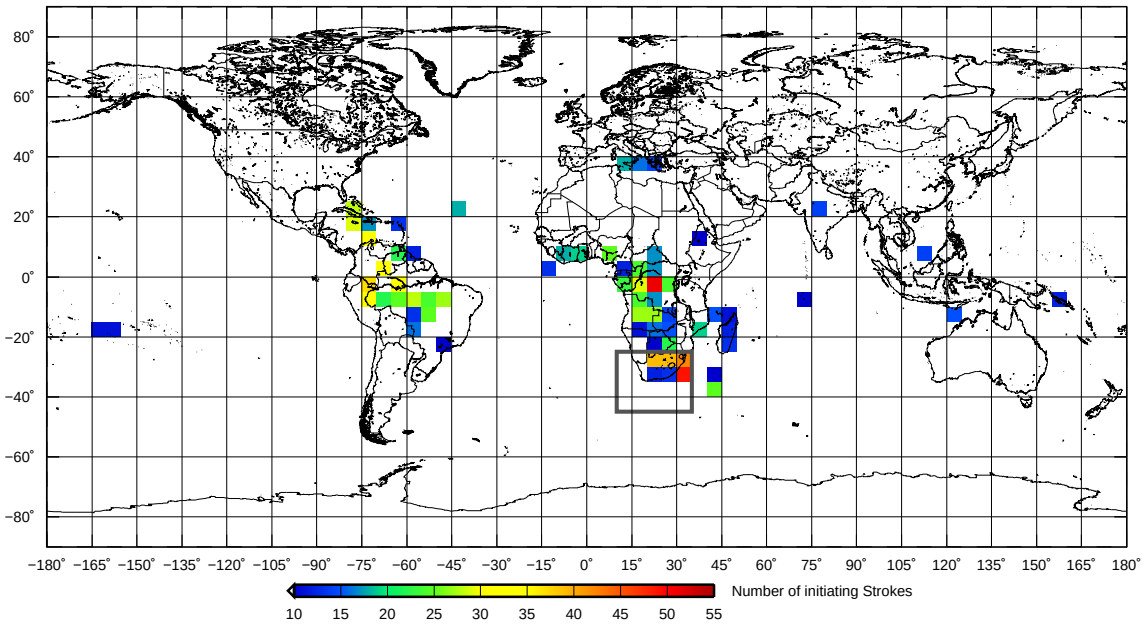

(a) Statistically significant correlation only.

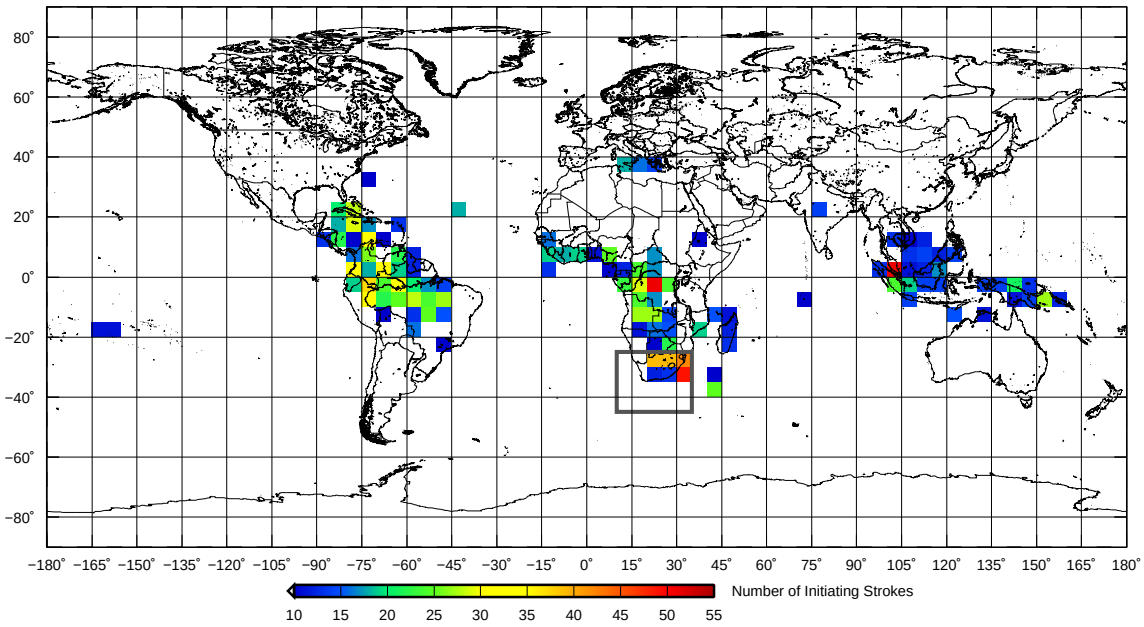

(b) Result with statistically insignificant results retained.

Figure 3.22: The result from Figure 3.16, with only statistically significant cells retained (a). The map in (b) is a reproduction of Figure 3.16.

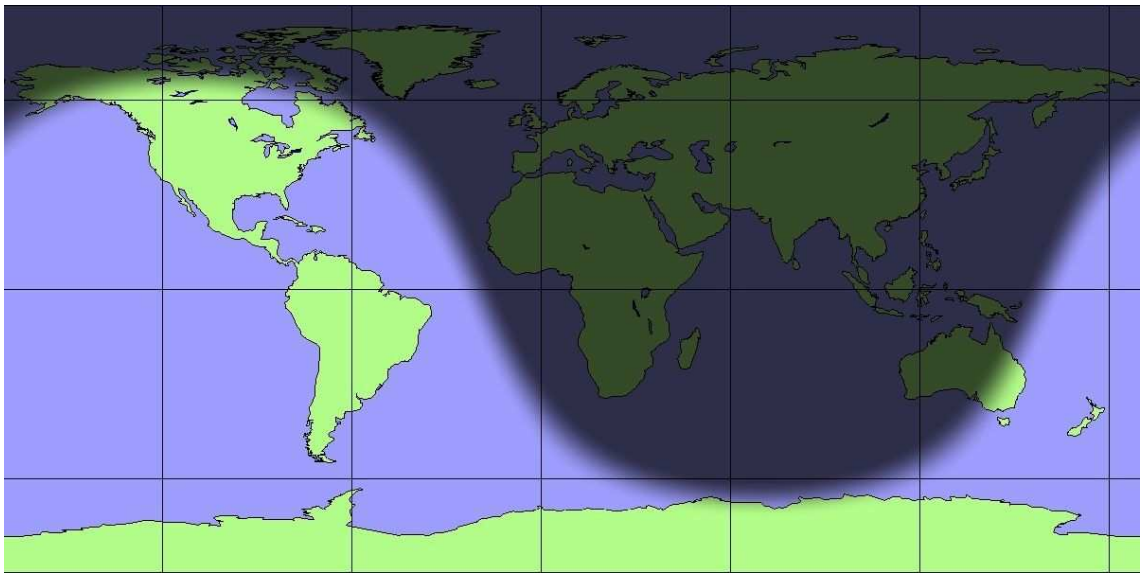

Figure 3.23: The terminator configuration at 20:00 UT, during the Austral summer solstice. The Maritime Continent is just a few hours prior to dawn, the burst region is at just before midnight, and South America is in the late afternoon, just before dusk.

The results presented in this Chapter show that the burst region is the principle source for the whistlers, but the context of this result should be considered. WWLLN detects many more lightning strokes in South America than in the burst region. Also, the time of day at which the analysis occurs favours lightning generation over South America to that in the burst region. These two factors add even more weight to the ability to detect whistlers originating from lightning in the burst region.

3.4.5 Conclusion

The results presented here support the theory of whistler generation provided by Storey [1953]. The main result showed that the most probable source for whistlers in the magnetosphere at the altitude of LEO satellites is lightning strokes directly beneath the satellite. This is not strictly true, since even at LEO, some guiding by the magnetic field has occurred, so that lightning strokes near the footpoint of the field line under the satellite are most likely to result in a whistler being recorded on the satellite. The resolution of the data presented here is not high enough to show this effect, but the study by Fiser *et al.* [2010] showed that this should be the case.

These new results also confirm the results of Collier *et al.* [2009], who showed that the source region for whistlers received at Tihany is much larger than the immediate vicinity of the conjugate point, which was the previously expected case. There is, however, an aspect of the method used in their correlation method that bears some discussion. Since lightning in their study is being correlated with single hop whistlers, there is no indication of the path that the whistlers used to get to Tihany. For instance, a whistler originating from a spheric in South America may have entered the magnetosphere directly above the stroke, propagated on to the conjugate point, and then the fully formed whistler could propagate in the EIWG to Tihany. A second scenario involves the spheric traveling from the stroke point to Tihany's conjugate point, entering the magnetosphere there, and propagating magnetospherically to Tihany. Actually, there are an infinite number of paths that the whistler may have taken to Tihany, and these are not distinguished by their method.

The method used in this analysis, however, only considers whistlers which have propagated

through the EIWG into the burst region before entering the magnetosphere, and propagating up to the satellite. This means that it is possible for a spheric to travel through the EIWG to the burst region, and penetrate through the ionosphere into the magnetosphere, convert into the whistler mode, and arrive at the LEO satellite. There is no guarantee that these whistlers would then make it to Tihany, as they may not be ducted at this point. Further analysis would be required to determine the proportion of such whistlers which propagate to Tihany. This presents a possibility for the extension of this work.

This work does show that even when there is no lightning below a certain point in space, that it is possible to receive whistlers there. This is of particular interest to the PLASMON project, since it means that the number of whistlers received at a location is not only a function of local lightning around the conjugate point, but also lightning which occurs over the chimney regions of the Earth. Thus, possible sites might not need to have a high level of conjugate lightning activity. Since the majority of the southern hemisphere is ocean, and only minimal lightning is observed over the majority of the ocean (except above warm ocean currents), many locations in the northern hemisphere are not precluded from whistler observations, since conjugate lightning is not necessary. This effect also has applications to radiation belt loss mechanism studies.

Chapter 4

Unusual Observation of Chorus at Marion Island

4.1 Introduction

On 4 August 2010 (day 216) chorus was observed at Marion Island ($46.9°$S $37.1°$E, $L = 2.60$, LT = UT$+3$). The chorus transformed into a hiss band spanning the same frequency range, before reverting to chorus again. This was the first time that the recording instruments at Marion Island were able to detect the presence of chorus since their installation in 2007. This was most likely due to operational reasons, since chorus is a regularly occurring phenomenon at $L = 2.4$ [Golden *et al.*, 2011; Spasojevic and Inan, 2005]. Chorus is frequently observed at SANAE IV, Antarctica ($71.4°$S $2.51°$W, $L = 4.32$, LT = UT) by a similar set of recording instruments, which have been in operation much longer. This first chorus observation at Marion Island presented an opportunity to study chorus which occurs at a lower L-value than is typically expected.

In this chapter the results of detailed analysis of the chorus are presented. Broadband data from Halley Bay and SANAE IV, both of which are Antarctic stations, are also presented. The geomagnetic conditions leading up to and including the event are discussed. The location of the plasmapause is inferred from models and compared to the value obtained from a knee whistler observation. A statistical analysis of DEMETER VLF data is used to determine the relative rarity of this observation at the longitude and L-value of Marion Island, during this phase of the solar cycle.

Chorus is related to whistlers only by their shared frequency range and consequently their propagation characteristics. They are generated by completely different mechanisms and related to different space and atmospheric weather conditions. Chorus is none the less still an interesting phenomenon which warrants study. During the period of this PhD , increasing solar activity has resulted in more chorus and other interesting observations being made at Marion Island and SANAE IV. This event is of particular interest given the recent findings of Bortnik *et al.* [2008, 2009], as this observation presents ground based evidence supporting their idea that hiss is generated by chorus.

4.2 Specifics of the Observation

Chorus was observed at Marion Island on 4 August 2010, during an extended period of low geomagnetic activity. This was about 2 years before the solar maximum set to occur at the end of 2012. As such, the sustained period of lower geomagnetic activity was contrary to expectations for this period. This low level of geomagnetic activity leaves the magnetosphere in a quiescent

state, which is not conducive to the development of VLF emissions due to the lack of free energy from particle injections. With these factors considered, this occurrence stands out against the background of low VLF activity at Marion Island experienced during the preceding months.

Spectrograms showing the evolution of the chorus recorded on Marion Island with resolution of $50\ \mathrm{ms}$ are shown in Figure 4.1. Data were recorded in synoptic mode, and each panel represents 1 hour of data. These figures show an overview of how the emission structure changed with time. The chorus initially spanned a frequency range of $2 - 4\ \mathrm{kHz}$. The spectral structure was not constant throughout the duration of the event. The event rose out of a quiet, uniform background at 03:00 UT as discreet rising tone elements indicative of chorus. The chorus started with a fairly low amplitude $\sim 10\ \mathrm{dB}$ above the background. The chorus elements began to increase in amplitude until about 04:30 UT where the amplitude leveled off at $\sim 20\ \mathrm{dB}$ higher than it was at the onset of the event. During this period, the upper edge of the frequency envelope increased from 4 to $5\ \mathrm{kHz}$. Also at this time, a hiss band superimposed itself on top of the chorus. This hiss band spanned the same frequency range as the chorus initially, but the chorus elements are still visible beneath the hiss band, indicating that two distinct emissions were being observed. As the evolution proceeded, the lower edge of the hiss envelope increased, while that of the chorus remained the same. The hiss dissipated by 05:50 and only the chorus remained. After this the chorus began to decrease in intensity before fading out completely at 07:00 UT.

Spectrograms showing a more detailed view of the chorus and hiss are plotted in Figure 4.2. Each of these panels represent 1 minute of data, and one panel is plotted per hour of the event. The chorus is evident in the minutes of data starting at 03:05, 04:05 and 06:05 UT (panels (a), (b) and (d)), and hiss at 05:05 UT (panel (c)). One can clearly see the structure of the chorus in the chorus panels, but the chorus is still clearly visible in panel (c). The power difference between the chorus in panel (a) and (b) is also apparent.

Broadband data from VLF receivers at SANAE IV were also available for this period. SANAE IV is an Antarctic station at a higher L-value than Marion Island, and is 3 magnetic local hours west of Marion Island. Chorus was also observed at SANAE IV on 4 August 2010, although the chorus there did not span the same universal time interval as at Marion Island. Additionally, the chorus at SANAE IV is structurally different from that observed at Marion Island. Overview spectrograms analogous to those shown in Figure 4.1 for SANAE IV are shown in Figure 4.3.

The difference between these two occurrences of chorus are quite striking. Firstly they occurred at different UT, and secondly the chorus structure is different at times when the two were observed simultaneously. This is illustrated in Figure 4.4, where detailed spectrograms for the SANAE IV chorus data are plotted for 05:05 (a), 06:05 UT (b), 07:05 UT (c), and 08:05 (d). The times of the data plotted in Figure 4.4 (a) and (b) are chosen to correspond with panels (c) and (d) in Figure 4.2. For instance, at 05:05 UT, chorus and hiss were observed at Marion Island, and no chorus is evident in the SANAE IV data. At 06:05 UT chorus was observed at both stations, but it spanned a different frequency range at each station. The chorus at SANAE IV spanned a frequency range of $0.5 - 2.5\ \mathrm{kHz}$, which is significantly different from that observed at Marion Island. This indicates that resonance has occurred between two different electron populations in the magnetosphere, or more likely between electrons at different L-values, which has resulted in two different frequency bands being amplified in each case. From these observations one can conclude that the two observations are independent.

These broadband data sets form the basis of the observations for this study. However, there are a host of complimentary data sets from which one may draw to better understand the mechanics of the event. The geomagnetic conditions at the time of the event are of interest since an increase in geomagnetic activity is usually a precursor to chorus and hiss observations. As already mentioned, up to the observation of this chorus, the year 2010 was geomagnetically quiet. To illustrate this, the Dst and $\mathrm{K_p}$ indices for the period from 1 January 2010 to 31 August 2010 are plotted in Figure

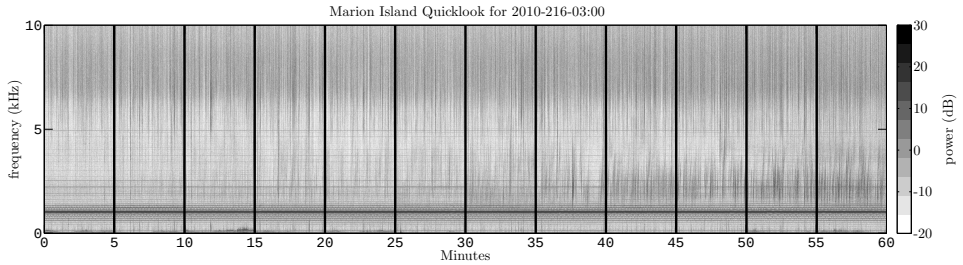

(a) 03:00 – 04:00 UT

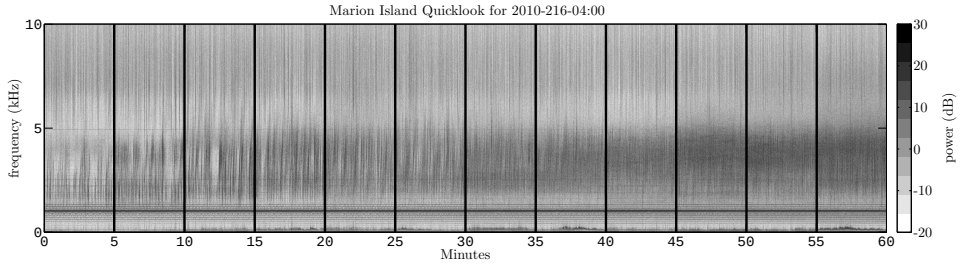

(b) 04:00 – 05:00 UT

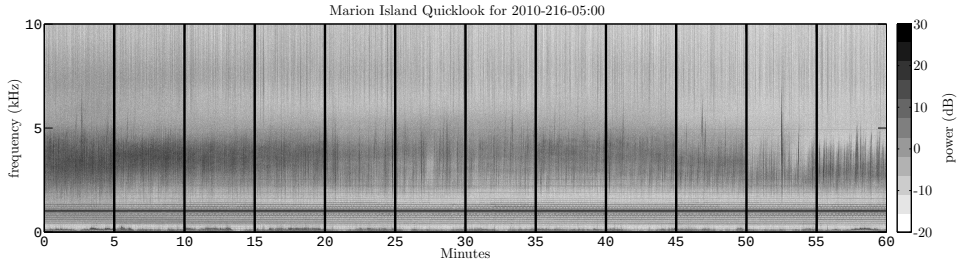

(c) 05:00 – 06:00 UT

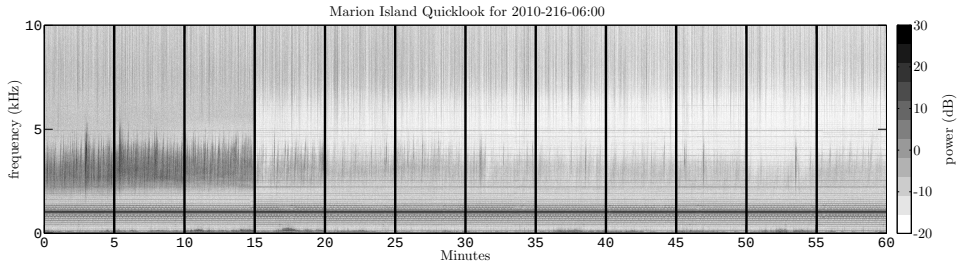

(d) 06:00 – 07:00 UT

Figure 4.1: The evolution of chorus at Marion Island over 4 hours from 03:00 - 07:00 UT on 4 August 2010 with time resolution of $50\ \mathrm{ms}$. Each panel represents 1 hour of data, and each vertical slice represents 1 minute of data sampled every 5 minutes. The chorus transformed into hiss at 04:30 UT in (b), which evolves back to chorus at 05:50 in (c). There were changes to the upper boundary of the frequency envelope during the evolution.

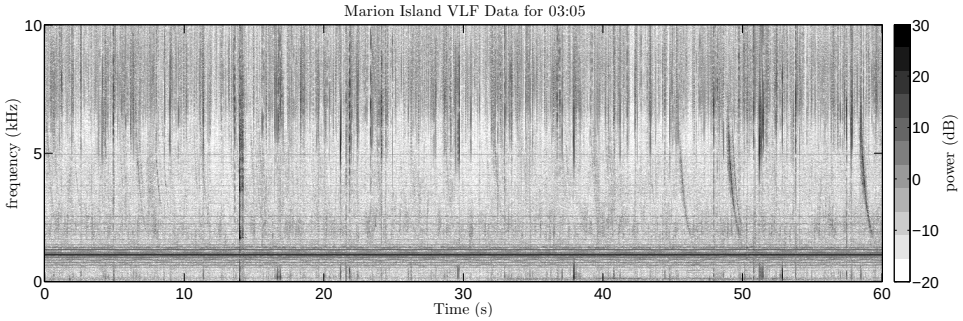

(a) 03:05 UT

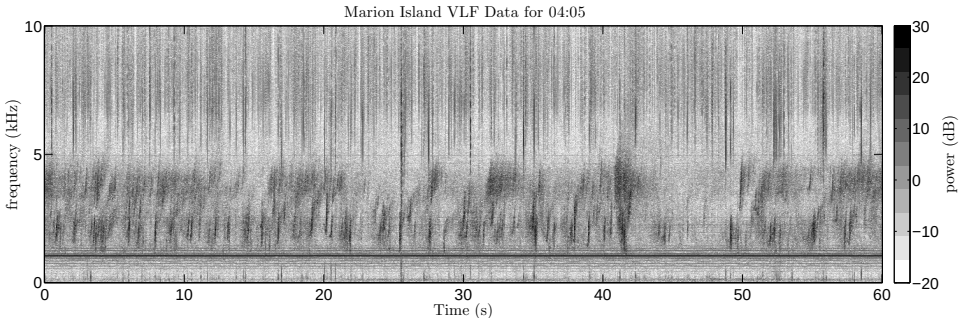

(b) 04:05 UT

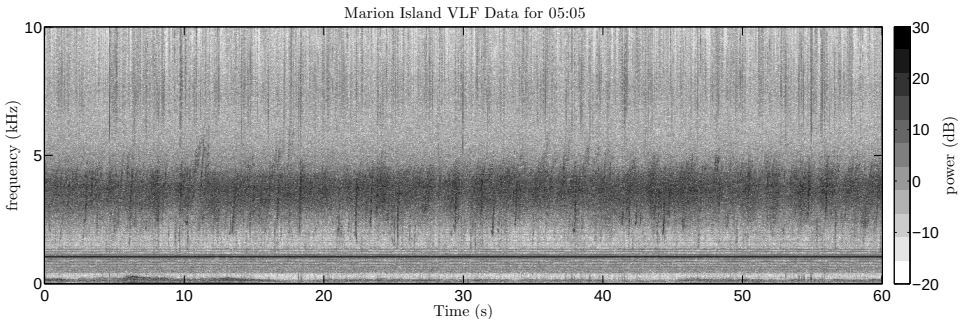

(c) 05:05 UT

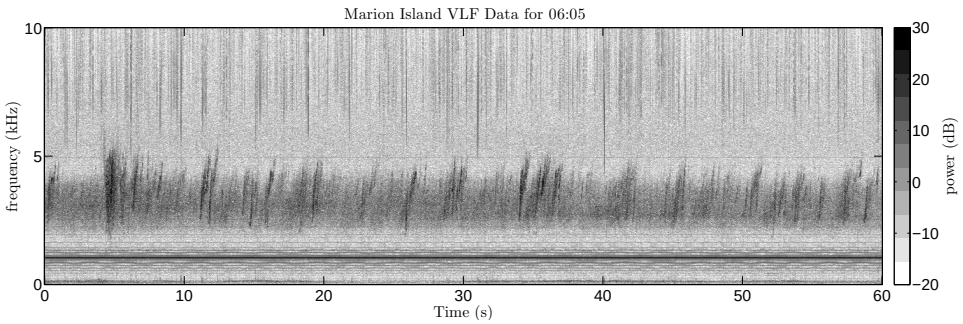

(d) 06:05 UT

Figure 4.2: Detailed spectrograms of the chorus (a), (b), and (d), and hiss (c). The structure of the chorus elements is visible in all the panels, and even in (c), one can see that chorus elements are still present beneath the hiss.

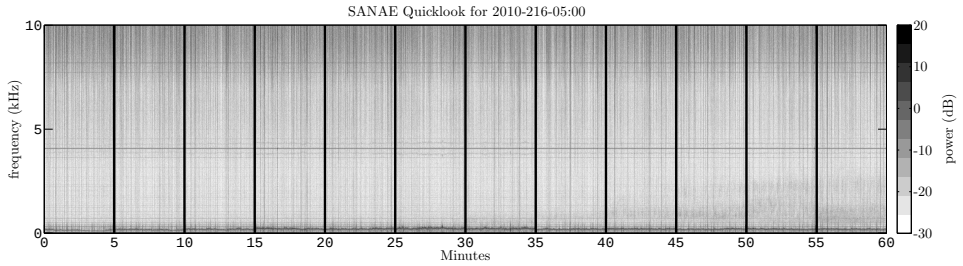

(a) 05:00 – 06:00 UT

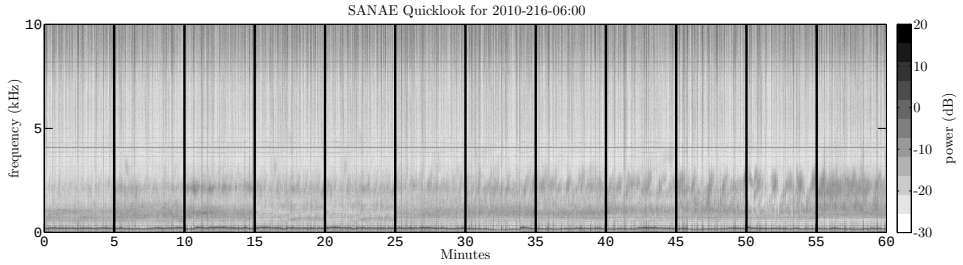

(b) 06:00 – 07:00 UT

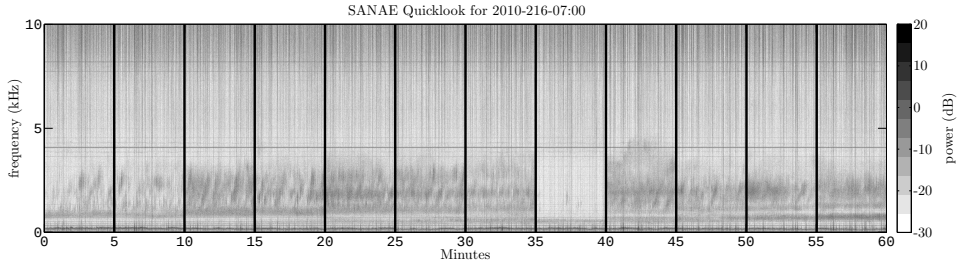

(c) 07:00 – 08:00 UT

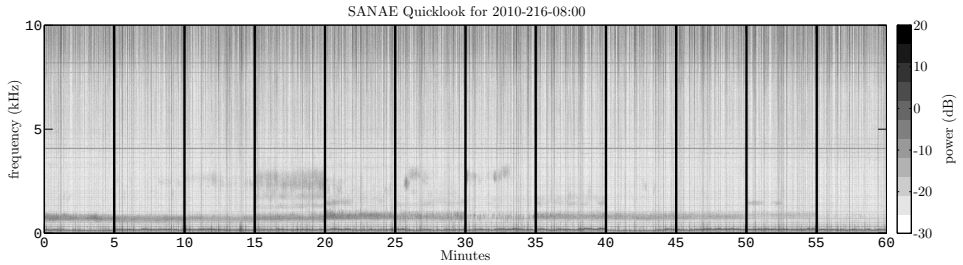

(d) 08:00 – 09:00 UT

Figure 4.3: The evolution of chorus at SANAE IV over 4 hours from 05:00 - 09:00 UT on 4 August 2010. The spectrograms have the same format as those represented in Figure 4.1. This chorus is different from that observed at Marion Island, beginning faintly at 05:50 UT in (a), and building in strength until 06:50 UT in (b). It had vanished by 08:35 UT in (d).

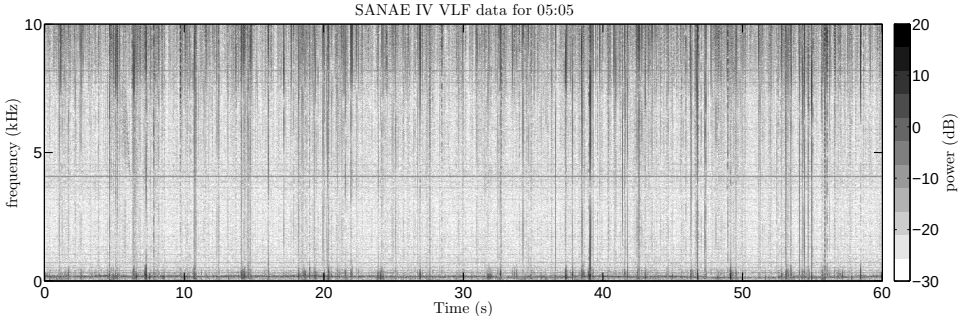

(a) 05:05 UT

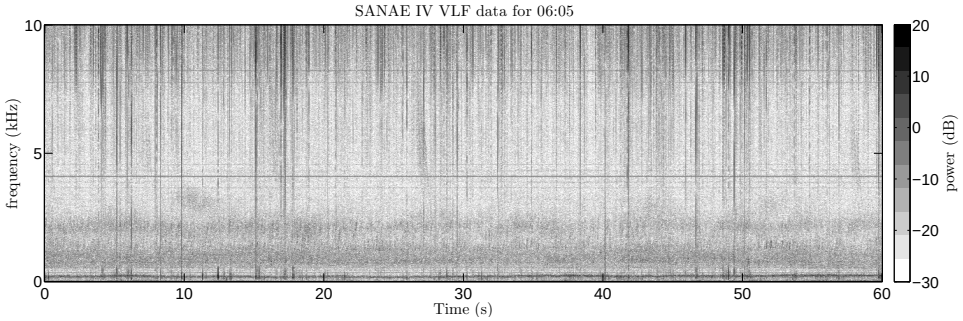

(b) 06:05 UT

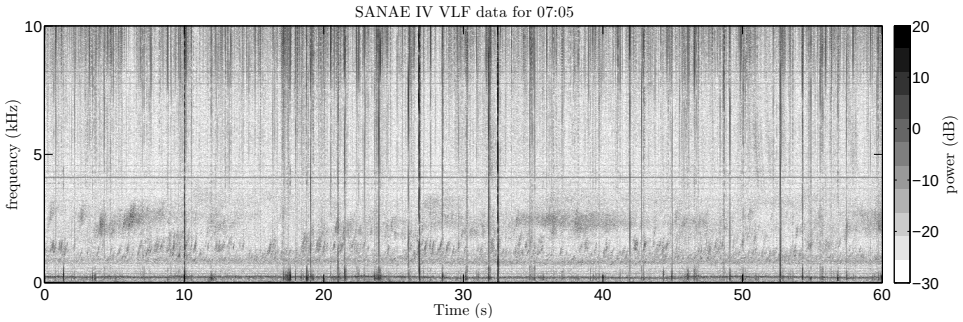

(c) 07:05 UT

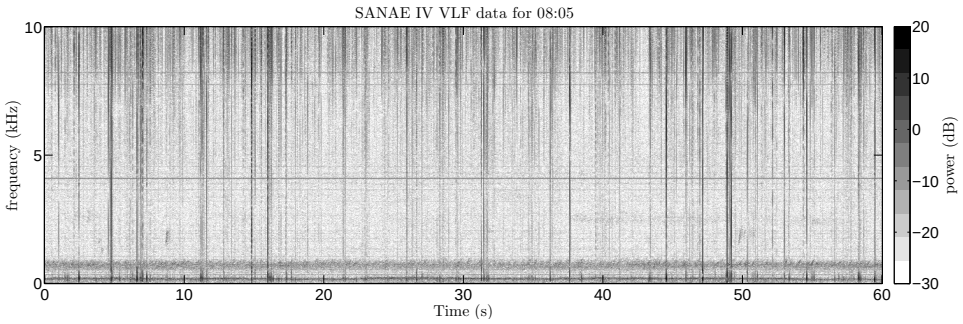

(d) 08:05 UT

Figure 4.4: Detailed spectrograms of the VLF data recorded at SANAE IV at 05:05 (a), 06:05 (b), 07:05 (c), and 08:05 (d) UT. The times of (a) and (b) coincide with panels (c) and (d) of Figure 4.2, where the differences between the two emission's structure are readily apparent.

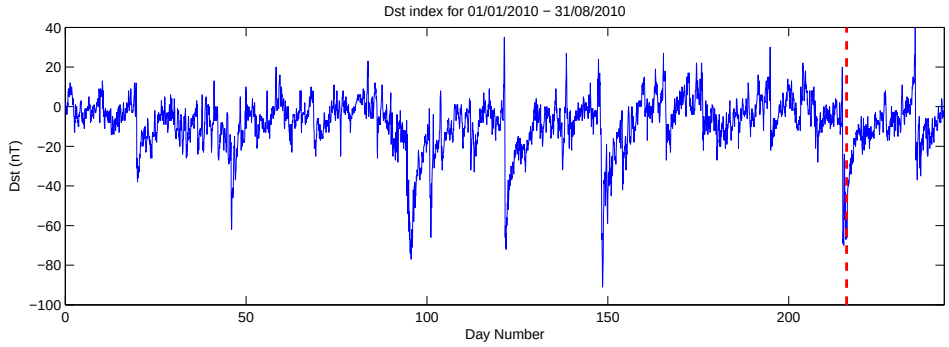

(a)

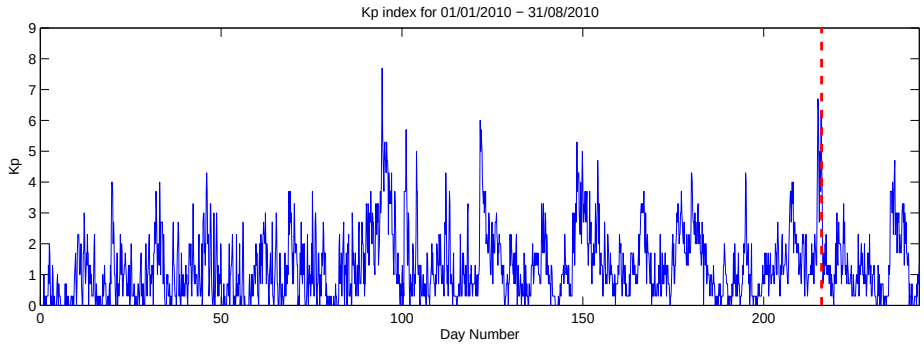

(b)

Figure 4.5: The Dst (a) and $\mathrm{K_p}$ (b) indices from 01/01/2010 to 31/08/2010. There are a few periods of low to moderate activity depicted, but overall these represent a period of low geomagnetic activity. The red dashed line marks 4 August 2010 (Day 216).

4.5. Geomagnetic activity manifests in the Dst index manifests as a decrease to a negative value, and the magnitude of the activity is proportional to the magnitude of the decrease. A geomagnetic storm can be identified in this data as a rapid increase in Dst during the SSC, followed by a rapid decrease, followed by an exponential recovery to normal levels. An increase in $\mathrm{K_p}$ implies an increase in activity, where typically a $\mathrm{K_p} > 5-$ implies moderately disturbed conditions.

The Dst data above show that during these 8 months, there were 8 noteworthy geomagnetic storms, and the largest of these exhibited a Dst of -90 nT, which is by no means a severe geomagnetic storm (the Halloween storm in 2005 had Dst -300 nT for instance). The $\mathrm{K_p}$ index also shows a few increases to disturbed conditions during this period, although there were no increases above $8-$ (7.67). There were three occasions where $\mathrm{K_p} > 5-$ (4.67), and these were for very short periods of time. Even so, these peaks are not high enough to be considered major disturbances. Both plots in Figure 4.5 show that conditions had been relatively quiet up to the observation of the chorus at Marion Island. Figure 4.5 show that the level of activity around 4 August 2010 (Day 216) was among the largest of the year. In Figure 4.6 the Dst and $\mathrm{K_p}$ indices for the period from 2–7 August 2010 are shown, focusing on the event day. Here the increase in activity is readily visible.

The Dst plot shows that a moderate geomagnetic storm occurred just prior to the observation of chorus on Marion Island. While the geomagnetic storm was not particularly strong (Dst ~ -70 nT), it was large enough to elevate the $\mathrm{K_p}$ index to $7-$ (6.67), which is the lower limit of severe activity levels. These moderate levels of geomagnetic activity resulted in preconditioning of the magnetosphere for the amplification of VLF waves.

This storm was likely attributed to an impulsive increase in solar wind speed which was mea-

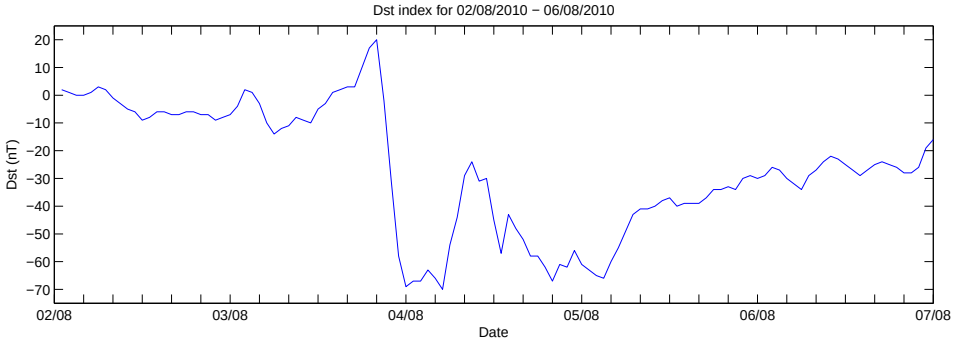

(a)

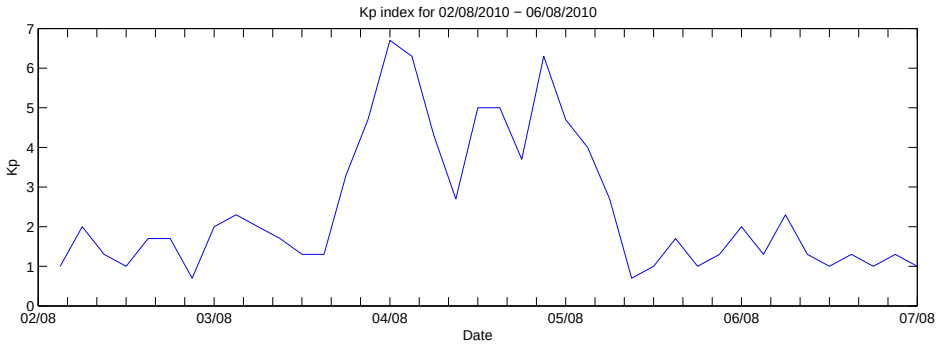

(b)

Figure 4.6: The Dst (top) and $\mathrm{K_p}$ (bottom) indices from 2 to 7 August 2010. The signature of a geomagnetic storm is evident in Dst at 00:00 UT on 4 August 2010, 3 hours before the onset of the chorus at Marion Island. There is a rapid increase in $\mathrm{K_p}$ at this time.

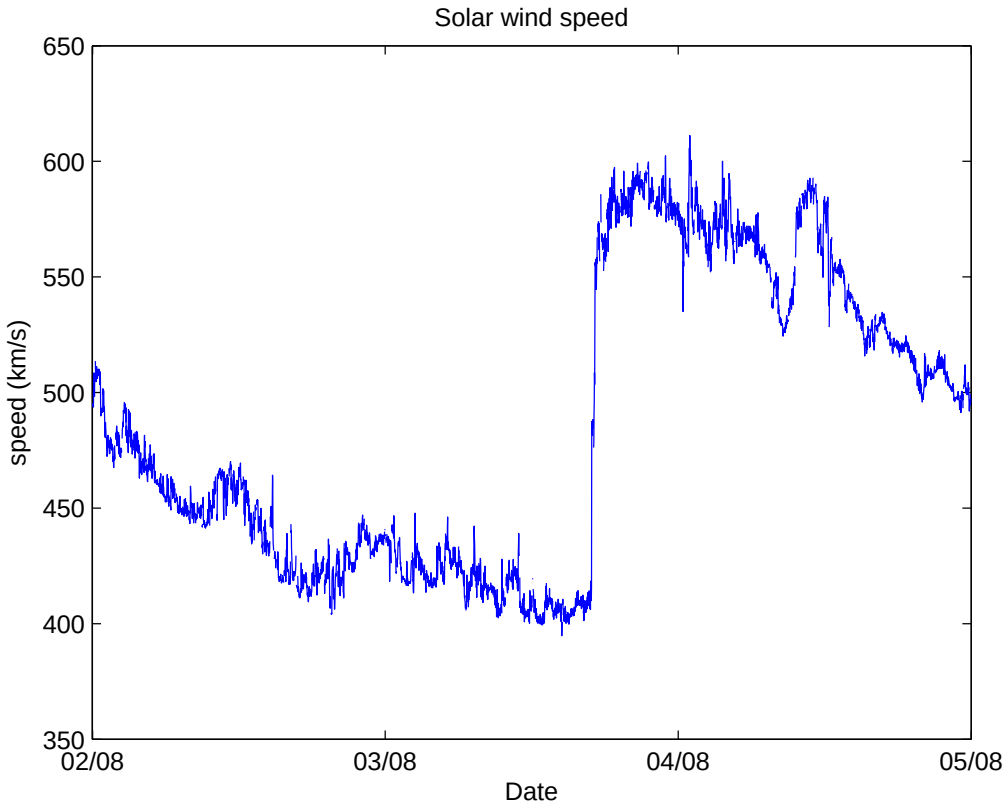

Figure 4.7: The flow speed of the solar wind as measured by the SWEPAM experiment on board ACE from 2 August to 4 August 2010. There is substantial increase in the measure speed a few hours prior to 4 August 2010.

sured by the Advanced Composition Explorer (ACE) satellite at the first Lagrangian point between the the Earth and the Sun, at ~ 0.01 AU from Earth. At typical solar wind speeds it takes roughly 1 hour for conditions in the solar wind to travel from ACE to Earth's magnetosphere. The ACE solar wind speed data are plotted in Figure 4.7. This sudden increase occurred roughly 8 hours before midnight on 4 August 2010. Looking back to the Dst plot in Figure 4.6, one can see that the solar wind speed increase and the SSC occur at roughly the same time. The elevated solar wind speed increased pressure on the magnetosphere, which in turn compresses it, resulting in the SSC. Unfortunately, solar wind density data were not available from ACE during this time.

The large Halloween storms of 2003 caused a reconfiguration of the Earth's outer radiation belts, and the causative CME compressed the magnetosphere, pushing energetic radiation belt particles from $L \sim 4$ to below $L = 4$. This reconfiguration of the radiation belts persisted for several days before being restored to regular levels [Baker *et al.*, 2004]. Despite the lower severity of the August 2010 event, a similar reconfiguration was also experienced during the main phase of this storm, with the radiation belt only being restored to its normal configuration during the course of the next few days. This radiation belt reconfiguration is evidenced in the LANL electron flux [Friedel *et al.*, 2008] data in Figure 4.8. There is a clear depression in counts across all three energy channels at the time of the rapid increase in geomagnetic activity, and is most evident in the highest energy channel (bottom panel, $E > 1.25$ MeV). After this initial depression in the fluxes, there was an enhancement in energetic electron fluxes which persisted for three days after the storm. This reconfiguration is similar to that observed during the 2003 Halloween storms.

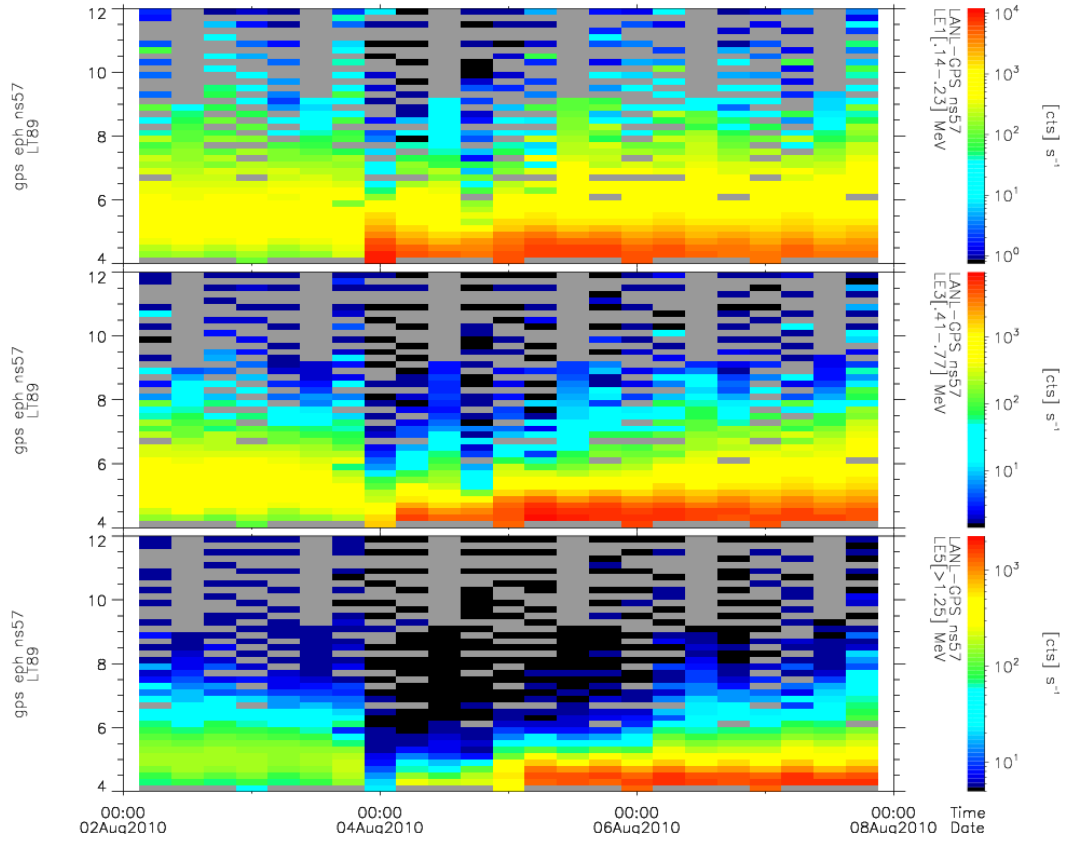

Figure 4.8: Electron flux data obtained from detectors on LANL satellite NS57 in the range $L = 4$–12, for three energy channels. There is a depletion in the radiation levels at the time of the storm onset, and an increase in density at $4 \leq L \leq 5$ for the next three days.

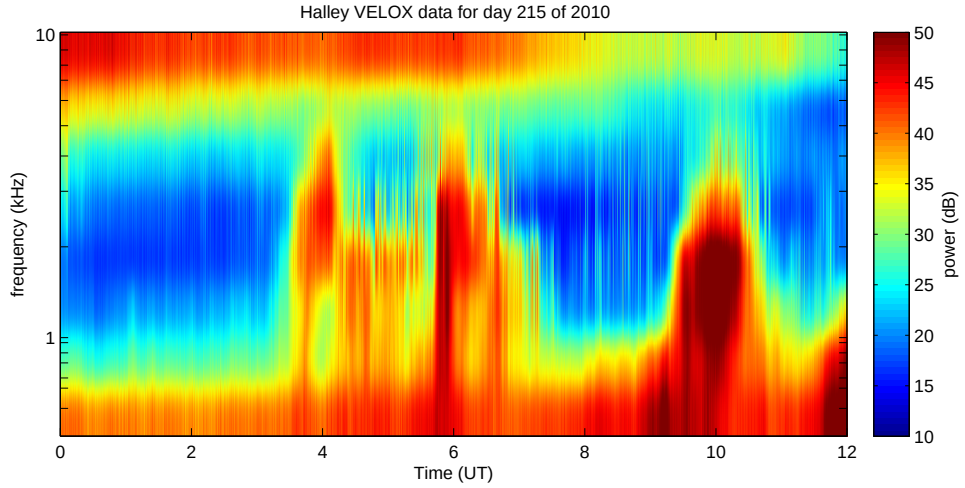

(a) Day 215

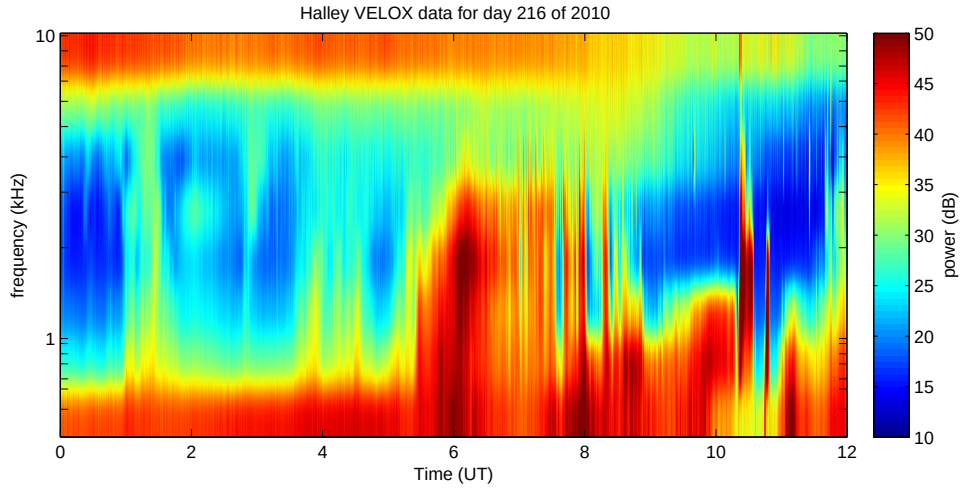

(b) Day 216

Figure 4.9: Broadband VLF data obtained at Halley Bay from 00:00 – 12:00 UT on the 3 and 4 of August 2010 with time resolution of 2 minutes. There is an onset of activity at 01:00 UT on 4 August 2010.

Data was obtained from the VELOX (VLF/ELF Logger Experiment) [Smith, 1994] operated at Halley Bay, Antarctica ($75.58°$S $26.56°$W, $L = 4.48$, LT = UT-2). The VELOX data have a time resolution $\sim$2 minutes, which is much lower than the time resolution of the broadband receivers at Marion Island and SANAE IV, but these VELOX data still provide useful insight. The data for times before 12:00 UT for day 215 and day 216 are presented in Figure 4.9. In the data of day 216 one can see a small enhancement of VLF activity at around 01:00 UT, and then a significantly larger onset of activity at 06:00. Comparing this to the data for day 215, when no chorus was observed on Marion Island, one can see only the large onset at 06:00 UT, which is before the occurrence of the large geomagnetic storm. From this one can conclude that the activity which occurs around 06:00 UT was due to some other, more regularly occurring phenomenon, while the smaller onset of activity at 01:00 UT on day 216 was a special occurrence, and probably related to the chorus observed at the other two stations on this day. This is useful for providing relative timing and to track the emission generation region.

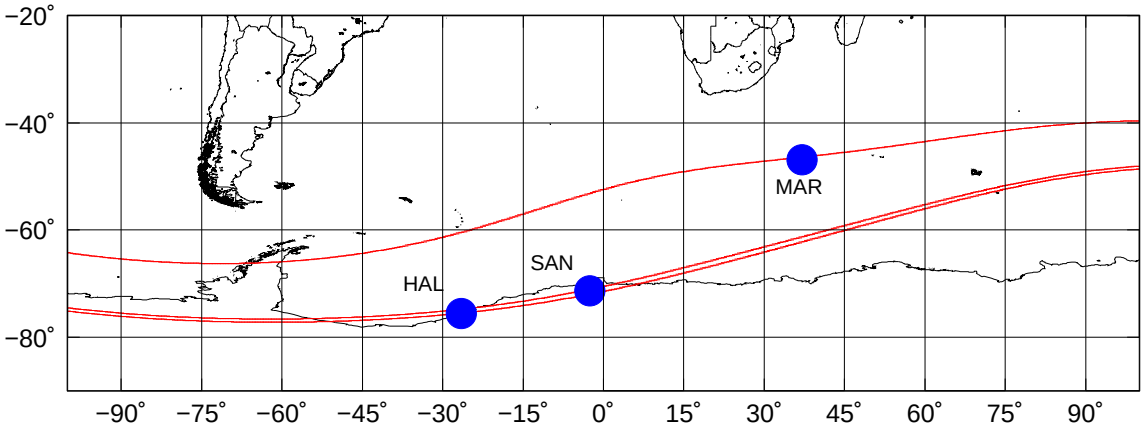

Figure 4.10: A map showing the relative positions of Halley Bay (HAL), SANAE IV (SAN) and Marion Island (MAR) with blue dots, as well as their L-shells (in red, at $L = 4.48$, $L = 4.32$ and $L = 2.60$ respectively) mapped down to the surface of the Earth.

With observations at three separate receivers it is possible to determine if the MLT of the generation region was changing. The first observation was at Halley Bay at 01:00 UT. The next observation was made at Marion Island at 03:00 UT. Finally, the chorus was observed at SANAE IV starting at 06:00 UT. The location of these stations and each of their L-shells is shown in Figure 4.10. From the relative positions of Halley Bay and Marion Island it seems that the chorus source region was moving eastward, which is consistent with the eastward drift of electrons within the magnetosphere. However, it is then unusual for the chorus to be observed at Marion Island before SANAE IV, since it lies between Halley Bay and Marion Island. One explanation for this is that the compression of the magnetosphere which resulted from the storm's onset pushed the generation region below the L-value of SANAE IV, and only later after the magnetosphere had relaxed somewhat was the chorus able to propagate from its source region to SANAE IV. Another explanation is that perhaps the VLF observed at Halley is something other than chorus, since the low resolution makes it impossible to discern chorus with absolute certainty.

A comparison between this chorus observation, and that made at Palmer Station [Spasojevic and Inan, 2005] during the Halloween storms of 2003 is interesting because there are some similarities and key differences between the two observations. In both cases chorus was observed at low latitude locations which have $L < L_{pp}$ during quiescent conditions. The Palmer event was also triggered by enhancements in the solar wind. In both cases, the chorus onset occurred during the main phase of a storm where the plasmapause was pushed inwards towards the observing station, and persisted into the recovery phase. The observations both occurred in the post midnight sector. The chorus observed at Palmer changed frequency fairly regularly during the period of its observation, which persisted for 3 days, while the Marion Island chorus had minimal frequency variations, and only endured for 4 hours. Although both events exhibited hiss, the structure of the hiss was different. The 2003 hiss (described as mid-latitude hiss by Spasojevic and Inan [2005]) spanned a larger frequency range than the chorus, and individual chorus elements were visible on top of the hiss. During the 2010 event, the hiss spanned the same frequency range as the chorus, and chorus elements were only visible towards the lower end of the spectrum. The long persistence of the chorus over several days at Palmer was possible since several geomagnetic storms occurred throughout this period. The 2003 event occurred during solar maximum, a period when the Sun was extremely active, while the 2010 event occurred near the end of a prolonged period where the Sun was unusually quiet. All of this points to the Marion Island chorus observations being less prevalent due to the lower level of geomagnetic activity experienced in the Marion Island case.

4.3 Data Analysis

The observational data sets presented in the previous section provide information about the structure of the chorus, and when and where it was observed. Here, more in-depth data analysis is presented. The broadband data from Marion Island and SANAE IV is further analysed so that further characteristics of the VLF signal can be identified. Plasmapause models are used to determine the location of the plasmapause during the observations. Broadband data from the DEMETER satellite provide a view into the VLF waves present in space. These are also analysed to determine the rarity of the event.

The transformation of the chorus into hiss at Marion Island is of immediate interest, since plasmaspheric hiss occurs inside the plasmasphere while chorus is generated outside the plasmasphere. This suggests that chorus propagated from outside the plasmasphere (from higher L) to Marion Island, while plasmaspheric hiss has propagated from inside the plasmasphere (lower L) to Marion Island. This is strong evidence that Marion Island was in the vicinity of the plasmapause at the time of the event. Both chorus and hiss emissions were able to propagate sub-ionospherically from their respective re-entry points to the receivers, even though the observations were made during daylight hours when sub-ionospheric propagation conditions are unfavorable. Thus, with VLF emissions having a reduced propagation distance, Marion Island must have been somewhere between their respective source regions, probably close to the plasmapause. No similar transformation in spectral structure was observed at SANAE IV, where the chorus spanned a different frequency range, which indicates that the resonant electrons (near SANAE IV) had higher energy or that the generation region for these waves was at a higher L.

There is a possibility that the hiss observed at Marion Island was in fact not plasmaspheric but rather mid-latitude, originating from outside the plasmasphere. This would contradict the above argument for Marion Island's proximity to the plasmapause, since then Marion Island could have been well outside the plasmapause and still receive both emissions. If this were the case, then with the plasmapause at lower L than Marion Island, mid-latitude hiss would have originated at an L between SANAE IV and Marion Island and should then also have been visible in the SANAE IV data. However, as can be seen from Figure 4.3, no hiss was observed at SANAE IV, and so we conclude that the hiss observed at Marion Island was most likely plasmaspheric.

Since chorus is generated outside the plasmasphere, and plasmaspheric hiss inside the plasmasphere, L_{pp} is an important piece of information for the analysis of this event. Several models for the location of the plasmapause have been developed based on empirical measurements of its location. An initial estimate of L_{pp} was obtained from the simple model of Carpenter and Park [1973], given in (2.11). This very crude estimate predicts a plasmapause which is circular in the equatorial plane, which is not a true reflection of reality. The value predicted by the model is most accurate in the dawn sector. From the lower panel of Figure 4.6 one can see that the appropriate value of $\mathrm{K_p}$ to use is $7-$. Using the model with this value substituted for $\mathrm{K_{pmax}}$ yields a value of $L_{pp} = 2.56$, which is slightly lower than the L of Marion Island. This crude model predicts that the plasmapause was indeed very close to Marion Island. There are newer improved empirical plasmapause location models which better reproduce the shape of the plasmapause, including the bulge at dusk [Carpenter and Park, 1973]. These are given in equations (2.13), (2.14) and (2.15).

For this study, and for consistency with (2.11), the L_{pp} given in (2.14) was used. The result of this model is shown in Figure 4.11. The L-value of Marion Island is represented by the blue circle, and the model result by the red contour. Since the model only depends on $\mathrm{K_{pmax}}$, which did not change during the course of the event at Marion Island, this contour is representative of the entire emission period. Marion Island's MLT at the beginning and end of the event are depicted by the radial lines between midnight and dawn. This plot indicates that Marion Island was very likely just inside the plasmasphere during the event, approaching the plasmapause as the event evolved.

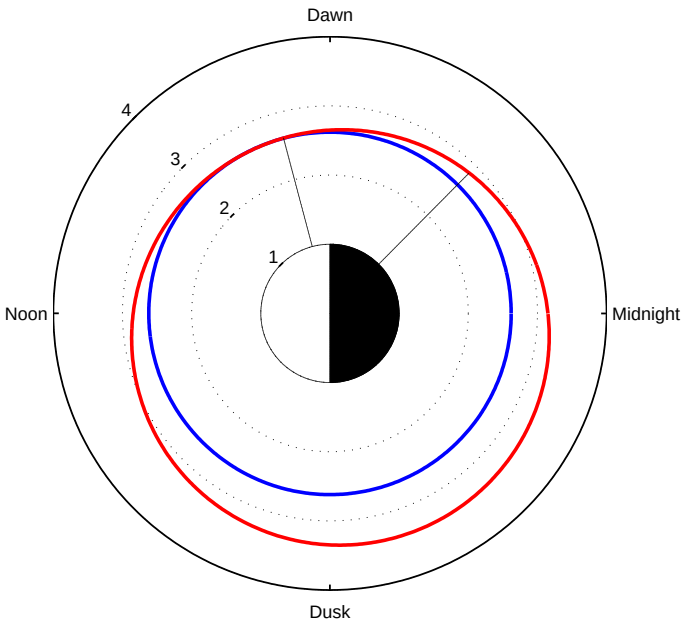

Figure 4.11: Polar plot of the equatorial plasmapause location obtained from the empirical model in (2.14) (red), and the L-shell of Marion Island mapped into the equatorial plane (blue). The radial black lines show MLT of the period for which chorus was observed at Marion Island. This indicates that the plasmapause was very likely close to Marion Island during the event.

It should be noted though that this model result (which could have an error $\sim 1R_E$) is not as reliable as a direct measurement. It does, however, produce a similar result to the one obtained using (2.11).

Ideally one would prefer a direct observation of plasmapause location for this analysis. Traditionally these have been obtained using IMAGE EUV data [Sandel *et al.*, 2000] or in situ observations from other satellites which cross the plasmapause during their orbits (such as CLUSTER and THEMIS). Other techniques for locating the plasmapause include using observations of FLRs from magnetometer chains or densities obtained from whistlers, or even better, knee whistlers [Carpenter, 1963]. In this case a rather fortunate observation of a knee whistler was made.

The knee whistler observed on 4 August 2010 at Dunedin, New Zealand ($45.78°$S $170.47°$E, $L = 2.7$) is shown in Figure 4.12, where the knee whistler occurs at $t = 0.8$s (identified by the arrow). As mentioned, this allows for a direct estimate of the plasmapause location [Carpenter, 1963]. A knee whistler is one for which some of the whistler traces have traveled inside the plasmasphere, and others outside of it. These two groups experience significantly different plasma densities, while the magnetic field strength along the propagation path is virtually the same. These factors are reflected in the dispersion of the whistler, with some of the traces displaying considerably different dispersions. Since a knee whistler has traveled virtually along the plasmapause, a measurement of the L-value along which the whistlers propagated provides an unambiguous value for L_{pp}. A spectrogram of the knee whistler is shown in Figure 4.12.

Analysis of this knee whistler by the AWDA [Lichtenberger *et al.*, 2008, 2010] identifies this as a knee whistler since some of the traces yield values of equatorial electron density of $227\ \mathrm{cm}^{-3}$ (ie: these traces have propagated outside the plasmasphere), while the other whistlers in the group show an equatorial electron density of $734\ \mathrm{cm}^{-3}$ (ie: propagated inside the plasmasphere). L_{pp} was determined using the AWDA, and it is found that L_{pp} = 3.5 at 13:12 UT at Dunedin, which

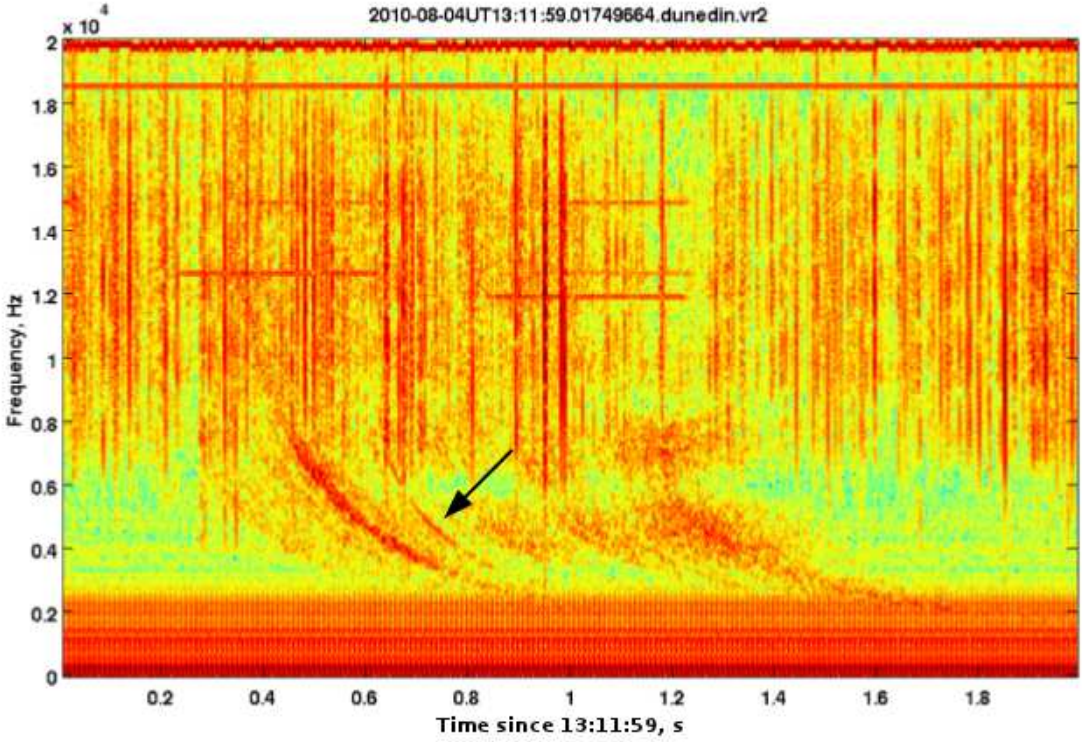

Figure 4.12: The knee whistler observed at Dunedin on 4 August 2010. The origin of the time axis is 13:11:59 UT. The knee whistler is the well defined trace at approximately 0.8s, indicated by the arrow.

corresponds to around 00:12 LT. The AWDA uses a Vertical Trace Transform (VTT) for extracting parameters from whistlers. This technique is still in development, and so a more traditional whistler scaling method was used to determine L_{pp} from the knee whistler [Lichtenberger, 2009], which has the benefit of providing the uncertainty range for the result. The results from this method are $L_{pp} = 3.542 \pm 0.085$, and equatorial electron density of $217 \pm 7\ \mathrm{cm}^{-3}$ for those traces outside the plasmasphere. Thus it appears that the values obtained using VTT fall within 1σ for L_{pp} and 2σ for the equatorial number density, and one can assume that they are an accurate result. For simplicity, the value of $L_{pp} = 3.5$ will be used from here on in the analysis.

This value of L_{pp} is somewhat larger than the L of Marion Island, or the values of L_{pp} derived from the models. One can argue that since this observation was made 6 hours later than that of the Marion Island chorus (at $\sim$ 13:00 UT), and one expects that the plasmasphere would have relaxed somewhat since 07:00 UT. This would imply an expansion of $\sim 1R_E$ in 6 hours, which is a typical rate of expansion (see Carpenter and Park [1973] for examples). The value of $L_{pp} = 3.5$ is thus an upper bound on L_{pp} during the chorus observed at Marion Island.

Both the model result depicted in Figure 4.11 and that obtained from (2.11) and (2.14), as well as the value of L_{pp} determined from the knee whistler analysis, indicate that Marion Island was within the plasmasphere during this event. Since chorus is generated outside the plasmasphere, one might naively expect chorus observations only during periods where the receiver is outside the plasmasphere. However, since VLF waves can propagate sub-ionospherically for significant distances, the observation of chorus is possible for ground stations located inside the plasmasphere, but close to the plasmapause. This is not an uncommon occurrence though, recalling that Golden *et al.* [2010] reported that chorus was most probable at Palmer Station when the receiver was just inside the plasmapause. Additionally, one would expect that hiss originating from inside the plasmapause would not be able to penetrate to the ground, due to reflection at the LHR frequency and at the ionospheric boundary. The plasmapause can guide these hiss emissions to the ground, if the waves are close enough to it. The waves can then propagate within the EIWG to the receiver, which might be inside or outside the plasmasphere, provided the receiver is close enough to the plasmapause. For both of these situations, the question remains: how "close" is close enough?

In Figure 4.13 circles at distances of 400 and $900\ \mathrm{km}$ from Marion Island (blue star) are plotted, as well as contours at $L = 2.60$ (the L of Marion Island), 3.00 (an intermediate L), and 3.50 (the upper bound of L_{pp}). This shows that the AWDA determined value of L_{pp} is as close as $900\ \mathrm{km}$ to Marion Island. In terms of VLF propagation distances, this is very close. It is known that, due to the low attenuation of $\sim 10\ \mathrm{dB/Mm}$ [Barr *et al.*, 2000] in the EIWG, VLF waves can travel sub-ionospherically for thousands of kilometers. The emissions shown in Figure 4.1 are $\sim 30\ \mathrm{dB}$ above the background, which would allow for these waves to propagate at least $3000\ \mathrm{km}$ from their sub-ionospheric entry point to the receiver. It is thus reasonable to propose that $900\ \mathrm{km}$ between the receiver and the plasmapause is close enough.

There is significance in the fact that the chorus and hiss observed at Marion Island spanned the same frequency range. Recent studies [Bortnik *et al.*, 2008, 2009; Wang *et al.*, 2011] have hypothesised that chorus outside the plasmasphere may generate plasmaspheric hiss. Bortnik *et al.* [2009] observed chorus outside the plasmasphere and hiss inside of it on two THEMIS satellites which were on either side of the plasmapause. These emissions were found to be in the same frequency range. This observation supported the earlier modeled results of Bortnik *et al.* [2008]. The theory proposed in these papers is that chorus waves launched from the equatorial plane, outside the plasmasphere, can propagate towards the plasmapause. Here, the waves are refracted into the plasmasphere. The chorus undergoes several reflections, becoming more and more dispersed as it propagates further through the plasmasphere, eventually becoming homogenised, ie: hiss-like. Chorus and hiss are often observed simultaneously on the ground at low L, but for them to occur in the same frequency band is uncommon [Golden *et al.*, 2009]. In contrast, the Marion

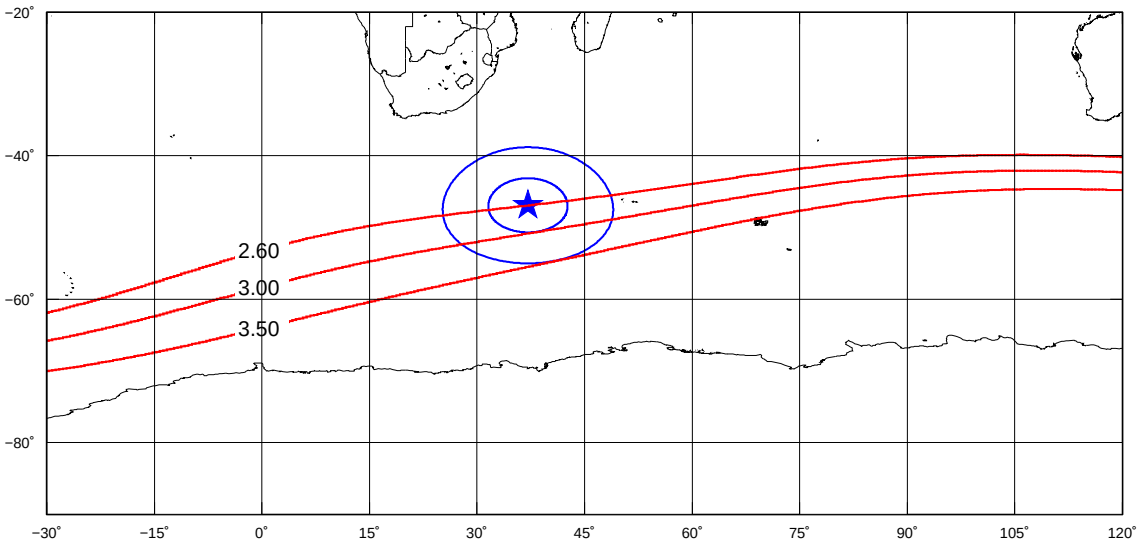

Figure 4.13: The location of Marion Island plotted as a blue star. The 2 blue circles have a radius of 400 and 900 km respectively. L-shell contours are plotted at $L = 2.60, 3.00$ and 3.50. The $L = 3.50$ shell intercepts the 900 km circle.

Island chorus and hiss did occur in the same frequency band (as shown in Figure 4.1), and hence this is a ground based observation supporting the hiss generation theory of Bortnik *et al.* [2008]. The chorus originated from outside the plasmasphere, and generated plasmaspheric hiss inside the plasmasphere. These data also indicate that this conversion can take some time to occur, which may reflect the complexity of the chorus waves gaining access to the plasmasphere (i.e. that chorus does not always enter the plasmasphere). This can be explained by the simulations of Bortnik *et al.* [2008], which showed that only chorus waves with certain wave normal angles are able to penetrate through the plasmapause. As discussed above, the plasmaspheric hiss is allowed to pass through the ionosphere by the strong guiding provided by the plasmapause.

Alternatively, this observation might be more like those of Santolík *et al.* [2009] who showed a case of chorus and hiss both being generated in the same region, in the equatorial plane near $L = 4.25$. They suggested that chorus and hiss were independently generated in roughly the same region. Both emissions were also found to have large wave normal angles, meaning that they could propagate across magnetic field lines, to lower or higher L-shells. One thing to note about these observations is that the chorus and hiss seem to be independent of each other, while the data presented here show that the hiss was superimposed on top of chorus (as shown in Figure 4.2 (c)). This might mean that the source regions of the chorus and hiss were distinct. It has also been shown in Figure 4.4 that while chorus was observed at higher L at SANAE IV, no hiss was evident there. For these reasons it is proposed that this is a case where the conversion of chorus to hiss occurs inside the plasmasphere.

With the benefit of crossed loop antennas at both Marion Island and SANAE IV, it is possible to calculate the polarisation of the waves received at these locations. Whistler mode waves are right hand circularly polarised, but upon entering into the EIWG, reflections at the ionosphere and the surface of the Earth result in changes to the polarisation, converting them to linearly polarised waves. This means that a wave which has entered into the EIWG at a position close to the receiver will be right hand circularly polarised [Yearby and Smith, 1994]. To this end, the polarisation of the signal received at Marion Island and SANAE IV have been determined using the technique outlined in Manninen [2005]. The polarisation of the signal received at Marion Island is displayed in Figure 4.14. The amplitude spectrograms for these data are plotted in Figure 4.2. A similar

figure for SANAE IV, using data whose amplitude spectra are plotted in Figure 4.4, is shown in Figure 4.15.

These figures show that both the chorus and hiss which were received at Marion Island had a strong right handed polarisation, and therefore entered the EIWG near to the receiver. This could only have happened if Marion Island was close to the plasmapause. On the other hand, the chorus observed at SANAE IV has a linear polarisation, which shows that this chorus originated from some distance away.

The paths of five DEMETER half orbits which occurred just before (orbit 32592), during (orbits 32593 and 32594) and after (orbits 32595 and 32596) the chorus observations at Marion Island are plotted in Figure 4.16. These half orbits begin at a position east of Marion Island and move westward until they are well west of Marion Island. Note that these half orbits were all descending passes of the satellite, as the corresponding ascending half orbits occurred on the opposite side of the globe. Figure 4.17 displays VLF spectra from the ICE instrument on DEMETER, for the 5 half orbits depicted in Figure 4.16. The vertical dotted lines show the L-value of Marion Island in both hemispheres, and the horizontal dotted lines enclose the $2 - 5$ kHz range which corresponds to the edges of the frequency envelope of the chorus observed at Marion Island. Using these data one is able to determine the extent of the chorus generation region in both longitude and L. One can see enhanced VLF activity in the vicinity of Marion Island in half orbits 32594 and 32595. VLF activity in the correct frequency band, but only in the Northern hemisphere is visible in half orbit 32593.

As in the case of the VELOX data, with this low resolution data, it is impossible to discern the exact frequency content of the data. It could be chorus, hiss, or some other noise. The assumption up to now has been that the enhanced VLF activity detected by DEMETER must be chorus, since this is what is observed on the ground. During half orbit 32594, the DEMETER satellite switched into its high resolution burst mode for a brief period while within the region where chorus was observed in the southern hemisphere. These broadband data are plotted in Figure 4.18, and clearly show that chorus was indeed present at this time. Here, the values of dB used have been confined to a range close to the value of the activity peaks observed in Figure 4.17.

A statistical approach was used in the analysis of the DEMETER data in an effort to establish that the observed chorus is not a regularly occurring phenomenon in this longitude and L-range, during this period of the solar cycle. Golden *et al.* [2009, 2011] showed that chorus and hiss are frequently observed at $L = 2.4$ at Palmer Station. Their results, however, showed that chorus and hiss occurrence rates are minimised during solar minimum, but that some observations of chorus were made during 2010. It would thus be interesting to quantify the rarity of chorus at Marion Island for a period around the event. Data from 215 DEMETER half orbits, from April to September 2010 were used in the analysis. Only low resolution survey mode data (like those plotted in Figure 4.17) were used for this. The first step in doing this was to generate an average spectrogram (μ) from the DEMETER data. This was done by obtaining data from many half orbits which occur at the same time of day and in the same geographic region, thereby eliminating MLT dependence. Spectrograms for each of these were then generated. The arithmetic average, μ, of these spectrograms was computed by adding all the arrays representing the spectrograms together. Each element in this array was then divided by the number of arrays used in the average. The average spectrogram resulting from these computations is plotted in Figure 4.19. Note that the expected power in the chorus band near Marion Island's L is small.

In order to calculate the statistical significance of a given observation, the standard deviation σ of the data must also be calculated. This is done in a fashion analogous to the calculation of μ. The standard deviation spectrogram is shown in Figure 4.20.

$$z_i = \frac{X_i - \mu}{\sigma}. \tag{4.1}$$

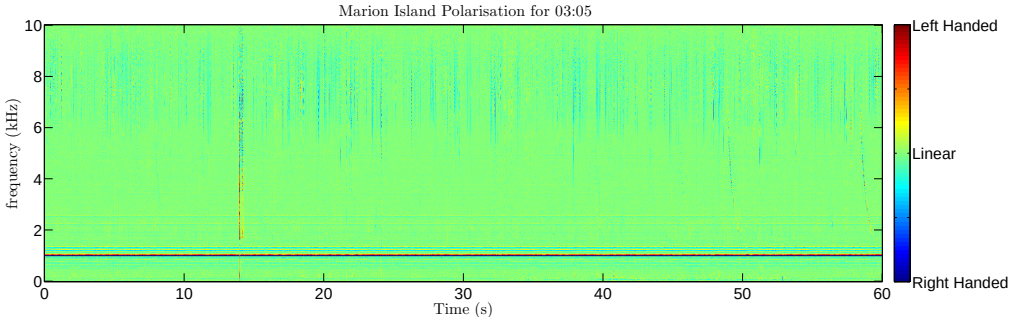

(a) 03:05 UT

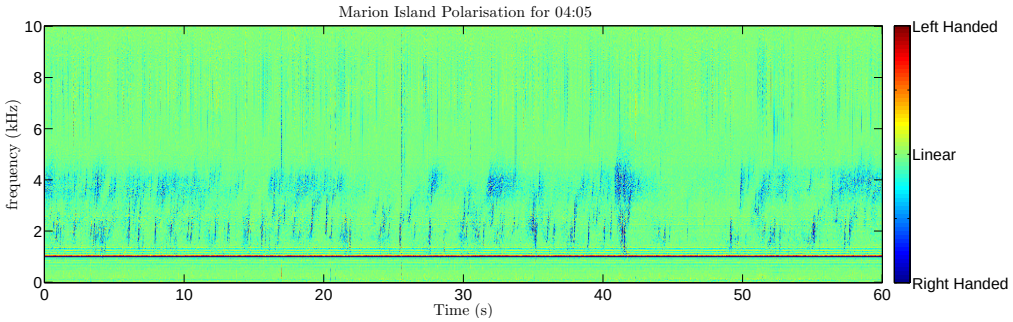

(b) 04:05 UT

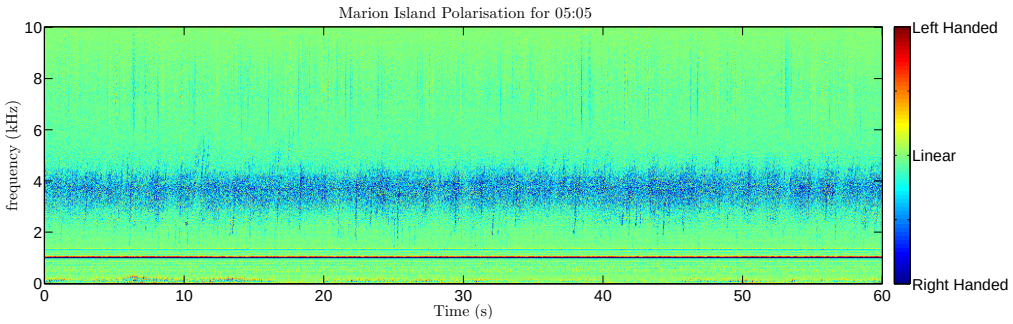

(c) 05:05 UT

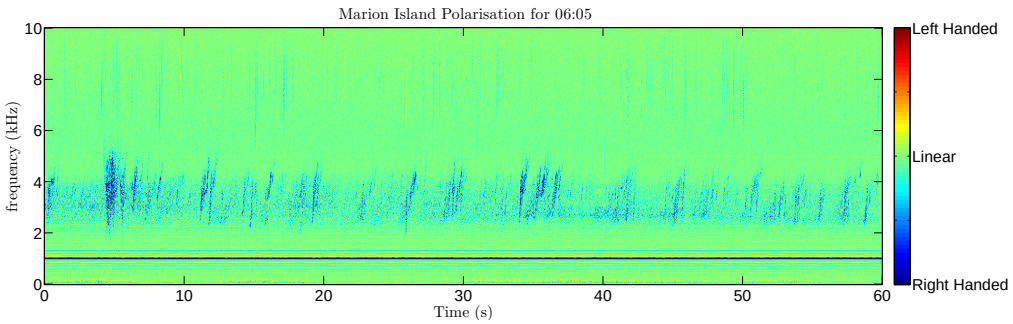

(d) 06:05 UT

Figure 4.14: Polarisation of the signal received at Marion Island. Note the strong right handed polarisation of the chorus and hiss, indicating a nearby entry into the EIWG. The amplitude spectrograms for these samples are shown in Figure 4.2.

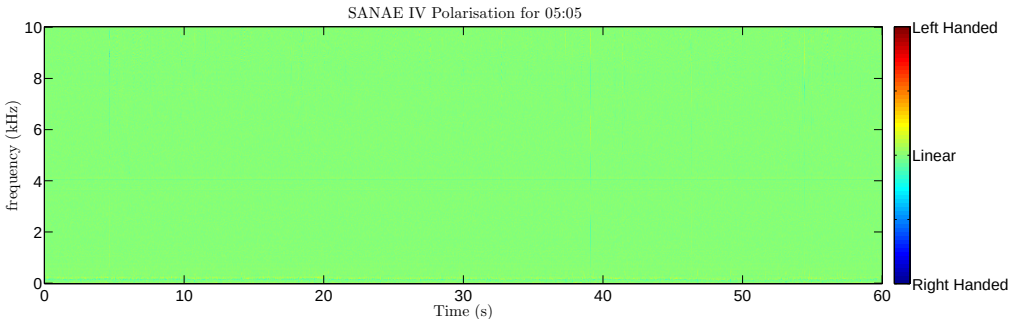

(a) 05:05 UT

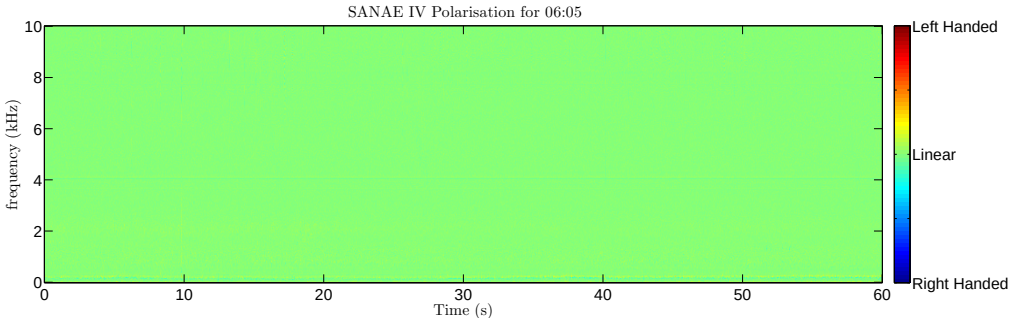

(b) 06:05 UT

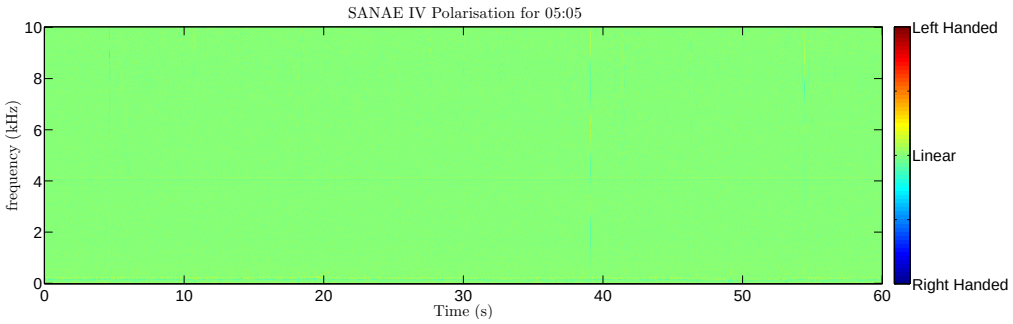

(c) 07:05 UT

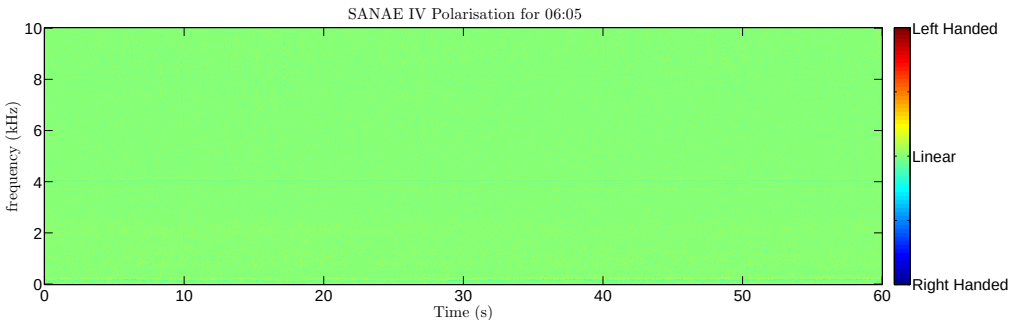

(d) 08:05 UT

Figure 4.15: Polarisation of the signal received at SANAE IV. The signal here is linearly polarised, indicating a distant entry into the EIWG. The amplitude spectrograms for these samples are shown in Figure 4.4.

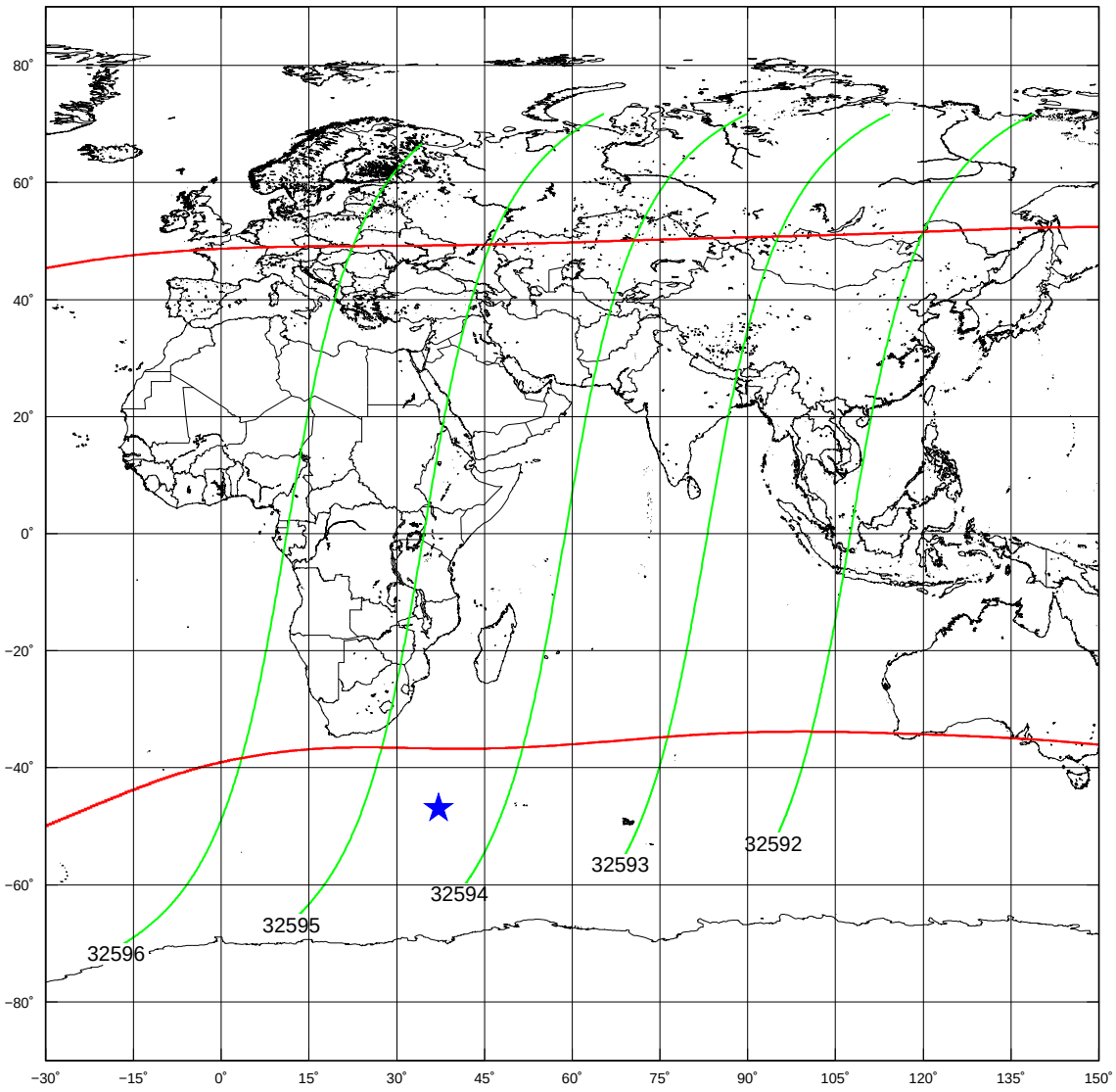

Figure 4.16: The path of five DEMETER half orbits which occurred from an hour before, to an hour after the observations at Marion Island and SANAE IV. The location of Marion Island is depicted by the blue star. The red lines show the $L = 2.00$ shell mapped to the surface of the Earth.

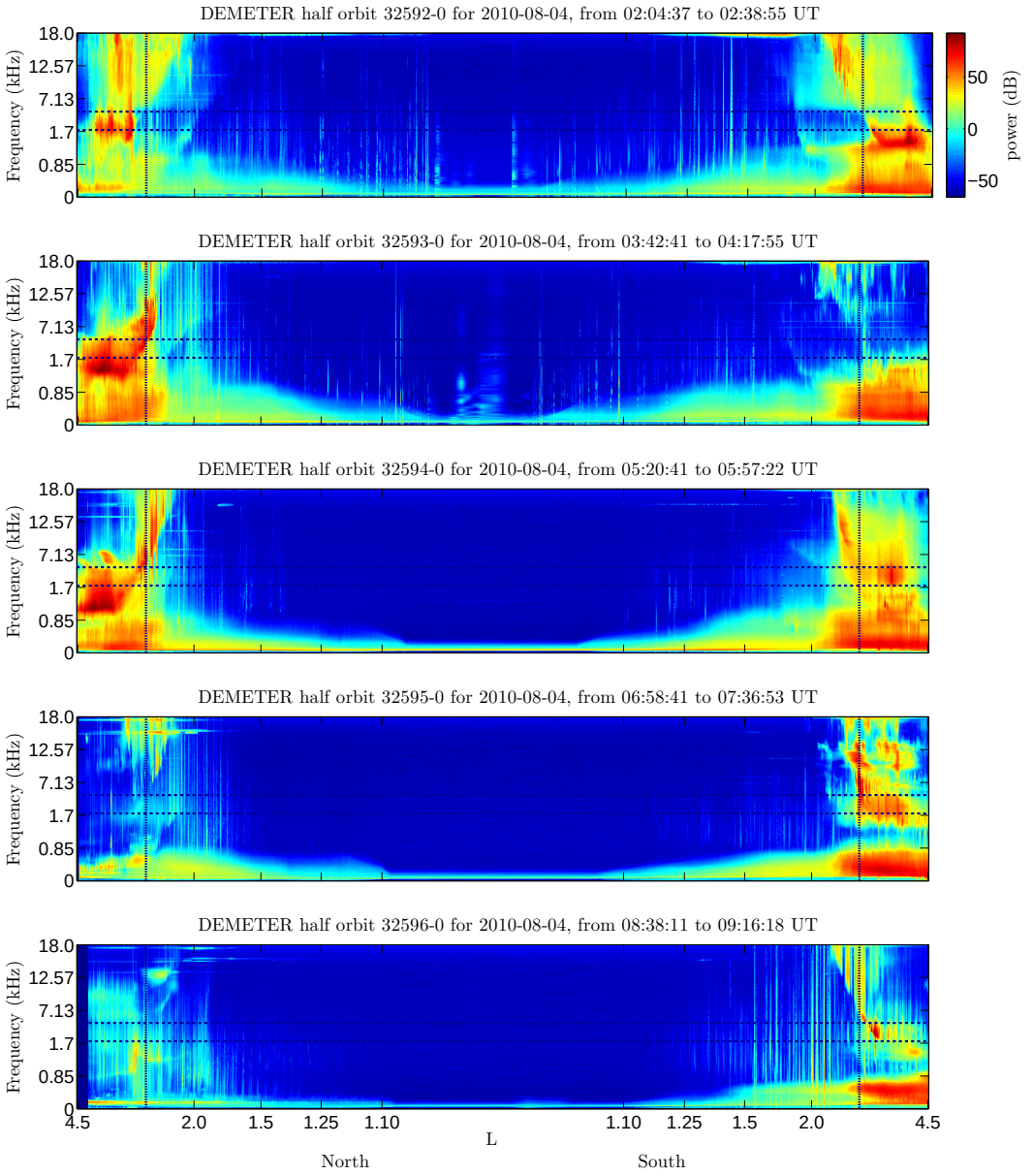

Figure 4.17: Broadband VLF data from the 5 descending DEMETER half orbits shown in Figure 4.16. The vertical dotted lines are the L-value of Marion Island ($L = 2.60$) in both hemispheres, and the horizontal dotted lines represent the frequency envelope of the chorus observed on Marion Island.

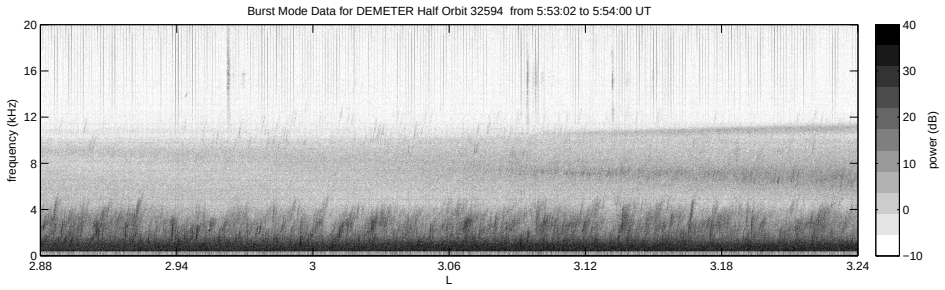

Figure 4.18: Burst mode VLF data from DEMETER half orbit 32594 which shows chorus. These data are for a one minute period while the satellite was in the southern hemisphere. The position of this spectrogram relative to those plotted in Figure 4.17 can be inferred from the L-values.

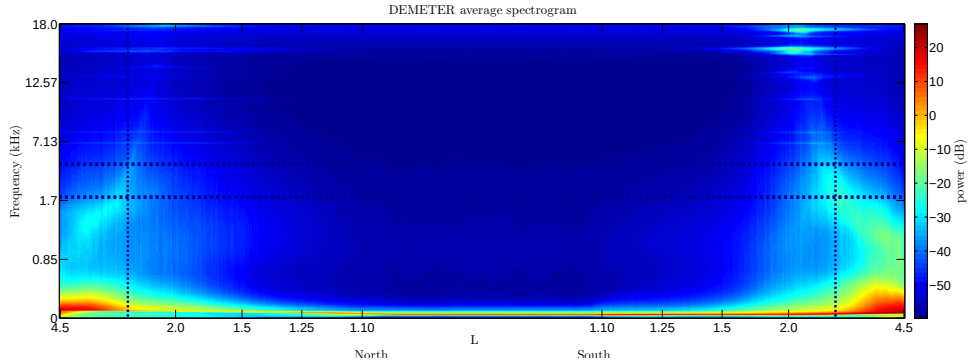

Figure 4.19: The average spectrogram obtained from the DEMETER data. This shows the expected power at each frequency and L.

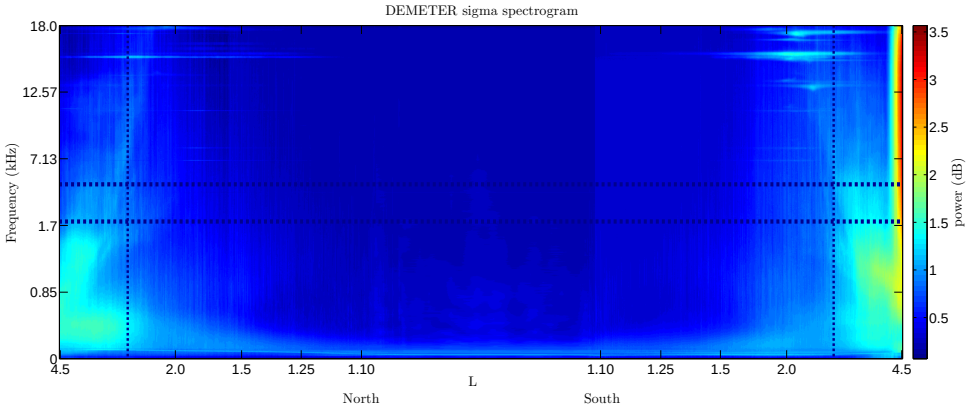

Figure 4.20: The standard deviation spectrogram obtained from the DEMETER data. This shows the deviation of received power from the average in Figure 4.19 at each frequency and L.

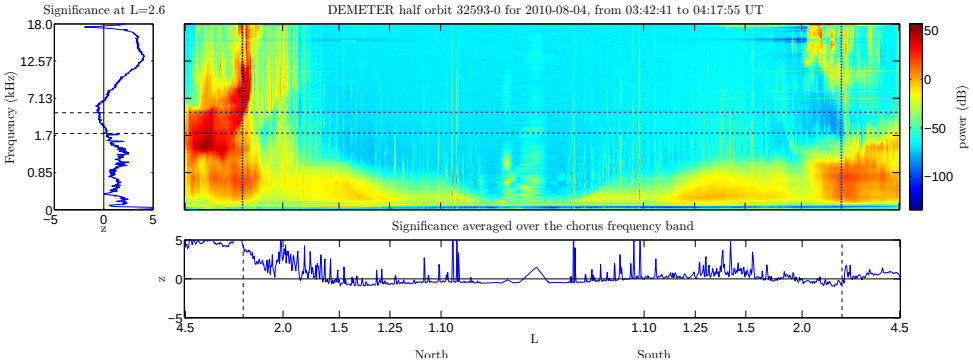

(a) 32593

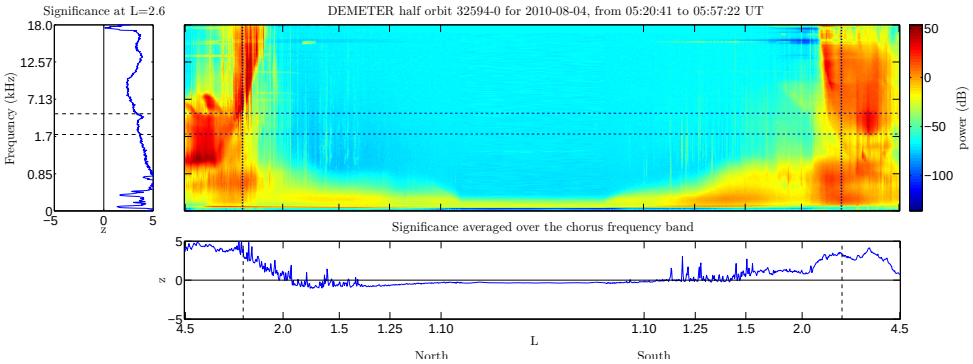

(b) 32594

Figure 4.21: Residuals for descending DEMETER half orbits 32593 (a) and 32594 (b). The left hand plots show the z-value obtained at the magnetic latitude of Marion Island. The bottom plots show the z-value averaged over 2–5 kHz. The z-value is large during periods of high chorus activity, and small during periods of no chorus.

The collection of z_i can be used to infer a p-value for the data. For this analysis, it should be thought of in terms of a 2D spectrogram, where each pixel of the spectrogram transforms to a p-value for that half orbit. A $p \leq 0.05$ indicates a result significant at the 5% level and corresponds to $|z| \geq 1.96$ in a one sided normal distribution such as that of powers which occur in the DEMETER data [p: 613, Hogg and Tanis, 1989]. In Figure 4.21 the residuals of DEMETER half orbits 32593 and 32594 are plotted.

Half orbit 32593 (panel (a) in Figure 4.21) shows no chorus activity in the vicinity of Marion Island. The z-value obtained for this half orbit in the vicinity of Marion Island is close to zero, and so is not of statistical significance. In other words, this level of activity was commonly observed in the data. On the other hand, half orbit 32594 (panel (b) in Figure 4.21) shows intense chorus activity in the vicinity of Marion Island with an associated z-value > 2, which indicates a high statistical significance. This shows that chorus was not frequently observed in the data.

The effectiveness of calculating z-values is highlighted in the differences between the two panels in Figure 4.21. The z-value is ~ 0 during periods of little or no chorus activity, while it increases drastically when chorus is present. It allows one to determine when some activity is occurring in the data which should be interesting, as it is unusual. This technique would be useful for analogous studies in other broadband data sets, either ground based or in situ.

The DEMETER data also allows one to view the VLF spectra across a range of L-values, while the MLT is slowly changing. The VLF spectra are most clearly shown in Figure 4.22, where the residuals of descending half orbits 32592-32596 are plotted. For the reasons above,

these spectrograms offer a clear look into the emission activity, since all background activity is suppressed. Comparing these to Figure 4.16, it is apparent that most of the VLF activity in the chorus and hiss frequency range was confined to the region poleward of $L = 2.00$ (red curve in Figure 4.16). The southern hemisphere VLF activity is most intense in half orbits 32594 and 32595, which are those closest to Marion Island. This indicates that the generation region was localised near Marion Island, at $L > 2$ for the duration of the VLF activity.

Another interesting observation from Figure 4.22 is the apparent asymmetry in the chorus activity between the two hemispheres. In half orbits 32592, 32593 and 32594 there is activity in the northern hemisphere. However, in the southern hemisphere there is chorus in half orbits 32592 and 32594, and not 32593. It appears as though the satellite had moved through some gap in the chorus generation region. This asymmetry is not expected given the nature of chorus generation (and also based on observations by Meredith *et al.* [2003]). Three possible reasons for this anomaly are proposed:

1. A half orbit is ~ 45 minutes for DEMETER, thus, there is some delay between observations at the top and bottom of a half orbit. This time delay is long enough for chorus generation to switch on or off before reaching the opposite end of the field line. One might be able to discount this factor since the chorus in the northern hemisphere persists for 3 half orbits.

2. DEMETER does not orbit along magnetic meridians, and so the top and bottom of the half orbit are separated in magnetic longitude. The satellite can thus move out of or into the chorus generating region along a single half orbit.

3. The electrons require positive thermal anisotropy for wave growth. It is possible that conditions were such that the southward traveling particles (i.e.: those resonating with northward propagating waves) had negative anisotropy. Upon mirroring in the southern hemisphere, $T_{\|}$ was reduced in the system as particles were lost by collisions in the neutral atmosphere, leading to positive anisotropy on the northward trip (resonance with southward propagating waves). This allows for enhancement of the southward propagating waves while reducing the anisotropy in the system, and they remained so after the next mirror in the northern hemisphere.

The third reason may seem like a rather convenient set of circumstances, but Marion Island lies east of the SAA. This results in particles penetrating to a greater depth in the southern hemisphere (and hence having a larger bounce loss cone) than in the northern hemisphere. This serves to reduce $T_{\|}$ only on the southern hemisphere bounce.

Data from the UltraMSK [Clilverd *et al.*, 2009] receiver located at Marion Island were analysed to determine if any particle precipitation resulting from the chorus was evident. It was found that the only possible evidence of precipitation was in the signal received from NWC, which is on the north western coast of Australia. Analysing UltraMSK data can be a difficult problem, because one is looking for small deviations from the expected behavior of a signal which can have very erratic structure. A quick and effective way to address the irregularity of the data is to formulate quiet day curves by averaging the data from several days in which there is no external modulation (eg: from precipitation or solar flares) of the signal. Plotting the day of interest's data superimposed on top of the quiet day curve then yields a way to determine where events of interest occur in the data.

The amplitude of NWC recorded by the Marion Island receiver for 4 August 2010, as well as the mean and 1σ obtained from 14 days of data centered on 4 August 2010, are plotted in Figure 4.23. There is a small deviation from the quiet day curve ~ 30 minutes prior to the observation of the chorus. Since NWC is directly east of Marion Island, it is possible that this was caused by precipitation from the VLF waves observed in the northern hemisphere in half orbit 32592 (see

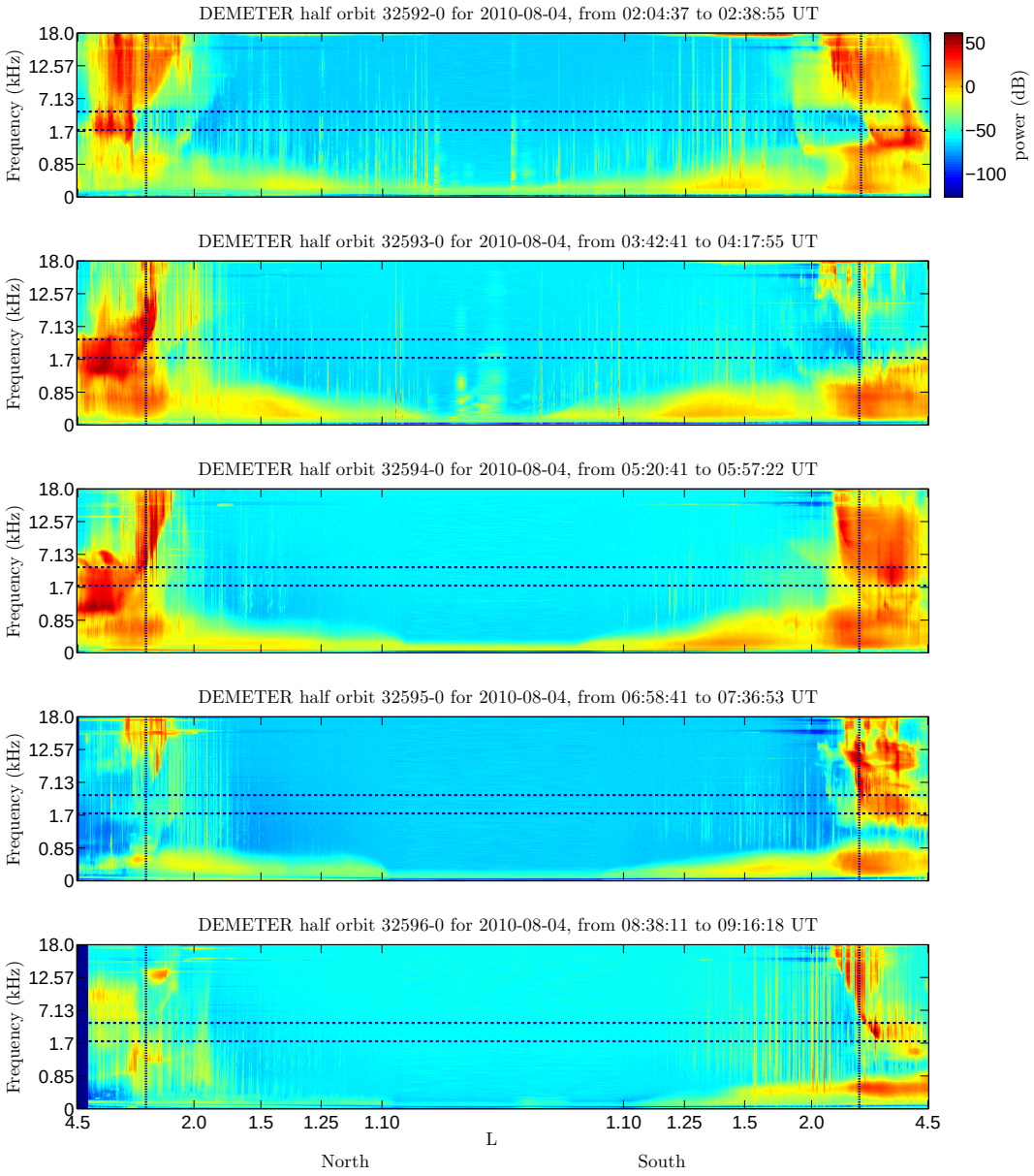

Figure 4.22: Residuals after a subtraction of the mean of the DEMETER data presented in Figure 4.17. The chorus is much more evident in these plots. The vertical lines show the L-value of Marion Island in both hemispheres. The two horizontal lines show the frequency range 2–5 kHz.

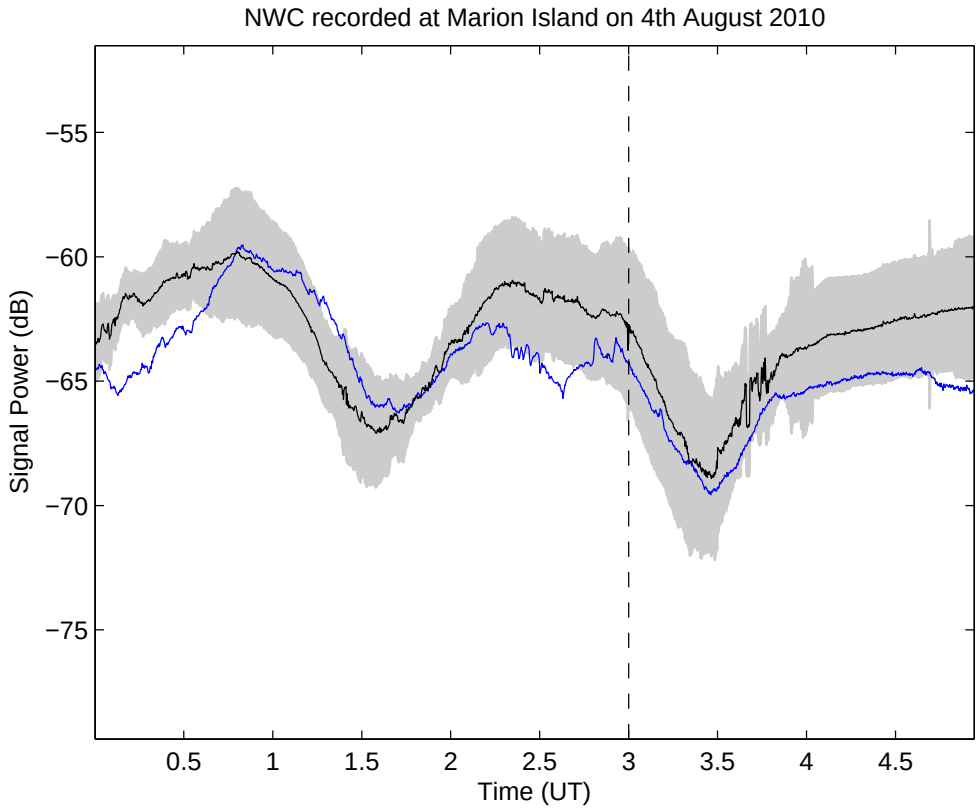

Figure 4.23: Amplitude of NWC observed at Marion Island (blue), with the mean over a 14 day period centered on 4 August 2010 (black). The grey area represents 1σ on either side of the mean. There is a significant deviation from the mean at 02:30 UT, which may be attributed to particle precipitation from chorus. The vertical dashed line corresponds to the time of chorus onset at Marion Island.

Figure 4.22), which occurred when DEMETER was east of Marion Island. This slow variation of amplitude does not resemble that of short-lived FAST events [Rodger *et al.*, 2007, 2010], but appears more likely to be caused by hiss generated by the chorus. This may, however, be a random fluctuation in amplitude, since the signal level is rather variable.

The signal used in this analysis was recorded while the UltraMSK system at Marion Island was not yet operating efficiently. The data from the system has seen dramatic improvements over the last 2 years. This does, however, show that evidence of particle precipitation can be found in this noisier Marion Island UltraMSK data, even before the use of rigorous Principal Component Analysis techniques [Collier, 2009], which would no doubt further illuminate the effect.

4.4 Conclusion

At its outset, the research of this chorus observation was undertaken because of it being the first chorus observed by the Marion Island VLF receiver system. The research very quickly became more focused as the spectral structure of the chorus showed that it converted to hiss, which was relevant to the recently published papers indicating that chorus was the source of plasmaspheric hiss.

This chorus was observed between 03:00–07:00 UT on the 4 August 2010 during a period of

unusually low geomagnetic activity. The event was compared to an observation of chorus made in 2003 at Palmer Station, which has a similar L-value to Marion Island, during the previous solar maximum. The 2003 event was triggered by a severe geomagnetic storm which compressed the plasmapause to an L-value below that of Palmer. The 2010 event was also preceded by a geomagnetic storm, although, it was much less intense than that experienced in 2003. However, observations indicate that the plasmapause was pushed close to the L-value of Marion Island, although Marion Island was probably still inside the plasmasphere during the event.

This proximity to the plasmapause made for a remarkable observational opportunity. VLF emissions from both inside and outside the plasmasphere were able to propagate to Marion Island, giving a continuous view of these two regimes. This allowed for the simultaneous observation of chorus and plasmaspheric hiss at a single terrestrial receiver. A similar observation was made in space by Bortnik *et al.* [2009] using two THEMIS satellites positioned on either side of the plasmapause. The observations at Marion Island seem to support their findings that chorus penetrating into the plasmasphere is the source of plasmaspheric hiss.

Data from two other stations are used to track the motion of the chorus generation region, and it was shown that the generation region was probably moving eastward, which consistent with the eastward drift of electrons in the magnetosphere. The location of the plasmapause was determined with the use of two models based on geomagnetic activity. A serendipitous observation of a knee whistler at Dunedin, New Zealand, allowed for a direct estimate of the location of the plasmapause. The use of the AWDA system here shows the potential of the system to make continuous mappings of the plasmasphere, and the usefulness that this will have for research. There was a significant disparity between the value of L_{pp} obtained from the knee whistler analysis and the modeled result, but these differences were attributed to inaccuracies of the model, as well as the knee whistler being observed later in the day.

DEMETER VLF data were used to determine the size of the generation region. The generation region was found to be poleward of $L = 2.00$, and the data showed that at the time of DEMETER observations, the region was localised to Marion Island, which indicates that the region was likely small. An averaging technique was used to highlight uncommon features in the VLF data, and a direct measure of the statistical significance of particular features in the data was obtained. Using this analysis allowed for a quantitative measure showing that chorus was not commonly observed in the vicinity of Marion Island during this period of the solar cycle. This technique could be directly applied to any other spectrogram type data sets, allowing for easy (and quite possibly automated) identification of interesting features in broadband data.

Marion Island was in a favourable position for viewing this event. The L-value of Marion Island puts it close to where one might expect to find the plasmapause during moderately disturbed periods. The plasmapause acts as a dividing layer between two VLF generation regimes in the magnetosphere (refer to Figure 2.6), and either or even both of these can be viewed at any given time. Additionally, it was discussed how the plasmapause itself may have played a role in guiding plasmaspheric emissions through the LHR reflection layer. Marion Island's location just east of the SAA also means that electrons drifting towards Marion Island have just passed through the SAA, which would cause dramatic reconfigurations to their velocity distribution, and consequently on the direction of net energy exchange between waves and particles.

These observations were made possible by a rather unique set of circumstances and a particular level of geomagnetic activity. Higher levels of activity would have resulted in a more extreme compression of the magnetosphere, and thus only chorus being observed, as was the case for Palmer in 2003. On the other hand, sufficient activity was required to shift the plasmapause close enough to Marion Island to allow for the sub-ionospheric propagation of hiss to the receiver. While this chapter presents an interesting case study which confirms several previous theories and conclusions made from satellite observations, it has also outlined a new method for analysing VLF

spectrograms and identifying uncommon occurrences in that data.

Chapter 5

Twin Whistlers

5.1 Introduction

During a 3 month period in 2009 whistlers were detected by AWD systems at both Rothera (67.57° S 68.12° W, $L = 2.71$) and SANAE IV (71.40° S / 2.51° W, $L = 4.36$). These stations are in close proximity to each other, separated by only $\sim 2500\ \mathrm{km}$, but with significantly different L-values. Light travels the distance between the two receivers in $8\ \mathrm{ms}$. Since the distance between the two stations is less than typical wave guide propagation distances, there exists the possibility for the same whistler being received at both receivers. The two whistlers would be have the same dispersion characteristics, regardless of the relative distance propagated by each whistler to its receiver, since both would have had an identical path through the magnetosphere. There might, however, be amplitude differences between them, since attenuation in the EIWG is proportional to distance propagated, and the two whistlers would probably have propagated different distances in the EIWG. Since they have the same shape and only differ slightly, they have been given the name twin whistlers.

An analysis to identify twin whistlers in the Rothera and SANAE IV data should shed light on the issue of how far whistlers can travel within the EIWG. Since whistlers have had their energy smeared out over a longer time than their initiating spheric, it is reasonable to assume that the propagation distances of whistlers and their initiating spheric will not be comparable. So, while a spheric can travel distances $\sim 10000\ \mathrm{km}$ through the EIWG, the same is not necessarily true of whistlers propagating from their EIWG re-entry point to a receiver. Furthermore, there are some interesting differences between the number of whistlers received at each site, which the analysis of twin whistlers may explain.

As reported by Collier *et al.* [2011], Rothera receives on average many more whistlers than most other AWD sites, despite having comparable lightning activity near its conjugate point. Their analysis found that the primary source region for Rothera was on the east coast of the United States and over the Gulf stream. A similar analysis (currently unpublished) for SANAE IV show that it shares its whistler source region with Rothera. The source regions for Rothera and SANAE IV whistlers are shown in Figure 5.1. AWD data from Rothera were available from 13/05/2008 to 31/12/2009, and from SANAE IV from 12/09/2009 to 31/12/2009. That means that there is an overlap from 12/09/2009 to 31/12/2009, or 81 days. During this period, 80117 whistlers were received at SANAE IV, while 229135 were received at Rothera.

The fact that these two sites have a similar source region is somewhat surprising, given the massive disparity between the number of whistlers received at each site. At Rothera an average of 6.75 million whistlers are received per year, while at SANAE IV an average of 400 000 whistlers are received per year. This is a massive difference for two sites which have essentially the same source region. The difference in whistler counts must be due to the locations of the two sites.

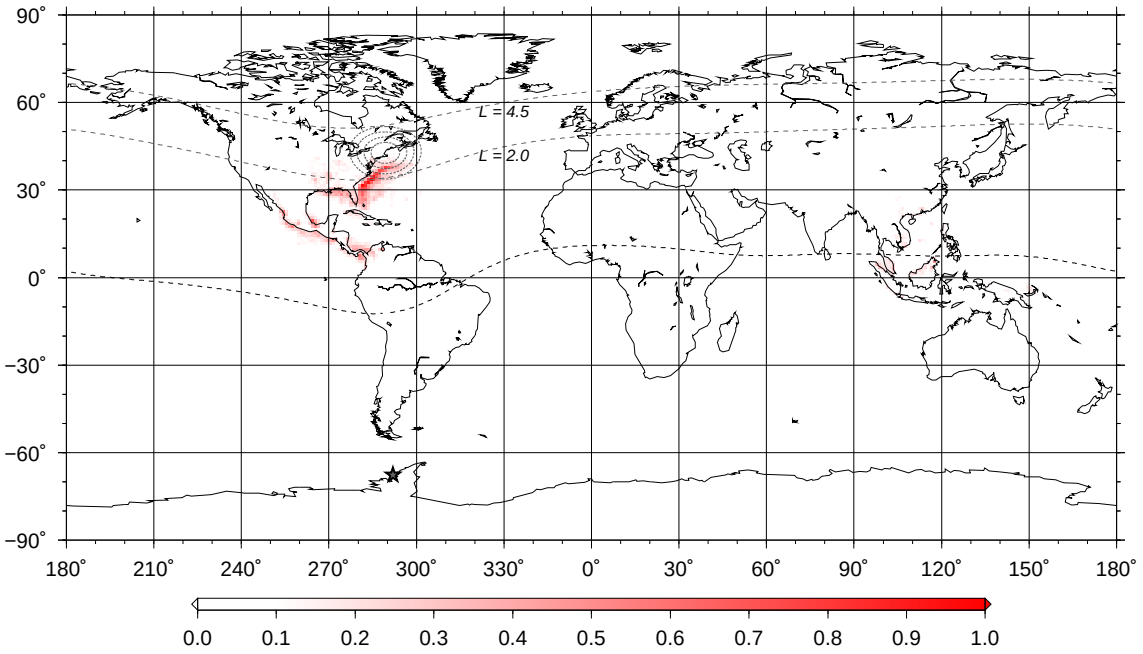

(a) Rothera Source Region

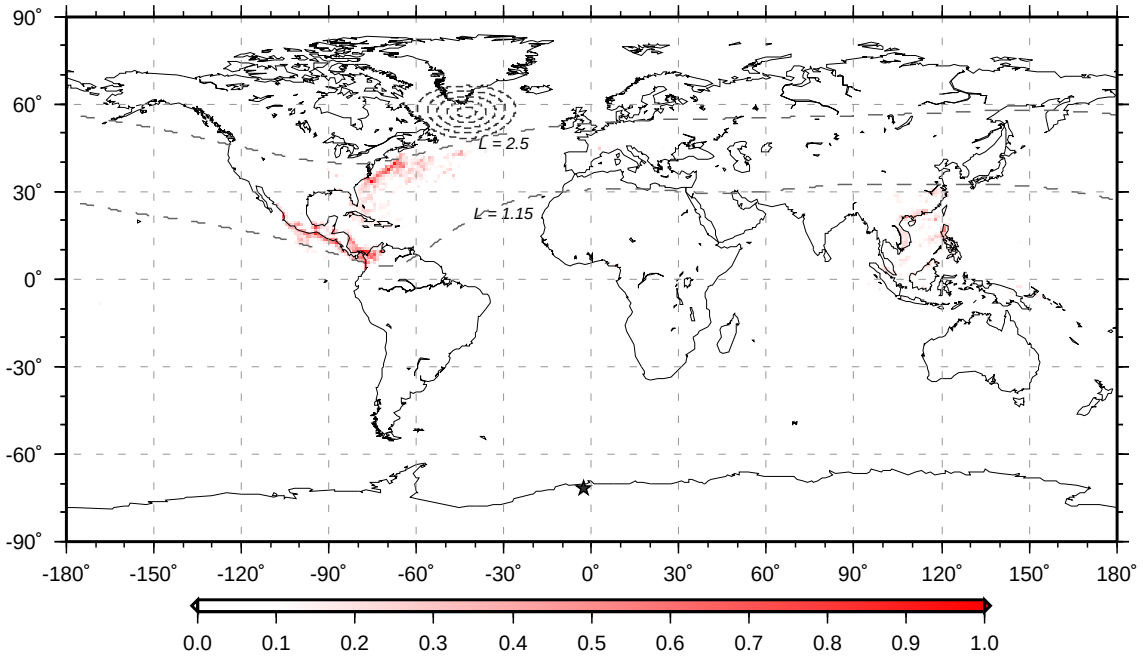

(b) SANAE IV Source Region

Figure 5.1: The whistler source regions of Rothera after Collier *et al.* [2011] (a). The source region for SANAE IV was determined using a similar analysis, and is shown in (b). The result in (b) is currently unpublished. The whistler source regions of these stations are roughly the same.

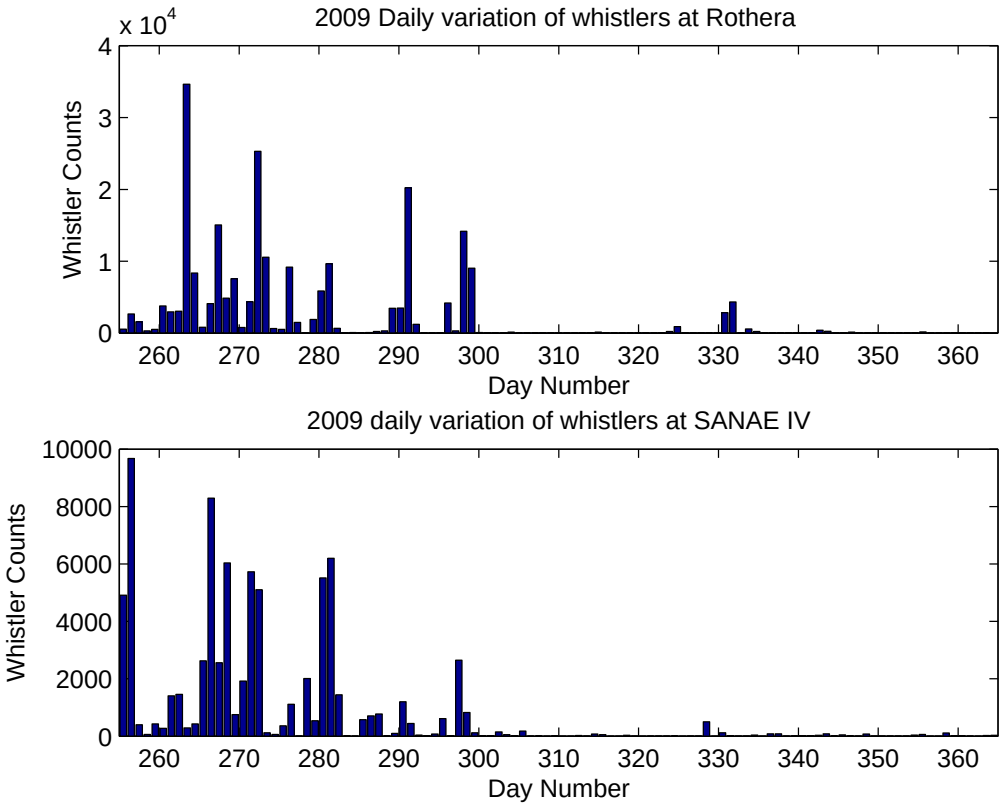

Figure 5.2: The daily whistler counts at Rothera (top) and SANAE IV (bottom) for the period of overlapping data. There are three periods of comparable whistler activity near days 270, 280 and 300.

Before the whistlers are paired on a one to one basis, some statistics of the whistlers received at each site during the period of overlapping observations should be checked. In Figure 5.2 the daily variation in whistler counts at Rothera and SANAE IV are plotted. Superficially, it seems that these two distributions are very similar, with many whistlers seen by both stations before day 300, and nearly none seen after that day. However, on closer inspection, the agreement between the two is not very good. There are days when SANAE IV records many whistlers while Rothera records relatively few (eg: day 264), and other days where this is reversed (eg: days 255 and 256). There are however 3 periods which show comparable relative whistler counts at each station. These are around days 270, 280 and 300. These periods are possibly favoured for twin whistler observation, and are possibly due to the EIWG entry point being midway between the two stations.

In Figure 5.3, the diurnal variations of the whistlers received at Rothera and SANAE IV are displayed. From this figure it is clear that the peaks in whistler activity occur at different times of day at each station. This is not too surprising, given that the two stations are in different local times, and that whistler reception is typically favoured at night. In Figure 5.4, the same diurnal distributions are plotted, except that they are transformed into LT. The LT distributions have their peaks at the same time of day, which means that the effects of the time of day have a stronger effect on whether whistlers are received than the presence of source lightning.

These results seem to suggest that there is not a strong link between the whistlers received at both sites. However, the data shown in Figure 5.2 suggest that on at least some occasions there is the potential for twin whistler observations.

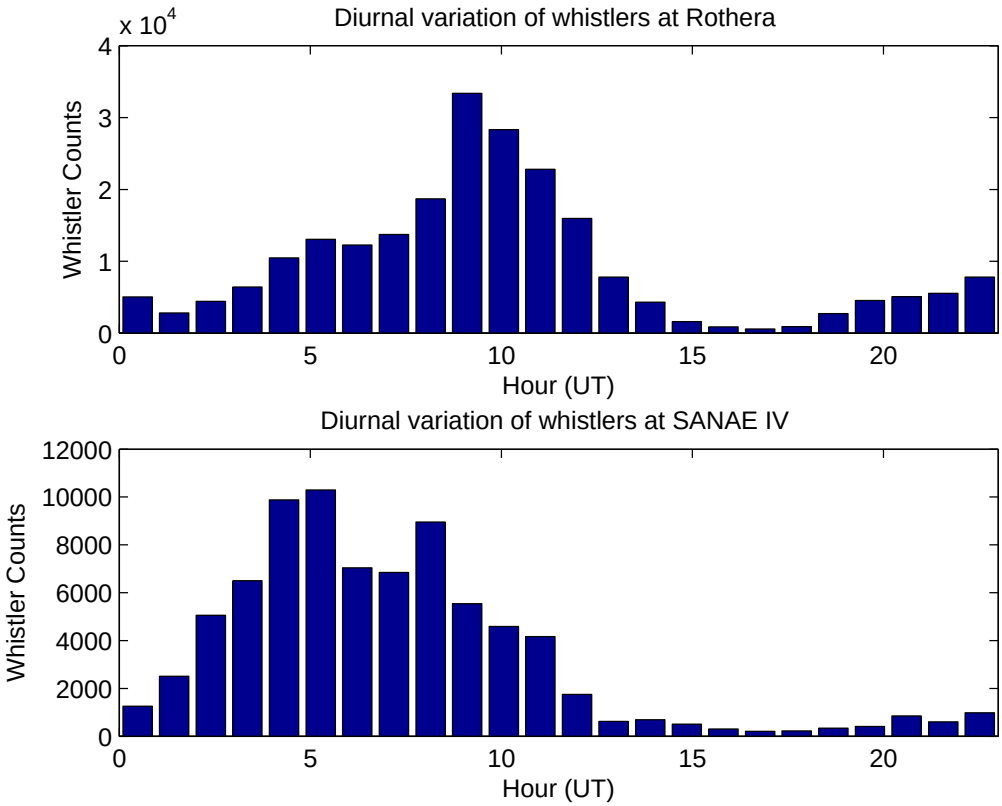

Figure 5.3: The diurnal variations of whistler counts at Rothera (top) and SANAE IV (bottom) for the period of overlapping data, plotted in UT. The peaks in whistler activity occur at different times of day.

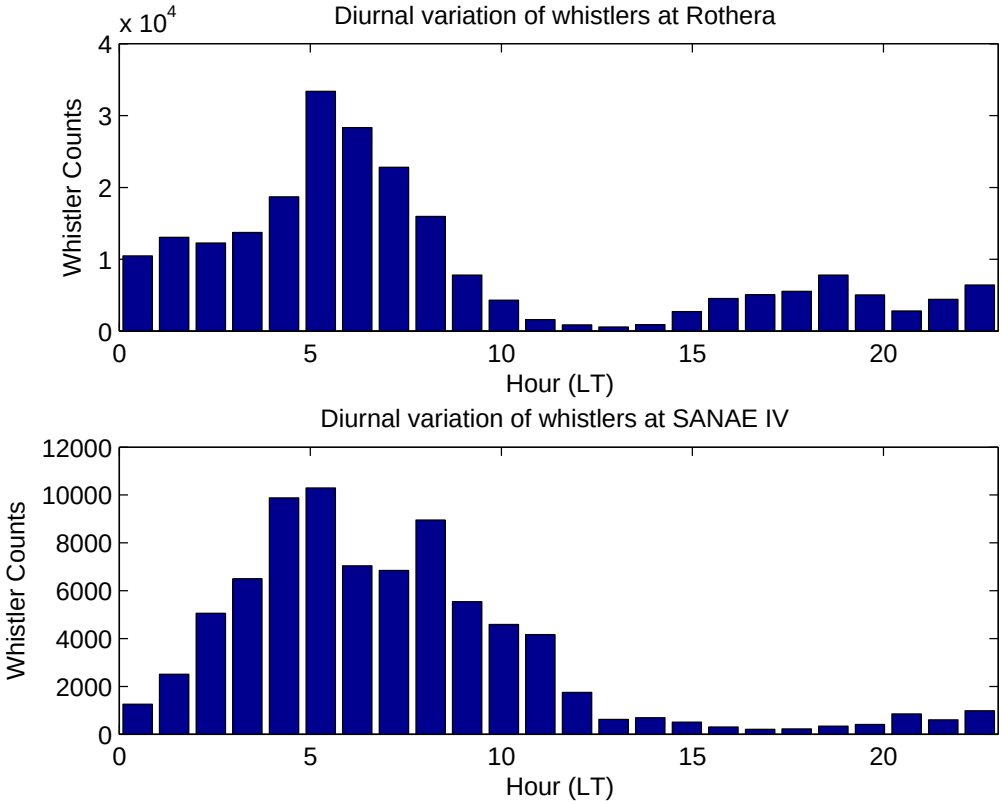

Figure 5.4: The diurnal variations of whistler counts at Rothera (top) and SANAE IV (bottom) for the period of overlapping data, plotted in LT. The peaks in whistler activity occur at the same local time, indicating that ionospheric effects are dominant.

5.2 Twin Identification Method

Twin whistlers are identified using the time they were recorded as reported by the respective AWD system at each station. The AWD produces only times at which whistlers (more accurately the nose frequency) are received at the station. The task of identifying twin whistlers is rather straightforward. Since the whistlers have entered the EIWG at some point between the two stations, there will be a relative delay between the whistlers at each receiver. There are several possible scenarios to consider. Figure 5.5 illustrates these different scenarios, which are described below:

1. The spheric propagates subionospherically from the source region to the conjugate point of Rothera. It travels through the ionosphere here and propagates through the magnetosphere to the location of Rothera. It crosses the ionosphere and arrives immediately at Rothera, and propagates from there to SANAE IV, resulting in a $8\ \mathrm{ms}$ delay (a).

2. The spheric propagates subionospherically from the source region to the conjugate point of SANAE IV. It travels through the ionosphere here and propagates through the magnetosphere to the location of SANAE IV. It crosses the ionosphere and arrives immediately at SANAE IV, and propagates from there to ROTHERA, resulting in a $8\ \mathrm{ms}$ delay (b).

3. The spheric crosses the ionosphere directly above the stroke and propagates through the magnetosphere to the point conjugate to the source region. It crosses the ionosphere here, propagates subionospherically to Rothera first, and later arrives at SANAE IV. Since the conjugate of the source region is west of Rothera, the delay will also be $\sim 8\ \mathrm{ms}$ (c).

4. The spheric propagates subionospherically to some random location. It travels through the ionosphere here and propagates through the magnetosphere to the conjugate point of this random location. It propagates through the EIWG to Rothera and SANAE IV. The delay here depends on the position of the EIWG entry point, but it will be less than $8\ \mathrm{ms}$ in all cases (d).

Using the relative delay is useful, since it never exceeds $8\ \mathrm{ms}$, and so the matching occurs more readily as the scope of possible matches for each whistler is minimised. Also, the delays calculated are relative to when the SANAE IV whistler is received, so that a delay of $-8\ \mathrm{ms}$ is expected with case 2, while a delay of $+8\ \mathrm{ms}$ is expected for case 1. A positive delay implies sub-ionospheric re-entry closer to Rothera, and a negative delay implies sub-ionospheric re-entry closer to SANAE IV. The method used to identify twins is as follows. For each whistler received at SANAE IV, those which were received at Rothera within $8\ \mathrm{ms}$ before and after are chosen. Frequently there was only one whistler which met this condition, and so it was selected as the twin. If more than one fulfilled the condition, then the one which minimised the delay was selected as the twin.

5.2.1 Significance of These Results

As before, it is important to evaluate the statistical significance of these results, since the twin identification only uses the relative timing data. It is thus possible that these matches are merely coincidental, and not that the whistlers are twin whistlers. Of course, comparison of the dispersions of whistlers would provide virtually irrefutable evidence that a pair are twin whistlers, since they are expected to have identical dispersions. In the absence of this data however, some simple calculations can go some way to proving that the matches are probably not due to coincidence.

As described above, the whistlers analysed occurred during an 81 day window. For a whistler pair of whistler to be considered twins, they must be received within the same $16\ \mathrm{ms}$ window. During the 81 days, there are 437400000 ($= 81$ days $\times 24$ hours $\times 3600$ seconds $/0.016$) such

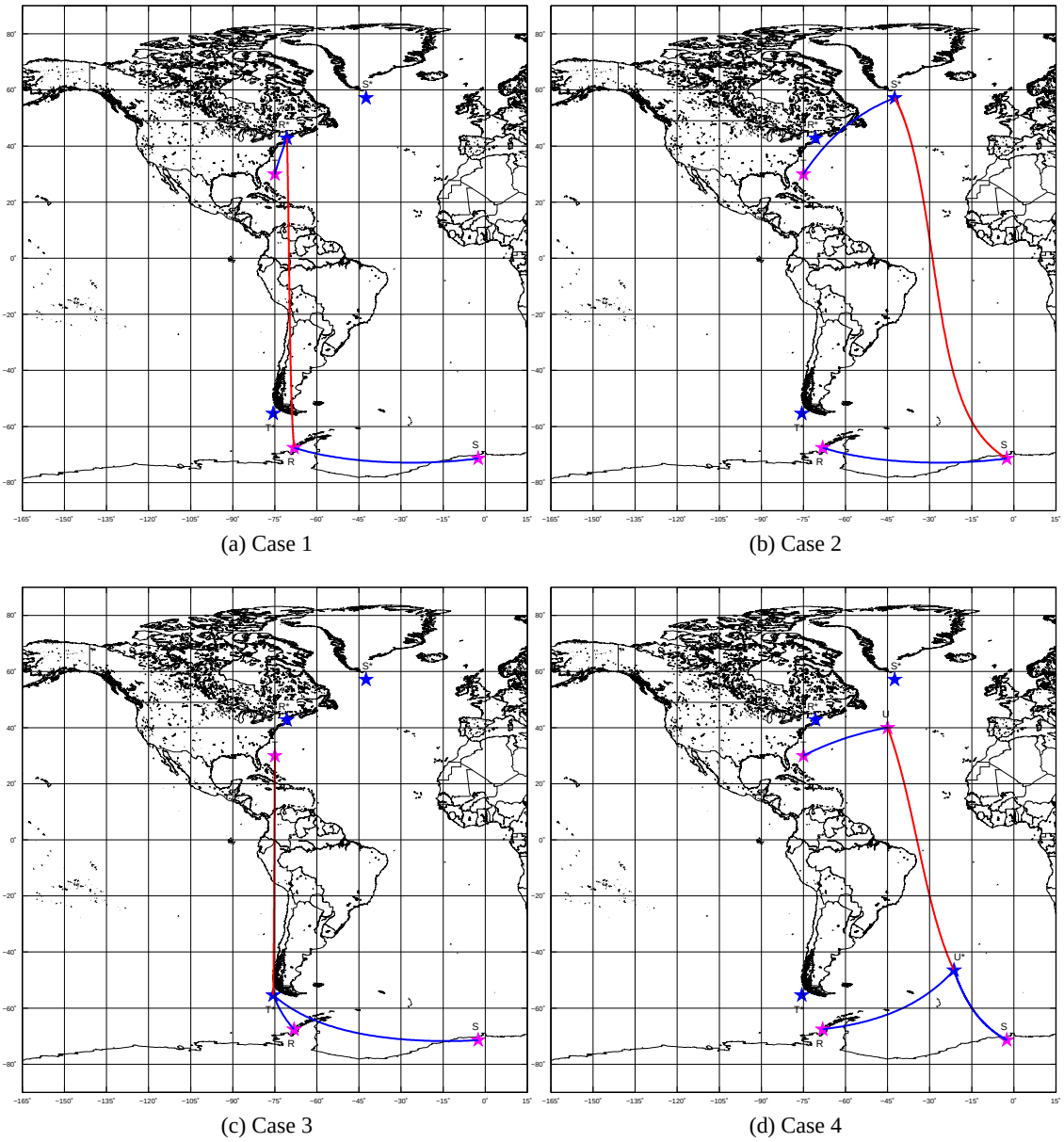

(a) Case 1

(b) Case 2

(c) Case 3

(d) Case 4

Figure 5.5: SANAE IV (labeled as S), Rothera (labeled as R) and their whistler source region (labeled as T) are depicted by purple stars. Their conjugate points (labeled as S*, R* and T* respectively) are demarcated by blue stars. A blue path indicates sub-ionospheric propagation, while a red path indicates magnetospheric propagation. Description 1-4 above refer to (a), (b), (c) and (d) respectively. In the final panel, a new point U (with conjugate point U*) is some random ionospheric transit location.

windows. The diurnal variation of whistlers at both sites show that whistlers are mainly received during a 12 hour window, so that this number can be divided by two, since only half of the windows are most likely to contain any whistlers. Furthermore, the daily variation shows that the whistlers were only mainly only received during the first half of the 81 day period, so that the number of possible intervals can again be halved. This leaves a total of 109350000 intervals.

Now, the probability that one of the 229135 whistlers received at Rothera will fall within a particular interval is 0.0021. Similarly, the probability that a SANAE IV whistler will fall into a particular (not necessarily the same) bin is 0.00073. Now, the probability that a whistler received at both sites will fall into the same interval, and thus be identified as twin, is given by the product of these two probabilities, which is 1.53×10^{-6}. This means that there is a very small chance for just a single twin whistler to be identified by chance, let alone for many.

5.3 Discussion

Twin whistlers were only found for 2% of the whistlers detected at SANAE IV (thus the fraction of Rothera whistlers which were twins is even lower). This shows that whistlers are not frequently able to propagate the distance between SANAE IV and Rothera, before being attenuated to below background levels, and so are only detected by one of the two receivers. In fact, the minimum distance which a whistler would need to travel before being received at both sites is $\sim 1250\mathrm{km}$. This provides some indication of the distance from a receiver a whistler must re-enter the EIWG if it is to be detected.

The daily distribution of the matched whistler counts is shown in Figure 5.6. This figure shows that the matched whistlers occur in isolated patches. Comparing this with the distributions shown in Figure 5.2, it is clear that the peaks in twin whistlers occur when SANAE IV and Rothera see increased numbers of whistlers on the same days, which is probably due to a duct exit located somewhere between the two stations. Since the diurnal variation of whistlers received at SANAE IV and Rothera is so strongly governed by the LT at the receiver, it may be possible to determine if a particular EIWG re-entry is common for twin whistlers. In Figure 5.7 the diurnal distribution of twin whistlers is plotted at 3 different local times: LT = UT, LT = UT-2, and LT = UT-4. Comparing these distributions to those plotted in Figure 5.4 show that there is some similar pattern in the distributions. Although the peaks are not in the same place, Figure 5.4 shows that whistlers are received principally between 00:00 and 10:00 LT, and the twin whistler distribution plotted with LT = UT-2 most closely resembles this. This is tested quantitatively using a Pearson's χ^2 test, as follows:

1. Since the twin whistler diurnal distribution should have similarities to both the diurnal distributions of SANAE IV and Rothera, a target distribution is created by averaging the distributions of SANAE IV and Rothera.

2. Since the peaks of the target distribution will obviously have larger magnitude than the twin whistler distributions, all the distributions are normalised, so that only the positions of the peaks, and not their height, are considered.

3. Finally, the χ^2 test is performed between each of the twin whistler diurnal distributions from Figure 5.7 and the target distribution.

The above analysis yields correlations of 78% for LT = UT - 0, 80% for LT = UT - 2, and 73% for LT = UT - 4, where the p-values in each case are $\sim 6 \times 10^{-5}$. This implies a location midway between Rothera and SANAE IV is the preferred EIWG re-entry point for twin whistlers. These differences are small, however, and a more correct conclusion would be that the twin whistlers enter the EIWG anywhere between SANAE IV and Rothera.

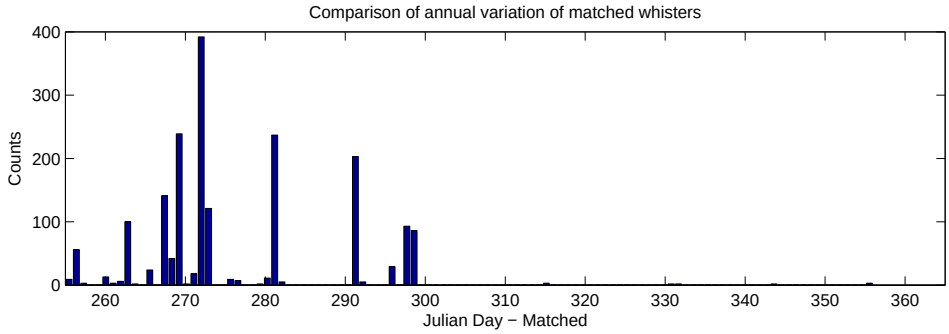

Figure 5.6: The daily variation of twin whistler counts. The peaks in this distribution occur on days when both SANAE IV and Rothera show elevated whistler levels, as seen in Figure 5.2.

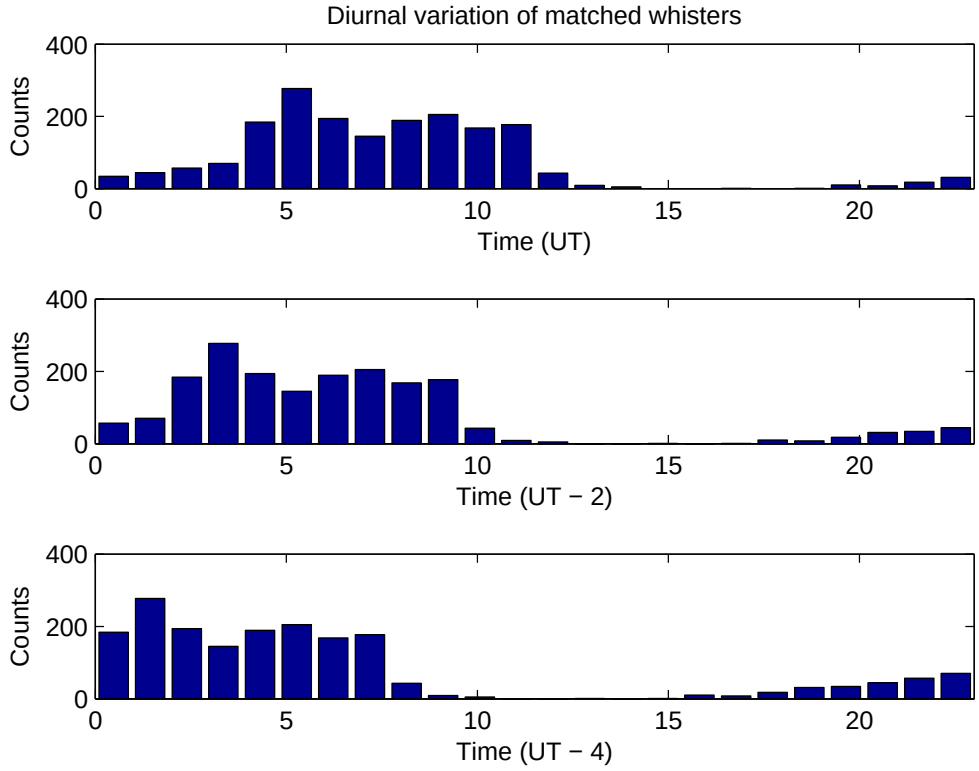

Figure 5.7: The diurnal variations of twin whistler counts plotted in 3 different local times. The distribution with LT = UT−2 most closely resembles the diurnal distributions plotted in Figure 5.4.

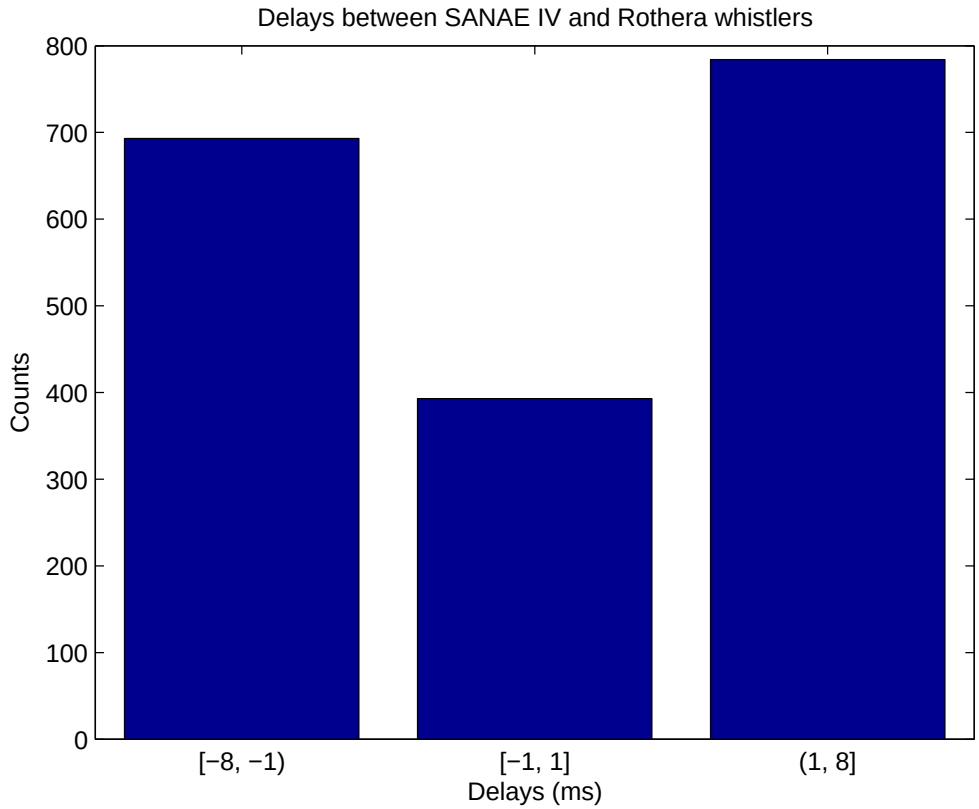

Figure 5.8: The distribution of delays calculated during the matching. The distribution shows that there are more negative delays than positive ones, and that a relatively small number of the twin whistlers had 0 ms delays.

Finally, a distribution of the delays between the reception of twin whistlers at SANAE IV and Rothera is plotted in Figure 5.8. This figure shows that the delays are more or less uniform across the range of values. There are a large proportion of delays around 0 ms, with 21% of the delays falling into this 2 ms window. The distribution also shows that there are more delays which are > 1 ms (42%), than those which are < -1 ms (37%). This suggest that a EIWG re-entry closer to Rothera is preferred, but that re-entry half way between SANAE IV and Rothera is relatively probable. This is what one would expect, given the relative positions of the two stations. First, a midpoint EIWG re-entry is probable, since this allows for a minimum propagation distance to both receivers, and thus the highest probability of a twin whistler being received. Second, re-entry closer to Rothera is expected to be favoured, since it is closer to the conjugate point of the source region.

5.4 Conclusion

The results presented in this chapter are not definitive, but do point towards some ideas which further investigation may strengthen. The fact that such a small fraction of twin whistlers was found suggests a possible reason for the massive disparity in the number of whistlers received at SANAE IV and Rothera. Since whistlers are not frequently able to propagate the distance between Rothera and SANAE IV, under the extreme attenuation which ice provides, it should be expected that Rothera, which is much closer to the conjugate point of their mutual source region,

receives vastly more whistlers than SANAE IV. This is supported by the fact that the percentage of twin whistlers received is very low, but it is comparable to the ratio between whistlers received at SANAE IV and those received at Rothera.

The statistics gathered indicate that for twin whistlers to be received, they should arrive in the southern hemisphere at a location between the two receivers, thus minimising the distance traveled to both stations. It should be mentioned that the statistics are very poor due to the low number of twin whistlers found. This presents an idea for future study, namely to repeat this analysis on a larger overlapping data set. With more AWD data becoming available, the number of twin whistlers observed will increase. This expanded data set could be used to better understand the differences between whistler observations at SANAE IV and Rothera and add further light to the disparity between whistler frequencies at these two sites.

Since only the times of whistlers occurrence were used in this technique, there is no absolute guarantee that the two whistlers which are identified here as twins are in fact identical. A spectral comparison (as well as the time information) of these whistlers would be definitive proof of this. This presents a further opportunity to expand upon this work.

Another point of interest would be to add AWD data from Palmer into the analysis. Palmer is $< 500\ \mathrm{km}$ from Rothera, and shares its source region. Yet there is also a huge disparity in the number of whistlers received at these two locations, with Palmer having half the yearly number of whistler observations of Rothera (as shown by AWD data). With the two stations being so much closer, one expects a higher proportion of twin whistler observations. This analysis would hopefully further contribute to the study.

Chapter 6

Tropical Cyclone Tracking

6.1 Introduction

Tropical cyclones are destructive and unpredictable natural phenomena. They have the capacity for great destruction in populated areas. Tropical cyclones are associated with heavy rainfall, high wind speeds and lightning. These represent an appreciable threat to human life and can also result in major economic losses. The rain causes flooding, which in turn causes damage to infrastructure. This can result in transportation and communication losses in populated areas. Homes are also at risk during these storms, and the displacement of people is always a concern when a tropical cyclone is in the vicinity [Knapp *et al.*, 2010; Kohn *et al.*, 2011].

The tremendous destruction caused by Hurricane Katrina in 2005 had most of its major effects felt in the coastal city of New Orleans. The flooding resulted in many deaths, and the destruction of homes and buildings, which has still not been remedied. Tropical cyclones are also a threat to the east coast of South Africa, where they have made landfall in the past. Perhaps the most famous, was tropical cyclone Demoina, which resulted in severe flooding.

Tropical cyclones are the result of intense heating over warm oceans, which results in deep low pressures forming. The convection which occurs due to this results in energy being extracted from the warm ocean surface, leading to the formation of a storm cell. The abundant energy supplied to the tropical cyclone by the warm ocean results in intensification of the low pressure. When the edge of the tropical cyclone reaches land, it dramatically increases rainfall there. When the eye of the tropical cyclone moves over land, it loses the abundant source of energy from the warm ocean and begins to weaken. If the storm moves back out over the ocean again, however, then it will regain its strength. Even while over the ocean, the high wind speeds of the tropical cyclone cause the height of waves to increase, which can cause damage to buildings, or harm people, directly along the coast [Knapp *et al.*, 2010].

Recently, tropical cyclone Irina developed off the east coast of Africa. It then moved down the coast, through the channel between Africa and Madagascar, towards South Africa. Figure 6.1 shows the track of Irina moving southward, and then westward towards the east coast of South Africa. After moving closer, the tropical cyclone moved away from South Africa, before finally turning back and moving towards South Africa again. Fortunately, it lost strength and dissipated before reaching land again. During the period when Irina was near South Africa, it caused significant flooding, which resulted in the loss of lives and the destruction of property. The track data plotted in Figure 6.1 was obtained from the Regional and Mesoscale Meteorology Branch (http://rammb.cira.colostate.edu/).

These positions in Figure 6.1 are determined using satellite imagery. In this case, the best time resolution was 12 hours, which leaves long periods of time between each observation. Due to the unpredictable nature of a tropical cyclone, its path can change rapidly in the space of twelve hours.

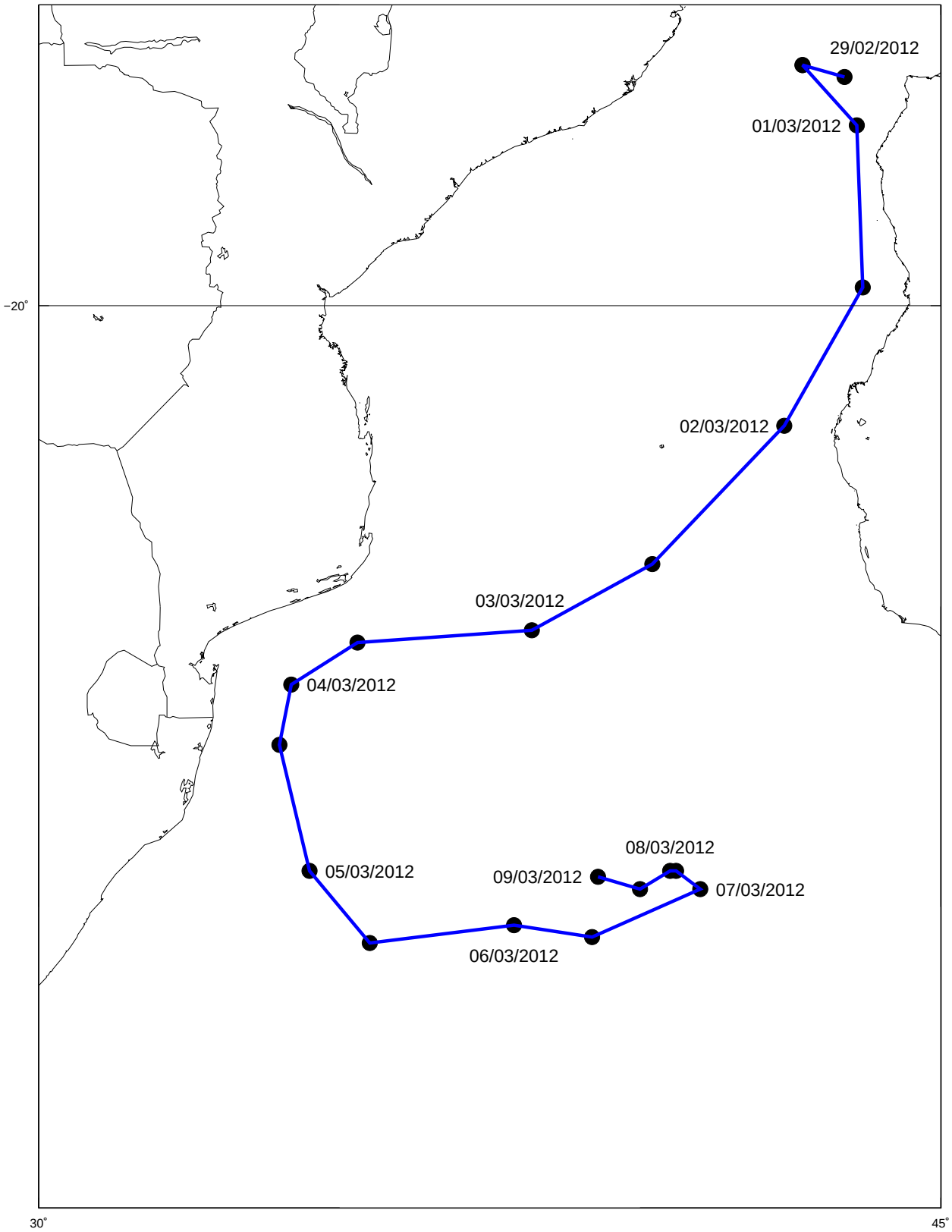

Figure 6.1: The track of tropical cyclone Irina shown with filled circles. The first reported position was at 29/02/2012 00:00 UT. Every successive position is 12 hours after the previous, with the final position reported on 09/03/2012 00:00 UT.

More regular tracking would provide a better tool for issuing early warnings of landfall, and help to better mitigate any fallout in coastal areas.

Lightning has been well correlated with rainfall [Batton, 1965], [Carte and Kidder, 1977] and [Pessi and Businger, 2009]. There have been many successful attempts at tracking lightning producing storm cells. Some have used data radar measurements [Dixon and Wiener, 1993]. Others have relied on satellite measurements [Zinner *et al.*, 2008]. There have also been tracks which rely on lightning data from various lightning location systems [Betz *et al.*, 2008].

Since tropical cyclones are frequently associated with lightning [Price *et al.*, 2007, 2009], a lightning detection network could provide a means of tracking the tropical cyclone in near real time. Unfortunately, most commercial lightning networks only operate on land, and so they do not help with the problem of tracking a tropical cyclone over the ocean. WWLLN, however, has the ability to locate lightning strokes which occur over the ocean. Figure 2.1 clearly shows lightning over warm ocean currents, such as off the east coast of South Africa. It should thus be possible to track such storms using WWLLN data.

The structure of tropical cyclones has been studied using lightning obtained from WWLLN [Solorzano *et al.*, 2008]. This showed the evolution of the lightning production within a tropical cyclone was accurately captured by WWLLN data, including the intensification of eyewall lightning which is associated with the intensification of a tropical cyclone [Molinari *et al.*, 1999].

6.2 Tracking Method

Kohn *et al.* [2011] described a technique for thunderstorm tracking, using VLF located lightning strokes. The algorithm employed is called k-means clustering. This allows for clusters of lightning locations to be identified, differentiating them from isolated lightning discharges. One associates heavy thunderstorms with these clusters. The outer bounds of the clusters are then taken as the boundary of the thunderstorm. After some time step, the algorithm is repeated, and the new location of the thunderstorm is determined. Multiple iterations allow for a storm track to be found. The details of the k-means clustering algorithm are not described here, but many scientific computing languages have their own implementation of the algorithm. Of interest here is the use of the algorithm to track storm cells associated with tropical cyclones.

The algorithm used for tracking tropical cyclones is as follows. Every hour, the WWLLN data from the previous hour are used. This will allow for cyclone tracking with 1 hour timing intervals. This resolution can be increased, although to compensate for the low DE of WWLLN, the value of 1 hour is chosen. In each one hour sample, the clusters are determined using the k-means algorithm. This allows for some tuning, namely how easily the algorithm will expand the area of a particular cluster (thereby decreasing the stroke density in the cluster) to include one more stroke. This tuning can probably be optimised in one region, since it mostly depends on the DE of WWLLN is that region. With the clusters determined, all strokes which are not part of any clusters are discarded. Since two closely spaced points can still constitute a cluster in the k-means algorithm, clusters which are smaller than 5 strokes are discarded.

The last known location of the tropical cyclone is used to seed the algorithm, and the clusters which are within $1000\ \mathrm{km}$ of the last known location of the center of the tropical cyclone are selected. The new center of the tropical cyclone is then the median of the positions of all the strokes in those selected clusters. Every 12 hours, the seed location of the tropical cyclone is set to that found by the satellite at that time.

The method described above was tested on the recent tropical cyclone Irina. Since this tropical cyclone had already occurred, the test is run in pseudo real time after the fact.

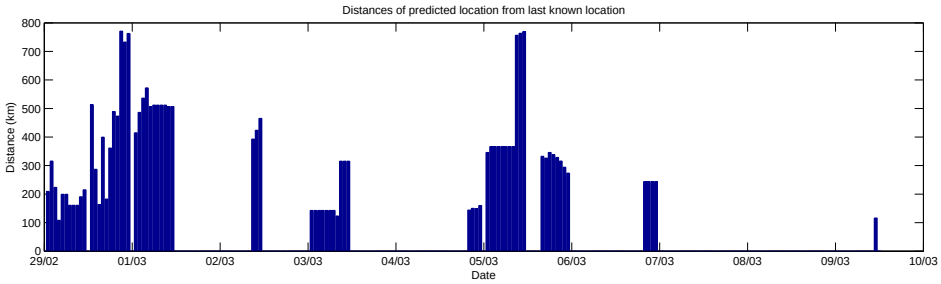

Figure 6.2: The distribution of distances between the current prediction, and the last known satellite position. This distance is reset to zero every 12 hours due to the seeding. Values of zero after these resets imply that no new location was found using the WWLLN data. The figure shows that the algorithm produced locations for three periods of time.

6.3 Results and Discussion

The algorithm is run over the 11 day duration of Irina. The performance of the algorithm over the 11 day period can be determined by checking the distance between predicted locations, and the last known satellite location. The evolution of this value is shown in Figure 6.2. Since the seed location is set to the satellite location every 12 hours, the distance in the histogram is reset to zero every 12 hours. If no new location can be found using the WWLLN data, then this distance remains at zero. This figure shows that the algorithm found locations for the tropical cyclone during the first 36 hours, for 12 hours after 03/03/2012, and for most of 05/03/2012.

It seems as though the algorithm found locations for the tropical cyclone on relatively few occasions. The lack of performance may be attributed to there being few lightning strokes detected by WWLLN during some periods. This may be because of the low DE of WWLLN, or otherwise because the tropical cyclone was not actively producing much lightning at these times. Regardless, it is important to focus on periods where the algorithm had sufficient data to work. In Figure 6.3, the output of the algorithm for two hours where the algorithm had good locations is shown.

The top panel of Figure 6.3 shows a predicted location 4 hours after satellite update, while the lower panel shows a predicted location 1 hour before an update. In (a), the next updated satellite position of the tropical cyclone is further to the west. This motion is captured by the algorithm, as the predicted location in Figure 6.3(a) is to the west of the last known position. In (b), the tropical cyclone was moving towards the south during the period shown in the lower panel of Figure 6.3. The predicted location just one hour before the tropical cyclone position is updated by satellite, is to the north west. In this case, the algorithm has missed the movement of the tropical cyclone. Since it is moving very quickly during this phase of its evolution, it is possible that missing the location early on causes the algorithm to lose the track completely, due to the maximum distance from the last known location used in the algorithm. A possible fix for this would be to retrieve the tropical cyclone speed from the satellite data, and use this to determine the maximum distance from the last known location to search for clusters. Even better, the speed of the cyclone could be determined by the algorithm, and used to update this distance every hour.

There was one period where the algorithm seemed to track the tropical cyclone with particularly good accuracy. In Figure 6.4, 6 locations found during a 12 hour period are shown. During the first hour of this track, the algorithm predicted a location to the west of the last known position (b). During the next few hours, there was insufficient lightning data available to make any predictions about the location, and so the prediction is left at its previous location (c). At 09:00, more lightning is observed, and this moves the prediction west again (d). During the next 2 hours, no new predictions are made (e). At 12:00, the satellite makes another observation (f). The position

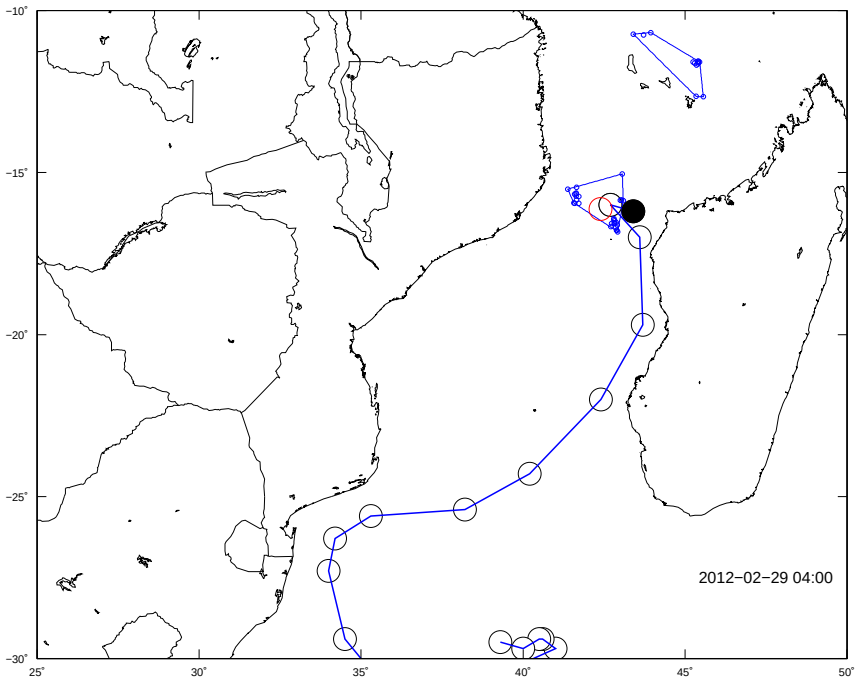

(a) Sample prediction 1

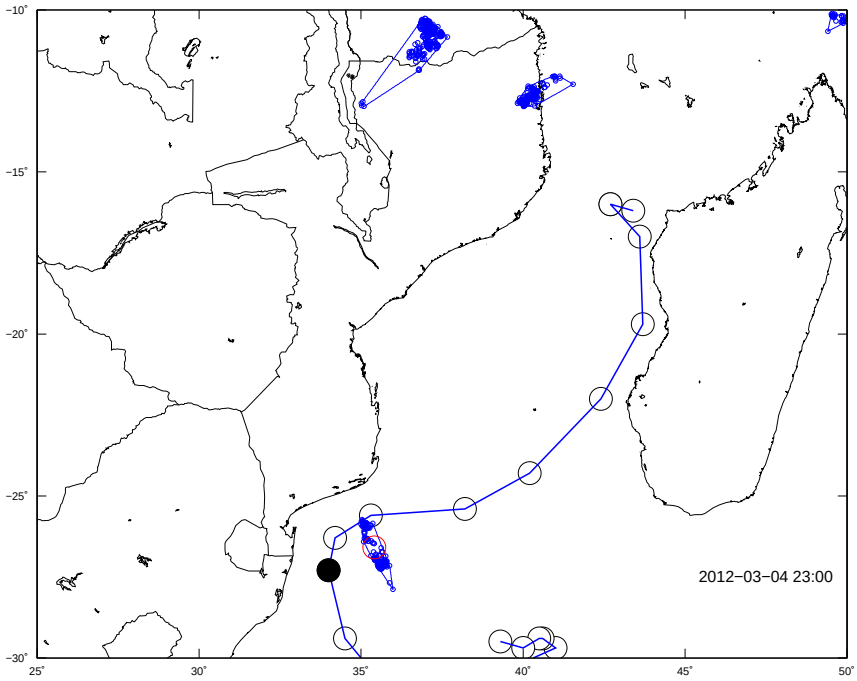

(b) Sample prediction 2

Figure 6.3: The output from the algorithm for two 1 hour periods where locations for the tropical cyclone were found. The predicted location during the hour is shown by the red circle, and the black dot shows the last known position of the tropical cyclone determined by satellite, with black circles showing the entire path of the tropical cyclone. The small blue circles are individual lightning strokes, and the blue polygons represent the area of a cluster. The date and the top of the hour are labeled in the lower right corner of each map. The top panel represents a time 8 hours before the update from satellite shows the tropical cyclone moving to the west, while the lower panel represents a time one hour before the satellite showed the tropical cyclone is moving towards the south.

at 11:00 is very close to the next determined satellite location shown at 12:00. The predicted locations follow the track with good accuracy, indicating that the track was largely accurate during this 12 hour period.

6.4 Conclusion

The method described in this chapter outlines the basics of a tropical cyclone tracking system which uses lightning data from WWLLN. The system uses a mathematical tool called k-means clustering to find clusters in the lightning data. These clusters are then used to discard the lightning data which is only associated with less than moderate lightning activity. The locations of these clusters are then compared to the last known location of the tropical cyclone, either from the algorithm, or from satellite observation. The strokes which belong to the clusters which satisfy this condition are then used to find the next predicted location. The next location is the median of the locations of these strokes.

The method described above was tested on tropical cyclone Irina. The algorithm performed well during most periods in which sufficient data were available. Possible reasons for the lack of performance at other times were a lack of lightning produced by the tropical cyclone, low WWLLN detection efficiency, and finally the tropical cyclone moving too fast for the algorithm to keep track of it. The first problem is beyond human control, as this is a property of the random nature of weather. The second factor may be less of an issue in other areas where WWLLN data has higher efficiency.

The lightning maps which are produced also fail to reveal the complex structure of tropical cyclone Irina, as previous studies using WWLLN data have. This too may be attributed to the lack of lightning produced by this tropical cyclone, and the lower detection efficiency of WWLLN in the southern Indian Ocean when compared to other oceans over which these studies occurred.

A method for taking the speed of the cyclone into account was discussed. This involved using the speed calculated by the satellite imagery to expand or contract the range within which the algorithm looks for clusters. This could be even better implemented if the speed is determined from the algorithm itself, using the predicted locations to predict the speed and adjust its parameters accordingly.

The work here has shown that the WWLLN data is adequate for tropical cyclone tracking near South Africa. While there is definitely room for improvement in the current algorithm, this should serve as a proof of concept. Even though some aspects of the poor tracking cannot be improved, the track would prove worthwhile as it adds extra data for tropical cyclone tracking and warning systems. The algorithm described here should not replace such systems, but rather supplement them, and thus improve forecasting tropical cyclone movements.

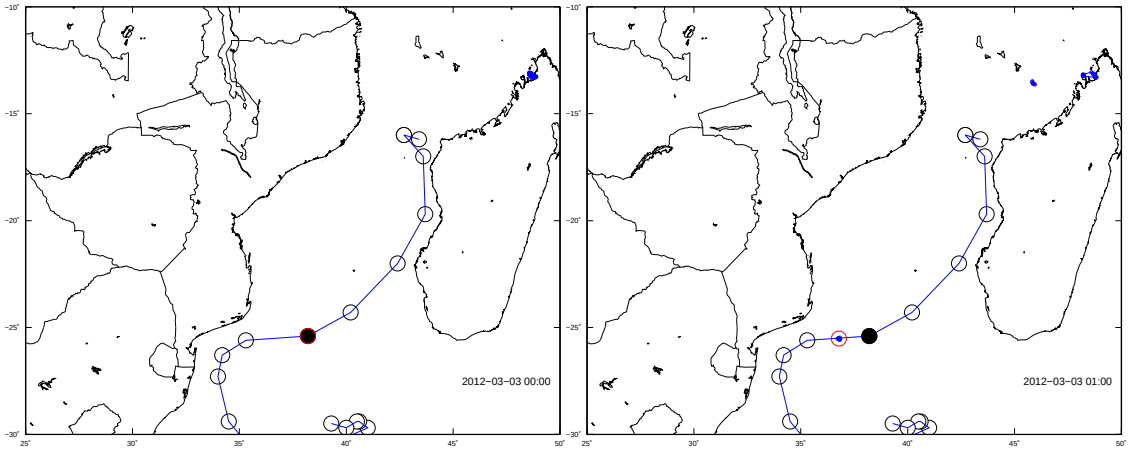

(a) 00:00 UT (b) 01:00 UT

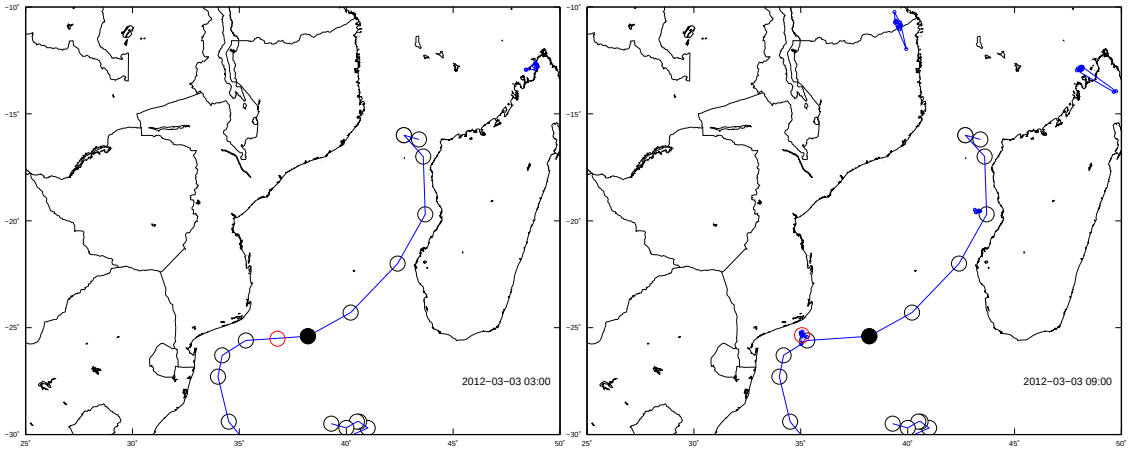

(c) 03:00 UT (d) 09:00 UT

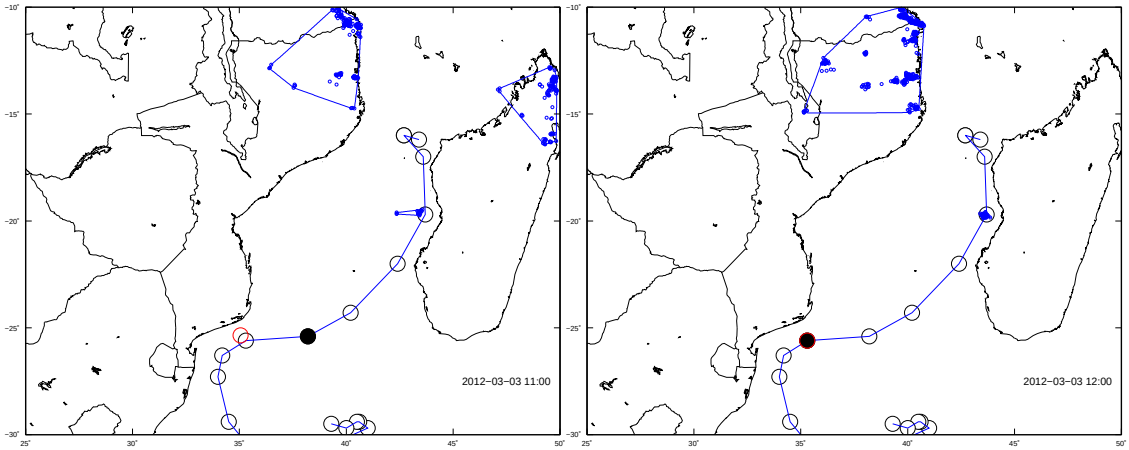

(e) 11:00 UT (f) 12:00 UT

Figure 6.4: The track from the algorithm for 12 hours, starting 03/03/2012 00:00 UT. The maps are of the same form as Figure 6.3. (a) shows the position found by satellite at 00:00. At 01:00, the algorithm moved the predicted location to the west (b). At 03:00 (c), the predicted location had not changed, and this remained the case, until 09:00 (d), where the prediction moved to the west again. It had not moved by 11:00 (e), and at 12:00 the next satellite location coincided almost exactly with the prediction from 11:00 (f).

Chapter 7

Conclusion

This thesis has undertaken a number of studies aimed at better understanding of whistlers, chorus and lightning. The interest in whistlers was prompted by the PLASMON project, of which the SPRI was a member. During the course of this thesis, an exciting observation of chorus was made at Marion Island, which prompted an in-depth analysis. This led to some new analysis techniques being developed. Since whistlers are generated by lightning, study of anything associated with lightning was also of interest. With access to the lightning data provided by WWLLN, another useful application of lightning tracking was investigated, namely the use of WWLLN to track a tropical cyclone. An algorithm was developed and tested on the recent tropical cyclone Irina.

7.1 Source of Whistlers Above South Africa

The results of Collier *et al.* [2009] were not in complete agreement with the mechanism proposed by Storey [1953]. They found that the source region for whistlers received at a location could be as far as $10000\ \mathrm{km}$ from the conjugate point of the receiver.

In Chapter 3, the correlation between whistlers detected on DEMETER while near Tihany's conjugate point and WWLLN lightning was computed. The data recorded by DEMETER was corrected by calculating a time correction factor using lightning data from the SALDN. Finally, the results obtained were refined under statistical testing, and any measurements which were statistically insignificant were discarded. The final result of the analysis is shown in Figure 3.22.

These results showed that:

- Strokes from the region directly beneath the satellite initiated the most whistlers.
- Strokes from a nearby region in Central Africa also initiated a high number of whistlers.
- Strokes from South America initiated a moderate number of whistlers.
- No strokes from the Maritime Continent initiated whistlers on DEMETER while within the burst region.

The first three of these points are in good agreement with the results of Collier *et al.* [2009], while the final one is not. This was found to be due to the times at which DEMETER was within the burst region, which were not times at which lightning was typically observed over the Maritime Continent.

The results presented were only for whistlers traveling a few hundred kilometers to LEO. These whistlers would not necessarily propagate to Tihany and be detected on the ground. An idea for future work would be to find out which of the whistlers detected on DEMETER were

able to propagate to Tihany, by doing a correlation between DEMETER whistlers and whistlers received by the Tihany AWD. One should then be able to say which lightning strokes detected by WWLLN have resulted in whistlers being detected at Tihany. This work presented in this chapter is being submitted for publication.

7.2 Chorus Observed at Marion Island

In Chapter 4, a remarkable observation of chorus which was made at Marion Island was discussed. This was of immediate interest, since Marion Island is typically inside the plasmasphere, and chorus is generated outside the plasmasphere. A number of important conditions surrounding this observation were discussed. It was found that:

- The chorus transformed to hiss.
- Marion Island was close to the plasmapause at the time of the observation.
- Despite the associated geomagnetic storm being of lower intensity than that associated with the chorus observation made at Palmer in 2003, a similar reconfiguration of the radiation belts had occurred.
- A technique using survey mode DEMETER data was developed to quantify the rarity of the observation. This showed that the observation was uncommon near Marion Island for the particular level of solar activity.
- The DEMETER data showed that there was some asymmetry in chorus observation between northern and southern hemisphere, and this was explained in terms of particle temperature anisotropy and the SAA.
- The event presented a ground based observation supporting the recent ideas suggesting that chorus generated plasmaspheric hiss.

The technique used to determine the rarity from DEMETER data could be applied to any spectrogram data set to find features in the data which did not occur frequently, and could be used to create a VLF emission finder. This work has been accepted for publication in the Journal of Geophysical Research (Space Physics).

7.3 Twin Whistlers

Rothera and SANAE IV are both Antarctic research stations where regular VLF recordings are made. AWDs are run at both stations. Analysis of the AWD data has shown that the two receivers share the same whistler source region. The whistler rates for the two stations differ significantly, with Rothera observing on average 15 times more whistlers than SANAE IV.

Chapter 5 briefly described the observation of twin whistlers at Rothera and SANAE IV. These were whistlers which had a single ionospheric exit point into the EIWG (and so had propagated along the same magnetospheric path), and propagated from this exit point to both receivers. Since they had the same magnetospheric path, they would have the same dispersion (and consequently appearance), and hence named “twin whistlers”. An analysis of these twin whistlers revealed the following:

- Only a small fraction (2%) of the SANAE whistlers had a twin in the Rothera data.

- The majority of twin whistlers were observed on days during which Rothera and SANAE IV received an increased number of whistlers.
- These whistlers entered the EIWG preferentially closer to Rothera, with a relatively high probability of re-entry nearly midway between the two receivers.

While the statistics of these results are poor, they do suggest a reason why Rothera observes so many more whistlers than SANAE IV. This is possibly due to the fact that whistlers are entering the EIWG closer to Rothera, and so suffer less attenuation during propagation to the receiver, and consequently have a higher chance of detection. Of course, it is also possible that Rothera, which has a much lower L-value than SANAE IV, is more favorably located with respect to the plasmasphere for the observation of whistlers. The results presented in Chapter 5 are in no way a confirmation of this possibility however.

The analysis presented in Chapter 5 could be improved by using a larger set of overlapping data, which is now available. Furthermore, there also exists a huge disparity between the number of whistlers received at Rothera and Palmer, despite them having the same source region and being only $500\ \mathrm{km}$ apart. Analysis of twin whistlers received at these sites will surely also have interesting results.

7.4 Tropical Cyclone Tracking

In Chapter 6 a technique for tracking tropical cyclones using lightning data from WWLLN is described. This provides a useful long range remote observation tool for tracking the movement of a tropical cyclone. Since WWLLN is a global lightning network, it provides lightning locations over oceans where tropical cyclones are generated, unlike other HF based lightning networks which only operate effectively over land.

The tracking algorithm was applied to the tropical cyclone Irina which made landfall in South Africa in 2012, where it caused severe flooding and led to the loss of several lives. The tracking algorithm performed well for a few days of the tropical cyclone's lifetime. It was able to track the tropical cyclone as it moved towards South Africa before making landfall.

There is room for improvement in the algorithm, but the work presented here serves as a proof of concept that WWLLN data can be used to track tropical cyclones. A possible improvement which could be made is to incorporate speed and direction measurements made by satellite into the algorithm, or to calculate these parameters during the tracking with the algorithm.

Bibliography

G. M. Allcock and J. C. Mountjoy. Dynamic spectral characteristics of chorus at a middle-latitude station. *Journal of Geophysical Research*, *75*(13), 2503–2510 (1970). doi:10.1029/JA075i013p02503.

R. R. Anderson and K. Maeda. VLF emissions associated with enhanced magnetospheric electrons. *Journal of Geophysical Research*, *82*(1), 135–146 (1977). doi:10.1029/JA082i001p00135.

W. C. Armstrong. Lightning triggered from the Earth's magnetosphere as the source of synchronised whistlers. *Nature*, *327*, 405–407 (1987).

D. N. Baker, S. G. Kanekal, X. Li, S. P. Monk, J. Goldstein, and J. L. Burch. An extreme distortion of the Van Allen belt arising from the Halloween solar storm in 2003. *Nature*, *432*, 878–881 (2004).

R. Barr, D. Jones, and C. J. Rodger. ELF and VLF radio waves. *Journal of Atmospheric and Solar-Terrestrial Physics*, *62*(17-18), 1689–1718 (2000). doi:10.1016/S1364-6826(00)00121-8.

L. J. Batton. Some Factors Governing Precipitation and Lightning from Convective Clouds. *Journal of Atmospheric Sciences*, *22*(1), 79–84 (1965). doi:10.1175/1520-0469(1965)022⟨0079:SFGPAL⟩2.0.CO;2.

L. Bernard. A new nose extension method for whistlers. *Journal of Atmospheric and Terrestrial Physics*, *35*(5), 871–880 (1973). doi:10.1016/0021-9169(73)90069-X.

S. L. Bernstein, M. L. Burrows, J. E. Evans, A. S. Griffiths, D. A. McNeil, C. W. Niessen, I. Richer, D. P. White, and D. K. Willim. Long-range communications at extremely low frequencies. *Proceedings of the IEEE*, *62*(3), 292–312 (1974).

J. J. Berthelier, M. Godefroy, F. Leblanc, M. Malingre, M. Menvielle, D. Lagoutte, J. Y. Brochet, F. Colin, F. Elie, C. Legendre, P. Zamora, D. Benoist, Y. Chapuis, J. Artru, and R. Pfaff. ICE, the electric field experiment on DEMETER. *Planetary and Space Science*, *54*(5), 456–471 (2006). doi:10.1016/j.pss.2005.10.016.

H. D. Betz, K. Schmidt, W. P. Oettinger, and B. Montag. Cell-tracking with lightning data from LINET. *Advances in Geosciences*, *17*, 55–61 (2008).

D. J. Boccippio, S. J. Goodman, and S. Heckman. Regional differences in tropical lightning distributions. *Journal of Applied Meteorology*, *39*(12), 2231–2248 (2000). doi:http://dx.doi.org/10.1175/1520-0450(2001)040⟨2231:RDITLD⟩2.0.CO;2.

J. Bortnik, W. Li, R. M. Thorne, V. Angelopoulos, C. Culley, J. Bonnel, O. L. Contel, and A. Roux. An observation linking the origin of plasmaspheric hiss to discrete chorus emissions. *Science*, *324*, 775–778 (2009). doi:10.1126/science.1171273.

J. Bortnik, R. Thorne, and N. Meredith. The unexpected origin of plasmaspheric hiss from discrete chorus emissions. *Nature*, *452*(7183), 62–66 (2008). doi:10.1038/nature06741.

N. Brice. Fundamentals of very low frequency emission generation mechanisms. *Journal of Geophysical Research*, *69*(21), 4515–4522 (1964).

K. Bullough, A. R. W. Hughes, and T. R. Kaiser. VLF emissions on Ariel 3. *Proceedings of the Royal Society of London A*, *311*, 563–590 (1969).

N. L. Bunch, M. Spasojevic, and Y. Y. Shprits. On the latitudinal extent of chorus emissions as observed by the Polar Plasma Wave Instrument. *Journal of Geophysical Research*, *116*(A4) (2011). doi:10.1029/2010JA016181.

W. J. Burtis and R. A. Helliwell. Banded chorus: A new type of VLF radiation observed in the magnetosphere by OGO-1 and OGO-3. *Journal of Geophysical Research*, *74*(11), 3002–3010 (1969). doi:10.1029/JA074i011p03002.

D. L. Carpenter. Whistler evidence of a 'knee' in the magnetospheric ionization density profile. *Journal of Geophysical Research*, *68*(6), 1675–1682 (1963). doi:10.1029/JZ068i006p01675.

D. L. Carpenter. Relations between the dawn minimum in the equatorial radius of the plasmapause and Dst, Kp, and local K at Byrd Station. *Journal of Geophysical Research*, *72*(11), 2967–2971 (1967).

D. L. Carpenter and R. R. Anderson. An ISEE/whistler model of equatorial electron density in the magnetosphere. *Journal of Geophysical Research*, *97*(A2), 1097–1108 (1992). doi: 10.1029/91JA01548.

D. L. Carpenter and C. G. Park. On what ionospheric workers should know about the plasmapause-plasmasphere. *Reviews of Geophysics and Space Physics*, *11*(1), 133–154 (1973).

A. E. Carte and R. E. Kidder. Lightning in relation to precipitation. *Journal of Atmospheric and Terrestrial Physics*, *39*(2), 139–148 (1977). doi:10.1016/0021-9169(77)90107-6.

F. F. Chen. *Introduction to plasma physics and controlled fusion, Volume 1*. Plenum Press (1984).

H. J. Christian, R. J. Blakeslee, D. J. Boccippio, W. L. Boeck, D. E. Buechler, K. T. Driscoll, S. J. Goodman, J. M. Hall, W. J. Koshak, D. M. Mach, and M. F. Stewart. Global frequency and distribution of lightning as observed from space by the Optical Transient Detector. *Journal of Geophysical Research*, *108*, 4005–4019 (2003). doi:10.1029/2002JD002347.

J. Chum, F. Jiříček, O. Santolík, M. Parrot, G. Diendorfer, and J. Fiser. Assigning the causative lightning to the whistlers observed on satellites. *Annales Geophysicae*, *24*, 2921–2929 (2006). doi:10.5194/angeo-24-2921-2006.

S. Church. On the origin of plasmaspheric hiss: Ray path integrated amplification. *Journal of Geophysical Research*, *88*(A10), 7941–7957 (1983). doi:10.1029/JA088iA10p07941.

M. A. Clilverd, C. J. Rodger, R. Gamble, N. P. Meredith, M. Parrot, J. J. Berthelier, and N. R. Thomson. Ground based based transmitter signals observed from space: Ducted or nonducted. *Journal of Geophysical Research*, *113* (2008). doi:10.1029/2007JA012602.

M. A. Clilverd, C. J. Rodger, N. R. Thomson, J. B. Brundell, T. Ulich, J. Lichtenberger, N. Cobbett, A. B. Collier, F. W. Menk, A. Seppälä, P. T. Verronen, and E. Turunen. Remote sensing space weather events: Antarctic-Arctic Radiation-belt (Dynamic) Deposition-VLF Atmospheric Research Konsortium network. *Space Weather*, *7*(4), S04 001 (2009). doi: 10.1029/2008SW000412.

A. B. Collier. Principal Component Analysis of sub-ionospheric propagation conditions. *Proceedings of the 11th International Conference on Ionospheric Radio Systems and Techniques*, 86–90 (2009).

A. B. Collier, S. Bremner, J. Lichtenberger, J. R. Downs, C. J. Rodger, P. Steinbach, and G. Mcdowell. Global lightning distribution and whistlers observed at Dunedin, New Zealand. *Annales Geophysicae*, *28*, 499–513 (2010). doi:10.5194/angeo-28-499-2010.

A. B. Collier, B. Delport, A. R. W. Hughes, J. Lichtenburger, P. Steinbach, J. Oster, and C. J. Rodger. Correlation between global lightning and whistlers observed at Tihany, Hungary. *Journal of Geophysical Research*, *114* (2009). doi:10.1029/2008JA013863.

A. B. Collier and A. R. W. Hughes. Modelling substorm chorus events in terms of dispersive azimuthal drift. *Annales Geophysicae*, *22*, 4311–4327 (2004). doi:10.5194/angeo-22-4311-2004.

A. B. Collier and A. R. W. Hughes. A harmonic model for the temporal variation of lightning activity over Africa. *Journal of Geophysical Research*, *116*(D05105) (2011). doi:10.1029/2010JD014455.

A. B. Collier, J. Lichtenberger, M. A. Clilverd, C. J. Rodger, and P. Steinbach. Source region for whistlers detected at Rothera, Antarctica. *Journal of Geophysical Research*, *116*(March), 1–13 (2011). doi:10.1029/2010JA016197.

N. Cornilleau-Wehrlin, R. Gendrin, F. Lefeuvre, M. Parrot, R. Grard, D. Jones, A. Bahnsen, E. Ungstrup, and W. Gibbons. VLF electromagnetic waves observed onboard GEOS-1. *Space Science Reviews*, *22*(4), 371–382 (1978). doi:10.1007/BF00210874.

J. H. Crary and D. D. Crombie. Antarctic ice cap attenuation rates of VLF signals determined from short and long great circle paths. *Radio Science*, *7*(2), 233–238 (1972).

C. M. Culley, J. W. Bonnell, and R. E. Ergun. THEMIS observations of long-lived regions of large-amplitude whistler waves in the inner magnetosphere. *Geophysical Research Letters*, *35* (2008). doi:10.1029/2008GL033643.

M. Dixon and G. Wiener. TITAN: Thunderstorm Identification, Tracking, Analysis, and NowcastingA Radar-based Methodology. *Journal of Atmospheric and Oceanic Technology*, *10*(6), 785–797 (1993). doi:10.1175/1520-0426(1993)010⟨0785:TTITAA⟩2.0.CO;2.

R. L. Dowden, J. B. Brundell, and C. J. Rodger. VLF lightning location by time of group arrival (TOGA) at multiple sites. *Journal of Atmospheric and Solar-Terrestrial Physics*, *64*(7), 817–830 (2002).

N. Dunckel and R. A. Helliwell. Whistler mode emissions on the OGO 1 satellite. *Journal of Geophysical Research*, *74*, 6371–6385 (1969). doi:10.1029/JA074i026p06371.

J. W. Dungey. Interplanetary Magnetic Field and the auroral zones. *Physical Review Letters*, *6*(2), 47–48 (1961). doi:10.1103/PhysRevLett.6.47.

Y. Ebihara, M. C. Fok, J. B. Blake, and J. F. Fennel. Magnetic coupling of the ring current and the radiation belt. *Journal of Geophysical Research, 113* (2008). doi:10.1029/2008JA013267.

A. Egeland, G. Gustaffson, S. Olsen, J. Aarons, and W. Barron. Auroral zone emissions centered at 700 cycles per second. *Journal of Geophysical Research, 70*(5), 1079–1082 (1965). doi: 10.1029/JZ070i005p01079.

J. Fiser, J. Chum, G. Diendorfer, M. Parrot, and O. Santolík. Whistler intensities above thunderstorms. *Annales Geophysicae, 28*, 37–46 (2010). doi:10.5194/angeo-28-37-2010.

J. C. Foster and T. J. Rosenberg. Electron precipitation and VLF emissions associated with cyclotron resonance interactions near the plasmapause. *Journal of Geophysical Research, 81*(13), 2183–2192 (1976).

C. R. Francis, H. J. Strangeways, and K. Bullough. Discrete VLF emissions (7-9 kHz) displaying unusual banded and periodic structure. *Planetary and Space Science, 31*(5), 537–557 (1983). doi:10.1016/0032-0633(83)90043-0.

R. H. Friedel, T. E. Cayton, and A. Varotsou. Detailed observations of the outer radiation belt with LANL GPS instruments. *AGU Fall Meeting Abstracts*, A42 (2008).

D. I. Golden, M. Spasojevic, F. R. Foust, N. G. Lehtinen, N. P. Meredith, and U. S. Inan. Role of the plasmapause in dictating the ground accessibility of ELF/VLF chorus. *Journal of Geophysical Research, 115* (2010). doi:10.1029/2010JA015955.

D. I. Golden, M. Spasojevic, and U. S. Inan. Diurnal dependence of ELF/VLF hiss and its relation to chorus at L = 2.4. *Journal of Geophysical Research, 114*, 5212–5222 (2009). doi:10.1029/2008JA013946.

D. I. Golden, M. Spasojevic, and U. S. Inan. Determination of solar cycle variations of midlatitude ELF/VLF chorus and hiss via automated signal detection. *Journal of Geophysical Research, 116* (2011). doi:10.1029/2010JA016193.

J. K. Hargreaves. *The Solar-Terrestrial Environment*. Cambridge University Press (1992). doi: 10.1017/CBO9780511628924.

M. Hayakawa, K. Bullough, and T. R. Kaiser. Properties of storm-time magnetospheric VLF emissions as deduced from the Ariel 3 satellite and ground-based observations. *Planetary and Space Science, 25*(4), 353–368 (1977). doi:10.1016/0032-0633(77)90051-4.

K. Hayashi and S. Kokubun. VLF emissions during post breakup phase of polar substorm. *Report Ionosphere Space Research Japan, 25*(4), 369–382 (1971).

R. A. Helliwell. *Whistlers and Related Ionospheric Phenomena*. Stanford University Press, Stanford, California (1965).

R. A. Helliwell. Low-frequency waves in the magnetosphere. *Reviews of Geophysics, 7*(1), 281–303 (1969). doi:10.1029/RG007i001p00281.

R. A. Helliwell, J. P. Katsufrakis, and M. L. Trimpi. Whistler-induced amplitude perturbations in VLF propagation. *Journal of Geophysical Research, 78*(22), 4679–4688 (1973).

R. V. Hogg and E. A. Tanis. *Probability and Statistical Inference*. Macmillan Publishing Company, New York, 3rd edition (1989).

U. S. Inan and T. F. Bell. The plasmapause as a VLF wave guide. *Journal of Geophysical Research*, *82*(19), 2819–2827 (1977).

U. S. Inan, T. F. Bell, and R. R. Anderson. Cold plasma diagnostics using satellite measurements of signals from ground transmitters. *Journal of Geophysical Research*, *82*, 1167–1176 (1977a).

U. S. Inan, T. F. Bell, D. L. Carpenter, and R. R. Anderson. Explorer 45 and Imp 6 observations in the magnetosphere of injected waves from the Siple Station VLF transmitter. *Journal of Geophysical Research*, *82*, 1177–1187 (1977b).

U. S. Inan, R. A. Helliwell, and W. S. Kurth. Terrestrial versus Jovian VLF chorus: a comparative study. *Journal of Geophysical Research*, *88*(A8), 6171–6180 (1983). doi:10.1029/JA088iA08p06171.

A. R. Jacobson, R. H. Holzworth, R. F. Pfaff, and M. P. McCarthy. Study of oblique whistlers in the low-latitude ionosphere, jointly with the C/NOFS satellite and the World-Wide Lightning Location Network. *Annales Geophysicae*, *29*, 851–863 (2011).

F. Jiříček, D. R. Shklyar, and P. Triska. LHR effects in nonducted whistler propagation - new observations and numerical modelling. *Annales Geophysicae*, *19*, 147–157 (2001).

C. F. Kennel and H. E. Petschek. Limit on stably trapped particle fluxes. *Journal of Geophysical Research*, *71*(1), 1–28 (1966).

K. Kersten, C. A. Cattell, A. Breneman, K. Goetz, P. J. Kellogg, J. R. Wygant, L. B. Wilson III, J. B. Blake, M. D. Looper, and I. Roth. Observation of relativistic electron microbursts in conjunction with intense radiation belt whistler-mode waves. *Geophysical Research Letters*, *38*(L08107) (2011). doi:10.1029/2011GL046810.

I. Kimura. Whistler mode propagation in the earth and planetary magnetospheres and ray tracing techniques. *Space Science Reviews*, *42*, 449–466 (1985).

M. G. Kivelson and C. T. Russel. *Introduction to Space Physics*. Cambridge University Press, first edition (1995).

K. R. Knapp, M. C. Kruk, D. H. Levinson, H. J. Diamond, and C. J. Neumann. The International Best Track Archive for Climate Stewardship (IBTrACS) Unifying Tropical Cyclone Data. *Bulletin of the American Meteorological Society*, *91*(3), 363–376 (2010). doi:10.1175/2009BAMS2755.1.

M. Kohn, E. Galanti, C. Price, K. Lagouvardos, and V. Kotroni. Nowcasting thunderstorms in the Mediterranean region using lightning data. *Atmospheric Research*, *100*(4), 489–502 (2011). doi:10.1016/j.atmosres.2010.08.010.

S. Kokubun, K. Hayashi, T. Oguti, K. Tsuruda, S. Machida, T. Kitamura, O. Saka, and T. Watanabe. Correlations between very low frequency chorus bursts and impulsive magnetic variations at L $\sim$ 4.5. *Canadian Journal of Physics*, *59*(8), 1034–1041 (1981). doi:10.1139/p81-136.

H. C. Koons. The role of hiss in magnetospheric chorus emissions. *Journal of Geophysical Research*, *86*(A8), 6745–6754 (1981).

H. C. Koons, B. C. Edgar, and A. L. Vampola. Precipitation of inner zone electrons by whistler mode waves from the VLF transmitters UMS and NWC. *Journal of Geophysical Research*, *86*(A2), 640–648 (1981).

P. Kulkarni, U. S. Inan, T. F. Bell, and J. Bortnik. Precipitation signitures from ground-based VLF transmitters. *Journal of Geophysical Research, 113* (2008). doi:10.1029/2007JA012569.

H. Le, L. Liu, X. Yue, and W. Wan. The ionospheric behaviour in conjugate hemispheres during the 3 October 2005 solar eclipse. *Annales Geophysicae, 27*, 179–184 (2009).

J. Lichtenberger. A new whistler inversion method. *Journal of Geophysical Research, 114*(A07222) (2009). doi:10.1029/2008JA013799.

J. Lichtenberger, C. Ferencz, D. Hamar, P. Steinbach, C. J. Rodger, M. A. Clilverd, and A. B. Collier. Automatic Whistler Detector and Analyzer system: Implementation of the analyzer algorithm. *Journal of Geophysical Research, 115*(A12), 1–7 (2010). doi:10.1029/2010JA015931.

J. Lichtenberger, C. Ferencz, R. L Bodnár, D. Hamar, and P. Steinbach. Automatic whistler detector and analyzer system: Automatic whistler detector. *Journal of Geophysical Research, 113*(A12201) (2008). doi:10.1029/2008JA013467.

W. A. Lyons, M. Uliasz, and T. E. Nelson. Large peak current cloud-to-ground lightning flashes during the summer months in the contiguous United States. *Monthly Weather Review, 126*, 2217–2233 (1998). doi:10.1175/1520-0493(1998)126⟨2217:LPCCTG⟩2.0.CO;2.

J. Manninen. *Some aspects of ELF-VLF emissions in geophysical research*. Ph.D. thesis, University of Oulu (2005).

F. W. Menk. Monitoring spatial and temporal variations in the dayside plasmasphere using geomagnetic field line resonances. *Journal of Geophysical Research, 104*(A9), 19 955–19 969 (1999). doi:10.1029/1999JA900205.

F. W. Menk. Monitoring the plasmapause using geomagnetic field line resonances. *Journal of Geophysical Research, 109*(A4), 1–17 (2004). doi:10.1029/2003JA010097.

N. P. Meredith, R. B. Horne, R. M. Thorne, and R. R. Anderson. Favoured regions for chorus-driven electron acceleration to relativistic energies in the Earth's outer radiation belt. *Geophysical Research Letters, 30*(16) (2003). doi:10.1029/2003GL017698.

S. R. Moiser, M. L. Kaiser, and L. W. Brown. Observations of noise bands associated with the upper hybrid resonance by the Imp 6 Radio Astronomy Experiment. *Journal of Geophysical Research, 78*(10), 1673–1679 (1973). doi:10.1029/JA078i010p01673.

O. A. Molchanov and M. Hayakawa. Subionospheric VLF signal perturbations possibly related to earthquakes. *Journal of Geophysical Research, 103*(A8), 17 489–17 504 (1998).

M. B. Moldwin, L. Downward, H. K. Rassoul, R. Amin, and R. R. Anderson. A new model of the location of the plasmapause: CRRES results. *Journal of Geophysical Research, 107*(A11), 1339–1347 (2002). doi:10.1029/2001JA009211.

J. Molinari, P. Moore, and V. Idone. Convective structure of hurricanes as revealed by lightning locations. *Monthly Weather Review, 127*, 520–534 (1999). doi:10.1175/1520-0493(1999)127⟨0520:CSOHAR⟩2.0.CO;2.

T. P. O'Brien and M. B. Moldwin. Empirical plasmapause models from geomagnetic indices. *Geophysical Research Letters, 30*(4) (2003). doi:10.1029/2009GL016007.

M. N. Oliven and D. A. Gurnett. Microburst phenomena: 3. An association between microbursts and VLF chorus. *Journal of Geophysical Research, 73*(7), 2355–2362 (1968). doi:10.1029/JA073i007p02355.

T. Ondoh, Y. Nakamura, S. Watanabe, and T. Murakami. Latitudinal variation of chorus frequency observed in the topside ionosphere. *Journal of Radio Research Laboratories*, *29*, 1–13 (1982).

M. Parrot, O. Santolík, D. Gurnett, J. Pickett, and N. Cornilleau-Wehrlin. Characteristics of magnetospherically reflected chorus waves observed by CLUSTER. *Annales Geophysicae*, *22*(7), 2597–2606 (2004). doi:10.5194/angeo-22-2597-2004.

A. T. Pessi and S. Businger. Relationships among Lightning, Precipitation, and Hydrometeor Characteristics over the North Pacic Ocean*. *Journal of Applied Meteorology and Climatology*, *66*(4), 833–848 (2009). doi:10.1175/2008JAMC1817.1.

J. H. Pope. A high-latitude investigation of the natural very-low-frequency electromagnetic radiation known as chorus. *Journal of Geophysical Research*, *63*(1), 83–99 (1963). doi:10.1029/JZ068i001p00083.

C. Price, M. Asfur, and Y. Yair. Maximum hurricane intensity preceded by increase in lightning frequency. *Nature*, *2*, 329–332 (2009). doi:10.1038/NGE0477.

C. Price, Y. Yair, and M. Asfur. East African lightning as a precursor of Atlantic hurricane activity. *Geophysical Research Letters*, *31*(L09805) (2007). doi:10.1029/2006GL028884.

J. A. Ratcliffe. *An introduction to the ionosphere and magnetosphere*. Cambridge University Press (1972).

W. K. M. Rice and A. R. W. Hughes. Whistlers, Trimpis and evidence that electron precipitation-may trigger atmospheric discharges. *Journal of Atmospheric and Solar-Terrestrial Physics*, *60*, 1149–1158 (1998).

C. J. Rodger, J. Brundell, and R. Holzworth. Growing detection efficiency of the world wide lightning location network. *AIP Conference Proceedings*, 15–20 (2009). doi:10.1063/1.3137706.

C. J. Rodger, M. A. Clilverd, A. Seppälä, N. R. Thomson, R. J. Gamble, M. Parrot, J. Sauvaud, and T. Ulich. Radiation belt electron precipitation due to geomagnetic storms: Significance to middle atmosphere ozone chemistry. *Journal of Geophysical Research*, *115*(A11), A11 320 (2010). doi:10.1029/2010JA015599.

C. J. Rodger, M. A. Clilverd, N. R. Thomson, R. J. Gamble, A. Seppälä, E. Turunen, N. P. Meredith, M. Parrot, J. A. Sauvaud, and J. J. Berthelier. Radiation belt electron precipitation into the atmosphere: Recovery from a geomagnetic storm. *Journal of Geophysical Research*, *112*(A11), 1–12 (2007). doi:10.1029/2007JA012383.

C. J. Rodger, M. A. Clilverd, T. H. Ulich, P. T. Verronen, E. Turunen, and N. R. Thomson. The atmospheric implications of radiation belt remediation. *Annales Geophysicae*, *24*, 2025–2041 (2006a). doi:10.5194/angeo-24-2025-2006.

C. J. Rodger, S. Werner, J. B. Brundell, E. H. Lay, N. R. Thomson, R. H. Holzworth, and R. L. Dowden. Detection efficiency of the VLF World-Wide Lightning Location Network (WWLLN): Initial case study. *Annales Geophysicae*, *24*, 3197–3214 (2006b). doi:10.5194/angeo-24-3197-2006.

T. Rosenberg, R. Helliwell, and J. Katsufrakis. Electron precipitation associated with discrete very low frequency emissions. *Journal Geophysical Research*, *76*(34), 8445–8452 (1971).

T. J. Rosenberg, J. C. Siren, D. L. Matthews, K. Marthinsen, J. A. Holtet, A. Egeland, D. L. Carpenter, and R. A. Helliwell. Conjugacy of electron microbursts and VLF chorus. *Journal of Geophysical Research*, *86*(A7), 5819–5832 (1981). doi:10.1029/JA086iA07p05819.

C. T. Russel, R. E. Holzer, and E. J. Smith. OGO 3 observations of ELF noise in the magnetosphere: 1. Spatial extent and frequency of occurrence. *Journal of Geophysical Research*, *74*(3), 755–777 (1969). doi:10.1029/JA074i003p00755.

S. S. Sahzhin and M. Hayakawa. Magnetospheric chorus emissions: A review. *Planetary and Space Science*, *40*(5), 681–697 (1992).

B. R. Sandel, A. L. Broadfoot, C. C. Curtis, R. A. King, T. C. Stone, R. H. Hill, J. Chen, O. H. W. Siegmund, R. Raffanti, D. D. Allred, R. S. Turley, and D. L. Gallagher. The extreme ultraviolet imager investigaion for the IMAGE mission. *Space Science Reviews*, *91*, 197–242 (2000).

O. Santolík, D. A. Gurnett, J. S. Pickett, and J. Chum. Oblique propagation of whistler mode waves in the chorus source region. *Journal of Geophysical Research*, *114*(A00F03) (2009). doi:10.1029/2009JA014586.

N. Sato and S. Kokubun. Interaction between ELF-VLF emissions and magnetic pulsations: ELF-VLF emissions associated with Pc3-4 magnetic pulsations and their geomagnetic conjugacy. *Journal of Geophysical Research*, *86*(A1), 9–18 (1981). doi:10.1029/JA086iA01p00009.

J. A. Sauvaud, R. Maggiolo, C. Jacquey, M. Parrot, J. J. Berthelier, R. J. Gamble, and C. J. Rodger. Radiation belt electron precipitation due to VLF transmitters: Satellite observations. *Geophysical Research Letters*, *35*(L09101) (2008). doi:10.1029/2008GL033194.

S. S. Sazhin, K. Bullough, and M. Hayakawa. Auroral hiss: A review. *Planetary and Space Science*, *41*(2), 153–166 (1993).

K. Schindler. *Physics of Space Plasma Activity*. Cambridge University Press (2007).

B. W. Sheeley, M. B. Moldwin, H. K. Rassoul, and R. R. Anderson. An empirical plasmasphere and trough density model: CRRES observations. *Journal of Geophysical Research*, *106*(A11) (2001). doi:10.1029/2000JA000286.

R. Singh, B. Veenadhari, A. Maurya, M. B. Cohen, S. Kumar, R. Selvakumaran, P. Pant, A. K. Singh, and U. S. Inan. D-region ionosphere response to the total solar eclipse of 22 July 2009 deduced from ELF-VLF tweek observations in the indian sector. *Journal of Geophysical Research*, *116* (2011). doi:10.1029/2011JA016641.

A. J. Smith. VELOX: A new VLF/ELF receiver in Antarctica for the global geospace science mission. *Journal of Atmospheric and Solar-Terrestrial Physics*, *57*(5), 507–524 (1994).

A. J. Smith, M. P. Freeman, and C. D. Reeves. Postmidnight VLF chorus events, a substorm signature observed at the ground near L = 4. *Journal of Geophysical Research*, *101*, 24 641–24 653 (1996).

N. N. Solorzano, J. N. Thomas, and R. H. Holzworth. Global studies of tropical cyclones using the World Wide Lightning Location Network. *Proceeding of the Third Conference on Meteorological Applications of Lightning Data, New Orleans* (2008).

M. Spasojevic and U. S. Inan. Ground based VLF observations near L = 2.5 during the Halloween 2003 storm. *Geophysical Research Letters*, *32*, 2001–2004 (2005).

L. R. O. Storey. An investigation of whistling atmospherics. *Philosophical Transactions of the Royal Society of London*, *246*(A. 908), 113–141 (1953). doi:10.1098/rsta.1953.0011.

D. Summers, R. M. Thorne, and F. Xiao. Relativistic theory of wave-particle resonant diffusion with application to electron acceleration in the magnetosphere. *Journal of Geophysical Research*, *103*, 20 487–20 500 (1998). doi:10.1029/98JA01740.

N. R. Thomson, C. J. Rodger, and M. A. Clilverd. Large solar flares and their ionospheric D-region enhancements. *Journal of Geophysical Research*, *110*(A06306) (2005). doi:10.1029/2005JA011008.

B. T. Tsurutani and G. S. Lakhina. Some basic concepts of wave-particle interaction in collisionless plasmas. *Reviews of Geophysics*, *35*(4), 491–502 (1997).

B. T. Tsurutani and E. J. Smith. Postmidnight chorus: A substorm phenomenon. *Journal of Geophysical Research*, *79*(118), 118–127 (1974). doi:10.1029/JA079i001p00118.

B. T. Tsurutani and E. J. Smith. Two types of magnetospheric ELF chorus and their substorm dependence. *Journal of Geophysical Research*, *82*(32), 5112–5128 (1977). doi:10.1029/JA082i032p05112.

J. R. Wait. Earth-Ionosphere cavity resonances and the propagation of ELF radio waves. *Radio Science*, *69D*(8), 1057–1070 (1965).

C. Wang, Q. Zong, F. Xiao, Z. Su, Y. Wang, and C. Yue. The relations between magnetospheric chorus and hiss inside and outside the plasmasphere boundary layer: Cluster observation. *Journal of Geophysical Research*, *116*(A7), 1–10 (2011). doi:10.1029/2010JA016240.

S. Westerlund and F. H. Reder. VLF radio signals propagating over the Greenland ice-sheet. *Journal of Atmospheric and Terrestrial Physics*, *35*(8), 1475–1491 (1973).

K. H. Yearby and A. J. Smith. The polarisation of whistlers received on the ground near L = 4. *Journal of Atmospheric and Solar-Terrestrial Physics*, *56*(11), 1499–1512 (1994).

T. Zinner, H. Mannstein, and A. Tafferner. Cb-TRAM: tracking and monitoring severe convection from onset over rapid development to mature phase using multi-channel Meteosat-8 SEVIRI data. *Meteorology and Atmospheric Physics*, *101*(3), 191–210 (2008).